Structural Characterisation of Porous Materials in Relation to Entrapment of Non-Wetting Fluids

By

Buhari Attahiru Bafarawa (MEng, AMIChemE)

Thesis submitted to The University of Nottingham for the degree of Doctor of Philosophy

Department of Chemical and Environmental Engineering

August 2014

Table of Contents

Page

I dedicate this thesis wholeheartedly to my family

Acknowledgement

First and foremost, I would like to thank and express my sincere gratitude to my supervisor, Dr Sean Rigby, for his time, motivation, and immense knowledge of the research topic. It has been an honour to be his PhD student. I would also like to thank my co-supervisor Dr Trevor Drage for his help and guidance throughout my PhD period.

I would like to thank Dr Adrienne and Shazad Aslam with their time and help in the acquisition of proton experiments, Dr Martin Corfield with his help in the acquisition and reconstruction of X-ray images, Keith Dinsdale with his help in Differential Scanning Calorimetry and mercury porosimetry. Also, I would like to thank Dr Chunyu Jin for his help with the analysis of over 1000 X-ray images.

I would also like to thank my colleagues in Nottingham Shoaib Malik, Dim Paul, Muhammad Rabi'u, and Artjom Nepryahin who have been a source of friendship as well as good collaborators.

Finally, I would also like to thank all my family members for their support and encouragement during these tough years. My special gratitude go to my Dad and Mum, who raised me, supported me, and loved me, whom without I wouldn't have been where I am today. Your dedication, care, encouragement, support and endless love have always been a great inspiration for me during these tough years.

Abstract

An understanding of the physical mechanisms by which non-wetting fluids become entrapped is important to oil recovery techniques from reservoir rocks, and the structural characterization of porous media. The mechanisms of entrapment and the spatial distribution of non-wetting fluid (mercury) within model materials with similar chemical and geometrical properties to oil reservoir rocks have been investigated using mercury porosimetry and computed X-ray tomography. The combination of both techniques has allowed the direct observation of entrapped mercury within the model materials.

In this thesis, a novel experimental technique involving combined mercury porosimetry and mercury thermoporosimetry techniques has been used to determine pore size distributions for disordered porous solids. Mercury porosimetry was conducted, and the mercury entrapped following porosimetry was used as the probe fluid for thermoporosimetry. The fully integrated combination of techniques described here permits the validation of assumptions used in one technique by another. Mercury porosimetry scanning curves were used to establish the correct correspondence between the appropriate Gibbs-Thomson parameter, and the nature of the meniscus geometry in melting, for thermoporosimetry measurements on entrapped mercury. Mercury thermoporosimetry has been used to validate the pore sizes, for a series of sol-gel silica materials, obtained from mercury porosimetry data using the independently-calibrated Kloubek correlations.

A Liquid-liquid exchange (LLE) process within mesoporous materials has also been investigated using NMR relaxometry and NMR diffusimetry experiments. In this method, a high affinity liquid (water) displaced a low affinity liquid (cyclohexane) from the sol-gel silica samples. Entrapment of low affinity liquid was observed which was similar to the entrapment of non-wetting fluid observed in mercury porosimetry. In addition, the molecular diffusion of *n*-pentane has been measured in mesoporous sample using PFG NMR method in a broad temperature range.

Publication

Combining mercury thermoporometry with integrated gas sorption and mercury porosimetry to improve accuracy of pore-size distributions for disordered solids. *Journal of Colloid and Interface Science* (2014), Volume 426, 72-79.

List of Figures

Chapter 2: Petroleum reservoir rocks

Chapter 3: Porous media characterisation methods

Chapter 4: Study of the Entrapment of non-wetting fluid using Mercury Porosimetry and X-ray tomography

Chapter 5: Using Thermoporosimetry to Improve Accuracy of Pore-size Distributions for Disordered Solids

Chapter 6: Porous media characterisation using NMR

Chapter 7: Conclusions and Recommendations

Appendix A: Supporting information for DSC Thermoporosimetry technique

Appendix B: Supporting information for mercury porosimetry experiments

Appendix D: Supporting information for NMR PFG technique

List of Tables

Chapter 2: Petroleum reservoir rocks

Chapter 3: Porous media characterisation methods

Chapter 4: Study of the Entrapment of non-wetting fluid using Mercury Porosimetry and X-ray tomography

Chapter 5: Using Thermoporosimetry to Improve Accuracy of Pore-size Distributions for Disordered Solids

Chapter 6: Porous media characterisation using NMR

Nomenclature

Greek alphabets

Symbol	Description
units	
α	Spins
β	Spins
β	Compressibility factor, Pa^{-1}
δ	Length of applied field gradient, s
μ	Angular momentum of an atomic nucleus
θ	Contact angle between the liquid and the wall of the pore, °
ζ	As defined in the text
ε	Voidage
ŋ	Viscosity, Pa.s
Δ	Diffusion time, s
ΔP	Pressure difference applied
ΔT	Temperature difference, K
Δρ	Density difference between two immiscible fluids, g/cm^3
γ	Gyromagneric or magnetogyric ratio T^{-1} s^{-1}
γ_{Hg}	Surface tension of mercury, Nm^{-1}
γ_{LV}	Surface energy of the solid-liquid interface, Nm^{-1}
σ_{SO}	Interfacial tension between solid and lighter fluid oil, dyn/cm
σ_{SW}	Interfacial tension between solid and denser fluid phase water

Latin Alphabets

Symbol	Definition
A_T	Adhesion tension
B_o	Magnetic field, Tesla
D	Diffusion coefficient, m^2/s
ħ	Plank's constant ($6.62608x10^{-34}$)
I	Spin quantum number
I	Intensity in the presence of diffusion time
I_o	Intensity in the absence of diffusion time
K	Darcy's law constant
K	Temperature, K
K_B	Boltzmann constant, JK^{-1}
R_p	Pore radius, nm
$\langle r^2 \rangle$	Mean square displacement, m^2
T_1	Longitudinal or spin relaxation time, s
T_2	Transverse or spin-spin relaxation time, s
T_o	Melting point of bulk probe liquid, K
T_d	Melting temperature of the probe liquid, K
t_o	Initial time of pulse sequence, s
t_1	Final time of pulse sequence, s
W_a	Energy of solidification of water, J/g
τ_p	Apparent tortuosity, dimensionless
τ_p	Pulse duration, s
V_m	Molar volume of frozen fluid, g/mol
ΔH_m	Latent heat of melting of the probe, J/g

Abbreviation

Acronym

AFM	Atomic force microscopy
BET	Brunauer Emmette Teller
BVI	Bound Volume Index
CPG	Controlled Pore Glasses
CPMG	Carr-Purcell-Meiboom-Gill
CXT	Computed X-ray Tomography
DSC	Differential Scanning Calorimetry
EOR	Enhanced oil recovery
ESEM	Environmental Scanning Electron Microscopy
FFI	Free Fluid Index
FID	Free induction decay
IUPAC	International Union of Pure Applied Chemistry
Kpa	Kilo-Pascal
MIP	Mercury intrusion porosimetry
MPa	Mega-Pascal
NMR	Nuclear magnetic resonance
NS	Number of Scans
PFG	Pulsed Field Gradient
PSD	Pore size distribution
r.m.s	Root mean square
µ-CT	Micro computed tomography
nwf	Non wetting fluid

Chapter 1: Introduction

1.1. Introduction

Oil reserves are spread almost everywhere around the world. The world proved oil reserves at the end of 2012 reached an estimate of 1.67 trillion barrels (OPEC, 2012). This may sound like a huge amount, but the problem is that with the rapid increase in human population and with the increase in consumption of oil year after year (from 86.7 million barrels per day in 2010 to 88.9 million barrels per day in March 2012) there is less than 42 years left in our oil reserves based on current usage figures (OPEC, 2012).

It is predicted that oil will run out sooner due to the consumption and demand of oil in the developing countries like China, India and Brazil where the usage has increase drastically in the past. There is no definite date but it is imminent. Due to this rapid oil consumption and with the price of oil going to an all-time high year after year, extreme measures have to be taken to get more oil from existing oil reservoirs. New technologies and techniques that will enhance the exploration of reservoirs are given more attention, thus enabling to meet the global demand of energy.

As the extraction of hydrocarbons from reservoir rocks becomes more prevalent around the world, the knowledge of the size and pore space in these reservoirs with respect to their potential for producing hydrocarbons becomes more important. However, the determination of the amount of oil reserves that is left after primary and secondary recovery processes is the first step before advancing on increasingly more expensive recovery processes. The amount left

is referred to as bound volume Index (BVI) that is also known as entrapment. The BVI are used to determine the economic viability of secondary recovery and how much oil will be left behind. Thence it's an important parameter used in the industry to detect whether to proceed with production. Mercury porosimetry and NMR CMPG are pore characterisation methods that are widely used in the catalyst and oil industries for the determination of BVI.

This chapter introduces the reader to the general introduction of the project, a brief introduction to petroleum reservoirs, oil recovery methods and the factors that can influence oil recovery. The Aims are outlined as well as the description of thesis chapters.

1.2. Oil reservoirs

Reservoirs are generally bodies of porous and permeable rocks that thence have both storage capacity and the ability to allow fluid to pass through it. Hydrocarbons, formed millions of years ago, start to migrate upward due to their relatively low density through tiny pore spaces until they reach the surface as seepage or become trapped below the surface by non-permeable cap rock that did not allow further migration. These hydrocarbons are formed when large volume of microscopic plant and animal material are deposited in marine, deltaic, or lake environments. The reservoir rocks that hold oil are either sandstones or limestone also referred to as carbonate rocks (Dandeker, 2006).

1.3. Oil recovery

Enhanced oil recovery (EOR) is a general term for any technique used to increase oil production after the primary and secondary production periods. It involves sweeping the oil by some other fluid. The recovery processes are very

important technologies that could help meet the growing demand for oil in the world. It is estimated that roughly 35% (Dawe and Egbogah, 1978) of the oil in place remains in the reservoir after primary and secondary recoveries. The remaining oil can be recovered by applying suitable tertiary recovery processes. There are typically three categories of oil recovery, primary secondary and tertiary (Ezekwe, 2010).

- **Primary recovery**: this is the first stage of oil recovery process. Usually, oil is forced to the surface when the underground pressure in the oil reservoir is sufficient enough. The oil reservoir also contains gaseous fuels, natural gas, or water, which also supply needed underground pressure. During the primary recovery, about 25-30% (Babusiaux and Gestion, 2007) of the oil in a reservoir is recovered.

- **Secondary recovery**: this type of recovery usually occurs in a mature oil reservoir where the inherent pressure has dropped until it is not able to force oil to the surface. It uses various techniques to aid the recovery of oil from low pressure reservoirs. Pumps, such as beam pumps, are usually used to bring the oil to the surface. Other techniques increase the reservoir's pressure by water injection, natural gas injection, and gas lift which inject air, carbon dioxide or other gas into the reservoir. The oil recovered during secondary recovery process is about 25% to 30% (Babusiaux and Gestion, 2007) of the reservoirs oil.

- **Tertiary recovery**: tertiary recovery also known as enhanced oil recovery only begins when secondary recovery is not capable of continuing with oil extraction but can be profitably. One such method

reduces the oil's viscosity to increase oil production. Methods such as thermal enhanced oil recovery are techniques that heat oil and make it easier to extract. Other methods include steam injection, which is the most common form of tertiary recovery method, and is often done with a cogeneration plant. This type of recovery method allows 5-10% (Babusiaux and Gestion, 2007) of oil to be extracted.

1.4. Factors affecting oil recovery

1.4.1. Wettability

One of the most important characteristics of a porous reservoir rock formation, which determines oil production efficiency, is its wettability (Maitland, 2000). This is defined as the tendency of a fluid to spread and wet a solid surface in the presence of other immiscible fluids. It is classified as a key parameter that affects the petro-physical properties of a rock. A fundamental knowledge of reservoir wettability is crucial in determining the reservoir rock properties such as distribution of gas, oil, and water within reservoir rock (Dandeker, 2006). In theory, it should be possible to determine the wettability of reservoir rock-fluid systems by Nuclear Magnetic Resonance (NMR) due to the surface sensitivity nature of NMR relaxation measurements. The measurements obtained can be used to determine the porosity and correlate pore size distribution, bound water and permeability with T_1 and T_2 spectra (Al-Mahrooqi et al., 2003).

1.4.2. Permeability

The permeability of a rock is a measure of its specific flow capacity. It characterises the ability to flow or transmit fluids through a rock when a single fluid, or phase, is present in the rock. By analogy with electrical conductance,

permeability represents the reciprocal of the resistance that the porous medium offers to fluid flow. It is also the proportionality constant between the fluid flow rate and the applied pressure or potential gradient (Dandeker, 2006). Permeability can be expressed by Darcy's law mathematically and is presented below based on the following assumptions:

- Steady state conditions
- The lateral sides of the rock are impervious to fluids
- The fluid does not react with the rock

$$Q = -\frac{K}{\mu} A \frac{dP}{dL} \tag{1.1}$$

Where

Q = the volumetric flow rate (m^3/sec)

K = is the proportional constant or the absolute permeability coefficient expressed in (m^2)

A = Cross sectional area in (m^2)

μ = fluid viscosity in (Nsec/m^2)

dP = pressure drop in (N/m^2) of flow

L = length of the pressure drop (m)

1.4.3. Porosity

Porosity is defined as the ratio of the pore volume (void space) in a reservoir rock to the total volume (bulk volume) occupied by the solid and it is expressed as a percentage (Dandeker, 2006). The pore volume is usually

regarded as the volume of open pores, but it may include the volume of closed pores. It is not always easy to differentiate between roughness and porosity or between pores and voids. In principle, porous materials are of various shapes, sizes and patterns that dictate the nature of pore channels through which fluids are able to flow. These storage capacities of reservoir rocks are called porosity (Dandeker, 2006). Techniques such as thermoporosimetry and mercury porosimetry have been used to characterise porous solids using parameters such as the overall voidage fraction, pore size distribution, specific surface area and pore connectivity (Rigby et al., 2003). These techniques will be discussed in more detail in chaptrer 3, whereas, the factors affecting oil recovery will be discussed in more details in chapter 2 of this thesis.

1.5. Scope of work

The work to be undertaken within this research is centred on the characterisation of mesoporous silica materials to act as model for reservoir rocks. Sandstones is the most common type of reservoir rocks, and its main component is quartz which is fairly a stable mineral, and which can not easily be altered by changes in pressure, temperature, or acidity of pore fluids, and thus makes it a safer and more straightforward choice to replicate sandstone reservoir rock. Also, as the reservoir rocks are chemically and geometrically heterogeneous in nature, understanding the transport processes in them will be difficult. Chemical heterogeneity is due to the presence of various minerals e.g. quartz and, or feldspar. In order to decouple the two types of heterogeneity model materials that are geometrically heterogeneous but not chemically heterogeneous will be used. Catalyst mesoporous materials with the same heterogeneity as reservoir sandstone rock will provide additional information

towards a better understanding of the mechanisms that affect the transport of non-wetting fluids and potentially leads to oil entrapment. The entrapment of oil in strongly water-wet reservoirs by analogy is similar to the displacement by air and subsequent entrapment of mercury as a non-wetting fluid following mercury porosimetry experiment on the silica materials.

Also, one of the key challenges in any oil and gas reservoir is to determine how fluids move through the rock structure during production. It is suggested that a better understanding of the effect of structure of reservoir rock on oil entrapment is useful and may lead to a better extraction of the valuable entrapped hydrocarbons. The total pore volume of reservoir rock is considered to be composed of movable and non-movable fluids which are referred to as the free fluid index (FFI) and bound volume index (BVI) respectively. The BVI and the FFI are usually used in formation evaluation of the economic potential of an oil reservoir as well as modelling of enhanced oil recovery. The BVI is the fluid volume remaining at a preselected capillary pressure, as determined by the centrifugal conditions. However, BVI can also be determined using mercury porosimetry, (Appel et al., 1998).

Carr-Purcell-Meiboom-Gill (CPMG) NMR method can also be used to measure the BVI and FFI of fluid in cores (Miller et al., 1990). An important, most attractive, feature to these measurements is that they can be done on both bench-top NMR instruments and down-hole using well logging tools. Placing the core plug in a magnetic field and applying a sequence of radio frequency pulses usually carry out the CPMG measurements. The pulses are separated by a pre-defined time interval known as the spin echo signal. The signal train comprises of a 90^{o} pulse, followed by a train of 180^{o} pulses. The observed

signal detected after each radio frequency pulse arises from the fluid in the pore space. Therefore for a fluid in a single pore, isolated pore, and for the condition known as the fast diffusion limit the magnetization, decays exponentially with time. The time constant, T_2 known as the transverse relaxation time is related to the pore surface to volume ratio, this was demonstrated by Cohen and Mendelson, (1982). However, this technique comes with several complications that have to be considered. First is the surface chemistry and surface roughness, which can affect the results. Secondly, is the assumption made that the pores are isolated. And thirdly is the effects of pore geometries, e.g., spherical vs. cylindrical, which can affect the relaxation time and pore length.

CPMG technique has been demonstrated by Gopinathan *et al*. (2012). This technique relies upon the measurement of the NMR relaxation properties for a liquid imbibed within the void space of the sample. These researchers used novel NMR approach, which is similar to that of Appel (1998) to determine the spartial location of coke in catalysts. They carried out an experiment on liquid-liquid exchange (LLE) to investigate the displacement of a low affinity liquid (cyclohexane) by a high affinity liquid (water) using CPMG technique. They found out that the displacement of low affinity liquid (cyclohexane) by high affinity liquid (water) occurs rapidly, and thereafter it is very slow. They also observed entrapment of low affinity liquid which was similar to that observed in mercury porosimetry.

Appel et al., (1998) used pulse field gradient (PFG) NMR method, to determine the BVI and FFI, which can also be used to measure the root mean square (rms) displacement of fluid molecules (Karger et al., 1998; Stejskal and

Tanner, 1965; Collaghan, 1991). However, the presence of pore size distribution in rocks will complicate the analysis of PFG data. These researchers adopted a simple model from the BVI and FFI analysis of the CPMG NMR data. They classify the pore size distribution into two categories. First, the pores contributing to the FFI are expected to be large and well-connected making the movement of fluid in these pores free of any restriction. Secondly, the pores contributing to BVI should be strongly restricted thereby making the fluid molecules to make multiple collisions with the pore wall. The model also assumes that there is no exchange of fluids between the fluids volume corresponding to the BVI and FFI. Furthermore, the BVI values obtained by PFG NMR are in good agreement with values from CPMG NMR and both agree well with the BVI values determined by mercury porosimetry and air-brine centrifugation measurements.

Mercury porosimetry is another technique that can be used to measure the BVI. This technique is widely used for the characterisation of pore structure of permeable media, particularly in the catalyst and oil industry. The method consists of gradual intrusion of mercury into an initially evacuated sample by increasing an imposed pressure in small increments, and followed by a gradual retraction of mercury by a stepwise decrease in pressure back to ambient. The mercury leaves the sample at a lower pressure than was required to force it into the structure initially, and some amount of mercury is permanently retained when the pressure has been returned back to ambient. This amount of mercury retention within the sample when the pressure has been reduced back to ambient is generally associated with BVI. Wardlaw and McKellar (1981) studied the pore geometry in sedimentary rocks to identify the characteristics

of pore systems which affect the trapping of non-wetting fluids (BVI), such as mercury during the injection and withdrawal of mercury within the pores. These workers found out that the cause of entrapment during mercury injection-withdrawal capillary test performed on petroleum reservoir rocks was due to non-random structural heterogeneity.

A typical feature of mercury porosimetry data is the hysteresis phenomena, which is found between the intrusion and extrusion curves (Lowell and Shields, 1981; Smithwick and Fuller Jr, 1984; Ternan and Mysak, 1987). Several different theories have been suggested which account for this phenomenon, including contact angle (Van Brakel et al., 1981), a pore potential effect, ink bottle effect (Moro and Bohni, 2002), or the energy requirement to generate a free meniscus on breaking the mercury ganglion at initiation of retraction (Giesche, 2006) Also, Rigby et al., (2003) carried out an experiment on sol-gel silica catalyst using mercury porosimetry, they found that the mercury entrapment occurs in heterogeneously distributed, macroscopic domains within the sample. They also found out that mercury remains stationary within the pore space for a long period of time and that the exact cause of hysteresis in given pore system is often not known. However, experimental studies are required to support these findings. As a result, a combination of mercury porosimetry and computer X-ray tomography methods would be used to reveal additional information on the mechanisms of entrapment so as to have more accurate prediction of the BVI.

Both mercury porosimetry and x-ray tomography are limited by some factors that can affect the experimental results and can lead to inaccurate conclusions. To address the limitations by mercury porosimetry, Androutsopoulos and mann (1979) developed a two-dimensional network model consisting of cylindrical pores assembled into square grids, and thus introduced pore connectivity that is essential in determining the accessibility of the interior of porous materials. However, their simulation model was based on two-dimensional networks that were limited to fixed connectivity and pore length. But yet, they found that mercury entrapment increased as the variance of the PSD got wider and that mercury was preferentially entrapped in larger pores. Also, because mercury must pass through the narrowest pores connecting the pore network, the mercury porosimetry cannot provide a true pore size distribution (Cook et al., 1999). The total porosity values obtained by mercury porosimetry also vary from those obtained by other techniques. However, on the other hand, mercury porosimetry porosities may be closer to actual values than those indicated by other techniques where mercury pressures can collapse small pores or break through isolated pores (Cook et al 1999). The mercury porosimetry is also limited by the "ink-bottle" effect and the possibility to determine only the effective porosity that depends on the kind of pycnometric medium. The mercury porosimetry is also a destructive method that captures mercury within the samples whereas the X-ray tomography in that point of view is a non-destructive method, so the sample are reusable at any conditions (Kovarova et al 2012).

1.6. Aims and Objectives

The aim of the research is to further the understanding of the structural characterisation of porous materials in order to improve the prediction of BVI by conducting mercury porosimetry experiments on sol-gel silica samples and other experimental techniques. The objectives of this work are given below:

- To generalise the theory and expand the experimental work of Rigby *et al.* (2006; 2008; 2011) by using mercury porosimetry on silica and alumina materials in other to obtain pore size distributions, pore surface area, and pore geometry and mercury entrapment on mesoporous materials.
- To utilise the X-ray tomography technique to visualize mercury intruded into disordered silica sample pellet at different equilibration times of 30 and 100s, so as to improve the interpretation of raw mercury porosimetry data, and to also look at time dependence of retraction and entrapment.
- To use mercury thermoporometry to validate the pore sizes, for a series of sol–gel silica materials, obtained from mercury porosimetry data using the independently-calibrated Kloubek correlations.
- Another objective is to check any correspondence that exists between the entrapment of non-wetting fluid from mercury porosimetry technique and the displacement of fluid by another using CPMG NMR.
- To determine the blob sizes of hydrocarbon using different experimental techniques.

1.7. Thesis structure

The overall thesis has been structured into seven chapters.

The first chapter introduces the reader to the general introduction of the project, a brief description of the petroleum reservoirs, oil recovery methods as well as factors that influence oil recovery. Research problems as well as the aims and objectives of the whole project have been mentioned in the first chapter.

The second chapter gives a full detailed description of the formation of petroleum reservoir rocks and also the reservoir rock types. Rock properties and more detailed factors that influence oil recovery are mentioned in section 2.5. Catalyst pellets used for experiments as a model for reservoir rock are also been mentioned at the end of the second chapter.

The third chapter is the literature review of the pore characterisation methods that have been used throughout the project with emphasis to the theory of each technique was outlined in this chapter. Also, limitations to each experimental technique and the scope of each technique were given at the end of each method. Four pore characterisation methods were used in this project.

The fourth chapter discusses the results of the mercury porosimetry intrusion/extrusion data. Semi-empirical alternatives to the Washburn equation also called Kloubek correlations were used to understand the hysteresis phenomena in mercury porosimetry. Also, in this chapter, the materials from MIP experiments were imaged using x-ray tomography to see the spatial distribution of mercury within the void space. It also consists of sample

preparation and the analysis of each data from the MIP and the X-ray tomography images.

Firth chapter introduces the reader to the thermal pore analysis alongside mercury porosimetry experiment, which was termed "mercury-thermoporometry" experiment. This novel technique was used in this project to analyse and determine the pores filled with either hemispherical or cylindrical menisci using the combination of differential scanning calorimetric technique and mercury porosimetry technique.

The sixth chapter looks into the study and behaviour of displacement of non-wetting fluid by wetting fluid using the nuclear magnetic resonance (NMR) technique. It was observed that water was able to displaced cyclohexane from the pores after a certain period of time leaving a small amount of cyclohexane entrapped within the pores such as seen in the entrapment of mercury in the mercury porosimetry technique. The technique was also used to study the equilibrium and dynamic properties confined within Mesoporous material. Molecular diffusion of pentane in silica material has been measured by means of Pulsed field gradient (PFG) NMR method for temperatures not exceeding the boiling point of pentane.

The seventh chapter discusses the general conclusion, future work of this project to be carried out, recommendations and also references.

1.8. Reference

AL-MAHROOQI, S. H., GRATTONI, C. A., MOSS, A. K. & JING, X. D. 2003. An investigation of the effect of wettability on NMR characteristics of sandstone rock and fluid systems. *Journal of Petroleum Science and Engineering,* 39**,** 389-398.

APPEL, M., STALLMACH, F. & THOMANN, H. 1998. Irreducible fluid saturation determined by pulsed field gradient NMR. *Journal of Petroleum Science and Engineering,* 19**,** 45-54.

BABUSIAUX, D. & GESTION, E. D. P. E. D. M. C. É. E. 2007. *Oil and Gas Exploration and Production: Reserves, Costs, Contracts*, Editions Technip.

COLLAGHAN, P. T. 1991. *Principles of Nuclear Magnetic Resonance Microscopy* Clarendon, Oxford.

DANDEKER, A. Y. (ed.) 2006. *Petroleum Reservoir Rock and Fluid Properties*: Taylor and Francis Group.

DAWE, R. A. & EGBOGAH, E. O. 1978. Recovery of Oil from Petroleum Reservoirs. *Contemporary Physics,* 19**,** 355-376.

EZEKWE, N. 2010. *Petroleum Reservoir Engineering Practice,* Pearson Education.

GIESCHE, H. 2006. Mercury Porosimetry: A General (Practical) Overview. *Particle & Particle Systems Characterization,* 23**,** 9-19.

KÄRGER, J., PFEIFER, H. & HEINK, W. 1988. Principles and applications of self-diffusion measurements by nuclear magnetic resonance. *In:* WAUGH, J. (ed.) *Advances in Magnetic Resonance* Academic Press, Inc.

LOWELL, S. & SHIELDS, J. E. 1981. Influence of contact angle on hysteresis in mercury porosimetry. *Journal of Colloid and Interface Science,* 80**,** 192-196.

MAITLAND, G. C. 2000. Oil and gas production. *Current Opinion in Colloid & Interface Science,* 5**,** 301-311.

MILLER, M. N., PALTIEL, Z., GILLEN, M. E. & GANOT, J. 1990. Spin Echo Magnetic Resonance Logging: Porosity and Free Fluid Index Determination. *SPE Annual Technical Conference and Exhibition* New Orleans USA.

MORO, F. & BÖHNI, H. 2002. Ink-Bottle Effect in Mercury Intrusion Porosimetry of Cement-Based Materials *Journal of Colloid and Interface science,* 246**,** 135-149.

OPEC 2012. Global oil supply developments *Monthly Oil Market Report* Vienna, Austria.

RIGBY, S. P., FLETCHER, R. S. & RILEY, S. N. 2003. Determination of the cause of mercury entrapment during porosimetry experiments on sol-gel silica catalyst supports. *Applied Catalysis A: General,* 247**,** 27-39.

SMITHWICK, R. W. & FULLER JR, E. L. 1984. A generalized analysis of hysteresis in mercury porosimetry. *Powder Technology,* 38**,** 165-173.

STEJSKAL, E. O. & TANNER, J. E. 1965. Spin Diffusion Measurements: Spin Echoes in the Presence of a Time-Dependent Field Gradient *The Journal of chemical Physics,* 42**,** 288-292.

TERNAN, M. & MYSAK, L. P. 1987. Hysteresis caused by dimensional changes of porous solids during mercury porosimetry. *Powder Technology,* 52**,** 29-34.

VAN BRAKEL, J., MODRY, S. & SVATA, M. 1981. Mercury porosimetry: state of the art. *Powder Technology,* 29**,** 1-12.

Chapter 2: Petroleum Reservoir Rocks

2.1. Introduction

Chapter 2 of this thesis will introduce the reader to a brief discussion and characteristics of petroleum reservoir. The theory behind oil reservoir rock and its properties will be outlined. Oil recovery methods and the factors that can influence oil recovery will also be discussed.

2.2. Formation of petroleum reservoirs

Petroleum reservoir fluids are fossil fuels that were formed millions of years ago and are found, trapped in rocks in the earth, in both offshore and onshore locations. They are located at depths of up to 3 km, and at temperatures of the order of 350 K and pressure of 700 bar (Dawe and Egbogah, 1978). According to scientific research, petroleum reservoir fluids were formed millions of years ago when animal and plant matter settled into the seabed together with sand, silt and rocks, eventually resulting in a build-up of different layers along the coastline and the sea bottom.

Over geological time scales, pressure (due to burial and depth), and temperature (due to geothermal gradient related to depth) resulted in the conversion of the organic material into petroleum reservoir fluids and the mud, sand and silt into rock (Dandeker, 2006). Although, petroleum reservoir fluids are chemically composed of carbon and hydrogen their widely different molecular composition makes every reservoir fluid unique in nature. The rock containing the organic material that converted into petroleum reservoir fluid is referred to as *source rock*. These fluids start to move upwards due to lower

specific gravity than water through tiny connected pore spaces in the rocks. The pore spaces are usually of the order of 1-100 μm (Dandeker, 2006) wide and are interconnected so that fluids can flow through the reservoir rocks. Also, in the absence of impermeable barriers, some of the fluids move slowly to the surface of the earth.

However, nonporous rocks or other barriers that do not allow further migration trap most of the hydrocarbons. These underground traps of oil and gas are called *petroleum reservoirs*. The schematic diagram of one type of a petroleum reservoir is shown in Fig. 2.1 (Seed, 2011).

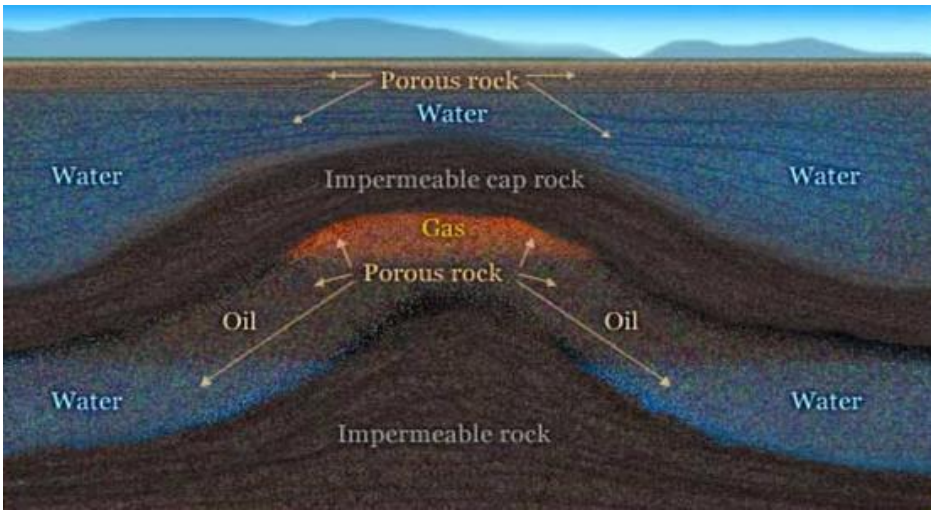

Figure 2. 1: A schematic representation of petroleum reservoir (Seed, 2011)

These petroleum reservoirs are created through a sequence of steps: the first is the deposition of organic matter followed by conversion/migration and entrapment. A normal trap is shown above (Fig. 2.1), which is an anticline. This kind of trap is where rocks have been buckled into the form of a dome. If the anticline has a seal of impermeable rock, hydrocarbons remain in this trap until they are drilled and brought to the surface. These reservoirs are found at

depths as shallow as 40 ft. (west Africa-Gabon) and as deep as 21,000ft in the North Sea-UKCS (Dandeker, 2006).

Petroleum reservoirs contain at least two fluid phases, either gas and water, or oil and water, however, some petroleum reservoirs might contain all the three phases; gas, oil, and water just as seen in Fig. 2.1. In theory, if the fluids are placed in an open container, gravity segregation should separate all three phases into two different layers as per their densities with gas on top followed by oil and water as shown in Fig. 2.1

2.3. Reservoir rocks

Reservoir rocks are basically heterogeneous in nature as well as unique in character. In a heterogeneous geological formation, rock properties vary from one location to another, sometimes drastically within a short horizontal or vertical distance. Reservoir rocks have some basic properties, which can be classified as: either Skeletal or Dynamic. The depositional environment determines the "skeleton" of rocks and different earth processes following deposition. And the 'dynamic' is related to the interaction of the rocks and fluids in the reservoir (Satter et al., 2008). There are three different types of Rocks, which are classified below.

- **Igneous Rocks**: the word igneous is derived from the Latin word 'ignis', which means fire. There a lot of molten metals and minerals inside the earth crust. These melts due to very hot temperature inside the earth and the hot material is called magma. It puts a lot of pressure on earth surface and sometimes earth surface breaks and the magma

comes out which is called lava and some is retain beneath the earth, which is called granite. The cooled lava are called ‘Basalt’

- **Sedimentary Rocks**: the word sedimentary means material that settles to the bottom of a liquid. They are formed by layers of sediments, which comprise rock, as well as dead plants and animals, which have been eroded by strong winds and a strong flow of water in rivers. Most of these particles ultimately reach the sea which gets deposited on the sea bed. As more and more particles get settled on each other, they press each other and compression happens. The sediments at the bottom change into sedimentary rocks. This process takes thousands of years. Examples of sedimentary rocks are limestone, chalk, sandstone, coal etc.
- **Metamorphic Rocks**: derived from the Greek words ‘meta’ and ‘morph’, this means to be change or to transform. Metamorphic rocks are changed forms of sedimentary and igneous rocks. They are formed when other types of rocks are changed due to a lot of heat or pressure. Typical examples are marble and slate.

Most oil and gas producing reservoir rocks are sedimentary in nature. Therefore, an understanding of the morphology is of great importance. The two major reservoir rocks are sandstones and carbonates and are explain in detail below.

2.3.1. Sandstones reservoir rocks

Sandstone rocks are aggregates of particles, and they come in graded types ranging from clean to dirty, coarse to very fine-grained, white to black, and no lime to limey. They are composed of mineral particles mainly grains of quartz (silica SiO_2), feldspars, and rock fragments which are fairly stable minerals and are not easily altered by changes in pressure or temperature. And also, they are formed by the re-deposition of pre-existing rocks as a consequence of erosion.

2.3.2. Carbonate reservoir rocks

Carbonate reservoir rocks are created in marine and sedimentary environments with little or no clastic material input. They consist of mostly limestone ($CaCO_3$) and dolomite ($CaCO_3$, $MgCO_3$). They are formed from chemical precipitates and organic constituents. Their physical characteristics range from spongy to chalks, and cavernous. The main biochemical agents in the formation of limestone are bacteria, algae, corals, bryozoa, and molluska.

2.4. Traps

Petroleum reservoir traps consist of a combination of physical factors that promote the accumulation and retention of petroleum in one location. The traps can be classified as either structural, or stratigraphic or a combination of the two, as seen in Fig. 2.2 below.

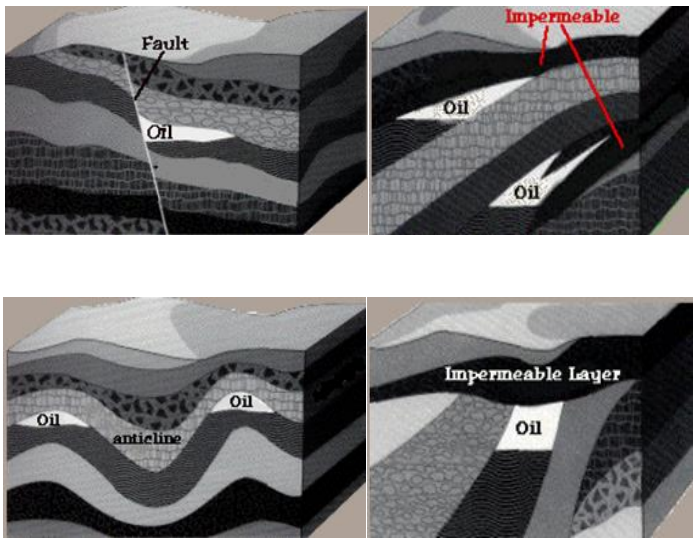

Figure 2. 2: Illustration of different types of trap in reservoir rock (Halliburton, 2001)

Processes such as faulting, folding, deposition and erosion create irregularities in the subsurface strata, which may cause oil and gas to be retained in a porous formation, thereby creating a petroleum reservoir. The rocks that form the barrier, or trap, are referred to as cap rocks (Halliburton, 2001)

2.5. Skeletal rock properties

2.5.1. Porosity

Petroleum reservoir rocks are mostly sandstones; they appear to be solid but are often not so solid. These sandstones start as individual sand particles of varying grain sizes that were buried and compressed as part of the depositional process, resulting in spaces remaining between the particles. The grains are of various shapes, sizes and patterns that dictate the nature of pore channels through which fluids are able to flow. The storage capacities of reservoir rocks are called porosity (Dandeker, 2006).

Porosity is the ratio of the pore volume (void space) to the total volume (bulk volume) and is usually expressed as a percentage. Mathematically, porosity is given by:

$$\phi = \frac{pore\ volume}{total\ or\ bulk\ volume} \tag{2.1}$$

2.5.1.1. Types of porosities

A solid material is said to be porous when it contains pores, i.e. cavities, or channels, which are deeper than they are wide. Some of the pores in the materials arise from agglomerated or aggregated powders in which the pores are interconnected with other void spaces and, as a result, from a network, while others are based on continuous solid network around pores. Some pores in the solid material are known to become completely isolated or closed from other void spaces because of cementation (Schubert and Husing, 2005).

Fig. 2.3 shows a schematic representation of a porous material. They are usually classified by describing their accessibility to an external fluid. The first category is the one that is totally isolated from their neighbours, as in region (a) are called closed pores. They influence macroscopic properties of the solid such as bulk density, mechanical strength and thermal conductivity, but they are inactive in terms of chemical reactions. However, pores that are open to the external surface of the solid, such as (b), (c), (d), (e), and (f) are referred to as open pores. Some may be open only at one end, such as (b), and (f), and they are described as blind pores. Others may be open at both ends (through pores) like (e). Pores may also be classified according to their shape. They may be cylindrical (either open (c) or blind (f)), ink-bottled shaped (b), funnel shaped

(d) or slit-shaped. Close to, but different from porosity is the roughness of the external surface, represented around (g) (Schubert and Husing, 2005).

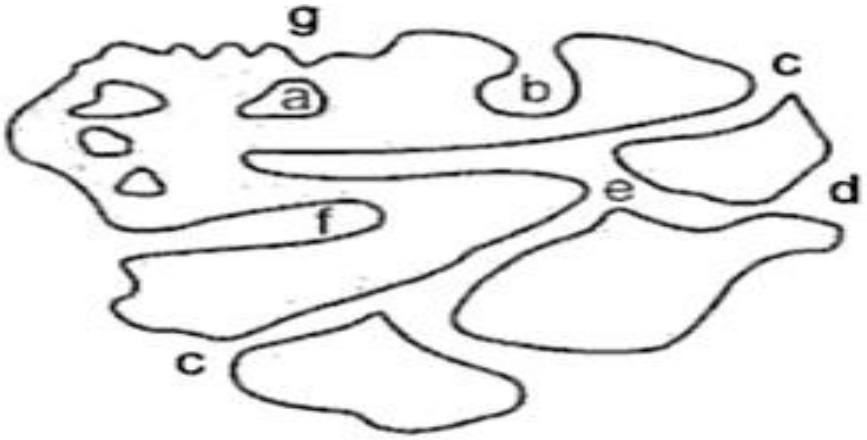

Figure 2. 3: Schematic representation of different types of pores (Schubert and Husing, 2005).

- **Absolute or Total porosity**: The total or absolute porosity is the ratio of the total void space in the reservoir rock to the total bulk volume of the rock:

$$\phi = \frac{total\ pore volume}{total\ or\ bulk\ volume} \tag{2.2}$$

Or

$$\phi = \frac{\begin{pmatrix} vol.of\ \text{int}erconnected\ pores + vol.of\ deadend \\ or\ culdesac\ pores + vol.of\ isolated\ pores \end{pmatrix}}{total\ or\ bulk\ volume} \tag{2.3}$$

- **Effective porosity**: It is defined as the ratio of the volume of interconnected pores and the dead-end or cul-de-sac pores to the total

or bulk volume. It is represented mathematically by the following expression as:

$$\phi = \frac{Vol.of\ \text{int}erconnected\ pores + vol.of\ deadend\ or\ cul-de-sac\ pores}{total\ or\ bulk\ volume} \quad \text{Or} \quad \phi = \frac{C}{B} \qquad (2.4)$$

Where;

C = Vol. of interconnected pores + Vol. Of dead-end pores

B = Total or bulk volume

It is worthy of mention that the effective porosity is the quantitative desired value, and is used in all calculations because it represents the pore space that is occupied by mobile fluids. The effective porosity of rocks varies between less than 1% to over 40%. It is often stated that porosity is:

- Low if ϕ < 1%
- Medium if 5%< ϕ <10%
- Average if 10%< ϕ <20%
- Good if 20%< ϕ <30%
- Excellent if ϕ >30%

- **Ineffective porosity:** It is defined as the ratio of the volume of isolated or completely disconnected pores to the total or bulk volume.

$$\phi = \frac{vol.of\ completely\ disconnected\ pores}{total\ or\ bulk\ volume} \quad (2.5)$$

However, the closed (isolated) or completely disconnected pores are ineffective in producing any petroleum reservoir fluids due to their isolation (Danfekar, 2006).

2.5.2. Classification of porosity

Reservoir rock porosity can be generally classified by its mode of origin, which is either original, or induced. Original or induced porosity is also known as primary or secondary porosity and is developed in the deposition of the material. Some geological processes following the deposition of the rock, on the other hand develop induced porosity. A good example of induced porosity is the development of fractures, which are commonly found in limestone. Reservoir rocks that have original porosity are more uniform in their characteristics than those rocks in which a large part of the porosity is induced.

2.5.3. Absolute permeability

The permeability of a rock is a measure of its specific flow capacity; it signifies the ability to flow or transmit fluids through a rock when a single fluid, or phase, is present in the rock. By analogy with electrical conductance, permeability represents the reciprocal of the resistance that the porous medium offers to fluid flow. It is also the proportionality constant between the fluid flow rate and the applied pressure or potential gradient (Dandeker, 2006). Permeability can be expressed by Darcy's law mathematically, and is presented below based on the following assumptions:

- Steady state conditions
- The lateral sides of the rock are impervious to fluids
- The fluid does not react with the rock

Let us consider a sample of length dx and a cross-sectional area A, saturated with a fluid of dynamic viscosity μ, and inversed horizontally by a flow rate Q (measured in the conditions of section dx) as shown in Fig. 2.4 (Cosse, 1993).

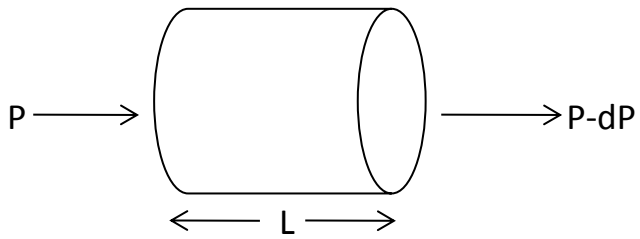

Figure 2. 4: Schematic representation of Darcy's Law

In steady state conditions, the upstream pressure is P, and the downstream pressure is P (-dP). Then:

$$Q = -\frac{K}{\mu} A \frac{dP}{dL} \tag{2.6}$$

Equation (2.6) is Darcy's law. It is absolute or specific permeability of the sample in the direction considered.

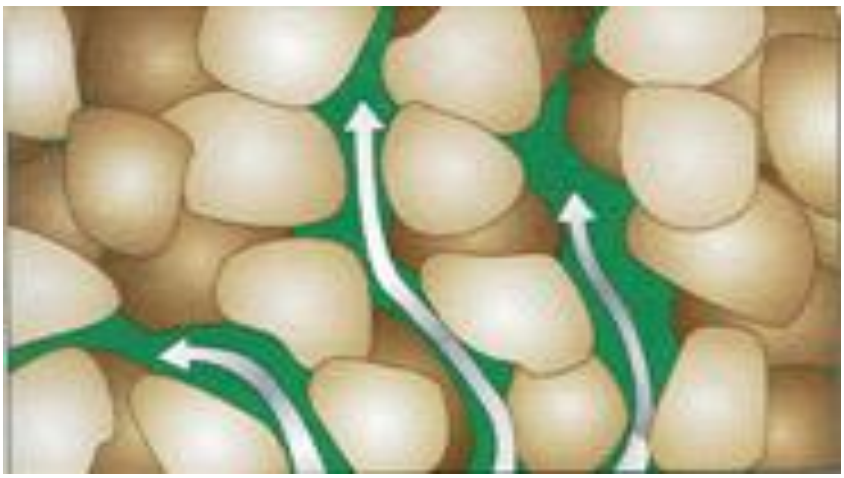

Figure 2. 5: Illustration of permeability of a reservoir rock (MPG Petroleum, 2011)

2.5.4. Relative permeability

Relative permeability is defined as the ratio of effective permeability of a particular fluid at a particular saturation to absolute permeability. The pore space of a reservoir rock or a pore volume does not contain one phase but multiple fluid saturations of gas, oil, and water, and the magnitude of these determines the distribution of the pore space (Dandeker, 2006). The concept of relative permeability provides a mechanism of quantifying the amount of flow for each phase in a multiphase situation. The relative permeability is considered to be one if a single fluid is present in a rock.

2.5.5. Pore Size Distribution

The pore size distribution (PSD) is typically a probability density function of pore size weighted by volume or number. Pore size distribution influences the fluid saturation distribution in a porous medium, permeability, and to some extent wettability. Pore with sizes in reservoir rock are characterized as small pores, medium pores, and large pores. They are also classified as nanopores, mesopores and micropores. Mercury injection and DSC thermoporosimetry are

common techniques used to determine pore size distribution in a rock sample. Table 2.1 shows the International Union of Pure and Applied Chemistry (IUPAC) classification scheme of pore sizes.

Table 2. 1: IUPAC classification of pore sizes

Porosity type	Size (d)
Micropores	2nm > d
Mesopores	50nm > d > 2nm
Macropores	d > 50nm

2.6. Dynamic Rock properties

2.6.1. Interfacial and surface tension

In petroleum reservoirs, three fluid phases, gas, oil, and water, may coexist. These fluid phases in a petroleum reservoir are generally immiscible at any reservoir conditions. When these fluid phases with a petroleum reservoir are in contact, they are separated by well-defined interface between gas-oil, gas-water, and oil-water pairs. However, when dealing with a multiple systems such as those encountered in petroleum reservoirs, it is necessary to consider the effect of the forces that exist at the interface when two immiscible fluids are in contact. The term interface indicates a boundary or dividing line between two immiscible phases (Dandeker, 2006). Different types of interface may coexist, namely: liquid-gas, liquid-liquid, liquid-solid, and solid-gas. For a liquid which is in contact with air or vapour of that liquid, the force per unit length required creating a unit surface area is usually referred to as the surface

tension. The macroscopic scale of interfacial tension (IFT) or surface tension (ST), a system of two immiscible fluids, oil and water is shown in Figure (2.6).

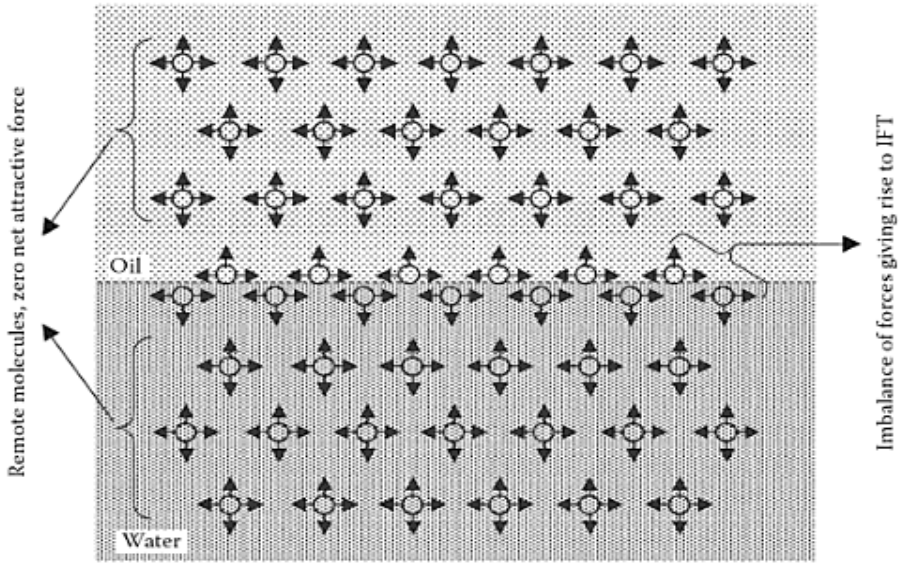

Figure 2. 6: The concept of interfacial tension (IFT) between two immiscible liquids (Dandeker, 2006).

Molecules of oil and water remote from the interface are surrounded by other oil and water molecules respectively, resulting in a net attractive force on the molecule as it is pulled in all directions. On the other hand, a molecule at the interface has force acting upon it from the oil lying immediately above the interface and water molecules lying below the interface. The resulting forces are not balanced because of the forces from below and above are different, and give rise to interfacial tension.

Interfacial tension between two immiscible liquids can be expressed in terms of the following:

$$\sigma = \frac{rhg\Delta\rho}{2\cos\theta} \tag{2.7}$$

Where σ is the interfacial tension (dyn/cm), r is the radius of capillary tube (cm), h is the height of the capillary column (cm), $\Delta\rho$ is the density difference between two immiscible liquids (g/cm^3), and θ is the contact angle.

2.6.2. Capillary pressure

Capillary pressure occurs in porous materials when two or more immiscible fluids are present in the pore space. Each immiscible fluid either side of the meniscus has a pressure that is different from that of the other immiscible fluid. This is due to the curvature of the interface that generally arises in confined geometries. This particular difference between the pressure of the non-wetting phase and the pressure of the wetting phase is called the capillary pressure and denoted as P_c. Capillary forces in a petroleum reservoir are due to the combined effect of surface and interfacial tensions, geometry, size of the pore, and wetting characteristics (Dandeker, 2006).

By considering a large vessel as shown in Fig. 2.7, where the interface at location 1 is a flat oil-water interface and the capillary pressure is zero, i.e. $P_{o1} = P_{w1}$ at the free water level in the large vessel (Dandeker, 2006).

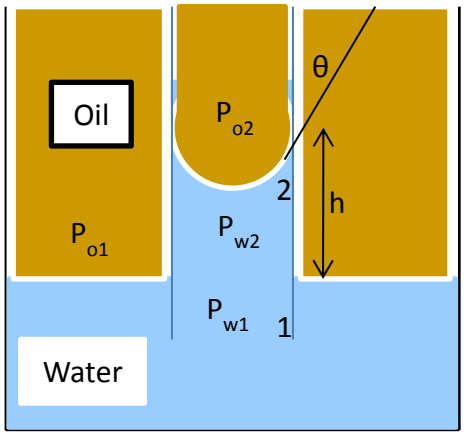

Figure 2. 7: Pressure relations in capillary tubes for an oil-water system (Dandeker, 2006).

If the oil and water are in equilibrium and not flowing, the capillary pressure must be in equilibrium with the gravitational forces. Capillary pressure between two immiscible fluids namely oil and water can be expressed mathematically in terms of the following.

$$P_{cow} = \frac{2\sigma_{ow}\cos\theta_{ow}}{r} \tag{2.8}$$

Where P_{cow} is the oil water capillary pressure, σ_{ow} is the oil-water interfacial tension, and θ_{ow} the contact angle.

2.6.3. Wettability

Wettability plays an important role in fluid distribution and flow behaviour within a reservoir. It is defined as the tendency of a fluid to spread and wet a solid surface in the presence of other immiscible fluids. It is also a key parameter that affects the fluid distribution within a core of a reservoir rock, thus the knowledge of reservoir wettability is crucial in determining the reservoir rock properties such as distribution of gas, oil, and water within a reservoir rock. Others are capillary pressure and relative permeability which are controlling parameters for fluid flow and displacement of one fluid by another (Zahoor and Derahman, 2013). The tendency of a fluid phase to spread over the surface of the solid indicates the wetting characteristics of the fluid for the solid. The most common method of determining rock wettability is by measurement of the contact angle, θ, between the rock surface and fluid system (Ezekwe, 2010).

For example, a system which comprises of oil, water (brine), and rock, (sandstone or a carbonate), one of the phases has a tendency to wet the rock. This concept of wettability is illustrated in Fig. 2.8.

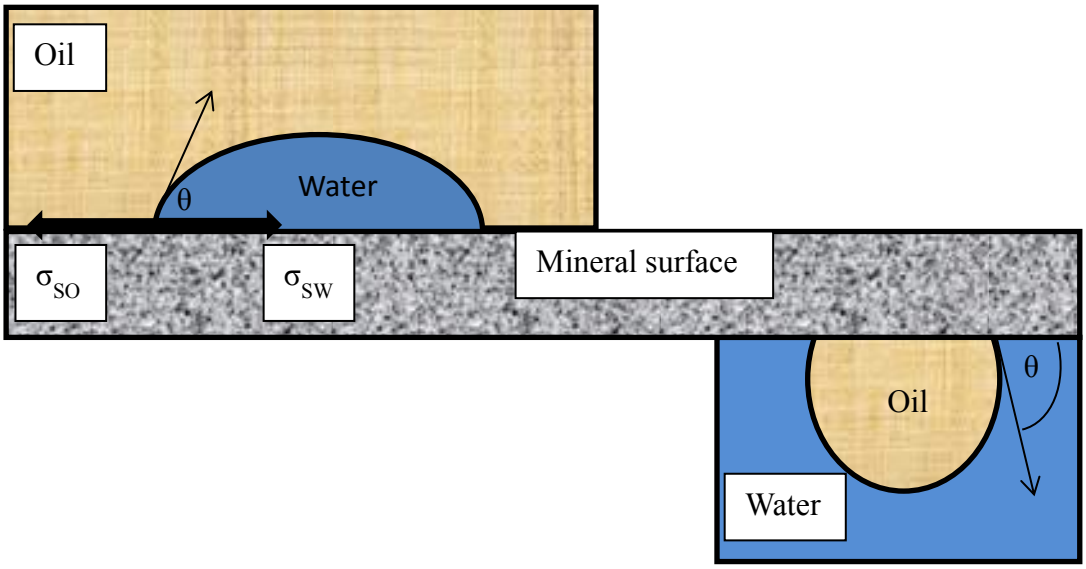

Figure 2. 8: A system of two immiscible liquids (oil and water) in contact with a mineral surface

The spreading tendency of a fluid can be expressed as adhesion tension A_T. Adhesion tension is a function of the interfacial tension and determines which fluid preferentially wets the solid. Considering a system of two liquids, such as oil and water that are in contact with solid as illustrated in Fig. 2.8 above, the adhesion tension is defined by:

$$A_T = \sigma_{SO} - \sigma_{SW} \tag{2.9}$$

Where σ_{SO} is the interfacial tension between the solid and the lighter fluid phase (oil in), and σ_{SW} is the interfacial tension between the solid and the denser fluid phase (water). The contact angle, θ at the liquid-solid surface is

shown in Fig. 2.8. This contact angle is measured through the denser liquid phase and can range from 0^0 to 180^0. By definition the cosine of the contact angle θ is

$$\cos\theta_{OW} = \frac{\sigma_{SO} - \sigma_{SW}}{\sigma_{OW}} \tag{2.10}$$

Combining the two equations yield:

$$A_T = \sigma_{OW} COS\theta_{OW} \tag{2.11}$$

According to equation 2.11, positive adhesion tension indicates that the denser phase (water) preferentially wets the solid surface, whereas a negative value of adhesion tension indicates a wetting preference by the lighter phase (oil) (Dandeker, 2006).

2.7. Catalysts pellets as model for reservoir rock

From section 2.3 it has been explained that majority of oil and gas producing reservoir rocks are made up of sandstones and carbonates. They can be found both in offshore and onshore locations. Also, as earlier mentioned in section 1.5, the reservoir rocks are chemically and geometrically heterogeneous in nature and contain some impurities such as iron, magnesium etc. They can be obtained by a process called coring, and are recovered undamaged preserving the physical and mechanical integrity of the rock (Dandeker, 2006).

Catalyst support pellets with the same chemical components as sandstone reservoir rocks are investigated in this study, which are free of impurities to determine the pore structure of a rock samples. These materials have the same

chemical and geometrical properties as the silica phase in sandstone rock core samples. Thus a direct comparison could be made in terms of basic surface chemistry and wettability effects. The silica materials are formed when a silicate solution such as sodium silicate is acidified; a gel of polymeric colloidal silicilic acid is formed as a collection of micro-particles. When the gel is heated, water is expelled from the silica leaving a hard, glassy structure with voids between the micro-particles which is equivalent to a mean pore diameter of about 3 nm and an internal surface of about 500,000 m^2/kg (Coulson, 2002). Sol-gel silica's are composed of packing of silica spheres like grains of sand in sandstones. The Mesoporous materials are produced when the reaction is carried out at the higher pH ~6 (Rouquerol et al., 2014). Also, as the temperature is increased during the processes, the pore volume and mean radius of silica and silica-alumina gels increases. However, the pore surface remains constant. The alumina samples are prepared by the controlled heating of hydrated alumina. Water molecules are expelled and the crystal lattice ruptures along planes of structural weakness which results in a well-defined pore structure and a mean pore diameter of about 4 nm and a surface area of 350,000 m^2/kg (Coulson, 2002). Furthermore, the determination of pore size distribution of a reservoir rock is often complicated than the simplified silica materials due to the presence of minerals deposits (e.g., feldspar, clays, or metal oxides)

Table 2.2 shows a list of different range of silica pellets that have been investigated in the literature and also used for this study. The majority of the materials have been used in the study of mercury entrapment and structural characterization by various researchers (Rigby et al., 2003; Rigby et al., 2008a;

Rigby et al., 2008b; Gopinathan et al., 2012; Shiko et al., 2013; Hitchcock et al., 2014). The pore sizes ranges from 7-40 nm. The materials are available commercially and were supplied by three different suppliers, namely: Micromeritics, SIGMA-ALDRICH CHEMIE, AND Johnson Matthey. These materials are widely used as inexpensive adsorbents, desiccants and catalyst supports. Fig. 2.9 is photomicrographs of a sandstone rock containing minerals of quartz, feldspar, and rock fragments. Fig. 2.10 is a scanning electron microscopy (SEM) image of a sandstone rock containing no impurities and minerals. Fig. 2.11 to Fig. 2.13 is the atomic force microscopy (AFM) images of G1 and G2 silica materials at different resolutions. In addition, Fig. 2.14 to 2.17 shows the environmental scanning electron microscopy (ESEM) images of a typical sample from controlled pore glasses (CPG) with different resolutions. The black patches are pores located within the CPG matrix. The pores are roughly circulated in cross section with sizes of ~24nm and 50nm respectively. Also, the spatial distribution of pores is also roughly uniform to the eye.

Table 2. 2: Details of different batches of silica samples studied in this work

Sample	Sample Denoted	Material	Pellet form	Nominal particle size (mm)	Surface area (m^2/g)
S980A	S1	Silica gel	Gel sphere	3	242±3.30
S980G	S2	Silica gel	Gel sphere	2.2	93±0.46
C10	G1	Silica gel	Gel sphere	3	540±3.01
C30	G2	Silica gel	Gel sphere	3	191±1.72
AL-3992E	A1	Alumina	Extrudate	3	314±4.40
Silica Alumina	S3	Silica/Alumina	Extrudate	0.5	386±2.23
AL-3984T	A2	Alumina	Tablet	3	168±2.32
CPG24	CPG	Glass	Powder	0.125	160.99±1.06

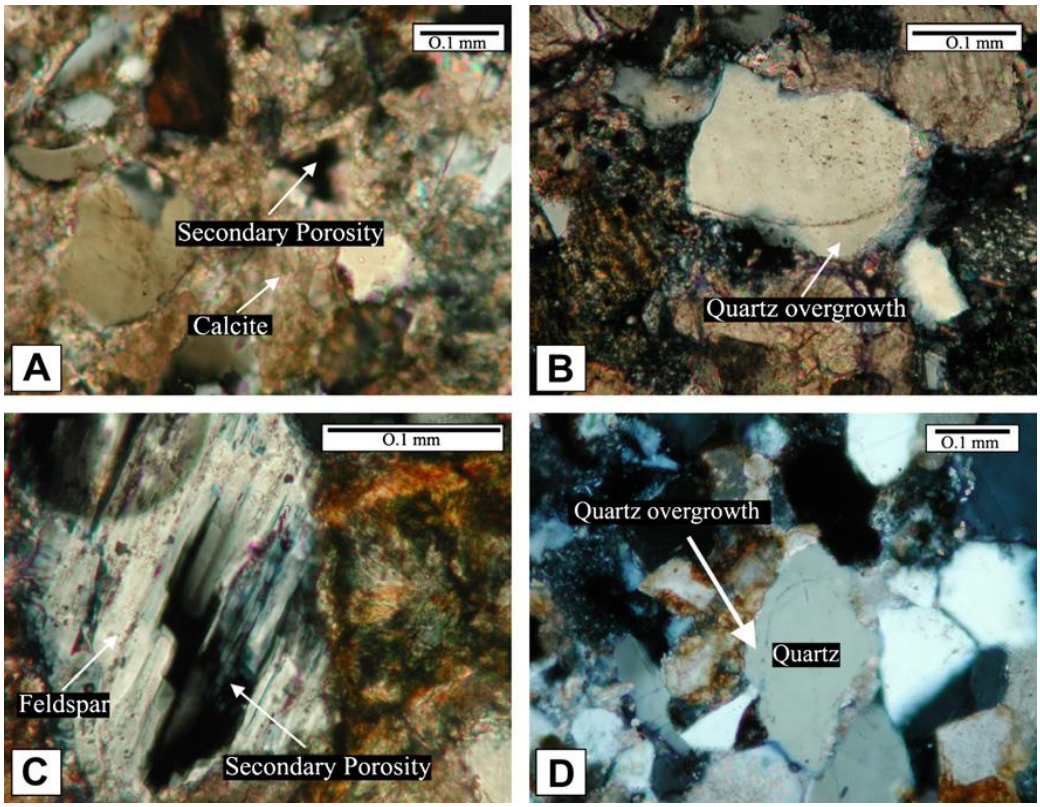

Figure 2. 9: Thin section photomicrographs: (A) quarts grains corroded and partially replaced by calcite cement: (B) detrital grains of polycrystalline quartz of metamorphic origin: (C) detrital grain of igneous origin: (D) feldspar grain corroded with partially replaced by drusy calcite cement (Khidir and Catuneanu, 2010)

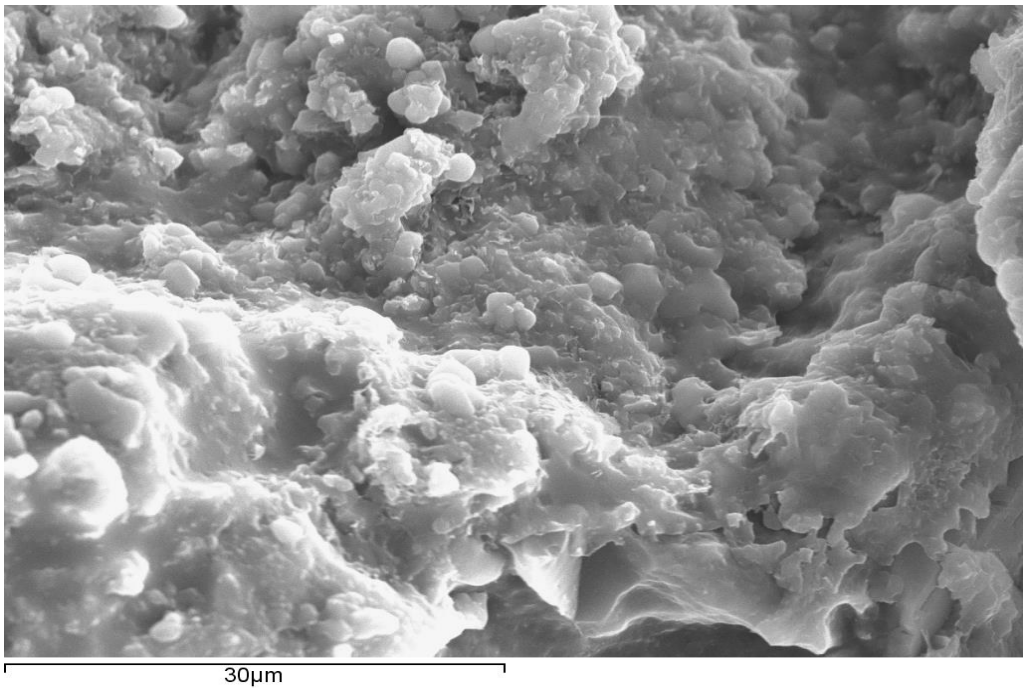

Figure 2. 10: sandstone rock imaged using SEM at 30 µm resolution

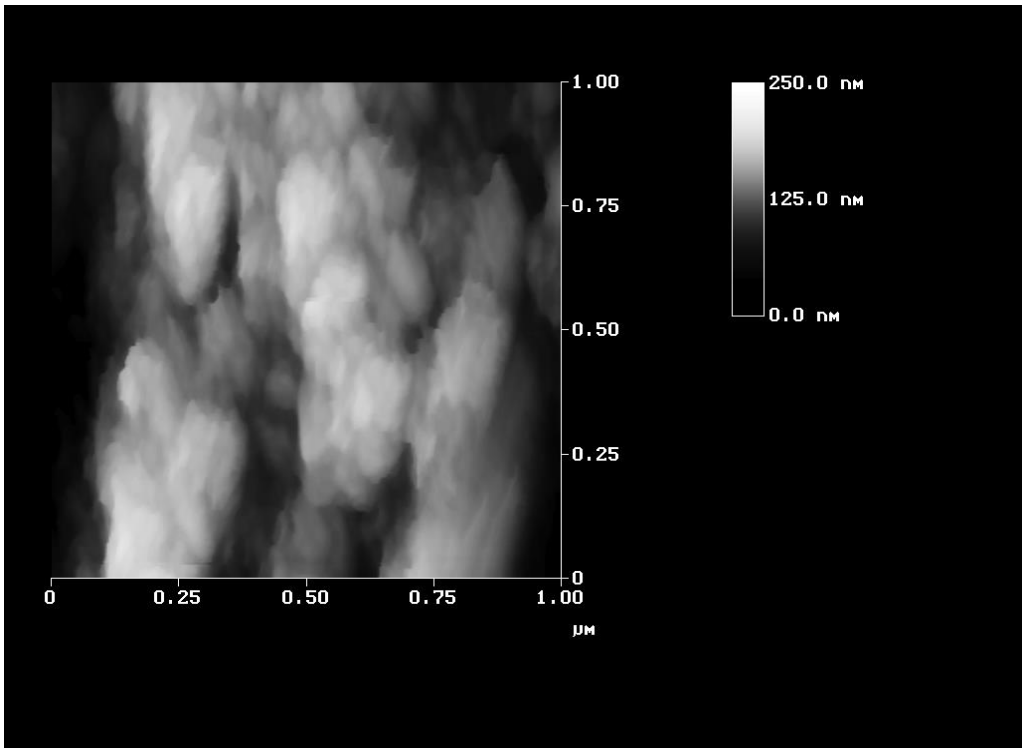

Figure 2. 11: AFM image of C30 at 1 µm field of view. Courtesy of the University of Bath

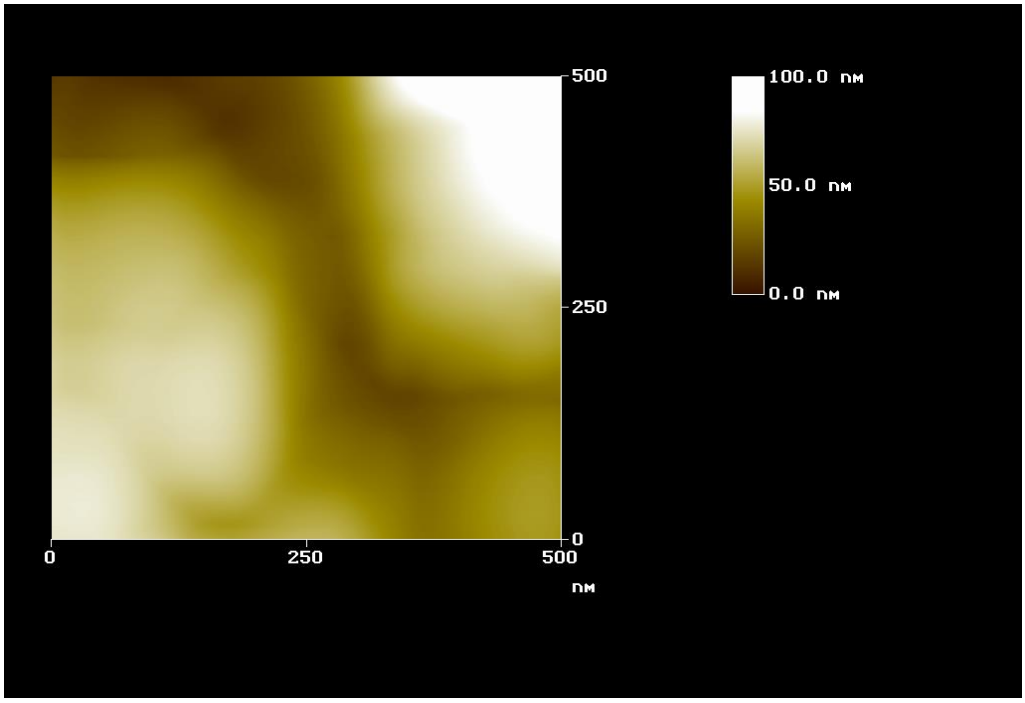

Figure 2. 12: AFM image of G1 at 500 nm field of view. Courtesy of the University of Bath.

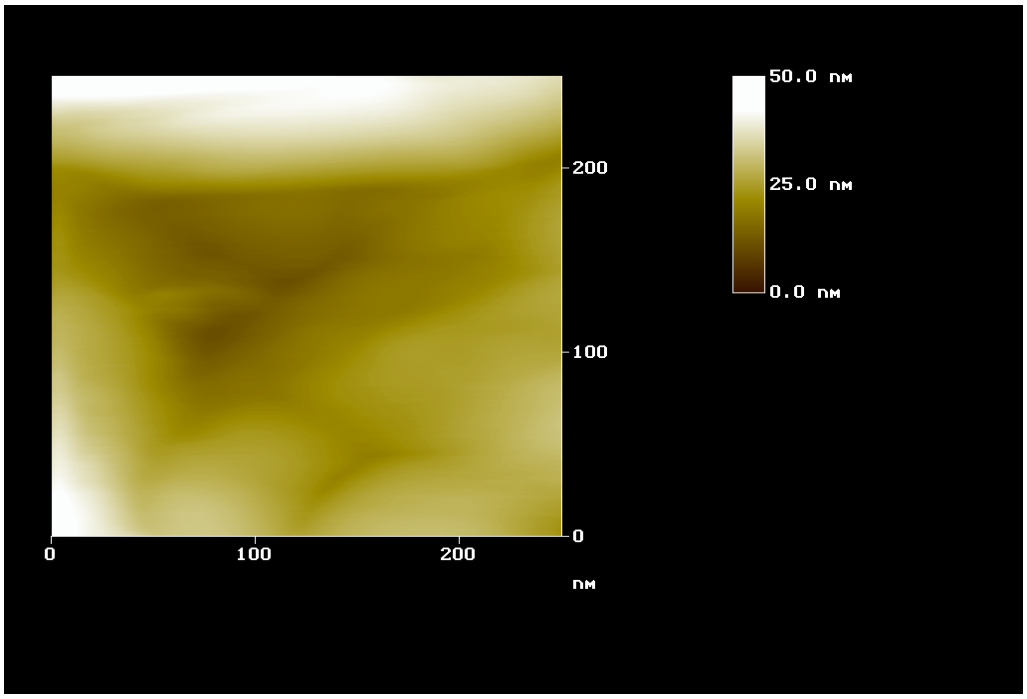

Figure 2. 13: AFM image of G2 at 200 nm field of view. Courtesy of the University of Bath

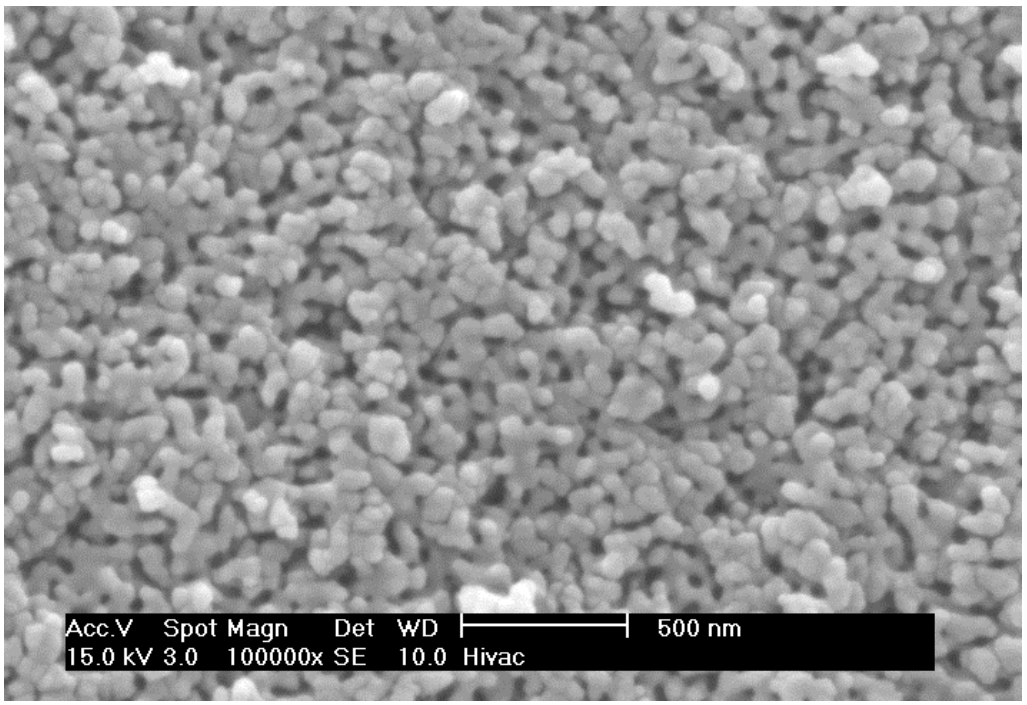

Figure 2. 14: Scanning electron micrograph image of nominal 24nm CPG 2400 at 500 nm field of view

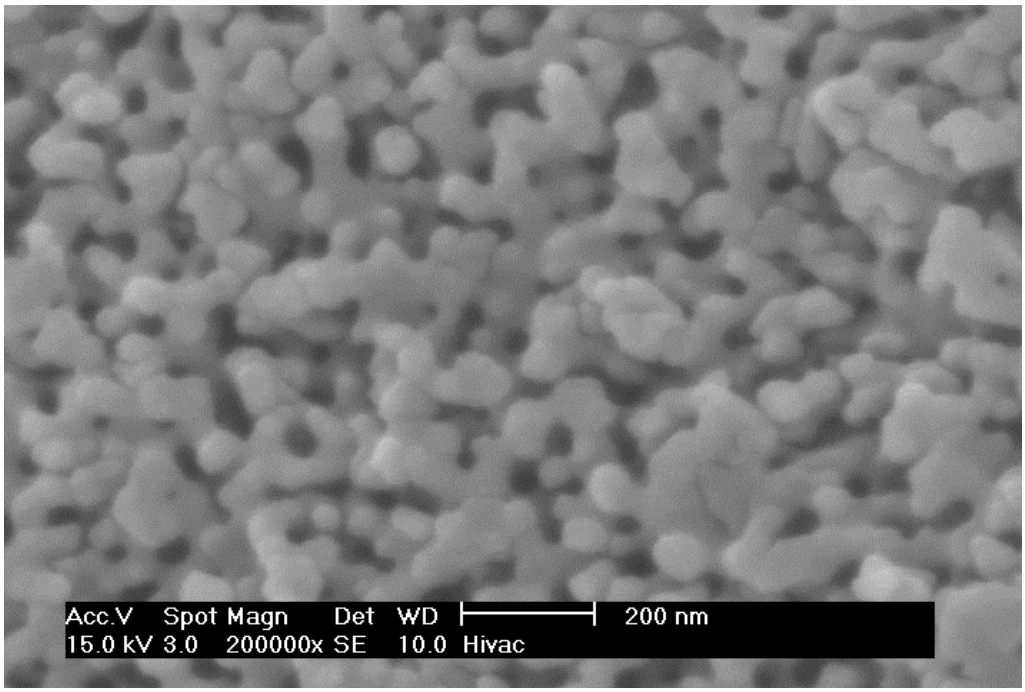

Figure 2. 15: Scanning electron micrograph image of nominal 24nm CPG 2400 at 200 nm field of view

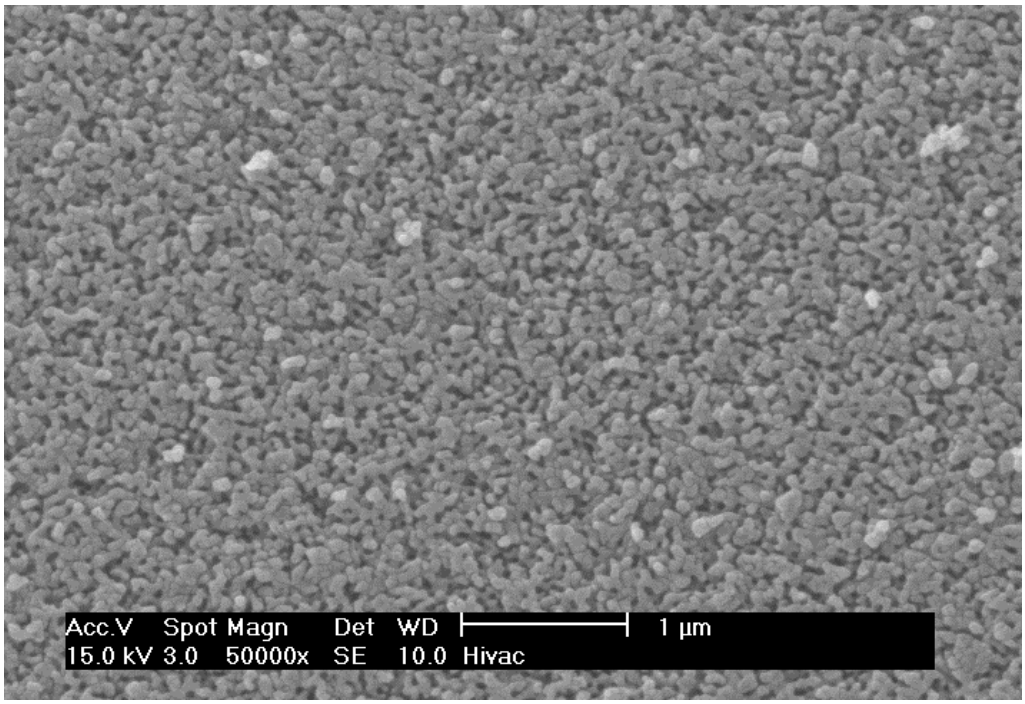

Figure 2. 16: Scanning electron micrograph image of nominal 50nm CPG 5000 at 1 µm field of view

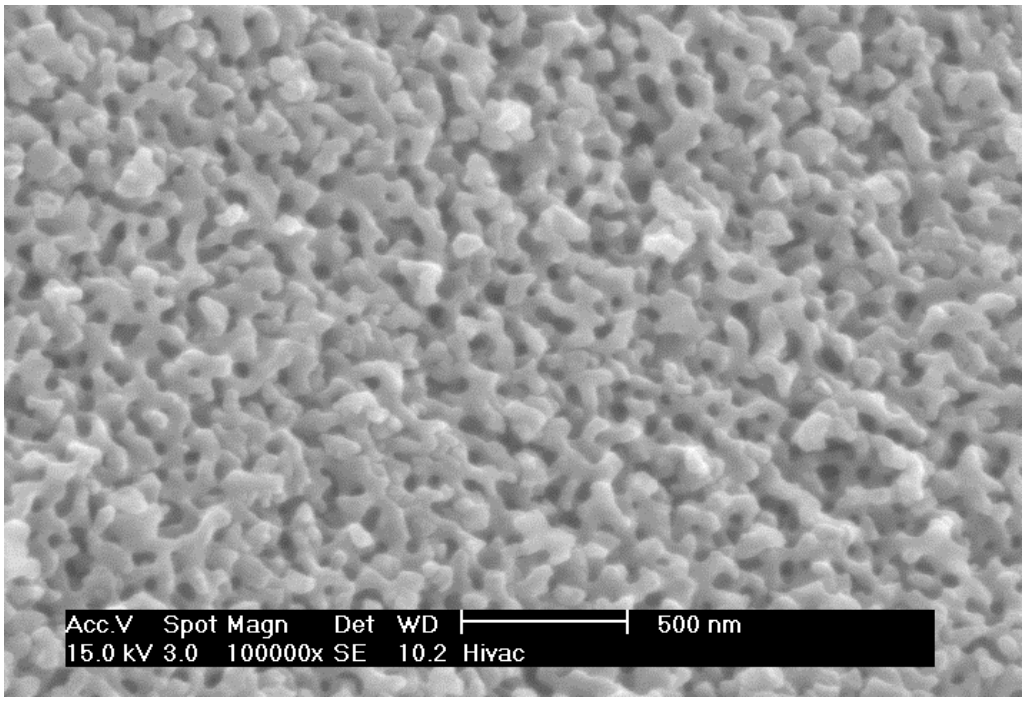

Figure 2. 17: Scanning electron micrograph image of nominal 50nm CPG 5000 at 500 nm field of view

2.8. Reference

COSSE, R. 1993. Basics of Reservoir Engineering. Editions Technip ed. paris.

COULSON, J. M., AND RICHARDSON, J.F., 2002. *Chemical Engineering: Particle technology, and*

Separation processes, Butterworth-Heinemann.

DANDEKAR, A. Y. 2006. *Petroleum Reservoir Rock and Fluid Properties*, Taylor & Francis.

DAWE, R. A. & EGBOGAH, E. O. 1978. The recovery of oil from petroleum reservoirs. *Contemporary Physics,* 19**,** 355-376.

EZEKWE, N. 2010. *Petroleum Reservoir Engineering Practice,* Pearson Education.

GOPINATHAN, N., GREAVES, M., LOWE, J. P., WOOD, J. & RIGBY, S. P. 2012. Determination of the location of coke in catalysts by a novel NMR-based, liquid-porosimetry approach. *Journal of Colloid and Interface Science,* 381**,** 164-170.

HALLIBURTON (ed.) 2001. *Basic Petroleum Geology and Log Analysis*.

HITCHCOCK, I., LUNEL, M., BAKALIS, S., FLETCHER, R. S., HOLT, E. M. & RIGBY, S. P. 2014. Improving sensitivity and accuracy of pore structural characterisation using scanning curves in integrated gas sorption and mercury porosimetry experiments. *Journal of Colloid and Interface Science,* 417**,** 88-99.

KHIDIR, A. & CATUNEANU, O. 2010. Reservoir characterization of Scollard-age fluvial sandstones, Alberta foredeep. *Marine and Petroleum Geology*, 27**,** 2037-2050.

MPG PETROLEUM, I. 2011. Available: http://www.mpgpetroleum.com/fundamentals.html [Accessed 2-03-2011.

RIGBY, S., CHIGADA, P., PERKINS, E., WATT-SMITH, M., LOWE, J. & EDLER, K. 2008a. Fundamental studies of gas sorption within mesopores situated amidst an inter-connected, irregular network. *Adsorption,* 14**,** 289-307.

RIGBY, S. P., CHIGADA, P. I., EVBUOMVAN, I. O., CHUDEK, J. A., MIRI, T., WOOD, J. & BAKALIS, S. 2008b. Experimental and modelling studies of the kinetics of mercury retraction from highly confined geometries during porosimetry in the transport and the quasi-equilibrium regimes. *Chemical Engineering Science,* 63**,** 5771-5788.

RIGBY, S. P., CHIGADA, P. I., WANG, J., WILKINSON, S. K., BATEMAN, H., AL-DURI, B., WOOD, J., BAKALIS, S. & MIRI, T. 2011. Improving the interpretation of mercury porosimetry data using computerised X-ray tomography and mean-field DFT. *Chemical Engineering Science,* 66**,** 2328-2339.

RIGBY, S. P., FLETCHER, R. S. & RILEY, S. N. 2003. Determination of the cause of mercury entrapment during porosimetry experiments on sol–gel silica catalyst supports. *Applied Catalysis A: General,* 247**,** 27-39.

RIGBY, S. P., WATT-SMITH, M. J., CHIGADA, P., CHUDEK, J. A., FLETCHER, R. S., WOOD, J., BAKALIS, S. & MIRI, T. 2006. Studies of the entrapment of non-wetting fluid within nanoporous

media using a synergistic combination of MRI and micro-computed X-ray tomography. *Chemical Engineering Science,* 61**,** 7579-7592.

ROUQUEROL, F., ROUQUEROL, J., SING, K. S. W., LLEWELLYN, P. & MAURIN, G. 2014. *Adsorption by Powders and Porous Solids, 2nd Edition*, Academic Press.

SATTER, A., IGBAL, G. M. & BUCHWALTER, J. L. (eds.) 2008. *Practical Enhanced Reservoir Engineering: Assisted with Simulation Software*: Pennwell Books.

SCHUBERT, U. & HUSING, N. (eds.) 2005. *Synthesis of Inorganic materials*: Wiley-Vch.

SEED. 2011. Available: https://www.planetseed.com/node/15250 [Accessed 27-05-2011.

SHIKO, E., EDLER, K. J., LOWE, J. P. & RIGBY, S. P. 2013. Probing hysteresis during sorption of cyclohexane within mesoporous silica using NMR cryoporometry and relaxometry. *Journal of Colloid and Interface Science,* 398**,** 168-175.

ZAHOOR, M. K. & DERAHMAN, M. N. 2013. New approach for improved history matching while incorporating wettability variations in a sandstone reservoir-Fielf implementation *Journal of Petroleum Science and Engineering,* 104**,** 27-37.

Chapter 3: Porous Media Characterisation Methods

3.1. Introduction

This chapter will introduce the reader to the different experimental techniques, which are used in this report. The first technique is mercury porosimetry, which provides wide range of information, which no other technique can provide. In mercury porosimetry, entrapment is observed from the completion of intrusion/extrusion cycle, where the retraction curve does not give zero volume (Lowell and Shields, 1981). Determination of entrapment of non-wetting fluids within the void space of porous media is important in many fields, such as catalyst characterisation and enhanced oil recovery. The materials entrapped with mercury were imaged directly using computed x-ray tomography (CXT) technique in order to determine the spatial distribution of entrapped mercury and porosity, within the void spaces of the porous media with high level of mercury entrapment following porosimetry as seen in Hellmuth, Siitari-Kauppi et al. (1999); Rigby, Watt-Smith et al (2006); and Rigby, Chigada *et al* (2011).

The third being thermal porosimetry, which is sometimes referred to as thermoporometry. It is is based on the thermodynamic relationship between pore size, and the solidification temperature of freezable pore water, which allows the determination of pore volume, pore sizes, and the internal surface area of wet solid before drying (Yamamoto et al., 2005). The measurements can be done very easily by means of Differential Scanning Calorimetry (DSC) and were performed on mesoporous samples containing pores of radius of 2-50

nm which can be studied by other alternatives such as the nuclear magnetic resonance (NMR) and mercury porosimetry.

Also, PFG NMR technique will be used to investigate fluid transport through porous media and the displacement of fluid by another fluid using the Carr-Purcell-Meiboom-Gill CPMG sequence. The scope of each technique will be outlined under each characterisation method.

3.2. Mercury porosimetry

This technique for characterising porous materials was first developed by Ritter and Drake (1945) and has remained popular ever since. The term "porosimetry" often refers to measurement of pore size, pore volume, pore size distribution and other related characteristics of porous materials. Porous solids are generally characterised by parameters such as the overall average voidage fraction (porosity), pore size distribution (probability density function), specific surface area, and pore connectivity (mean pore co-ordination number) (Rigby et al., 2003). Mercury porosimetry is a widely used pore characterisation method, particularly in the catalyst and oil industries.

Mercury porosimetry is used effectively for the characterisation of various properties of porous materials. This is clearly manifested in the International Union of Pure and Applied Chemistry's (IUPAC's), where it stated that mercury porosimetry is widely accepted as a standard tool for measuring total pore volume and pore size distribution in the macro- (i.e., pores of width >50nm) and mesopore (2<50nm) ranges (Physical And Biophysical Chemistry Division Commission et al., 1994). Mercury porosimetry is used to

characterise porous materials with pores ranging from 500µm to 3.5nm, depending on the equipment (Geische, 2006).

3.2.1. Theory of mercury porosimetry

The most basic assumption made in mercury porosimetry is the pore shape. The data analysis software on virtually all instruments assumes cylindrical pore geometry by using a modified Young-Laplace equation, which is mostly referred to as the Washburn equation (1921). Although pores are rarely cylindrical in reality, the Washburn equation provides a practical interpretation of pore distributions, yielding useful results. However, one can also show pores are cylindrical using cryoporometry (Perkins et al., 2008). Also, many researchers assumed cylindrical pores (Stejskal and Tanner, 1965; Kloubek, 1981; Lowell and Shields, 1981a; Portsmouth and Gladden, 1991; Tsakiroglou and Payatakes, 1998; Giesche, 2006) in mercury porosimetry. The cylindrical pore shape is illustrated in Fig. 3.1.

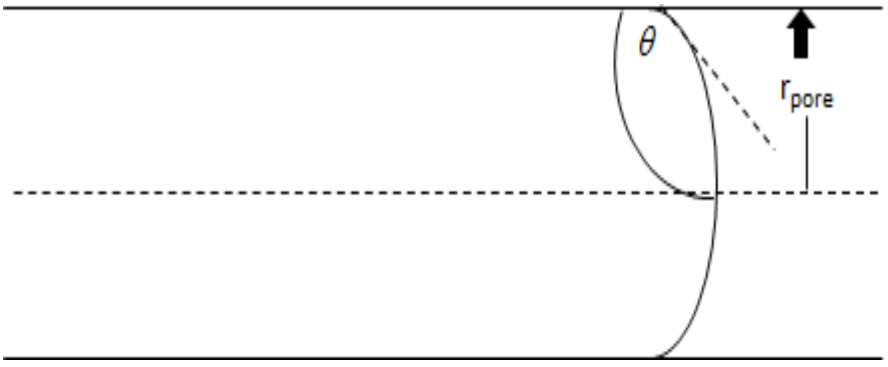

Figure 3. 1: Schematic representation of a cylindrical pore assumed by most instruments

Mercury porosimetry is based on the principles of the capillary law whereby, a non-wetting fluid (nwf), (i.e. one whose angle is greater than 90º for a particular solid) (mercury) requires an external hydrostatic pressure, ΔP, to be

applied to force the nwf into pores of radius r, and the pressure difference, (ΔP), will vary inversely with radius (r). Washburn (1921) applied the Young-Laplace equation to determine pore sizes for a cylindrical capillary model of a porous medium. This law forms the basis of interpretation in mercury porosimetry that is used to characterise porous materials. (Giesche, 2006). The Eq. 3.1 relates to the pressure difference across the curved mercury interface ((r_1 and r_2) describe the curvature of that interface) to the corresponding pore size (r_{pore}) using the surface tension of mercury γ_{Hg} and the contact angle (θ) between the solid and the mercury.

$$\Delta P = \gamma_{Hg}\left(\frac{1}{r_1} + \frac{1}{r_2}\right) = \frac{2\gamma_{Hg}\cos\theta}{r_{pore}} \qquad (3.1)$$

As indicated in Eq. 3.1 (the Washburn equation), the value of the surface tension and the contact angle between the solid and mercury needs to be known in order to determine the pore size – pore volume relation. According to Giesche (2006), a value of 0.845 Nm^{-1} at 25^{o}C is commonly accepted for the mercury liquid-vapour surface tension and a fixed value of 130^{o} for the contact angle irrespective of the material sample by many researchers, thus these values were adopted for this study. However, a large amount of authors have suggested in their literature that the value of the surface tension and contact angle may vary with pore size.

The validity of the Washburn equation has been questioned since its early development, as it fails to account for several features of porous media. Firstly, mercury intrusion in any porous structure starts within an interconnected network of pores that are not accessible to mercury penetration at the early

stage. The experimental procedure is based on the gradual intrusion of mercury into an evacuated porous medium by increasing the external pressure in small increments, or continuously, up to levels as high as 60000 Psi (414MPa) and measuring the volume of mercury entering the sample after each pressure increment with a typical commercial apparatus (Portsmouth and Gladden, 1991). The process is reversed by decreasing the external pressure which allows the gradual retraction of mercury from the sample down to ~16 Psi. This process of mercury intrusion and extrusion from the sample yields a cumulative volume against pressure curve, which can be used in order to determine the pore geometry of the sample (Tsakiroglou and Payatakes, 1991).

3.2.2. Hysteresis in mercury intrusion/extrusion data

As observed already by many researchers (Good and Mikhail, 1981;Kloubek, 1981; Lowell and Shields, 1981a; Smithwick and Fuller Jr 1984), mercury porosimetry curves display hysteresis, and this hysteresis occurs in most samples of mercury porosimetry data when at a given pressure, the volume indicated on the extrusion curve is larger than that on the intrusion curve, and at a given volume, the pressure indicated on the intrusion curve is greater than that on the extrusion curve (Lowell and Shields, 1981a). An illustration of hysteresis is shown in Figure 3.2; it shows trapping of mercury within the sample during the first intrusion process.

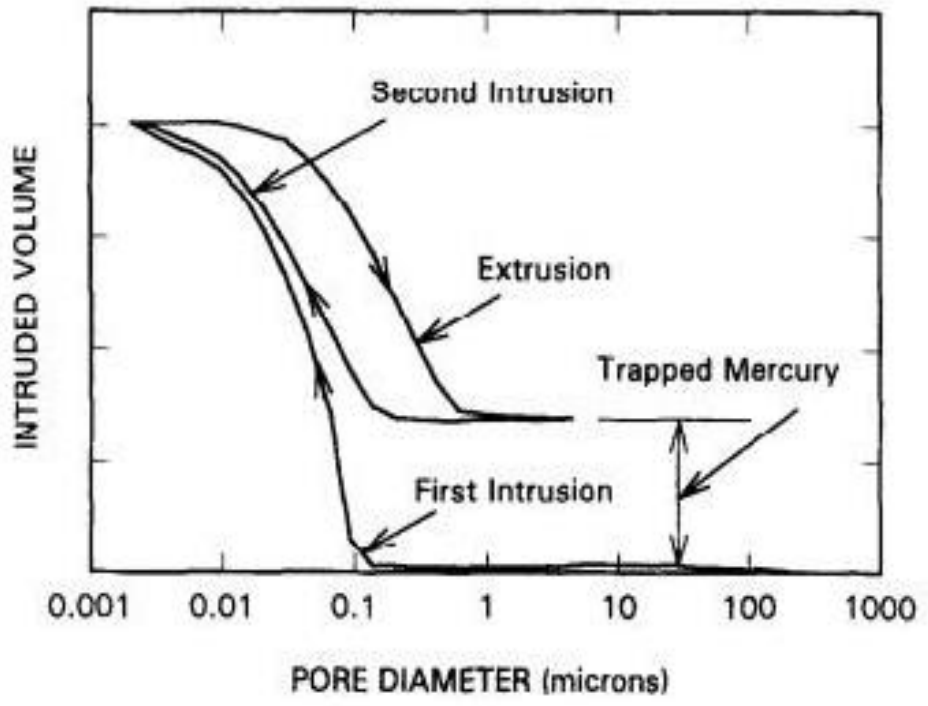

Figure 3. 2: Hysteresis Loop in Pore-Size Distribution obtained from Mercury porosimetry (Liu and Winslow, 1995)

Many researchers have also noted that the hysteresis observed in the mercury intrusion and extrusion data is consistent with advancing and receding contact angles respectively. While others (Lowell and Shields, 1981b; Salmas and Androutsopoulos, 2001) disputed that the hysteresis observed in porosimetry is only due to contact angles but also suggested it is due to the presence of ink-bottle-shaped pores. Several explanations have been proposed that give rise to the hysteresis phenomenon, which can either be due to contact angle hysteresis as proposed by Lowell and Shields (1981b) or by the domination of extrusion by pore bodies and intrusion by throats to the pore network (percolation connectivity model), (Giesche, 2006) .

The explanation for hysteresis during mercury porosimetry due to an ink-bottle shaped pore is as follows. An ink-bottle pore is when a smaller diameter neck

is connected to a wider diameter body. According to Eq. (3.1), a higher pressure would be required for mercury to penetrate the smaller neck. And when this pressure is high enough to penetrate the small neck, it will fill both the neck and the pore body. During the retraction of mercury, the mercury would retract from the smaller diameter pore neck at higher pressure, and from the larger diameter pore body at a lower pressure (Ternan and Mysak, 1987). Also, Giesche (2006) stated that the "*throat*" or entrance opening to a pore is smaller than the actual pore body. Therefore, mercury will enter the pore body at a pressure determined by the entrance size and not the actual body size. And during extrusion, the mercury thread will break in all the throats (narrower connections) between pores leaving a large amount of isolated packages of entrapped mercury inside the sample. This has been illustrated in Fig. 3.3.

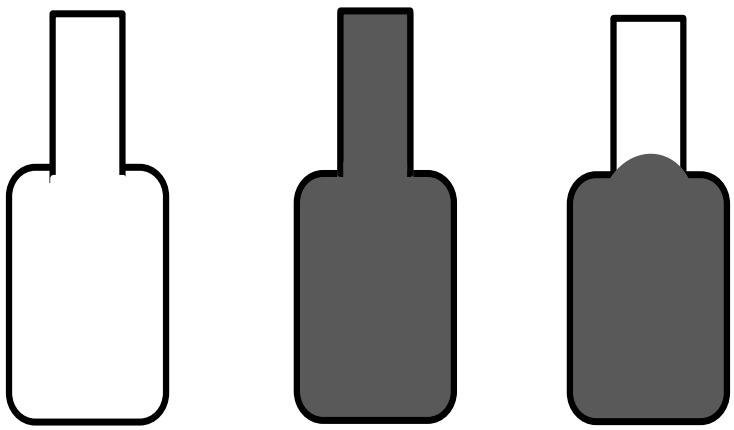

Figure 3. 3: (a) an empty ink bottle pore, (b) a full intruded mercury following porosimetry experiment, and (c) trapped mercury is visible in black during and after the mercury porosimetry experiment (Giesche, 2006)

As earlier mentioned, another phenomenon that may cause hysteresis is contact angle hysteresis. This hysteresis arises due to the difference between the advancing and receding contact angles of mercury in the porous material. An advancing contact angle of 130^{o}C is usually assumed for all samples run on mercury porosimetry because this angle is typical for mercury on smooth, flat, non-wetting surfaces. Some of the earliest researchers to investigate the cause of hysteresis were Liabastre and Orr (1978). These researchers measured the pressures required for intrusion into, and extrusion from, controlled pore glasses (CPGs) for which the pore size could be obtained independently using electron microscopy. However their work was limited with the assumption of cylindrical pore. Kloubek (1981) used the data derived by Liabastre and Orr (1978) to obtain correlations for the variation of the product of γ_{HG} and cosθ, in the Washburn Eq. 3.1, as a function of pore radius. Kloubek (1981) observed that the volume hysteresis in mercury porosimetry is caused by the contact angle and the remaining is considered to be associated with structural hysteresis. Rigby *et al* (2002; 2009) found that the Kloubek correlations could be used, with no amendments, to remove apparent contact angle hysteresis, and obtain superposition of the intrusion and extrusion curves, for some sol-gel silica materials with the same surface fractal dimension as the original CPG materials used by Liabastre and Orr (1978). Silica materials with a different degree of surface roughness required amendments to the Kloubek correlations to achieve a similar superposition (Rigby and Chigada, 2009). These trends in the effect of surface roughness on hysteresis were also observed in results from mean-field density functional theory (MFDFT) simulations of mercury intrusion and extrusion on models with rough surfaces (Rigby and Chigada,

2009). These findings suggested that mercury porosimetry hysteresis was a function of surface chemistry and roughness, and supported the use of Kloubek (1981) correlations to analyse porosimetry data for some sol-gel silicas. As will be seen in chapter 4 and 5 of the analysis section, analysing porosimetry data with the Kloubek correlations also allows an estimate to be made of the pore sizes that entrap mercury, but the method is indirect. The validity of the Kloubek correlations will be tested directly using mercury porosimetry scanning loops. In mercury porosimetry, scanning loops are achieved by reversing the progressive increase in pressure on the intrusion curve, respectively. Past studies (Wardlaw and McKellar, 1981; Portsmouth and Gladden 1991) have looked at the scanning loops experiment using mercury porosimetry.

The empirical equations derived by Rigby *et al* (2002) were used to analyse raw mercury porosimetry data for different silica/alumina samples to obtain the pore size and the size of the pore at the onset of mercury entrapment. This empirical equation takes into account varying values for contact angle and surface tension with pore size. For mercury intrusion and extrusion, the pore radius, *r* is given by:

$$r = \frac{-A+\sqrt{A^2-2BP_{Hg}}}{P_{Hg}} \qquad (3.2)$$

where P_{Hg}, is the applied pressure (MPa), A and B are constants that depend on the material and whether the meniscus is advancing or retreating (see Table 3.1). Although Eq. (3.2) was derived from empirical data for a controlled pore glass, and it is known that it can be used for many types of silica sample, the

validity and the applicability of Eq. (3.2) to silica-alumina will become apparent from the features of the mercury porosimetry curves derived using them. However, the equation is only valid for systems with piston type or parallel intrusion–extrusion mechanism.

Table 3. 1: Parameters for insertion into semi-empirical alternatives to the Washburn equation (Eq. 3.2.) (Rigby et al., 2004). The advancing meniscus values have a pore radius range of applicability of 6-99.75 nm and retreating values have a range from 4-68.5 nm. (d = surface fractal dimension)

Material	Advancing meniscus		Retreating meniscus	
	A	B	A	B
Silica (d = 2.2-2.3)	-302.533	-0.739	-68.366	-235.561
Silica (d = 2.5)	-302.533	-0.739	-96	-235.561

As seen in Fig. 3.3 in this section, the pore volume, surface area, and percentage of mercury entrapment for different samples will be determined from the raw mercury data.

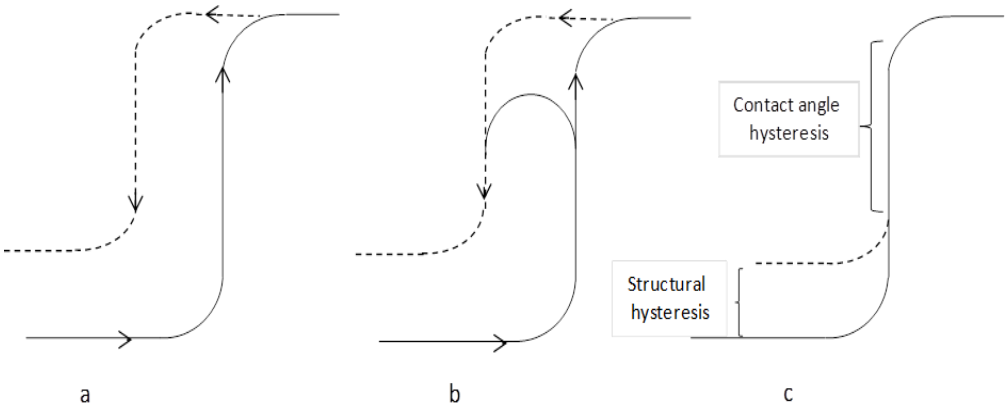

Figure 3. 4: (a) A typical mercury intrusion-extrusion cycle for a porous material, (b) the extrusion curve can be superimposed on the intrusion curve using Eqn 3.2, (c) Removal of contact angle hysteresis and showing only structural hysteresis.

The major theories that have been proposed to account for the hysteresis phenomena including the contact angle and structural hysteresis are summarised below (Terrence, 1997);

- **Contact angle:** It arises because the surface tension and contact angle from the Washburn (1981) Equation, which relates the imposed pressure to pore size, are known to depend on the radius of the pore, and whether the mercury is advancing or receding from a sample (Rigby et al., 2004). The difference in the advancing and receding contact angle will result in the retraction curve being different from the intrusion curve. Studies have shown that advancing macroscopic contact angle is greater during penetration than the receding macroscopic contact angle (Ternan and Mysak, 1987).

- **Ink-bottle pores**: The pores are said to have an ink-bottle shape where a smaller diameter neck is connected to a wider diameter body. A high pressure would be required to force mercury into the smaller neck, and, when the pressure is high enough, mercury would fill both the neck and the body. During the pore emptying, mercury will retract from the smaller diameter pore at high pressure, and from the larger diameter pore body at a low pressure. Mercury is trapped within the smaller pore body containing inkbottle shapes causing hysteresis.

- **Network effects**: The voids between particles, and the pores within them, are interconnected and narrow inlets lead to wide voids. During the extrusion process, mercury is trapped in the wide voids causing hysteresis.

- **Pore potential**: The mercury that is forced into a pore space will interact with the pore walls and be trapped in a potential well of energy U. During depressurization, a cylindrical pore of radius r will require an amount of energy E to separate the column such that:

$$E = 2\pi r^2 \gamma \quad (3.3)$$

If U ≥ E, the column will break, mercury will be trapped and this will cause the extrusion curve to intercept the volume axis above the zero. During pressurization the mercury column is under compression as it intrudes, whilst under depressurization the column is under tension, due to pore potential, and can break if the pore potential is high and the pore radius very small. In the case of hysteresis, it is necessary that the pore potential causes mercury to extrude from the pore at a lower pressure than it intrudes. Therefore, any shape of pore can result in hysteresis and cause mercury entrapment (Terence, 1997).

- **Surface roughness:** This can cause the mercury to 'slip-stick' so that mercury thread is broken.

3.2.3. Entrapment during mercury intrusion/extrusion

Entrapment of mercury is recognised from the observation that, at the completion of intrusion-extrusion cycle, the retraction curve does not give zero volume (Lowell and Shields, 1981a), leading to some mercury retained in the sample. Mercury retraction or withdrawal of mercury from a porous network is an imbibition process in which air displaces a non-wetting liquid (mercury) (Portsmouth and Gladden, 1991). When the external pressure starts to decrease to a value that permits mercury snap-off in throats, the mercury starts to

withdraw from the network. The throat is emptied either after snap-off, or with piston type retraction of a meniscus, depending upon whether both of the adjacent chambers are full, or only one. A chamber is emptied when the external pressure is lower than the minimum capillary pressure and when at least one of the adjoining throats is empty (Tsakiroglou and Payatakes, 1991).

A wide range of experiments has been carried out to determine the mechanism of the entrapment of non-wetting fluids (Lowell and Shields, 1981a; Rigby et al, 2006; Tsakiroglou and Payatakes, 1998). Wardlaw and McKellar (1981) conducted an experiment using mercury porosimetry on micromodels consisting of network of capillaries etched in glass. In the first glass model studied, the system consisted of pores of variable sizes that were connected to tubular throats of uniform size. When mercury was first injected into the model, it filled the larger pore elements and thereafter it filled the smaller pore elements as the pressure is raised. Once the pressure was subsequently decreased, mercury withdrew initially from the smaller pore elements. As the pressure was decreased further, the mercury then withdrew from the rest of the pore network. In the second glass micromodel, which consisted of tubes with different sizes randomly arranged in a square network with larger pores, no mercury entered the structure until the required pressure was achieved for mercury to enter the smaller pore elements. The model is then fully saturated with mercury under this pressure. As the pressure is reduced, mercury initially withdrew from the smaller pore elements until the residual mercury was entirely disconnected due to "snap-off" phenomenon. However, at this stage, there is extensive retention of residual mercury in the larger pores. Therefore, one cause of mercury entrapment was found to be the presence of spatially

extended structural heterogeneities. The results of these experiments are shown in Fig. 3.6. The results have shown that the levels of mercury entrapment in porous structures are due to the presence of non-random, structural heterogeneity.

Wardlaw and McKellar (1981) suggested that, once a meniscus is formed, the time (t) required for the meniscus to advance/retreat down a cylindrical pore of length l and radius r is given by:

$$t = \frac{4l^2\eta}{\Delta \mathrm{Pr}^2} \tag{3.4}$$

where η is the viscosity and ΔP is the pressure difference between the applied pressure and the equilibrium pressure required to maintain mercury in the pore. Hence, the volume of mercury leaving the pore space should be proportional to $t^{0.5}$.

During mercury retraction an amount of mercury is trapped in the pores of the network as earlier mentioned. Wardlaw and McKellar (1981) proposed that four aspects of pore systems might affect the movement of fluids and, in particular restrict the movement and trapping of non-wetting fluids during withdrawal from the pore system. These include:

- **Pore and throat sizes**: Throats are defined as smaller spaces linking pores that are larger spaces. The term pore system describes the total system of pores and throats. Trapping of mercury increases as pore to throat size ratio increases.

- **Throat to pore coordination number:** The coordination number of a pore system is defined as the average number of throats that connect with each other (see Fig. 3.5). It is also a measure of the connectivity of the network of throats and pores and determines the number of different pathways or access routes between pores.

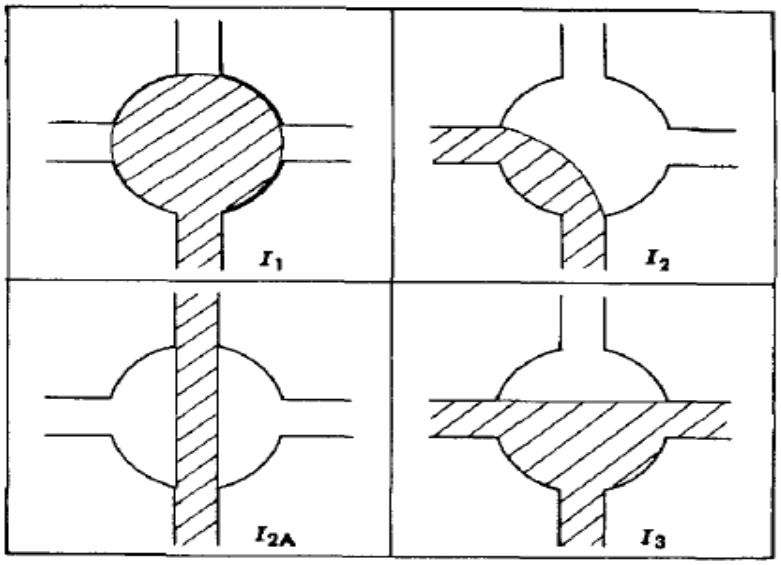

Figure 3. 5: Fluid topology of a pore with coordination number of four Shaded area represent non-wetting phase (Ioannidis et al., 1991)

- **Random and non-random heterogeneity:** Pores and throats of different sizes may be distributed randomly in a network (randomly heterogeneous) or they may be distributed non-randomly. In the latter case, the larger the elements may be clustered together in domains and likewise the smaller elements clustered together in other domains.

- **Surface roughness:** The surface roughness of pores in reservoir rocks for example varies greatly from the smooth crystal surfaces common in some dolomites to the commonly pitted or clay-coated surfaces of

many types of sandstone. The surface roughness affects advancing and receding contact angles.

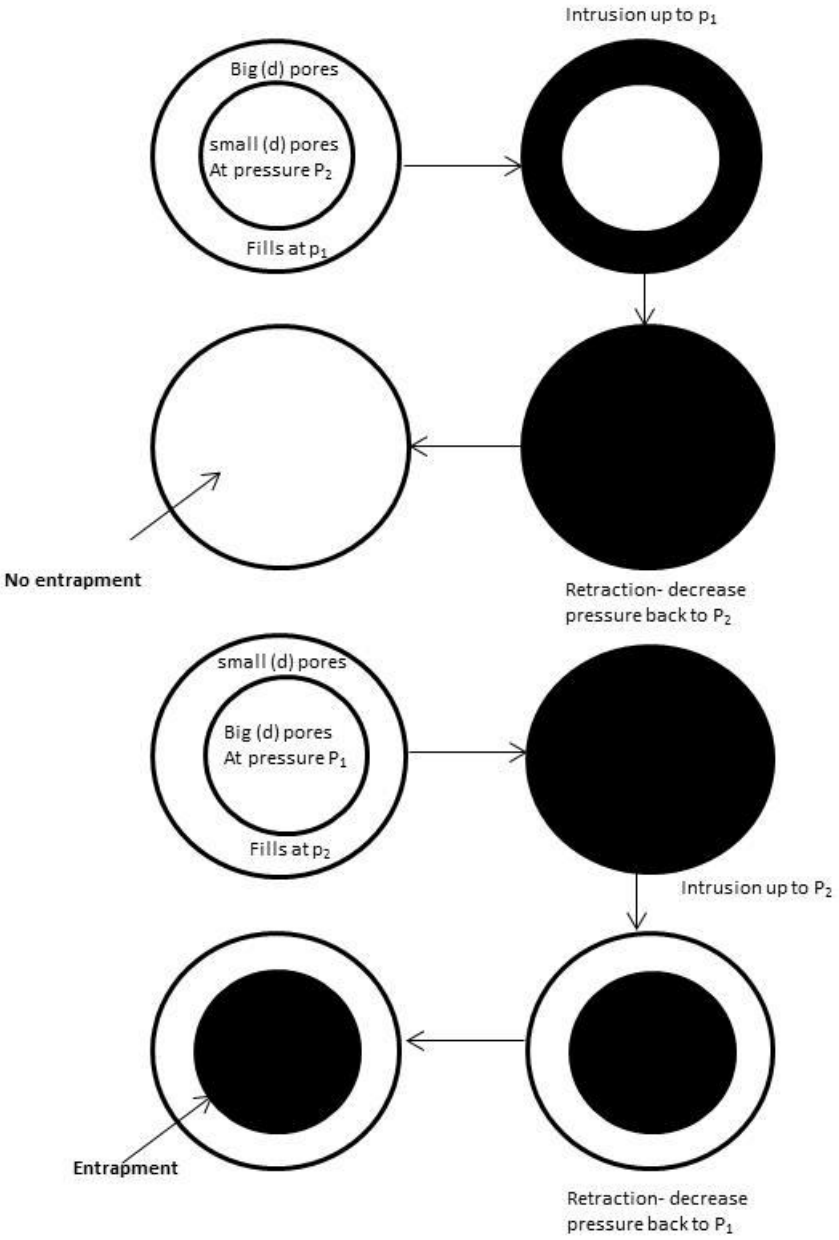

Figure 3. 6: A schematic diagram illustrating the mechanism of mercury entrapment observed in glass micromodels. D and d refer to the sizes of the large and small pores (Wardlaw and McKellar, 1981)

Over the past two decades, it has been (Portmouth and Gladden, 1991) assumed that the main cause of mercury entrapment is determined by the pore properties of the porous medium. Portsmouth and Gladden (1991) developed a three dimensional, spherical random network to investigate the effects of pore size distribution and pore connectivity on the features of mercury porosimetry experiments. They performed simulations of mercury intrusion and retraction on random pore bond network models, which reveals that mercury entrapment is a function of both the pore network connectivity and the width of the volume-weighted pore size probability density function.

Tsakiroglou and Payatakes (1990) presented a theoretical analysis of mercury porosimetry within a network model of spheres and capillaries that account for the mechanism of snap-off in cavity of throats. Snap-off mechanism is a phenomenon of primary importance during mercury retraction process. In these researchers' report mercury retraction is an imbibition process in which low-pressure gas (air and mercury vapour) displaces mercury (non-wetting phase). Mercury retraction is performed after the pore network has been completely filled with mercury, and as the pressure is lowered, new mercury menisci must be formed so that mercury can start retracting from the network. The retraction process leads to the formation of collars of the non-wetting fluid in the throats. These collars are saddle-shaped interfaces and as the pressure is lowered the curvatures of these collars decreases, leading to unstable interfaces. This mechanism is referred to as snap-off (Tsakiroglou and Payatakes, 1990)

Tsakiroglou and Payatakes (1997) did a further experimental and theoretical study on model lenticular capillaries. Their choice on lenticular capillaries was

due to the fact that several porous media of interest, such as sandstone reservoir rocks have pores of such a type. They measured the critical pressures for mercury intrusion and snap off experimentally and expressed them in dimensionless form and as a function of the pore aspect ratio (ratio of pore width to pore depth) and the contact angle. They observed a very good agreement in the case of mercury penetration over the whole region of pore width to pore depth aspect ratio. Also, the critical pressure for mercury intrusion decreases as the pore aspect ratio increases. Also, in another study, Tsakiroglou and Payatakes (1998) studied the entrapment of non-wetting fluid within a chamber and throat networks etched in glass micromodels. These researchers developed a mathematical expression for the critical pressure for the retraction and snap–off of mercury menisci in model porous media consisting of throats and chambers, which accounted for the effects of network topology and pore aspect ratio. They used their expressions to simulate mercury retraction from a chamber and throat network and compared the results with experimental data for chamber and throat networks in glass model porous media. A reasonable agreement between the theory and experimental data was obtained. However, the model used by these researchers (and in previous work (Wardlaw and McKellar, 1981)) had relatively regular pore structures, whereas the typical catalyst supports used in industry are amorphous and more like to have much more complex pore structures.

A more recent study (Watt-Smith et al., 2006) investigated the models representing the pore structures of amorphous, mesoporous silica pellets using magnetic resonance imaging (MRI) to obtain the spatial distribution of porosity and pore size. They used simulations of mercury porosimetry within

the structural models derived from MRI to predict the point of the onset of structural hysteresis and the levels of mercury entrapment for the silicas.

In a similar approach, Rigby *et.al* (2006) extended their research to the study of the entrapment of mercury within nanoporous silica materials following porosimetry using the combination of magnetic resonance imaging and micro-computed X-ray tomography (micro-CXT). They constructed structural models of a particular porous media using MRI to perform simulations of mercury intrusion and retraction with variations in the mechanism for the 'snap off' of the mercury menisci. Their simulation results revealed different predictions for the pattern of the macroscopic (>10μm) distribution of entrapped mercury, depending on the 'snap off' mechanism, which they compared with the corresponding experimental data obtained from micro-CXT images of real pellets containing mercury. Also, the simulation results reveal that the overall level of mercury entrapment was determined by the close interaction between the pellet macroscopic structure, and the microscopic mercury retraction mechanism.

Many authors have focused on the interpretation of mercury porosimetry data using more realistic models. A good representation of the pore space with regards to important geological media (e.g. oil and gas reservoir) is provided by a matrix of pore bodies interconnected through narrow pore throats (Ioannidis et al., 1993). Previous work by Rigby *et al*. (2004) shows that it is possible to use mercury porosimetry experimental data to determine the variation of average pore length with pore diameter for mesoporous solids. Their experimental result shows that mercury entrapment is caused by a mechanism involving macroscopic (>0.1nm) heterogeneities in the pore

structure. Also, their experimental results revealed that the entrapped mercury is confined to only the largest pores in the material for a particular type of sol-gel silica catalyst support.

3.2.4. Limitations of mercury porosimetry

One of the key limitations to mercury porosimetry is that it measures the smallest entrance of a pore and not the actual inner size of the pore (Giesche, 2006). Due to the isolation of closed pores, the tool cannot be used to analyse them, since mercury does not enter such a pore. Another point is the assumption made on the cylindrical pore shape and the contact angle of mercury from the Washburn Equation (Eq. 3.1). However, light microscopy images have shown that many silica and alumina samples appear to have random collection of packed spherical and hemispherical particles, as well as cylinders. Pre-treatment of the sample can also cause comminution that can change the internal pore space in two ways. First by breaking the pores of closed pores if present, and secondly by breaking particles along larger pores which will result in decrease of the relative volume of larger pores (Van Brakel et al., 1981).

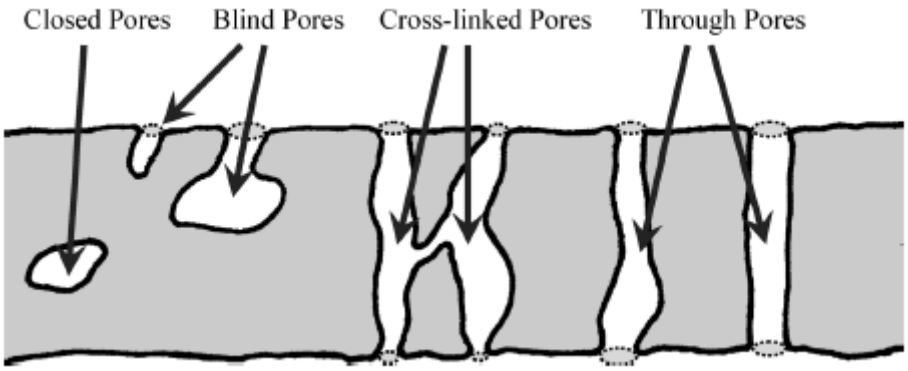

Figure 3. 7: Schematic representation of pores (Giesche, 2006)

Also, Diamond (2000) has also shown, using SEM, that the pores in hydrated cements are quite different from cylindrical pores as assumed by Washburn equation. The pore shape assumed in the model will clearly influence the result of mercury porosimetry pore size measurements. Nevertheless, their effect appears to be less important than the accessibility effect. The Washburn equation (Eq. 3.1) provides the means of calculating the pressure required to fill a cylindrical pore with mercury provided that the mercury is accessible to that pore.

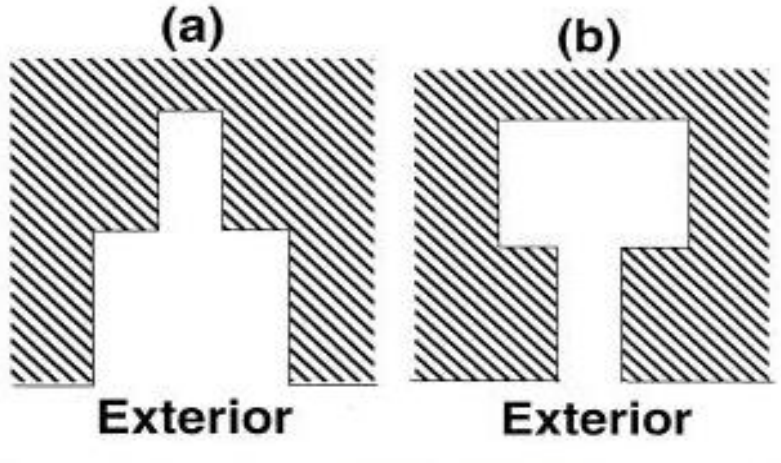

Figure 3. 8: Illustrative a diagram of a small and large cylindrical pore connected to the exterior (Diamond, 2000)

The accessibility effect is illustrated in Figure 3.8. It provides two-dimensional drawings of arrangements of pores consisting of both a large and a small pore. Many researchers have spent much effort on trying to improve mercury intrusion porosimetry so as to eliminate the impact of "accessibility effect". Liu and Winslow (1995) studied cement paste using mercury porosimetry in order to determine the pore-size distribution. These researchers intruded mercury to the maximum pressure, and then reduced the pressure to minimum,

and re-intruded to the maximum pressure. They found that the methods of intruding/extruding mercury into cement paste materials were fully reversible when appropriate advancing and receding contact angles are used. They conclude that the pore system of cement paste can be divided into two types, i.e. reversibility and irreversibility intruded pores. They drew a conclusion that the reversibility of the intruded pores was more accessible to mercury and more closely correlated with the transport properties of cement-based material.

In addition, Zhou et.al (2010) developed an innovative mercury intrusion porosimetry method that can provide a more accurate estimation of pore size distribution. The measurements are conducted following a unique mercury intrusion procedure, in which applied pressure is increased from minimum to the maximum by repeating pressurization-depressurization cycles instead of a continuous pressurization followed by a continuous depressurization. They suggested that, by following the experimental sequence, the volumes of the throat pores and the corresponding ink-bottle pores can be determined at every pore size. The values are then used to calculate the pore size distribution using the newly developed method. The method was further validated with other experimental techniques, including nitrogen sorption, scanning electron image analysis and numerical simulation.

3.2.5. Scope of work by mercury porosimetry technique

As earlier mentioned, porous solids are generally characterised by parameters such as the overall average voidage fraction (porosity), pore size distribution and pore connectivity (Rigby et al., 2003), and that mercury porosimetry technique is widely used in characterising these parameters. However half of

the data obtained in the form of retraction curve during mercury porosimetry experiments are simply not used which is associated with hysteresis and entrapment. Furthermore, few experimental works are found in the literature that explains the cause of hysteresis and entrapment in mercury porosimetry curves.

Previous work by Rigby *et al*. (2004) shows that it is possible to use integrated nitrogen sorption and mercury porosimetry experiments to determine the average pore length with pore diameter for mesoporous solids. Their experimental result shows that mercury entrapment is caused by a mechanism involving macroscopic (>0.1nm) heterogeneities in the pore structure. Also, their experimental results revealed that the entrapped mercury is confined to only the largest pores in the material for a particular type of sol-gel silica catalyst support.

In a subsequent study, Rigby *et al* (2008) studied the retraction process in mercury porosimetry using highly confined geometries of mesoporous materials with non-random heterogeneities in their void structure to extract accurate pore space description from the retraction curve. They concluded that the mercury retraction curve from a particular sol gel silica material is independent of equilibration time and thus probably results in the breaking of mercury ganglia at the boundaries of the region of smallest pores within the material.

In this work, different batches of silica and alumina samples will be studied using different equilibration times in order to understand the transport regime and how mercury is distributed with emphasis to entrapment of non-wetting

fluid after the retraction processes. The detailed study of mercury retraction curve is important for interpreting mercury porosimetry data. Scanning loops experiment will also be conducted to see the effect of applying Kloubek correlations from the raw porosimetry data. Also, in order to understand the mercury retraction process, computed x-ray tomography have been used to characterise in detail, the pore network structures of the test materials in which porosimetry has been studied.

In chapter 4 of this thesis, the results of different samples characterise by this technique will be presented. The materials will be examined using different equilibration time scales after initial porosimetry experiment to look at time dependence of retraction and entrapment. Furthermore, semi-empirical alternatives to the Washburn equation (Eq. 3.1) will be used for the interpretation of raw mercury porosimetry data.

3.3. Computed X-ray tomography

To understand the behaviour of fluids confined within porous media, one would like to have a complete picture of pore geometry, in which the smallest, as well as the largest pore-length scales are quantitatively represented. The use of x-ray tomography in characterizing the petro-physical properties of reservoir rocks is of great importance in predicting their quality and behaviour during oil production. An evaluation of the porous rock media will help in obtaining properties such as the, porosity, pore size distribution, permeability etc. (Appoloni et al., 2007) X-ray tomography technique is expanding rapidly in recent years, which offers a promising technique for predicting the petro-physical properties of a material from only a 3D microstructure. The technique

has been in existence since the early development of computed tomography (Vinegar et al., 1991). 3D imaging by tomography is needed to describe the internal structure of a heterogeneous material by size, orientation and/or connectivity of the phases with complex shapes (Kastner et al., 2011). X-ray tomography is also a completely non-invasive and non-destructive imagine technique that allows quantitative investigation of objects in three dimensions (Sinka et al., 2004). This method of pore imaging structures in a non-invasive way has made the application of this technology extremely popular across several areas of discipline, such as physics, mathematics, medicine, material science, powder technology and mineral processing, to name only a few (Al-Raoush and Willson, 2005; Gupta et al., 2005; Lin et al., 2010; Stock et al., 2008; Wildenschild et al., 2002).

3.3.1. Theory behind X-ray tomography

Computer X-ray tomography are generally used to characterize structure and fluid distributions within reservoir core material systems (Coles et al., 1998). It is a combination of X-ray microscopy and tomographical algorithms. Also, the acquisition of a three-dimensional, high resolution description of rock structure and pore level characterization has been of great importance in recent years (Ruiz de Argandona et al., 2009). The principle of X-ray tomography, as used in the industrial context is shown in Fig. 3.9. It consists primarily of an x-ray source and a detector. The sample is placed on top of the sample holder with the help of epoxy resin to hold the sample as shown in Fig. 3.10, and it is then positioned in the sample platform between the x-ray source and the detector. The sample under study rotates simultaneously around this axis in order to obtain multiple 2D projection images at different angles (0 to 360^{o}) leaving the

x-ray source and detector stationary. The set-up achieves a better mechanical stability, which is required at high resolution.

(a)

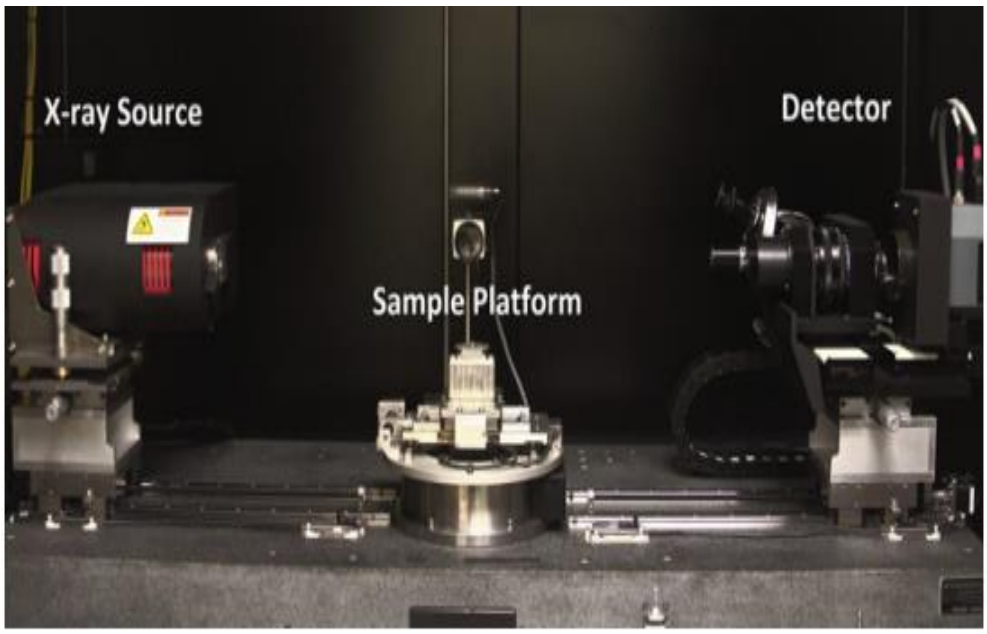

(b)

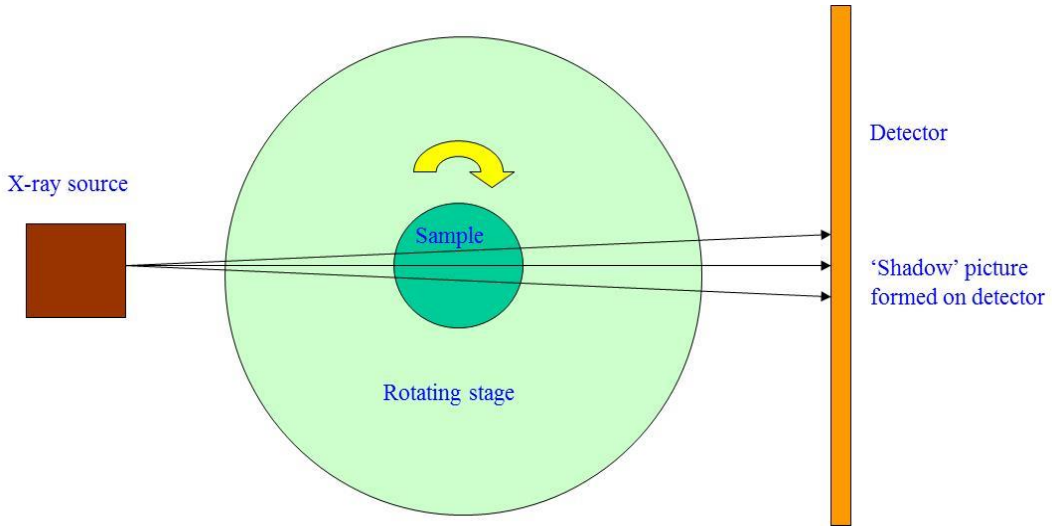

Figure 3. 9: An image of the Inside view of the Xradia Micro XCT-500 micro tomography system (a). Inside view of the μ-CT (b) Courtesy of Sean Rigby, University of Nottingham

Also, in this set-up, the x-ray beam makes geometrical magnification achievable by positioning the sample under study at any position between the x-ray source and the detector (Fig. 3.9). The detector source is used to measure the intensities of the x-ray beam transmitted through the sample, as the sample is rotated along the beam. This x-ray beam is characterized by its photon flux density, or intensity, and spectral energy distribution. When a beam of x-rays passes through homogeneous material, the sample under study becomes a source of secondary x-rays and electrons. Due to the secondary processes, a portion of the primary beam is absorbed or scattered out of the beam. The sample under study should be contained within a cone beam to obtain a 3D image; otherwise a special correction procedure has to be applied. The 3D reconstruction procedure is based on a pixel-based approach in which the 3D

image is directly reconstructed using a filtered back projection algorithm (Orlov et al., 2006).

A mathematical algorithm, formulated by Lambert-Beer's law, which states that each layer of material of equal thickness will absorb an equal fraction of the radiation through it, and is then used to generate the reconstructed images from the measured transmitted intensities and is given by the equation below:

$$I = I_o \, e^{-\mu(t)} \tag{3.5}$$

where I_o is the initial radiation x-ray intensity, which is the number of photons registered per second when the system is in vacuum; μ the linear attenuation coefficient of the material, which depends on the electron density of the material, the energy of radiation and bulk density of the material (Wildenschild et al., 2002). And t is the thickness of material. The energy-dependent linear attenuateion coefficient μ, is determined by four effects, i.e. photoelectric effect, incoherent scattering, coherent scattering and pair production.

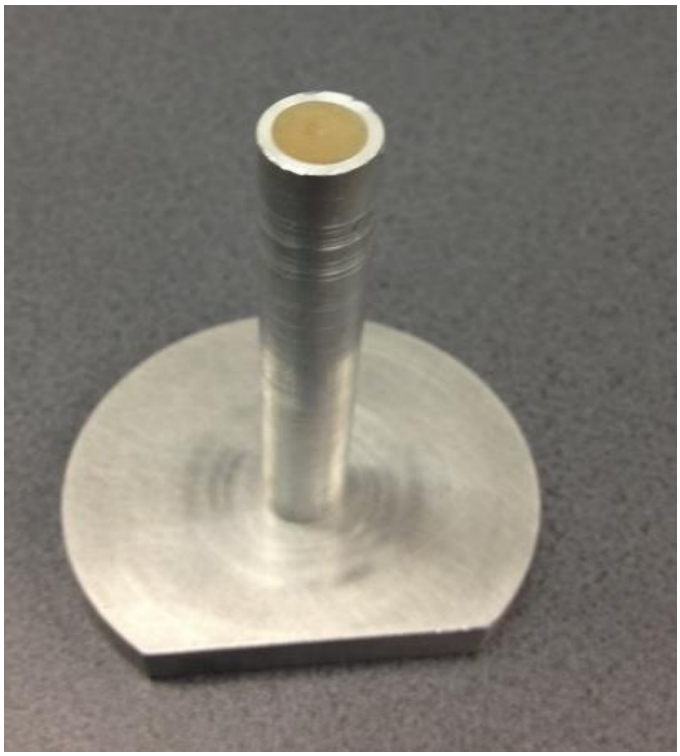

Figure 3. 10: Photograph of a 5mm sample holder.

3.3.2. X-ray tomography in porous media

Applications of X-ray tomography, in the literature, to porous media are numerous; one of the largest areas of applications of the X-ray CT is in the study and analysis of fluid flow and transport properties in porous media. Porous media present a great variety of internal structures as mentioned earlier in section 3.2. X-ray tomography will provide in detail the qualitative internal structure of porous media and has been studied by various researchers (Al-Raoush and Willson, 2005; Lin et al., 2010; Moreno-Atanasio et al., 2010).

Turner *et al*. (2004) studied the multiphase fluid flow during drainage in porous materials by looking at a three-dimensional image of a monodisperse bead pack and a sandstone sample. They observed that the residual (trapped) wetting phase in the bead pack is present as pendular rings between grains and lenses within pore throats. In a similar approach, Zhou Na *et al*. (2010) studied

the entrapment of non-wetting phase in porous media by obtaining three dimensional images of pore structure and trapped gas bubbles in sandstone cores using micro X-ray CT. They used a vertical and horizontal sandstone cores, 8 mm in diameter and 15 mm long. For the horizontal core, they observed that trapped bubbles have a pore network scale size and distribute over several pores. However for a vertical core the porosity fluctuates in the direction of flow due to layered structure.

In a different approach, Del Ferro *et al*. (2012) used a combination of mercury porosimetry technique and x-ray tomography to study the total porosity and pore size distribution of soil aggregates with a nominal pore size between 5-6 mm. They used a network model on pore size distribution curves to highlight structural properties affecting the aggregates. They found out that the mercury porosimetry revealed the smallest pore that were not detected by micro CT and it represent up to 70% of the total porosity. They also found out that the resolution of micro CT showed its inapplicability to pores smaller than few microns. However micro CT still provides a qualitative measure of pore size distribution that is more reliable than the mercury porosimetry since it is not affected by the ink-bottle effect (Dal Ferro et al., 2012).

Another study that uses the combination of mercury porosimetry and x-ray tomography was carried out by Fusi and Martinez-Martinex (2013) to study the structural and textural features of carbonate rocks. They analysed nine different carbonates lithologies. They analysed the carbonate rocks by running a mercury porosimetry experiment where mercury is impregnated into the materials. They found out that most of the quantity of mercury intruded during porosimetry test is entrapped at the end of the test itself. They also used micro

CT to image the entrapped mercury following porosimetry experiment. They concluded that the micro CT easily detects mercury impregnated cores with radius one order of magnitude smaller than the voxel size, due to high density contrast between mercury and carbonate rocks (Fusi and Martinez-Martinez, 2013).

3.3.3. Limitations of X-ray tomography

One of the main advantages of using the X-ray tomography technique is the ability to perform a three-dimensional imaging in a non-destructive way. It also comes with limitations or problems and one of which is the appearance of artifacts, which makes the quantitative interpretation of a 3D structure difficult. The artifacts come from different origins, but the main ones are beam hardening, ring artifacts, noise artifacts and motion artifacts. Beam hardening comes as a result of a strong attenuation of low energy x-ray in the spectrum, resulting in a homogeneous mass appearing denser at the boundary than in the centre (Krumm et al., 2008). Motion artifacts are due to the movement of objects within the scanned volume being imaged which results in blurry images. However, some of these artifacts can be removed partially or completely by filtering the images and using special algorithms that correct bad pixels or eliminate the noise from the image (Krumm et al., 2008). The second disadvantage is the spatial resolution. It describes the level by which details in an image can be resolved. It measures accurately the smallest separation distance for which attenuation values at two known points can be observed. The spatial resolution of CT images is highly dependent on the sample size, x-ray source and detector, distance between source, and the signal-to-noise ratio (Wildenschild et al., 2002). The smaller the diameter of

the sample, the better the X-ray CT resolution will be. Also, another limitation to X-ray CT is the contrast sensitivity. It is a measure of how well a feature can be differentiated with surrounding background. It is defined as the difference in attenuation between the feature and the background, divided by the ground attenuation.

3.3.4. Scope of work by X-ray tomography

Mesoporous silica and alumina materials are often used as supports for heterogeneous catalysts or absorbents. The geometry and topology of the void space determines the rate at which mass transport may be able to occur through the pore system (Rigby et al., 2005). As mentioned earlier in section 3.2 of the mercury porosimetry section, a combination of mercury porosimetry and X-ray tomography to investigate the behaviour of porous solids in relation to mercury entrapment within a sample will provide a better understanding of the structural architecture of the porous media. Furthermore, mercury intrusion into porous materials can improve the quality and resolution of micro CT images, because of the high density contrast between mercury and the surrounding porous material.

Previous work by Rigby *et al*. (2011) has shown that it is possible to use the combination of both mercury porosimetry and X-ray tomography to determine the distribution of non-wetting fluid in porous media. These researchers used a combination of two techniques, mean-field density functional theory (MF-DFT) and micro-computerized x-ray tomography to interpret mercury porosimetry data. They used the MF-DFT to show that the top of mercury intrusion and extrusion curves are associated with network structures where the

smallest pores are only formed through connections with larger pores. They also used CXT to study the pore potential theory of hysteresis and entrapment directly using a model porous material with spatially varying pore wetting properties. In addition, they studied the percolation properties and entrapment of mercury within a macroscopic pellet. They concluded that the CXT can be used directly to detect the percolation pathways in a macroporous alumina, and the spatial configurations of entrapped mercury ganglia within an amorphous material.

3.4. Thermoporosimetry by DSC technique

The word 'Thermoporometry' means thermal pore size measurement. It is a calorimetric method that determines pore size based on the melting or freezing point depression of a liquid confined in a pore (Landry, 2005). Thermoporosimetry is more suitable for studying the porous structure of porous solids immersed in a liquid. The most important assumption in the thermoporosimetry is the solid/liquid interfacial tension, which is not measured directly, contrary to the liquid/vapour interfacial tension (Brun et al., 1977). This method is not well recognised compared to adsorption or mercury porosimetry, probably because its experimental development is more recent.

Differential Scanning Calorimetry (DSC) is a technique which measures the change of the difference in the heat flow rate to the sample and to a reference sample while they are subjected to a controlled temperature (Hohne et al., 2003). The DSC is a suitable tool for the precise measurement of small temperature shifts due to the sensitivity of exothermic freezing and endothermic melting transitions. The basis for these shifts is that the

equilibrium temperature for a solid temperature is determined by the radius of the curvature of the interface between the solid and the liquid phases (Landry, 2005).

Thermoporosimetry has been found to be suitable for characterising a large variety of porous materials such as controlled pore glass (CPG) (Landry, 2005), silica gel (Ishikiriyama and Todoki, 1995), cellulose (Hay and Laity. 2000), polymer gels (Babba et al., 2003) and ordered mesoporous (MCM-41, SBA-15 etc.) (Webber, 2010). The main advantage of using this technique is that it is simple and easy to use; it also has the ability to perform measurements quickly. Another advantage in thermoporosimetry experiment is that there is no extraordinary sample preparation required. Despite its simplicity, it can be a powerful tool in characterising porous materials.

Also, several materials have been used in Thermoporometry to probe porous properties including benzene (Yamamoto et al., 2005), alkanes (Ehrburger-Dolle et al., 1990), acetone (Iza et al., 2000), and water (Hay and Laity, 2000; Landry, 2005). However, water is mostly used as the probe fluid, which is relevant for examining materials specifically to absorb aqueous solutions. Another advantage is that water has a high enthalpy of fusion, ΔH_f=334J/g (Perry et al., 1999), which enhances the sensitivity of the DSC technique to small volume of adsorbed liquid (Landry, 2005). Water as a probe fluid is also non-hazardous, readily available and its properties have been well studied. Thus, water will be used in this thesis to determine the PSD of some mesoporous materials. Whereas the major disadvantage of this method is that it is non-traditional and it’s not as widespread as mercury porosimetry and adsorption techniques. Also, another disadvantage in measuring the phase

transition using DSC is that it is measuring a dynamic process of freezing or melting, and therefore requires heating or cooling of the sample, which reduces the temperature resolution. Fig. 3.11 shows DSC equipment, equipped with a material sample cell and an empty reference pan. The two cells sit on a thermoelectric disk surrounded by a furnace.

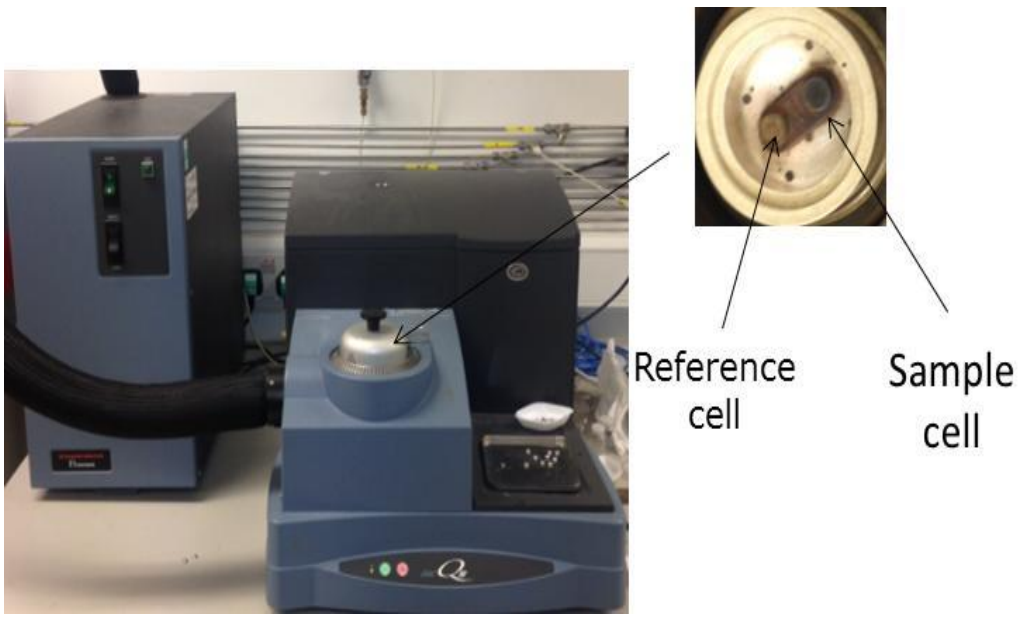

Figure 3. 11: Differential Scanning Calorimetric machine equipped with a reference and sample cell

3.4.1. Theory of thermoporosimetry using DSC

The basis of the Thermoporosimetry experiment is to measure the pore size distribution using DSC. The measurement is based on the melting point depression of a pore-filling substance, or adsorbate, in very small pores or capillaries. The technique is based on the thermodynamic relationship between pore size and the soilidification temperature of freezable pore water, which allows the determination of pore volume, pore sizes, and the internal surface area of wet solid before drying (Yamamoto et al., 2005). According to

Bearroies et.al. (2004), the peaks observed during the melting and cooling of the confined solid material are directly proportional to the pore size distribution as well as the pore geometry (Denoyel et al., 2004). Defay *et.al*. (1966) obtained a relation for the lowering of the triple point temperature. These authours developed a thermodynamic description of the lowering of the equilibrium temperature between three phases of liquid, gas, and solid in porous media with curved interfaces. However, in the case of thermodynamic equilibrium that is only governed by the liquid-solid interface, the treatment of Defay *et. al*. (1966) reduces to the Kelvin equation. Brun *et.al*. (1977) used the results of Defay *et al*. (1966) to work out the thermodynamic basis between the phase curvature and the shift in triple point temperature to determine the PSD from the freezing of a liquid inside the pores of a material, thus allowing the observation of the freezing and melting of material confined on the pores as a function of temperature. The following Gibbs-Thompson equation described the relationship between the pore diameter and the melting point depression, on the assumption that all pores are cylindrical;

$$\Delta T_m = T_o - T_m = \frac{V_m \gamma_{ls}\, T_o}{\rho \Delta h} \frac{dA}{dV} = -K \frac{dA}{dV} \qquad (3.6)$$

where ΔT is the melting point depression, T_o the melting point of the bulk probe liquid at normal pressure, γ_{LS} the surface tension of the solid-liquid interface of the probe, ρ is the density, Δh is the specific enthalpy of melting, dA/dV is the curvature of the solid liquid interface which is *1/r* for cylinders and *2/r* for sphere, where r is the radius of the curvature. K is defined as $K = \frac{\gamma_{ls}\, T_o}{\rho \Delta h}$. The curvature is defined as positive when the centre of curvature lies within the body and negative when the centre of curvature is outside the body.

For a spherical or hemispherical interface with radius of curvature *r*, of a solid in contact with liquid, Eq. 3.6 reduces to Eq. 3.7 below.

$$\Delta T_m = \frac{2V_m\gamma_{sl}T^o}{\rho\Delta hr} \tag{3.7}$$

The above Eq. 3.7 is mostly used in the analysis of the experimental melting point depressions of the materials confined in cylindrical pores. Many studies have shown that a layer of non-freezable liquid usually exists along the walls of a porous material (Landry, 2005). A model representing different types of pore water is shown by drawing in Fig. 3.12. The water that exists in mesoporous is classified into two types. First is the freezable pore water, which can form a cylindrical ice crystal in the pores, and the other is the non-freezable pore water that does not undergo a water ice crystal transition during the DSC measurements due to the strong interactions with the pore surface.

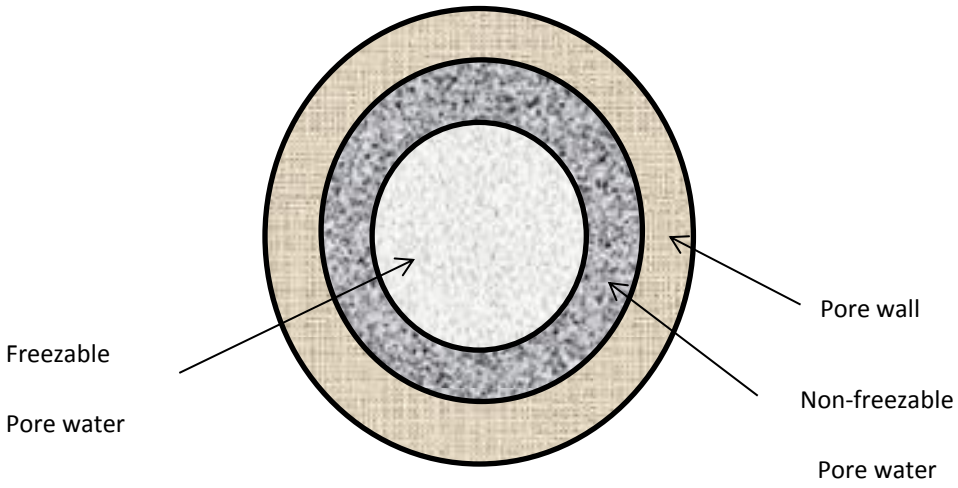

Figure 3. 12: Model of the different types of pore water (Yamamoto et al., 2005)

The pore radius can be calculated from the sum of the radius of an ice crystal formed in a mesopore, and the thickness of the non-freezable pore water layer.

The relevant physical properties of the probe liquids that were used in this study to determine the actual of pore size distributions of mesoporous materials are summarized in Table 3.2.

Table 3. 2: Physical properties of probe liquids (Atkins et al., 2006; Perry et al., 1999)

Probe fluid	T^o_m, K (^oC)	ΔH_f (J/g)	ρ_{liquid} (g/cm^3)	ρ_{solid} (g/cm^3)
Water	273.15	334	1.000	0.917
Mercury	234.32	11.6	15.534	13.534

Iza *et al*. (2000) presents a thorough evaluation of the DSC technique using different experimental protocols to examine mesoporous solids, specifically, controlled-pore glass. These researchers derived numerical expression for the variation of freezing/melting point temperature with pore radius in porous materials that were fully saturated with water. The equations they derived will be used in chapter 5 of this report to determine the pore size of mesoporous materials.

$$R_p(nm) = -\frac{64.67}{\Delta T(K)} + 0.57 \quad \text{(Freezing)} \tag{3.8}$$

$$R_p(nm) = -\frac{32.33}{\Delta T(K)} + 0.68 \quad \text{(Melting)} \tag{3.9}$$

Where $\Delta T = T\text{-}T^o$, is the shift in the triple point temperature.

In determining the pore radius distribution curve, an estimate of the energy of solidification is needed. The theoretical energy of solidification of water is given by:

$$W_{th} = T\Delta s \tag{3.10}$$

where Δs is the molar solidification heat of condensate. The above equation can be written in the following approximated form for slight variations of Δs with temperature:

$$W_{th} \approx T\Delta s\left\{1 - \frac{d\gamma_{ls}}{dT}\frac{\Delta T}{\gamma_{ls}}\right\} \tag{3.11}$$

knowing the values for Δs and the solid-liquid surface tension yield a numerical expression for the apparent energy of solidification.

$$W_a\left(\frac{J}{g}\right) = -5.56\,X\,10^{-2}\Delta T^2 - 7.43\Delta T - 332 \tag{3.12}$$

To sum up, Eq. (3.10), (3.11) and (3.12) allowed us to evaluate the efficiency of thermoporometry method to calculate the pore size and pore size distribution of a porous material filled with water.

3.4.2. Solid-liquid phase transition (melting and freezing)

There have been numerous experimental studies on freezing and melting phase transitions of confined fluids in porous materials. Various experimental techniques have been used in the study of melting and freezing processes in porous media including calorimetric, electron microscopy, neutron scattering and NMR. The melting of confined fluids can proceed in two ways. It can start from the surface of the pores and proceed towards the centre of the pore as

seen in Fig. 3.12. The other possibility is the initiation of melting at high energy locations or at closed end of the pore (Morishige et al., 2010).

The freezing process on the other hand can also occur in two ways. It can occur in the pores by heterogeneous nucleation outside the pores or inside the adjacent pore that has already been frozen, and hence displays a large kinetic supercoiling, independent of the pore size (Borisov et al., 1998; Morishige et al., 2010). On the other hand, if there is no nucleation centre present, the pore liquid will freeze by homogeneous nucleation. However, it is important to differentiate between the two situations where external solid phase is or not present outside the pores to act as nucleation centres. Schreiber *et al*. (2001) observed that the freezing temperature in the pores is lowered if no solid phase is present outside the pores and the freezing curve in thermoporometry or NMR cryoporometry does not represent the actual PSD of the sample.

Also, freezing and melting in partially filled pores present interesting phenomena and have been reported by numerous researchers (Schreiber et al., 2001; Hitchcock et al., 2011). Schreiber *et al.* (2001) studied the melting and freezing of water in series of mesoporous silica materials with hexagonal arrangements of cylindrical and narrow pore size distributions using DSC. They concluded that the DSC scans of the freezing of water and deuterium oxide (D_2O) in partially filled pores of SBA-15 reveal a peak pattern depending on the degree of pore filling. The different peaks observed are attributed to different states of the liquid in the pore space, that is to say pore water in completely filled regions, and water as an adsorbed film at the pore wall. They also concluded that the freezing peak of pore water is nucleated by external bulk ice and exhibits substantial supercoiling.

3.4.3. Melting-freezing hysteresis

The freezing and melting of materials is known to display large hysteresis loops, i.e., the freezing in pores is observed at lower temperatures compared to melting. The melting/freezing hysteresis can be monitored either by NMR (Hitchcock et al., 2011), or DSC (Beurroies et al., 2004). The reason behind the hysteresis is attributed to the shape of the pore (Brun et al., 1977) and, pore blocking effect (Petrov and Furo, 2011). An example of hysteresis in porous materials is given in Fig. 3.13 below. The nature of the hysteresis as well as the physical reasons for observed broadening of freezing and melting is still not clear in spite of several studies of the freezing and melting phase transitions in porous media. It is also not been established yet whether the melting or freezing in confinement takes place at equilibrium temperature. This equilibrium temperature is the temperature at which the free energies of both the solid and liquid in the pores are equal (Riikonen et al., 2011). There is therefore a need to improve the understanding of the hysteresis of melting-freezing in connection with pore structure. Petrov *et al.* (2011) conducted an experiment on two different samples of CPG and vycor using DSC (Fig. 3.13). It can be seen that the CPG sample has parallel branches, whereas the vycor has steeper freezing branch. They suggest that the abrupt freezing in vycor is as a result of pore blocking effect.

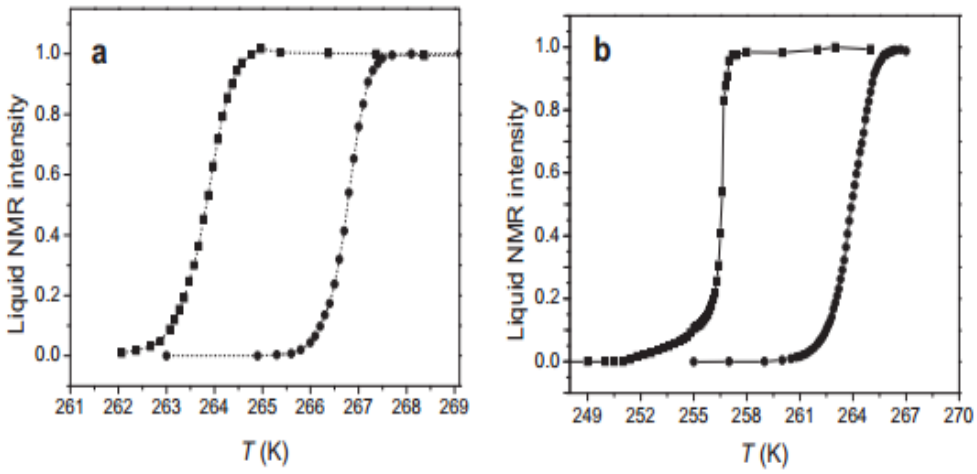

Figure 3. 13: Freezing (squares) and melting (circles) curves of water in CPG (a) and Vycor (b) (Petrov and Furo, 2011)

3.4.4. Pore size distribution

Disordered porous solids, such as sol-gel silicas, are often used in many applications, including as catalyst supports or chromatographic media. The performance of these materials in these applications depends strongly upon the structural characteristics of the void space. Experimental methods such as gas sorption or mercury porosimetry are generally used to obtain the pore size distributions (PSDs) for these materials. The most recent data analysis methods, to interpret raw gas sorption characterisation data for disordered materials, have been developed from studies using more ordered, model materials, such as MCM-41 and SBA-15. However, it is not clear that the theories and techniques developed for more regular structures, such as these, will give accurate PSDs for disordered materials with more complex and amorphous internal pore geometry, and more extensive void space interconnectivity. Previous work has suggested that conventional data analysis methods for gas sorption, such as the Barrett-Joyner-Halenda (BJH) algorithm and non-local density functional theory (NLDFT) software, neglect effects

such as variations in the causes of hysteresis around the boundary sorption curves, advanced condensation, and delayed adsorption (Esparza et al., 2004; Hitchcock et al., 2010; Shiko et al., 2012). It is thus necessary to both assess the level of systematic error introduced by these effects, and others, into the PSDs for disordered solids, and develop methods to remove this error.

3.4.5. Scope of work by DSC technique

A significant goal in the study of porous materials is the reliable estimation of pore size distributions (PSD). As earlier mentioned, PSDs are important in the development of models for the prediction of petro-physical parameters such as capillary pressure curves and permeability of rock samples from the oil reservoirs. Molecular transport properties are studied in many different experimental techniques in an effort to further the understanding of fluid behaviour in systems such as oil and rocks in porous media. Frequently, only the mercury porosimetry intrusion curve is used, for the purpose of obtaining the pore neck size distribution, and the extrusion curve is neglected. This is because, in general, the physical processes involved in retraction are more complex than those involved in intrusion. The variety of phenomena involved in retraction, such as contact angle hysteresis, snap-off, and entrapment, mean that interpretations of retraction curve are often ambiguous, and highly model dependent. However, some workers have attempted to use mercury data to determine pore network connectivity (Portsmouth and Gladden, 1991) or macroscopic heterogeneity in the spatial distribution of pore sizes (Rigby, 2002). These attempts at interpreting mercury retraction are often based upon results from glass, plastic or metal micromodels (Lenormand et al., 1983; Wardlaw and Mckeller, 1981). Partly as a means to improve the interpretation

of retraction curves, Rigby and co-workers (Rigby et al., 2004; Rigby et al., 2008) introduced the integrated nitrogen sorption and mercury porosimetry technique. This method employs a series of alternating gas sorption and mercury porosimetry experiments carried out on the same single sample, with any mercury entrapped following a porosimetry experiment frozen in place before a subsequent gas experiment is performed. The difference between the gas sorption isotherms before and after mercury entrapment can be used to infer information about the distribution of entrapped mercury, and thence, the retraction process.

In this work, water as a probe fluid will be used to determine the pore size distribution of mesoporous materials, by looking at the heat versus temperature curve from a thermoporosimetry experiment using DSC. Also, the calibration of the constants of proportionality in the Washburn and Gibbs-Thomson equation will be given more attention in this thesis chapter, with a view to studying the consistency of the pore structural information obtained from the two methods, mercury porosimetry, and thermoporometry. The difference between the comparison of results for these different techniques presented here, and that made previously by others (Beurroies et al., 2004; Gane et al., 2004), is that exactly the same sample can be used to make a comparison, and, additionally, that comparison can be further narrowed to a particular sub-set of pores within a disordered material, rather than comparing overall PSDs. Hence, the integrated technique can approach the degree of definitive study permitted for templated model materials, via their high levels of order, but for amorphous, disordered materials. This work will also attempt to reduce the number of arbitrary assumptions that have been necessary for indirect

characterisation methods in the past, such as the geometry of the meniscus at the phase transition and the applicability of physical parameters calibrated on model materials. Finally, this work will consider a potential explanation for the discrepancies observed between the different experimental techniques.

3.5. Nuclear Magnetic resonance

Nuclear magnetic resonance (NMR) is a phenomenon, which occurs when the nuclei of atoms are immersed in a static magnetic field and it is exposed to a second oscillating magnetic field. Some nuclei do not experience these phenomena but others do, depending on whether they possess a property called spin. NMR is a very important and complex analytical tool for the characterisation of underground hydrocarbon reservoirs. Parameters such as the porosity, water saturation, pore size distribution, wettability and permeability which are key parameters in rock characterisation can be determined using NMR. The NMR technique measures the frequency of a nuclear resonance with sufficient accuracy in the presence of a static external magnetic field.

3.5.1. NMR theory and applications in porous media

The basic principle of NMR is that sub atomic particles (e.g., proton, neutron, electron, etc.) possess a characteristic called spin angular momentum. Each particle has a spin value of either 1/2, 1, 3/2 etc, and is electrically charged. If an external magnetic field is applied, the spin angular momentum of nuclei with isotopes of overall non-zero spin will undergo a cone-shaped rotation called precession there by making an energy transfer possible between the lower (base) energy to a higher energy level. This transfer of energy takes

place at a wavelength that corresponds to radio frequencies and when the spin returns to its lower (base) level, energy is emitted at the same frequency. The signal that matches this transfer is measured and processed in many ways in order to yield an NMR spectrum for the nucleus concerned.

When a motion of a charged particle is associated with a magnetic field, a magnetic dipole is created. This corresponds to magnetic moment μ in a magnetic field. The magnetic moment **μ** is directly proportional to its spin angular momentum ***P***, which is the angular momentum quantum number, and sometimes referred to as the nuclear spin, with a proportionality constant called the magnetogyric ratio and is constant for each particular nucleus.

$$\mu = \gamma\rho \tag{3.13}$$

The angular momentum of an atomic nucleus rotating about a reference point is the measure of the extent to which it will continue to rotate about that axis unless acted upon by an external torque. Like many atomic properties, the angular momentum is quantized:

$$P = \hbar\sqrt{I(I+1)} \tag{3.14}$$

where $\hbar = h/2\pi$, h is Planck's constant (6.6256 x 10^{-34}Js) and *I* is referred to as the nuclear spin and can hold values of either integer or half integer, I,e. $0, \frac{1}{2}, 1, \frac{3}{2}, 2, \frac{5}{2},$ etc.

The energy of a magnetic dipole in a magnetic field with flux density is given by:

$$\boldsymbol{E = \mu_z B_o} \tag{3.15}$$

where B_o is the magnetic flux density. The energy difference between ΔE is found to be proportional to the strength of the applied magnetic field B_0 at the nucleus and is given by:

$$\Delta E = \gamma \hbar B_O \tag{3.16}$$

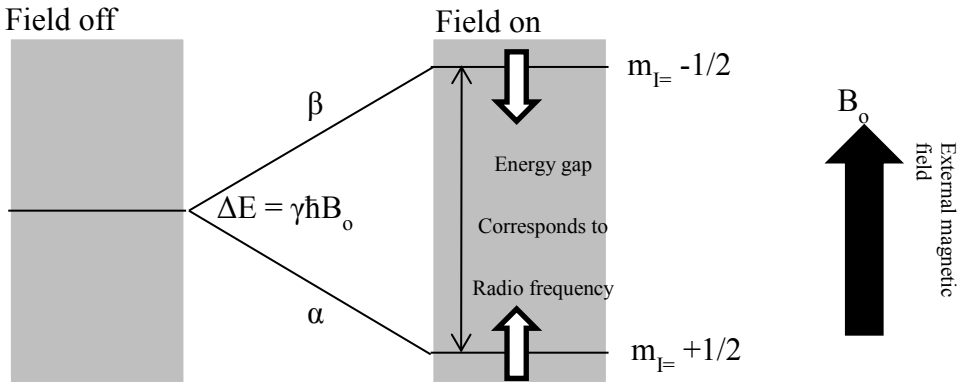

Figure 3. 14: The nuclear spin energy levels of a spin -1/2 nucleus in a magnetic field (Atkins et al., 2006)

Fig. 3.14 shows that the energy required for the spin-flip depends on the magnetic field strength of the nucleus. If there is no applied field, there will be no energy difference between the states. As the field increases so does the energy difference of the spin states and the radio frequency, which is referred to as resonance.

The energies $\boldsymbol{E}_{\mathbf{upper}}$ and $\boldsymbol{E}_{\mathbf{lower}}$ are separated by ΔE:

$$\Delta E = \boldsymbol{E}_{\mathbf{upper}} - \boldsymbol{E}_{\mathbf{lower}} \tag{3.17}$$

A cone about a strong magnetic field is traced by a motion of a magnetic moment in a uniform externally applied magnetic field under the condition of

constant total energy. This movement of magnetic moment is similar to the motion of a gyroscope running in friction free bearings under the influence of Earth's field as seen in Fig. 3.15. Such motion is referred to as Larmor precession. And the precession frequency ν_o is given by:

$$\nu_o = |\gamma| \frac{B}{2\pi} \tag{3.18}$$

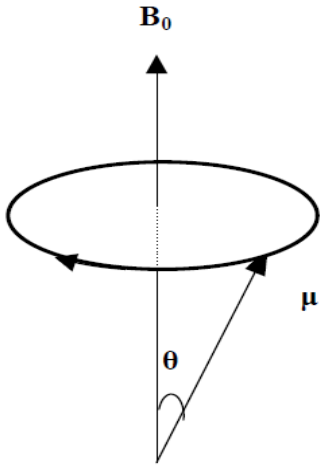

Figure 3. 15: Precession of a magnetic moment μ about an applied magnetic field B_o

Boltzmann statistics describe how nuclei are distributed throughout the various spin states available in a given macroscopic sample of a specific NMR-active nucleus. Energy from thermal collisions is used to place many nuclei from lower energy state to a higher energy state due to the low energy separation between the states.

$$\frac{N_{upper}}{N_{lower}} = e^{-\gamma B_o / KT} \tag{3.19}$$

where N corresponds to the values of nuclei in the respective spin states, k_B is the Boltzmann constant ($k_B = 1.3805 \times 10^{-23} JK^{-1}$) and T is the temperature in Kelvin (K).

At room temperature, the upper and lower energy states are equally populated with a very small excess in the lower energy state. The excess in lower energy state is in the region of parts per million (ppm). As the temperature decreases, so does the ratio N^-/N^+. Whereas the temperature increases, the ratio approaches one.

3.5.2. Principles of NMR measurement

In any NMR experiment, transitions are induced between different energy levels by irradiating the nuclei with a superimposed field B_1 of the correct quantum energy, i.e., with the appropriate frequency ν_1 (Friebolin, 1991). The resonance conditions are such that:

$$\Delta E = h\nu_1 \tag{3.20}$$

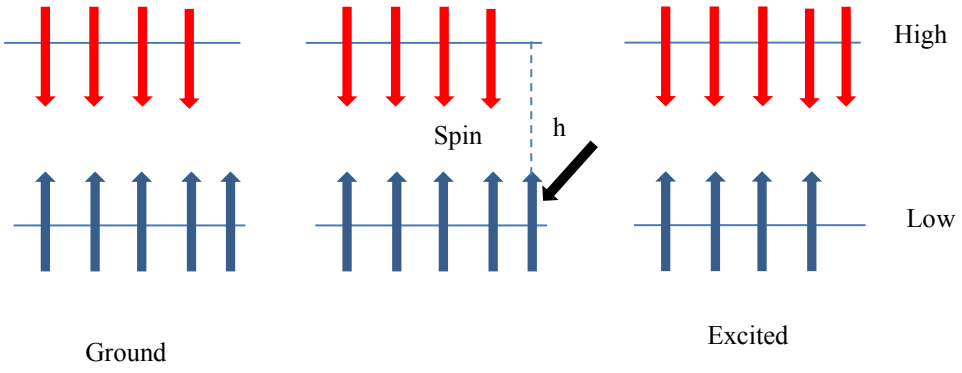

Figure 3. 16: Adsorption of nuclei from lower energy to higher energy state (Mc. GrawHill, 2011)

In Fig. 3.16, the transition of energy levels from lower to higher state corresponds to adsorption of energy while in the reverse direction corresponds to the emission of energy. Each transition is associated with the reversal of the spin orientation. The dominant process from the irradiating field is the adsorption of energy, which is due to the population excess in the lower level. This is observed as a signal whose intensity is proportional to the population difference N_α -N_β, and the total number of spins in the sample, and thus to the concentration. The adsorption and emission processes cancel each other out when the populations are equal $N_\alpha = N_\beta$, which results in no signal. This condition is called ***saturation.*** Since transitions only occur when the frequency v_1 of the electromagnetic radiation matches the Larmor frequency v_L, the resonance condition can be obtain as:

$$v_l = v_1 = \left|\frac{\gamma}{2\pi}\right| B_o \tag{3.21}$$

According to Friebolin (1991), transitions in a sample can generate a resonance frequency from the radio frequency transmitter when the resonance condition is satisfied. Two methods can be used to achieve this, either by varying the magnetic flux density (B_o) by means of sweep coils at constant transmitter frequency (v_1), or by varying the transmitter frequency (v_1) at constant value of (B_o). From the methods the spectrum is recorded point by point by varying magnetic flux density or transmitter frequency continuously. This is therefore called the continuous wave or CW method of recording spectra (Friebolin, 1991).

In the pulse method all the nuclei of one species in the sample are excited simultaneously by a radiofrequency pulse (see Fig. 3.17). A radio frequency generator usually operates at a fixed frequency (ν_f). However, if it is switched on for a short time (τ_p), a pulse is obtained of not just the frequency ν_f but also a continuous band of frequencies symmetrical about the centre frequency (Friebolin, 1991). In NMR experiments the pulse duration (τ_p) is of the order of few μs. The choice of a generator frequency (ν_1) depends of the magnetic flux density (B_o) and the nuclide to be observed.

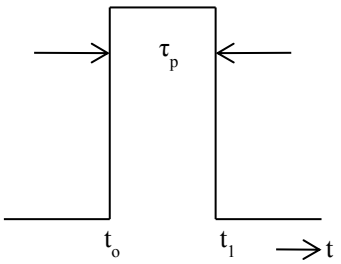

Figure 3. 17: Schematic representation of a pulse (Friebolin, 1991)

From the pulse diagram, the radio frequency generator (frequency ν_1) is switched on at time t_o and then off at t_1. The pulse duration τ_p is typically several μs. The choice of the generator frequency is determined by the magnetic field and the nuclide to be observed. Also, the pulse duration needed for any experiment depends on the width of the spectrum. For example if $\tau_p = 10^{-5}$s the frequency band is about 10^5 Hz wide.

3.5.3. NMR Relaxation

Spin lattice relaxation is also called the longitudinal relaxation. The sample in which nuclei are held is referred to as the lattice. When the nuclei in the lattice

are in vibrational and rotational motion, it creates a complex magnetic field. The motion of nuclei within the lattice, which is caused by the magnetic field, is called the *lattice field*. This lattice field has many components and some of these components will be equal in frequency to the larmor frequency of the nuclei of interest. The components of the lattice field interact with nuclei in the higher energy level and cause some of them to lose energy by returning to the lower energy state. The relaxation time T_1 is dependent on the magnetic ratio of the nucleus and the mobility of the lattice.

A second aspect of spin relaxation is the fanning out of the spins in the xy-direction if they precess at different rates. Immediately after a 90^o pulse, the magnetization vector is large when all the spins are bunched together. However, the bunching of spins is not at equilibrium. At this stage, the component of the magnetization would be zero. This randomnisation of spins occurs exponentially with a time constant called transverse relaxation time, T_2 (Fukushima and Roedar, 1981). T_2 can be determined using the Carr-Purcell-Meiboom Gill sequence (CPMG) measurement (Atkins et al 2006).

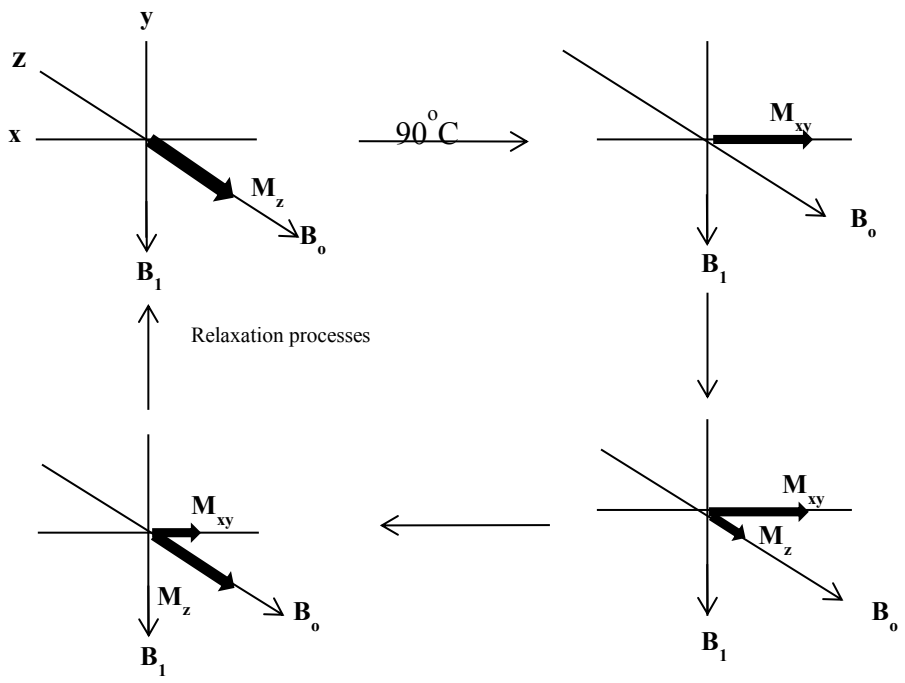

Figure 3. 18: The schematic representation of spin-spin relaxation process (Akitt, 1992)

Fig. 3.18 shows a schematic representation of a T_2 process. A 90º pulse is applied and it swings the magnetisation vector into *xy* plane around B_1 vector. Therefore, the magnetisation in the *z* direction is now zero. During the transverse relaxation process a spread of nuclear frequencies occur which causes the spins to fan out and reduce the resultant $\boldsymbol{M_{xy}}$. The magnetisation in the x-y direction decreases due to the T_2 process (Akitt, 1992). For a fluid in a single isolated pore, and for the condition known as the fast diffusion limit the magnetization, *m(t)*, decays exponentially with time:

$$M_{xy}(t) \propto M_{xy}(0)e^{-t/T_2} \tag{3.23}$$

The measurement of transverse relaxation time can be done using the spin echo experiment. Initially, a 90º pulse is applied in transverse plane along the x-axis that flips the magnetization into the xy plane, and lies it along the y-axis. The nuclei precess at different rates as time passes after the pulse is turned off. After a period of time τ, a 180 pulse is applied which flips all the spins to the

other side of the xy-plane and they continue precessing about the z-axis. Due to the flipping, the phases of spins with higher Larmor frequency lag behind whereas those with lower Larmor frequency are now ahead. Hence, at the same time delay τ is again allowed which phase all the spins again. Due to refocusing, an echo is build up and reaches its maximum after $t_E = 2\ \tau$. The refocused magnetization vector can be detected in the receiver coil and is called the spin echo signal. The maximum of the echo marks the point of maximal coherence of the spins. To ensure that the diffusion term is negligible during the measurement of transverse relaxation time, the amplitude of spin echo is recorded repeatedly at 2 τ, 4 τ, 6 τ, 10 τ, etc. this sequence is called the CMPG sequence and is illustrated in Fig. 3.19.

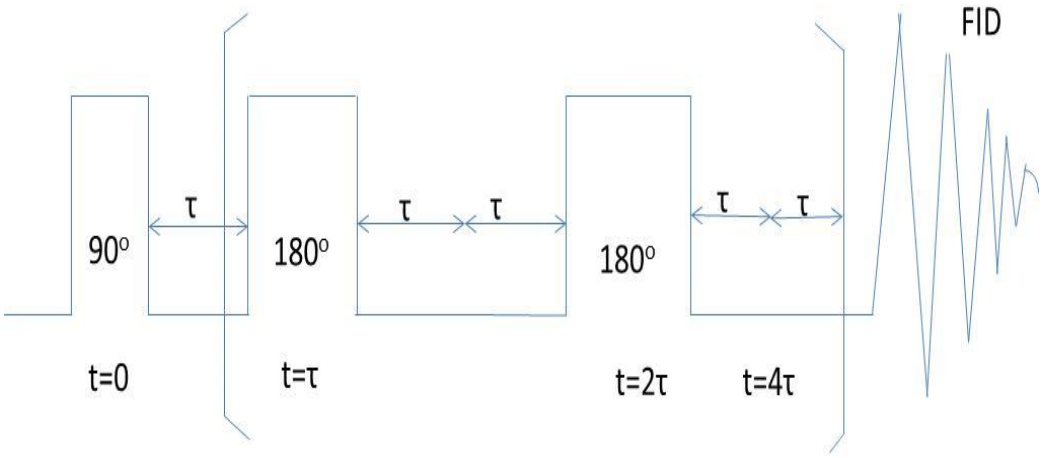

Figure 3. 19: CMPG pulse sequence used in determining the T_2 relaxation time constant derived from the Hahn spin echo sequence.

In an NMR experiment, fluid saturation in a pore space involves the interaction between the fluid molecules and the solid surface that can contribute to additional relaxation often known as surface relaxation. The source of this can be attributed to magnetic ions on the solid surface. When a water molecule

diffuse close to the surface, the fluctuating field can cause spin relaxation (Kleinberg et al., 1994). The governing equation for the NMR T_2 relaxation spectra is:

$$\frac{1}{T_2} = \frac{1}{T_{2b}}\left\{1 - \frac{\lambda S}{V}\right\} + \frac{\lambda S}{V}\frac{1}{T_{2S}} \ , \tag{3.24}$$

$$\frac{1}{T_2} = \frac{1}{T_{2b}}\left\{1 - \frac{\lambda}{r}\right\} + \frac{\lambda}{r}\frac{1}{T_{2S}} \ , \tag{3.25}$$

where T_2 is the average relaxation time of the liquid molecules within the pore, λ is the thickness over which surface relaxation takes place within the pore s/v is the surface to volume ratio of the pore, T_{2s} is the surface relaxation time of the liquid, T_{2b} is the relaxation time for the bulk liquid T_2. For a cylindrical pore s/v =2/r. Eq. 3.25 is usually written in the form of:

$$\frac{1}{T_2} = \frac{1}{T_{2b}} + \rho\frac{2}{r} \ , \tag{3.26}$$

As $T_{2B} >> T_{2S}$ Eq. 3.25 is written as:

$$\frac{1}{T_2} \approx \rho\frac{2}{r} \tag{3.27}$$

where ρ is the surface relaxivity parameter. In the fast diffusion limit, the surface relaxation dominates and relaxation for the wetting fluid is proportional to the surface area S divided by the volume V for a cylindrical pore:

$$\frac{1}{T_{2,}} \approx \rho\frac{S}{V} \tag{3.28}$$

According to Abraham et al (1988), a mathematical process known as the Fourier transformation can be used to interconvert data between the time and

frequency domains. This relationship between time and frequency domains can be expressed in the form of

$$F(\omega) = \int_{-\infty}^{\infty} f(t) \exp -i\omega t (dt) \tag{3.29}$$

F (ω) corresponds to the function of frequency, and f (t) to that of time. F (w) is a complex function, it consists of a real part *R*e and an imaginary part *Im*. In principle it is valid to place display the spectrum by using either the real part or the imaginary part, since both represent the frequency spectrum. However, since the phases of the signal differ by 90º, and thus in the first case an *absorption mode* signal is obtained. Whereas in the second case one has *dispersion mode* signal (Friebolin, 1991). Because of the method of detection used, one usually obtains, after Fourier transformation, signals containing both absorption and dispersion components. However, by means of a mathematical operation called phase correction, the dispersion component can be removed, so that all the signals in the spectrum are of the usual absorption form. The absorption and dispersion mode signal is shown in Figure 3.20.

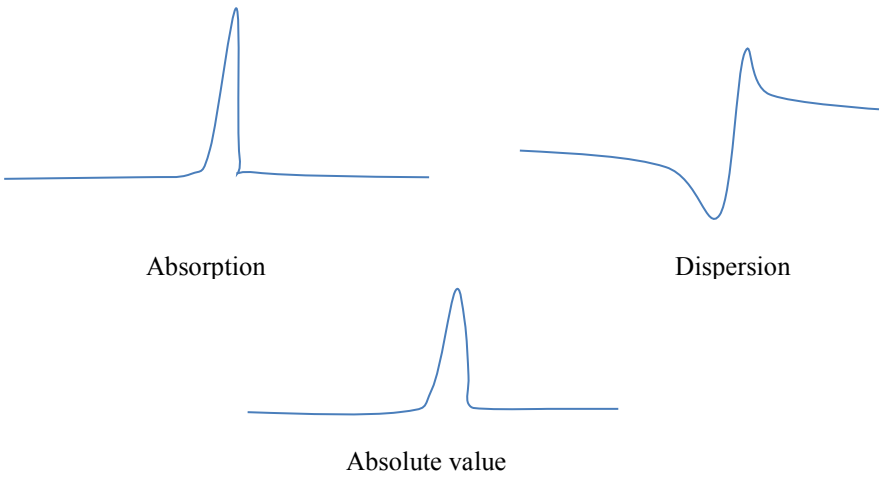

Figure 3. 20: The absorption, dispersion and absolute mode signals

In an NMR spectrometer, the raw observable magnetic resonance signal, before computer processing, is called free induction decay (FID) and is generated by the transverse component of magnetization precessing about the magnetic field. The form of the signal that we can expect is the oscillating decaying FID shown in Fig. 3.21.

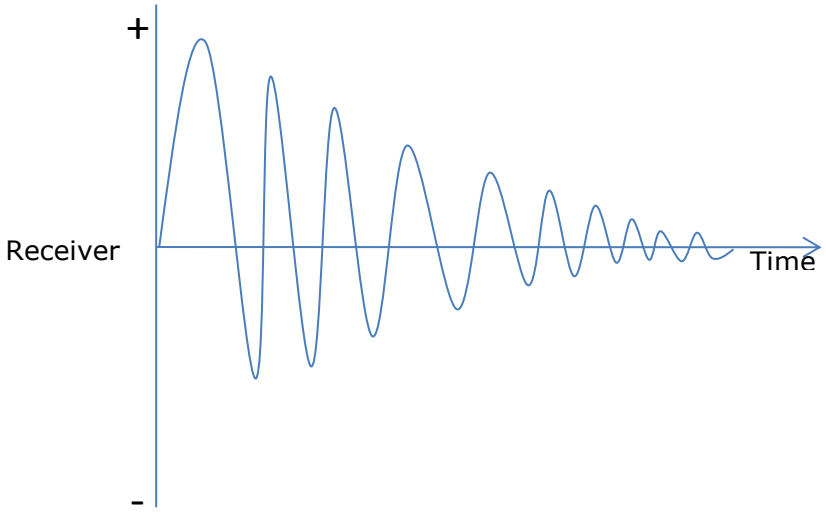

Figure 3. 21: A decaying AC signal resulting from the transverse magnetisation during relaxation

3.5.4. Diffusion measurement using NMR

In pulse gradient spin echo (PGSE) NMR, the echo attenuation, *R*, is defined as the ratio of the echo intensity in the presence of the gradient ***I*** to the echo intensity obtained in the absence of a gradient $\boldsymbol{I_o}$. The effective diffusion coefficient of a molecule within a sample can be determined using pulsed field gradient NMR. The echo intensity is given by (Hollewand and Gladden, 1995)

$$I = I_o \exp\left[-D\gamma^2 g^2 \delta^2 \left(\Delta - \frac{\delta}{3}\right)\right], \tag{3.30}$$

where D is the observed diffusion coefficient, γ is the gyromagnetic ratio, g is the field gradient strength, δ is the length of the applied field gradient, and Δ is

the diffusion time. In a diffusion experiment, a range of echo attenuations is obtained by changing g, δ or Δ. A plot of ln (I/I_o) versus $\gamma^2 g^2 \delta^2 \left(\Delta - \frac{\delta}{3}\right)$ yields the diffusion coefficient from the slope of the straight line obtained. This is also known as the log attenuation plot. The product of $\gamma^2 g^2 \delta^2 \left(\Delta - \frac{\delta}{3}\right)$ is given the symbol of Greek letter ζ.

For the diffusion coefficient measured for a liquid within a porous solid, the effective diffusivity of the liquid in the material is directly related to the molecular self-diffusion coefficient of the bulk liquid, *D*, Therefore, D_{eff} is given by (Hollewand and Gladden, 1995):

$$D_{eff} = \frac{D_\varepsilon}{\tau_P} \tag{3.31}$$

Where ε is the sample porosity and τ_{app} is the apparent tortuosity of the pore space occupied by the fluid. Also, for diffusion in a porous solid, the effective diffusivity of the liquid material, D_{eff}, is related to the molecular self-diffusion coefficient of bulk liquid, *D*, measured by PFG-NMR. Self-diffusion is the random translational motion of molecules driven by internal kinetic energy. Therefore D_{PFG} is given by:

$$D_{eff} = \varepsilon D_{PFG} \tag{3.32}$$

For diffusion within a porous solid, the tortuosity of a porous material can be derived using Eqs. (3.31) and (3.32), which yield an expression of:

$$\tau_p = \frac{D}{D_{PFG}} \tag{3.33}$$

The Stokes-Einstein relation gives the root mean square (rms) displacement travelled by a molecule undergoing free Brownian motion, during observation time t:

$$\langle r(t^2)\rangle = 6D_{PFG}t \tag{3.34}$$

3.5.5. Self-Diffusion in porous materials

Measuring diffusion of liquid confined within a porous medium using the PGSE NMR will yield qualitative information on the pore structure (Callaghan, 1984), which is of great importance to research concerning oil recovery, heterogeneous catalysis etc. The structure of the void space in a porous material constrains the fluid within it and hence influences macroscopic transport properties, such as effective diffusivity (Hollewand and Gladden, 1995). The effective diffusivity can be determined using various experimental techniques. This has been demonstrated in an earlier work done by Callaghan (1984). Also, the interactions with pore walls and competition between fluid-wall and fluid-fluid interactions can lead to various surface-driven effects. The first diffusion and relaxation measurements on molecular motion were first suggested by Hahn (1950), and Carr and Purcell (1954). The pulsed gradient spin echo method was first suggested by McCall, Douglass, and Anderson in 1963 and demonstrated by Stejskal and in 1965 (Stejskal and Tanner, 195). The PFG NMR technique is now a well-established as a method for measuring diffusion coefficients in systems ranging from mesoporous solids (Dvoyashkin et al., 2007) to reservoir sandstones (Holmes et al., 2001). Also, this technique has turned out to be suitable for revealing the influence of the pore walls on the dynamic properties of the confined fluid (Price, 1997).

Callaghan (1984) was one of the earliest researchers to determine self-diffusion of liquids undergoing Brownian motion. However, diffusion in partially-filled mesoporous materials, which is the subject of the present study, has been studied by various researchers using PFG NMR (Ardelean et al2003; D'Orazio et al., 1989; D'Orazio et al., 1990b). D'Orazio *et al.* (1989) have studied the influence of the vapour phase on the self-diffusion of water contained in partially saturated porous silica glass with pore sizes ranging from 47nm to 24nm and high porosity of 85%. The self-diffusion was found to increase when filling factor (volume of the liquid relative to the total space volume) was reduced. This is due to fast exchange between molecular transport in liquid and vapour.

In a subsequent study (D'Orazio et al., 1990a), the self-diffusivity of deionized water confined in the porous structure of a 3.5 nm porous silica glass and 35% porosity with different degree of pore filling has been reported. The experimental results were found to be linearly dependent on pore filling due to the amount of water corresponding to one monolayer. However, deviation was found below one monolayer, which is interpreted as a modification of the liquid-solid interface interaction, which causes the water molecules to become less mobile.

Also, in a different approach, Dvoyashkin *et al*. (2007) studied the equilibrium and dynamic properties of fluids confined in mesoporous materials. They measured the molecular diffusion of *n*-pentane in vycor porous glass within closed sample tubes using PFG NMR method for temperatures particularly exceeding the boiling point of the neat liquid. It was found that the temperature dependence of the diffusivity depends solely on the state of the liquid

surrounding the mesoporous. They also found that in an over saturated sample, (sample containing liquid outside of the porous material) the diffusivity in the mesopores followed Arrhenius dependence. Whereas in samples saturated by the liquid (without excess fluid), and with increasing temperature the diffusivity deviates from the Arrhenius dependence towards higher diffusivity. They conclude that with the measured filling factors, the resulting overall diffusivity is estimated by two region approach with diffusion occurring in either the liquid phase or the free space within the pore volume (Dvoyashkin et al., 2007).

3.5.6. Relaxation in porous media

As earlier mentioned, there is great interest in the oil industry in applying NMR relaxometry measurements to improve the characterisation of reservoir rocks, thus helping to reduce uncertainty in the prediction of BVI. The majority of NMR relaxometry experiments involve (^{1}H) NMR since an adsorbate consisting of water or an organic substance is most easily measured. The observed magnetization will be a measure of the number of proton spins in the liquid so if the liquid density remains constant, the signal will be proportional to the liquid volume. The major technique involve in measuring the intensity is the spin echo trains (Carr and Purcell, 1954; Meiboom and Gill, 1958). CPMG measurements are the primary NMR technique used for the evaluation of reservoir fluid properties in the well logging industry and laboratory sample analysis. The measurements are governed by the spin-spin, relaxation time T_2, the time taken for spins to diphase in their local dipolar fields. In rigid solids the T_2 value is short ranging in the order of microseconds whereas in liquids T_2 is much longer, ranging from milliseconds to seconds.

The signal from the solid and liquid components should then easily be distinguishable. However some adsorbate, such as cyclohexane has a long relaxation time and extra care must be taken to observe only the liquid signal (H. F. Both J. H, 1998).

Liquid-liquid exchange (LLE) experiments have been widely studied to probe the pore structure in porous media due to its relevance to understanding oil recovery. In LLE experiments, to displace the other, one liquid penetrates from the exterior of the porous material and thus follows a path reminiscent of an entering reactant molecule (Giesche, 2006). Feury *et al*. (2003) proposed a quasi-static experiment using NMR to determine the distribution of spin-spin relaxation times, T_2, which quantifies the amount of surface area that is wetted by either oil or by water at four different saturations states. They determine the dominant relaxation time of oil in the presence of a small amount of water at irreducible water saturation. They also determine the dominant relaxation time of water at oil residual saturation in the presence of small amount of oil. They proposed a new NMR wettability index that relates the surface wetted by oil and water when the porous medium is saturated with both fluids.

Recently Gopinathan *et al*. (2012) used a novel NMR technique to characterize properties of heterogeneous catalysts to study liquid-liquid exchange process using NMR relaxometry and NMR diffusimetry. Two model materials were used to validate their study. The first is pure sol-gel silica; with mono disperse pore space and the second model being an egg shell Pt-alumina catalyst. They found out that a high affinity liquid (water) displaces a low affinity liquid (cyclohexane) from the sol gel silica materials. They also

observed the entrapment of a low affinity liquid which is similar to that observed in mercury porosimetry.

3.5.7. Scope of NMR study

The displacement of oil by injected water in petroleum reservoirs is a process, which is both scientifically and economically important. It is known that liquids confined in a porous media show thermodynamic properties other than in bulk. Two different phases namely free liquid and adsorbed can be distinguished due to their different phases. The basic idea behind the use of NMR technique to characterize porous materials is the ability of the NMR to differentiate between when a fluid is confined within a porous media and when it is unconfined. Self-diffusion coefficients and NMR relaxation times are a powerful approach that can be used to investigate fluid infiltration into porous media. The relaxation studied in chapter 6 of this work is the spin-spin relaxation (transverse relaxation) T_2, in this study, we have also focused on the effect of temperature properties of fluids in mesoporous solids.

3.5.8. References

AKITT, J. W. (ed.) 1992. *NMR and Chemistry: An introduction to modern NMR spectroscopy,* New york: Chapman & Hall.

AL-RAOUSH, R. I. & WILLSON, C. S. 2005. Extraction of physically realistic pore network properties from three-dimensional synchrotron X-ray microtomography images of unconsolidated porous media systems. *Journal of Hydrology,* 300**,** 44-64.

APPOLONI, C. R., FERNANDES, C. P. & RODRIGUES, C. R. O. 2007. X-ray microtomography study of a sandstone reservoir rock. *Nuclear Instruments and Methods in Physics Research Section A: Accelerators, Spectrometers, Detectors and Associated Equipment,* 580**,** 629-632.

ARDELEAN, I., MATTEA, C., FARRHER, G., WONORAHARDJO, S. & KIMMICH, R. 2003. Nuclear magnetic resonance study of the vapor phase contribution to diffusion in nanoporous glasses partially filled with water and cyclohexane. *The Journal of Chemical Physics,* 119**,** 10358-10362.

ATKINS, P. W., WALTERS, V. & DE PAULA, J. 2006. *Physical Chemistry,* Macmillan Higher Education.

BABA, M., NEDELEC, J. M., LACOSTE, J., GARDETTE, J. L. & MOREL, M. 2003. Crosslinking of elastomers resulting from ageing: use of thermoporosimetry to characterise the polymeric network with n-heptane as condensate. *Polymer Degradation and Stability,* 80**,** 305-313.

BEURROIES, I., DENOYEL, R., LLEWELLYN, P. & ROUQUEROL, J. 2004. A comparison between melting-solidification and capillary condensation hysteresis in mesoporous materials: application to the interpretation of thermoporometry data. *Thermochimica Acta,* 421**,** 11-18.

BORISOV, B. F., CHARNAYA, E. V., PLOTNIKOV, P. G., HOFFMANN, W. D., MICHEL, D., KUMZEROV, Y. A., TIEN, C. & WUR, C. S. 1998. Solidification and melting of mercury in a porous glass as studied by NMR and acoustic techniques. *Physical Review B,* 58**,** 5329-5335.

BRUN, M., LALLEMAND, A., QUINSON, J.-F. & EYRAUD, C. 1977. A new method for the simultaneous determination of the size and shape of pores: the thermoporometry. *Thermochimica Acta,* 21**,** 59-88.

CALLAGHAN, P. 1984. Pulsed Field Gradient Nuclear Magnetic Resonance as a Probe of Liquid State Molecular Organization. *Australian Journal of Physics,* 37**,** 359-388.

CARR, H. Y. & PURCELL, E. M. 1954. Effects of Diffusion on Free Precession in Nuclear Magnetic Resonance Experiments. *Physical Review,* 94**,** 630-638.

COLES, M. E., HAZLETT, R. D., SPANNE, P., SOLL, W. E., MUEGGE, E. L. & JONES, K. W. 1998. Pore level imaging of fluid transport using synchrotron X-ray microtomography. *Journal of Petroleum Science and Engineering,* 19**,** 55-63.

D'ORAZIO, F., BHATTACHARJA, S., HALPERIN, W. P., EGUCHI, K. & MIZUSAKI, T. 1990a. Molecular diffusion and nuclear-magnetic-resonance relaxation of water in unsaturated porous silica glass. *Physical Review B,* 42**,** 9810-9818.

D'ORAZIO, F., BHATTACHARJA, S., HALPERIN, W. P. & GERHARDT, R. 1989. Enhanced self-diffusion of water in restricted geometry. *Physical Review Letters,* 63**,** 43-46.

D'ORAZIO, F., BHATTACHARJA, S., HALPERIN, W. P. & GERHARDT, R. 1990b. Fluid transport in partially filled porous sol-gel silica glass. *Physical Review B,* 42**,** 6503-6508.

DAL FERRO, N., DELMAS, P., DUWIG, C., SIMONETTI, G. & MORARI, F. 2012. Coupling X-ray microtomography and mercury intrusion porosimetry to quantify aggregate structures of a cambisol under different fertilisation treatments. *Soil and Tillage Research,* 119**,** 13-21.

DENOYEL, R., LLEWELLYN, P., BEURROIES, I., ROUQUEROL, F. & LUCIANI, L. 2004. Comparing the basic phenomena involved in three methods of pore-size characterization: Gas adsorption, Liquid intrusion and thermoporometry. *Particle and Particle Systems Characterization,* 21**,** 128-137.

DIAMOND, S. 2000. Mercury porosimetry: An inappropriate method for the measurement of pore size distributions in cement based materials. *Cement and Concrete Research* 30**,** 1517-1525.

DVOYASHKIN, M., VALIULLIN, R. & KÄRGER, J. 2007. Temperature effects on phase equilibrium and diffusion in mesopores. *Physical Review E,* 75**,** 041202.

EHRBURGER-DOLLE, F., MISONO, S. & LAHAYE, J. 1990. Characterization of the aggregate void structure of carbon blacks by thermoporometry. *Journal of Colloid and Interface Science,* 135**,** 468-485.

ESPARZA, J. M., OJEDA, M. L., CAMPERO, A., DOMíNGUEZ, A., KORNHAUSER, I., ROJAS, F., VIDALES, A. M., LÓPEZ, R. H. & ZGRABLICH, G. 2004. N2 sorption scanning behavior of SBA-15 porous substrates. *Colloids and Surfaces A: Physicochemical and Engineering Aspects,* 241**,** 35-45.

FRIEBOLIN, H. (ed.) 1991. *Basic One- and Two-Dimentional NMR Spectroscopy*: Wiley VCH.

FUKUSHIMA, E. & ROEDER, S. B. W. (eds.) 1981. *Experimental Pulse NMR: A Nuts and Bolts Approach*: Addison-Wesley.

FUSI, N. & MARTINEZ-MARTINEZ, J. 2013. Mercury porosimetry as a tool for improving quality of micro-CT images in low porosity carbonate rocks. *Engineering Geology,* 166**,** 272-282.

GANE, P. A. C., RIDGWAY, C. J., LEHTINEN, E., VALIULLIN, R., FURÓ, I., SCHOELKOPF, J., PAULAPURO, H. & DAICIC, J. 2004. Comparison of NMR Cryoporometry, Mercury Intrusion Porosimetry, and DSC Thermoporosimetry in Characterizing Pore Size Distributions of Compressed Finely Ground Calcium Carbonate Structures. *Industrial & Engineering Chemistry Research,* 43**,** 7920-7927.

GEISCHE, H. 2006. Mercury Porosimetry: A General (Practical) Overview. *Particle and Particle Systems Characterization,* 23**,** 9-19.

GIESCHE, H. 2006. Mercury Porosimetry: A General (Practical) Overview. *Particle & Particle Systems Characterization,* 23**,** 9-19.

GOOD, R. J. & MIKHAIL, R. S. 1981. The contact angle in mercury intrusion porosimetry. *Powder Technology,* 29**,** 53-62.

GOPINATHAN, N., GREAVES, M., LOWE, J. P., WOOD, J. & RIGBY, S. P. 2012. Determination of the location of coke in catalysts by a novel NMR-based, liquid-porosimetry approach. *Journal of Colloid and Interface Science,* 381**,** 164-170.

GUPTA, G., ZBIB, A., EL-GHANNAM, A., KHRAISHEH, M. & ZBIB, H. 2005. Characterization of a novel bioactive composite using advanced X-ray computed tomography. *Composite Structures,* 71**,** 423-428.

H. F. BOOTH J. H, S. 1998. Organic nanocrystals: an NMR study of cyclohexane in porous silica. *Molecular Physics,* 93**,** 263-269.

HAY, J. N. & LAITY, P. R. 2000. Observations of water migration during thermoporometry studies of cellulose films. *Polymer,* 41**,** 6171-6180.

HITCHCOCK, I., CHUDEK, J. A., HOLT, E. M., LOWE, J. P. & RIGBY, S. P. 2010. NMR Studies of Cooperative Effects in Adsorption. *Langmuir,* 26**,** 18061-18070.

HITCHCOCK, I., HOLT, E. M., LOWE, J. P. & RIGBY, S. P. 2011. Studies of freezing–melting hysteresis in cryoporometry scanning loop experiments using NMR diffusometry and relaxometry. *Chemical Engineering Science,* 66**,** 582-592.

HÖHNE, G., HEMMINGER, W. F. & FLAMMERSHEIM, H. J. 2003. *Differential Scanning Calorimetry,* Springer.

HOLLEWAND, M. P. & GLADDEN, L. F. 1995. Transport heterogeneity in porous pellets—I. PGSE NMR studies. *Chemical Engineering Science,* 50**,** 309-326.

HOLMES, W. M., GRAHAM, R. G. & PACKER, K. J. 2001. Diffusion in surface-wetting films in a two-phase saturated porous solid characterised by pulsed magnetic field gradient NMR. *Chemical Engineering Journal,* 83**,** 33-38.

IOANNIDIS, M. A., CHATZIS, I. & PAYATAKES, A. C. 1991. A mercury porosimeter for investigating capillary phenomena and microdisplacement mechanisms in capillary networks. *Journal of Colloid and Interface Science,* 143**,** 22-36.

IOANNIDIS, M. A., CHATZIS, I. & SUDICKY, E. A. 1993. The effect of spatial correlations on the accessibility characteristics of three-dimensional cubic networks as related to drainage displacements in porous media. *Water Resources Research,* 29**,** 1777-1785.

ISHIKIRIYAMA, K. & TODOKI, M. 1995. Pore Size Distribution Measurements of Silica Gels by Means of Differential Scanning Calorimetry: II. Thermoporosimetry. *Journal of Colloid and Interface Science,* 171**,** 103-111.

IZA, M., WOERLY, S., DANUMAH, C., KALIAGUINE, S. & BOUSMINA, M. 2000. Determination of pore size distribution for mesoporous materials and polymeric gels by means of DSC measurements: thermoporometry. *Polymer,* 41**,** 5885-5893.

KASTNER, J., HARRER, B. & DEGISCHER, H. P. 2011. High resolution cone beam X-ray computed tomography of 3D-microstructures of cast Al-alloys. *Materials Characterization,* 62**,** 99-107.

KIMMICH, R., STAPF, S., MAKLAKOV, A. I., SKIRDA, V. D. & KHOZINA, E. V. 1996. Self-diffusion in fluids in porous glass: Confinement by pores and liquid adsorption layers. *Magnetic Resonance Imaging,* 14**,** 793-797.

KLEINBERG, R. L., KENYON, W. E. & MITRA, P. P. 1994. Mechanism of NMR Relaxation of Fluids in Rock. *Journal of Magnetic Resonance, Series A,* 108**,** 206-214.

KLOUBEK, J. 1981. Hysteresis in porosimetry. *Powder Technology,* 29**,** 63-73.

KRUMM, M., KASPERL, S. & FRANZ, M. 2008. Reducing non-linear artifacts of multi-material objects in industrial 3D computed tomography. *NDT & E International,* 41**,** 242-251.

LANDRY, M. R. 2005. Thermoporometry by differential scanning calorimetry: experimental considerations and applications. *Thermochimica Acta,* 433**,** 27-50.

LENORMAND, R., ZARCONE, C. & SARR, A. 1983. Mechanisms of the displacement of one fluid by another in a network of capillary ducts. *Journal of Fluid Mechanics,* 135**,** 337-353.

LIN, C. L., VIDELA, A. R. & MILLER, J. D. 2010. Advanced three-dimensional multiphase flow simulation in porous media reconstructed from X-ray Microtomography using the He–Chen–Zhang Lattice Boltzmann Model. *Flow Measurement and Instrumentation,* 21**,** 255-261.

LIU, Z. & WINSLOW, D. 1995. Sub-distribution of pore size: A new approach to correlate pore structure with permeability. *Cement and Concrete Research,* 25**,** 769-778.

LOWELL, S. & SHIELDS, J. E. 1981a. Hysteresis, entrapment, and wetting angle in mercury porosimetry. *Journal of Colloid and Interface Science,* 83**,** 273-278.

LOWELL, S. & SHIELDS, J. E. 1981b. Influence of contact angle on hysteresis in mercury porosimetry. *Journal of Colloid and Interface Science,* 80**,** 192-196.

MC.GRAWHILL. Available: http://www.mhhe.com/physsci/chemistry/carey/student/olc/graphics/carey04oc/ref/ch13nmr.html [Accessed 09-05-2011.

MEIBOOM, S. & GILL, D. 1958. Modified Spin-Echo Method for Measuring Nuclear Relaxation Times. *Review of Scientific Instruments,* 29**,** 688-691.

MORENO-ATANASIO, R., WILLIAMS, R. A. & JIA, X. 2010. Combining X-ray microtomography with computer simulation for analysis of granular and porous materials. *Particuology,* 8**,** 81-99.

MORISHIGE, K., YASUNAGA, H. & MATSUTANI, Y. 2010. Effect of Pore Shape on Freezing and Melting Temperatures of Water. *The Journal of Physical Chemistry C,* 114**,** 4028-4035.

ORLOV, I. M., MORGAN, D. G. & CHENG, R. H. 2006. Efficient implementation of a filtered back-projection algorithm using a voxel-by-voxel approach. *Journal of Structural Biology,* 154**,** 287-296.

PERKINS, E. L., LOWE, J. P., EDLER, K. J., TANKO, N. & RIGBY, S. P. 2008. Determination of the percolation properties and pore connectivity for mesoporous solids using NMR cryodiffusometry. *Chemical Engineering Science,* 63**,** 1929-1940.

PERRY, R. H., GREEN, D. W. & MALONEY, J. O. 1999. *Perry's Chemical Engineers' Handbook*, McGraw-Hill.

PETROV, O. & FURÓ, I. 2011. A study of freezing–melting hysteresis of water in different porous materials. Part I: Porous silica glasses. *Microporous and Mesoporous Materials,* 138**,** 221-227.

PHYSICAL AND BIOPHYSICAL CHEMISTRY DIVISION COMMISSION ON, C., SURFACE CHEMISTRY INCLUDING, C., ROUQUEROL, J., AVNIR, D., FAIRBRIDGE, C. W., EVERETT, J., PERNICONE, N. & HAYNE S, M. J. 1994. Recommendations for the characterisation of porous solids: (IUPAC recommendations 1994). *Pure and Applied Chemistry,* 66**,** 1739-1758.

PORTSMOUTH, R. L. & GLADDEN, L. F. 1991. Determination of pore connectivity by mercury porosimetry. *Chemical Engineering Science,* 46**,** 3023-3036.

PRICE, W. S. 1997. Pulsed-field gradient nuclear magnetic resonance as a tool for studying translational diffusion: Part 1. Basic theory. *Concepts in Magnetic Resonance,* 9**,** 299-336.

RIGBY, P. S., FLETCHER, S. R. & RILEY, N. S. 2004. Characterisation of porous solids using integrated nitrogen sorption and mercury porosimetry. *Chemical Engineering Science,* 59**,** 41-51.

RIGBY, S., CHIGADA, P., PERKINS, E., WATT-SMITH, M., LOWE, J. & EDLER, K. 2008. Fundamental studies of gas sorption within mesopores situated amidst an inter-connected, irregular network. *Adsorption,* 14**,** 289-307.

RIGBY, S. P. 2000. A Hierarchical Structural Model for the Interpretation of Mercury Porosimetry and Nitrogen Sorption. *Journal of Colloid and Interface Science,* 224**,** 382-396.

RIGBY, S. P. & CHIGADA, P. I. 2009. MF-DFT and Experimental Investigations of the Origins of Hysteresis in Mercury Porosimetry of Silica Materials. *Langmuir,* 26**,** 241-248.

RIGBY, S. P. & EDLER, K. J. 2002. The Influence of Mercury Contact Angle, Surface Tension, and Retraction Mechanism on the Interpretation of Mercury Porosimetry Data. *Journal of Colloid and Interface Science,* 250**,** 175-190.

RIGBY, S. P., FLETCHER, R. S. & RILEY, S. N. 2003. Determination of the cause of mercury entrapment during porosimetry experiments on sol-gel silica catalyst supports. *Applied Catalysis A: General,* 247**,** 27-39.

RIGBY, S. P., WATT-SMITH, M. J., CHIGADA, P., CHUDEK, J. A., FLETCHER, R. S., WOOD, J., BAKALIS, S. & MIRI, T. 2006. Studies of the entrapment of non-wetting fluid within nanoporous media using a synergistic combination of MRI and micro-computed X-ray tomography. *Chemical Engineering Science,* 61**,** 7579-7592.

RIGBY, S. P., WATT-SMITH, M. J. & FLETCHER, R. S. 2005. Integrating Gas Sorption with Mercury Porosimetry. *Adsorption,* 11**,** 201-206.

RIIKONEN, J., SALONEN, J. & LEHTO, V.-P. 2011. Utilising thermoporometry to obtain new insights into nanostructured materials. *Journal of Thermal Analysis and Calorimetry,* 105**,** 811-821.

RUIZ DE ARGANDOÑA, V. G., CALLEJA, L., RODRÍGUEZ-REY, Á., SUÁREZ DEL RÍO, L. M. & CELORIO, C. 2009. X-ray Computed Tomography study of the influence of consolidants on the hydric properties of sandstones for stone conservation studies. *Engineering Geology,* 103**,** 69-75.

SALMAS, C. & ANDROUTSOPOULOS, G. 2001. Mercury Porosimetry: Contact Angle Hysteresis of Materials with Controlled Pore Structure. *Journal of Colloid and Interface Science,* 239**,** 178-189.

SCHREIBER, A., KETELSEN, I. & FINDENEGG, G. H. 2001. Melting and freezing of water in ordered mesoporous silica materials. *Physical Chemistry Chemical Physics,* 3**,** 1185-1195.

SHIKO, E., EDLER, K. J., LOWE, J. P. & RIGBY, S. P. 2012. Probing the impact of advanced melting and advanced adsorption phenomena on the accuracy of pore size distributions from cryoporometry and adsorption using NMR relaxometry and diffusometry. *Journal of Colloid and Interface Science,* 385**,** 183-192.

SINKA, I. C., BURCH, S. F., TWEED, J. H. & CUNNINGHAM, J. C. 2004. Measurement of density variations in tablets using X-ray computed tomography. *International Journal of Pharmaceutics,* 271**,** 215-224.

SMITHWICK, R. W. & FULLER JR, E. L. 1984. A generalized analysis of hysteresis in mercury porosimetry. *Powder Technology,* 38**,** 165-173.

STEJSKAL, E. O. & TANNER, J. E. 1965. Spin Diffusion Measurements: Spin Echoes in the Presence of a Time-Dependent Field Gradient. *The Journal of Chemical Physics,* 42**,** 288-292.

STOCK, S. R., DE CARLO, F. & ALMER, J. D. 2008. High energy X-ray scattering tomography applied to bone. *Journal of Structural Biology,* 161**,** 144-150.

TERENCE, A. 1997. *particle size measurement*, Chapman & Hall.

TERNAN, M. & MYSAK, L. P. 1987. Hysteresis caused by dimensional changes of porous solids during mercury porosimetry. *Powder Technology,* 52**,** 29-34.

TSAKIROGLOU, C. D. & PAYATAKES, A. C. 1990. A new simulator of mercury porosimetry for the characterization of porous materials. *Journal of Colloid and Interface Science,* 137**,** 315-339.

TSAKIROGLOU, C. D. & PAYATAKES, A. C. 1991. Effects of pore-size correlations on mercury porosimetry curves. *Journal of Colloid and Interface Science,* 146**,** 479-494.

TSAKIROGLOU, C. D. & PAYATAKES, A. C. 1998. Mercury intrusion and retraction in model porous media. *Advances in Colloid and Interface Science,* 75**,** 215-253.

VALIULLIN, R., KORTUNOV, P., KÄRGER, J. & TIMOSHENKO, V. 2005. Concentration-dependent self-diffusion of adsorbates in mesoporous materials. *Magnetic Resonance Imaging,* 23**,** 209-214.

VAN BRAKEL, J., MODRY, S. & SVATA, M. 1981. Mercury porosimetry: state of the art. *Powder Technology,* 29**,** 1-12.

VINEGAR, H. J., DE WAAL, J. A. & WELLINGTON, S. L. 1991. CT studies of brittle failure in castlegate sandstone. *International Journal of Rock Mechanics and Mining Sciences & Geomechanics Abstracts,* 28**,** 441-450.

WARDLAW, N. C. & MCKELLAR, M. 1981. Mercury porosimetry and the interpretation of pore geometry in sedimentary rocks and artificial models. *Powder Technology,* 29**,** 127-143.

WATT-SMITH, M. J., RIGBY, S. P., CHUDEK, J. A. & FLETCHER, R. S. 2006. Simulation of nonwetting phase entrapment within porous media using magnetic resonance imaging. *Langmuir,* 22**,** 5180-8.

WEBBER, J. B. W. 2010. Studies of nano-structured liquids in confined geometries and at surfaces. *Progress in Nuclear Magnetic Resonance Spectroscopy,* 56**,** 78-93.

WILDENSCHILD, D., VAZ, C. M. P., RIVERS, M. L., RIKARD, D. & CHRISTENSEN, B. S. B. 2002. Using X-ray computed tomography in hydrology: systems, resolutions, and limitations. *Journal of Hydrology,* 267**,** 285-297.

YAMAMOTO, T., ENDO, A., INAGI, Y., OHMORI, T. & NAKAIWA, M. 2005. Evaluation of thermoporometry for characterization of mesoporous materials. *Journal of Colloid and Interface Science,* 284**,** 614-620.

Chapter 4: Study of the Entrapment of Non-Wetting Fluid Using Mercury Porosimetry and X-ray Tomography

4.1. Introduction

This chapter introduces the reader to two experimental techniques that were used to study the entrapment of non-wetting fluids within the void spaces of the materials used. The first technique is the mercury porosimetry technique. This technique has been utilised in this thesis to characterise the porous structure of silica/alumina materials only in order to obtain the porosity, pore volume, surface area and also to look at entrapment of mercury within the void space. The Kloubek correlation (Eq. 3.2) was used to analyse the raw mercury porosimetry data where there was hysteresis of the intrusion and extrusion curves. A superimposition was achieved at smaller mesopore sizes where no apparent structural hysteresis and entrapment were observed at this stage. However, at larger mesopore sizes, entrapment and structural hysteresis do occur. In addition, to understand the behaviour of non-wetting fluids trapped within the void spaces of these materials, one would like to have a picture of the pore geometry in which the smallest as well as the largest pore length are quantitatively represented. An X-ray tomography technique was used to image and visualise silica pellets earlier studied following porosimetry technique to give more detailed information in terms of the spatial distribution of mercury within the void spaces of the material used in this study. The theory behind these two techniques and there limitations has been mentioned already in section 3.2 and 3.3 respectively.

4.2. Methodology and sample preparation

4.2.1. Mercury porosimetry

The experiments were carried out using a Micromeritics Autopore IV 9500, which is capable of obtaining pressures of up to 60,000 psia (~414 MPa). The instrument is designed to perform two low and one high-pressure analysis at the same time. The instrument measures the intruded volume (per mass of the sample) at a specific pressure; this pressure can be converted to pore radius by using the Young-Laplace equation (Eq. 3.1). A value of 0.485 Nm^{-1} at 25 $^{\circ}C$ for the surface tension and 130 $^{\circ}C$ for the contact angle were used for this study, as they are generally accepted by most researchers (Giesche 2006). Also, because it is difficult to clean the entrapped mercury from a given sample after an experiment for re-use in a further mercury porosimetry experiment, each experiment was instead repeated on several samples from the same batch

Silica samples were dried under vacuum to a temperature of 150 $^{\circ}C$ for 15 hours, as they are prone to adsorb water. The purpose of the thermal treatment was to drive off any physisorbed water content on the sample but leave the morphology of the sample unchanged. A range of different thermal pre-treatment procedures has been considered in the past (Rigby and Edler, 2002) in order to determine whether the experimental results were sensitive to the temperature or time period used. The weight of the dried sample and the penetrometer were taken separately, prior to introducing the sample into the penetrometer. The sample (~0.5 g) is then put into a penetrometer, which consists of a sample cup that is attached to a metal-clad and a glass capillary

stem. The sample is then sealed and placed in a low-pressure port. A sample file is then created which describes the sample and the analysis conditions and other parameters. This file has a pressure input table that lists the pressure points at which the data is collected during the experiment.

In the low-pressure system, the sample is initially evacuated to remove air, residual moisture, or other liquids, from the pore system. A complete evacuation is important in order to avoid air pockets and contamination issues. The sample cell is then filled with mercury as the entire system is still under low pressure. Data points are taken at a pressure of 3-4 KPa (0.5 psia) or higher. At the end of the low-pressure part of the analysis, the weight of the penetrometer filled with mercury and the sample is then measured, which allows the calculation of bulk density of the sample by using the corresponding blank runs as reference. Also, the penetrometers used to carry out the experiments were calibrated, and the baseline error of each penetrometer was obtained from analysis without a sample. The precision of the volume measurement with this equipment is 1% of the stem volume, according to the manufacturer. The accuracy of the pressure transducer is 0.1% of the maximum pressure.

The weighted sample from the low-pressure port is then transferred to a high-pressure port which is being surrounded by hydraulic liquid for the second part of the analysis. The chamber is then tightly closed with sufficient pressure fluid drawn into the vent valve and a pressure of up to 414 MPa (60,000 psia) is applied in an isostatic way for all the samples, after which the extrusion process follows. Scanning curves were also performed on some of the mesoporous materials after analysing the data using Kloubek Correlations.

4.2.2. Correction methods

Prior to any MIP experiment conducted during this report, a blank correction was run without sample, which shows no intrusion or extrusion. Any intrusion that does appear will be attributed to baseline error and can be subtracted from subsequent sample runs, thus removing the baseline error from the data. The baseline error in the blank run is usually caused by the compressibility and thermal effects of the mercury and thermal effects of the sample material which can be corrected using a non-porous sample of the same material. The compressibility, β, is defined as the fractional change in volume per unit pressure. For most solids the compressibility value lies between the ranges of 10^{-3} to 10^{-4} $(Pa)^{-1}$. Hence, a 1 cm sample will compress by about 0.006 to 0.06 cm^3 at the final pressure of 400MPa (Giesche, 2006).

4.2.3. Acquisition of X-ray CT images

The X-ray imaging of the samples containing entrapped mercury were run by Martin Corfield, of the Department of Electrical and Electronics Engineering, University of Nottingham, and were carried out using a high resolution Xradia versa XRM-500 machine capable of operating at a voltage of 160kV electrical power and current of 62 µA. It consists of an X-ray detector of a 1024x1024 pixel resolution with 64 bit dynamic range, and a camera connected to a computer (Fig. 3.9). An Epoxy resin was used to hold the sample to the sample holder (Fig. 3.10) so as to avoid any vibration when the sample is rotating. The range of X-ray energies used in X-ray tomography allows X-rays to be transmitted through dense objects. This technique gives an opportunity for a non-destructive examination of the internal mercury distributions in the materials studied. Following a porosimetry experiment, the sample is

transferred to an x-ray machine which is placed on a sample holder and then installed on a rotary stage between the matrix detector and the cone beam as shown earlier in section 3.4, Fig. 3.9. X-rays are passed through the sample, which is then rotated, step-by-step inside the x-ray chamber so as to be viewed from different angles, which takes a projection of images at each angular position. A computer records each of the projected images and measures the intensity of the x-ray beam after passing through the material. Once the first sets of data images (projected images) are obtained then, via a filtered back projection using the computer, we can reconstruct non-destructively virtual magnified slices through the object. A total of 1003 μ-CT slices are produced as a stack of 2D cross-sections for the entire sample, thereby revealing the internal microstructure of the G2 sample. A 3D image can be obtained by combining all the horizontal slices on top of one another.

4.3. Results

The results section presents the raw data and the corresponding analysed data for each of the samples used after mercury porosimetry as well as x-ray projected images and the reconstructed images for the G2 silica beads following mercury porosimetry. The materials studied in this work are different batches of sol gel silica and alumina pellets with spherical or cylindrical geometry as given in Table 4.1-4.7. Equilibration times of 10s and 30s were used in the experiments to check whether it result in any variation of mercury entrapment within the void spaces of all the materials. Separate experiments conducted at different equilibration times of 10, 30, 50 and 100s for G2 sample using same input pressure tables have shown that different

equilibration times used make no significant change to the final shapes of the intrusion and extrusion curves.

4.3.1. Silica Samples

A complete set of raw data for silica/alumina materials using mercury porosimetry experiment at different equilibration times of 10 and 30s are shown in Figs. 4.1(a) to Fig. 4.9(a). Fig. 4.1(a) to Fig. 4.4(a) shows the raw data for mercury porosimetry experiments performed on whole pellets of silica samples from batches S1, S2, G1 and G2. All the samples were subjected to a full intrusion (up to 414 x 10^6pa (60,000 psia)) and followed by a retraction back down to atmospheric pressure. The volume of the intruded mercury is plotted against the pressure of mercury intrusion. As the pressure starts to build up from low to high pressure, mercury starts to intrude at pressures of 0.005-0.01 MPa into gaps between pellets, this is followed by a long horizontal plateau before significant intra-particle intrusion starts at pressure of ~10-100MPa before reaching a flat plateau at the highest pressure point of 414MPa as seen in Fig. 4.1(a). The small initial intrusion of mercury is due to the inter-pellet penetration of mercury, before intra-pellet intrusion begins at ~1-10 MPa. Also, the horizontal plateau at the highest pressure point suggests that all pores are filled at the highest pressure and no mercury can intrude the sample.

As the pressure is decreased, there is a flat plateau region for samples from batch S1, S2 and G2 before mercury extrudes from the sample, which suggest that there is virtually no change in mercury volume until a pressure of ~35 MPa. In contrast, to S1, S2, and G2, the extrusion curve for batch G1 is not characterised by an initial flat plateau. Once the pressure is reduced beyond

this point for S1, S2, and G2, there is a large step decrease in mercury volume. This large step decrease in mercury volume is a function of equilibration time, and increases with increased equilibration time. From Fig 4.1(b), sample S1, it can be seen that the extrusion curve does overlay the intrusion curve. Also, at a pressure of ~ 0.1MPa, no mercury extrudes from the sample, resulting in mercury entrapment of ~22% using 10s equilibration time. It can be seen that all the silica samples exhibits hysteresis. This raw data results were analysed using the standard Washburn equation (Eq. 3.1), with values of surface tension and contact angle given in section 4.2.1. All the experiments were conducted twice to check the repeatability of the results.

In order to determine whether the length of equilibration had any effect on the shapes of intrusion and/or extrusion curves, special attention is given to G2 (as it is the most affected by the equilibration time-scale used) sample as seen in Fig. 4.4(a), where mercury retraction curves were obtained at different equilibration times between the ranges of 10, 30, 50 and 100s. It can be seen from the initial part of the retraction curve all exhibit almost a horizontal flat plateau. Hence, onset of the retraction curve is independent of experimental time scale, as it appeared to be governed narrowing necks of mercury to form a free meniscus. It can also be seen that there is virtually no change of mercury volume until a pore size of ~12 nm, which results in a step decrease in mercury volume. Also, the shapes of subsequent retraction curves are very similar, although the amount of mercury entrapment is also a function of equilibration time.

The raw data from the mercury porosimetry experiments on the silica samples have been analysed using the semi-empirical alternatives to Washburn

equation (Eqn. 3.2) as described in section 3.2 of the theory section. The results are shown in Fig. 4.1(b) to Fig. 4.4(b) for the silica samples. It can be seen that the entire silica samples at the initial part of mercury retraction curves all exhibit almost a horizontal plateau. Also, at small mesopore sizes, the intrusion and extrusion curves are completely superimposed over each other. This is as a result of the removal of contact angle hysteresis as described in previous work (Rigby, 2002; Rigby et al., 2003a) and leaving the structural hysteresis as explained in the theory section. Fig. 4.8(a) and 4.9(a) shows the scanning loop experiments of a batch of silica sample. It can be seen that the retraction curve no longer possess an initial flat horizontal plateau at the highest pressure of the intrusion curve. This is as a result of the less pore volume of mercury filled at the required pressure of 124 MPa and 76 MPa respectively.

The parameters obtained from mercury porosimetry runs during the intrusion and extrusion of mercury from samples is given in Table 4.1 to 4.7. From the tables, the pore diameter was obtained by using the Washburn equation (Eq. 3.1). The total pore volume is the total volume of intruded mercury, and these can be obtained from mercury intrusion curve. The surface area was calculated by using the Rootare and Prenzlow (1967). An estimate of the total mercury entrapped after mercury is intruded and extruded from the sample was found from the mercury retraction curve. The level of entrapped mercury determines the level of remaining open porosity. The entrapped mercury is the difference between the volume at the end of the retraction curve and corresponding pressure point on intrusion curve (separating inter-particle an intra-particle intrusion).

A comparison on the entrapment value obtained for all samples at two different equilibration times of 10 and 30 sec is given in Table 4.8. It can be seen that there is no significant change in the entrapment found at different equilibration time scales for all samples. However, it can be seen that there is a great deal of variability occurring with respect to the equilibration time scales for C30 sample. The entrapment value obtained for this particular sample was found to be the highest and varied substantially with equilibration time scales.

(a)

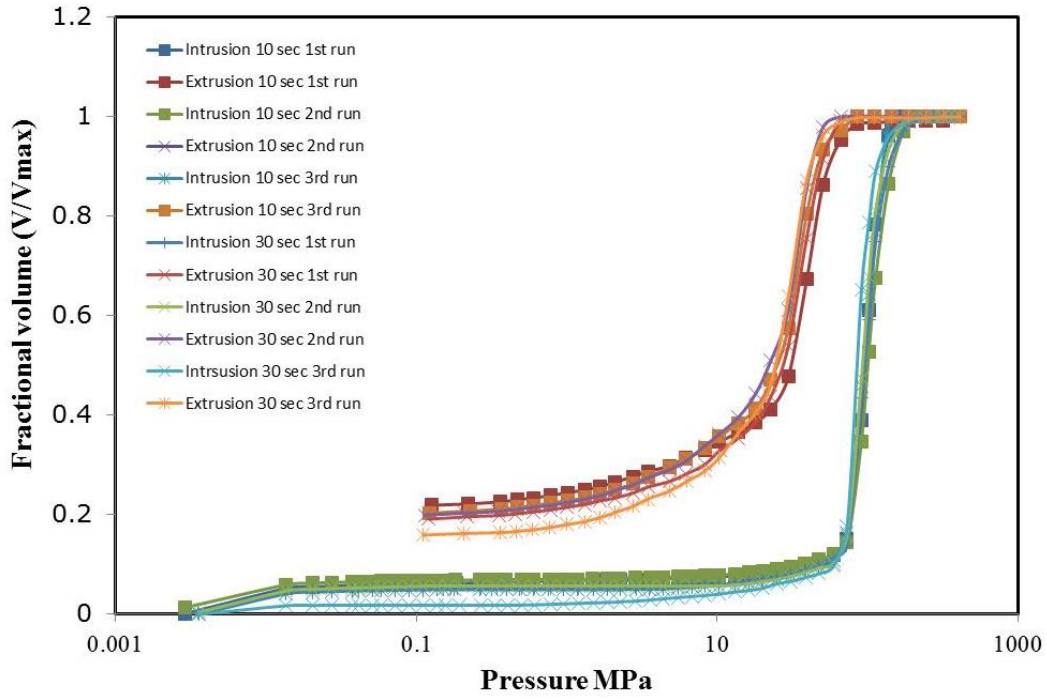

(b)

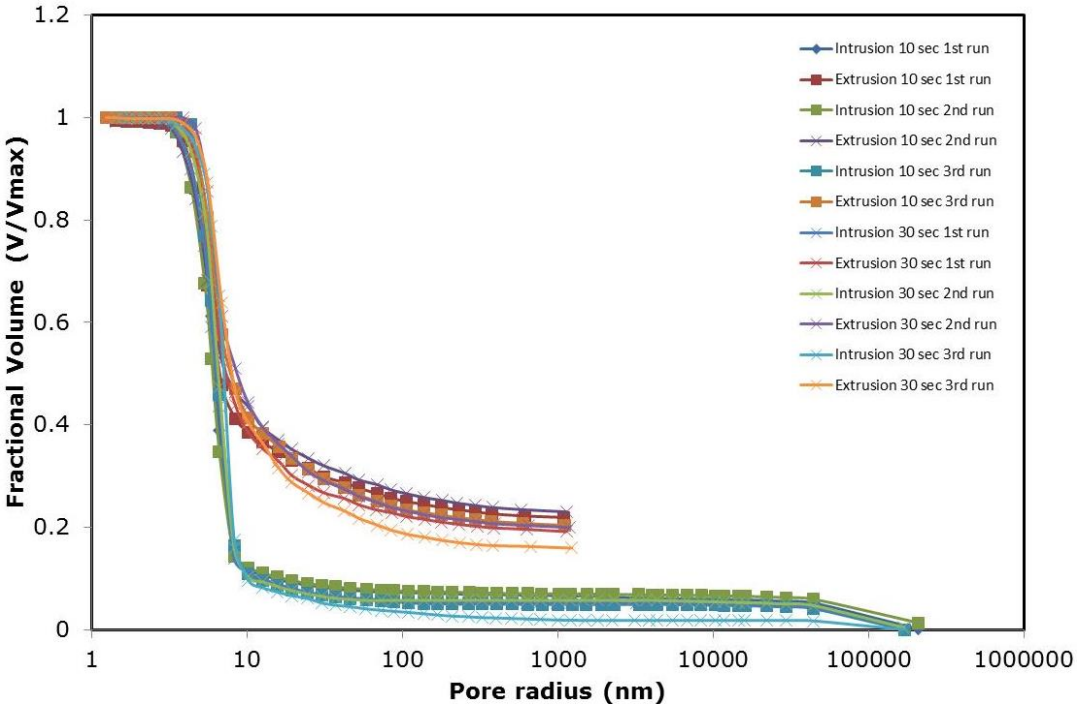

Figure 4. 1: (a) Raw mercury intrusion and extrusion data for S980A (S1) samples at different equilibration times of 10s (■) and 30s (x). (b) Mercury intrusion/extrusion curves S1 sample analysed using Kloubek correlations. The lines shown are to guide the eye.

(a)

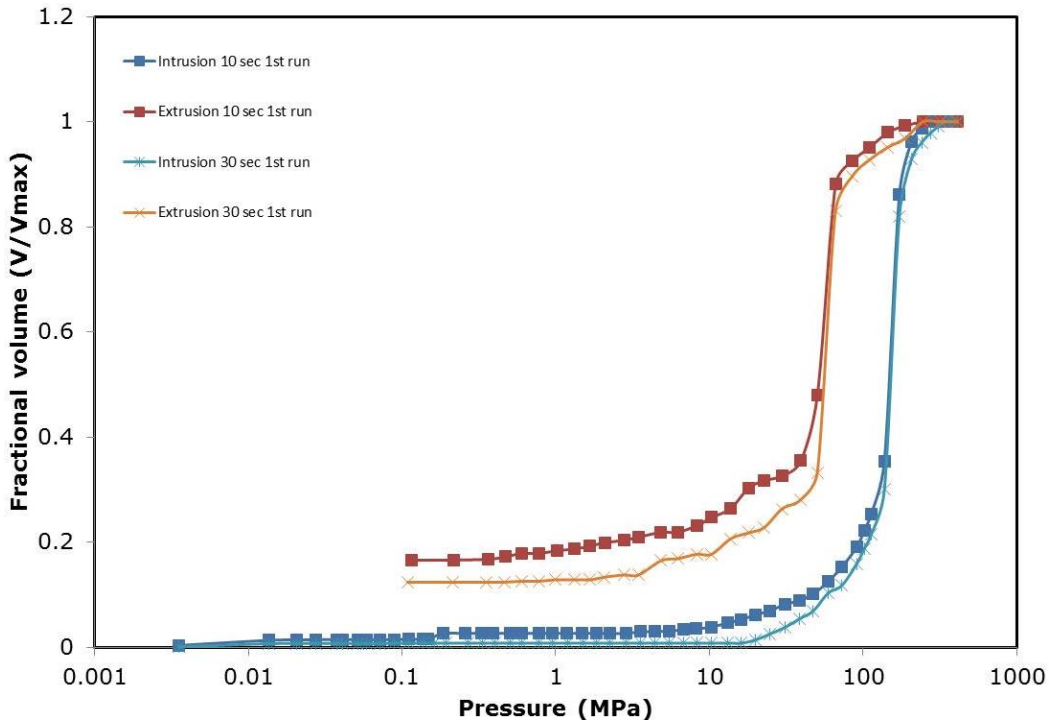

(b)

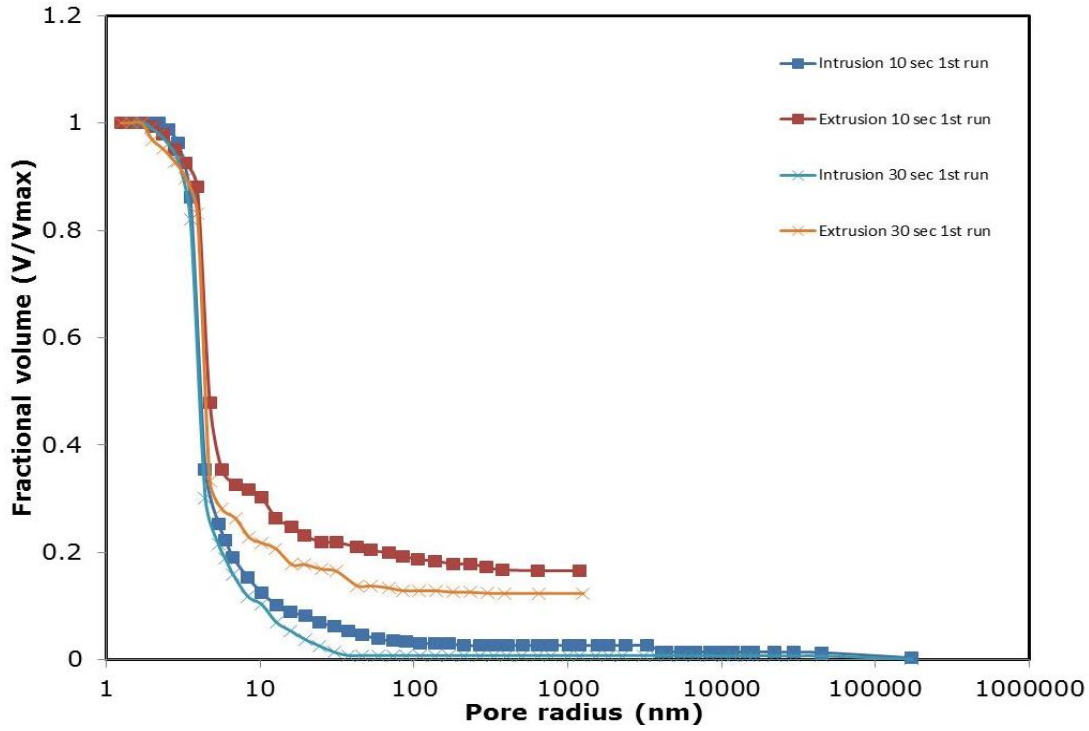

Figure 4. 2: (a) Raw mercury intrusion and extrusion data for (G1) samples at different equilibration times of 10s (■) and 30s (x). (b) Mercury intrusion/extrusion curves G1 sample analysed using Kloubek correlations. The lines shown are to guide the eye.

(a)

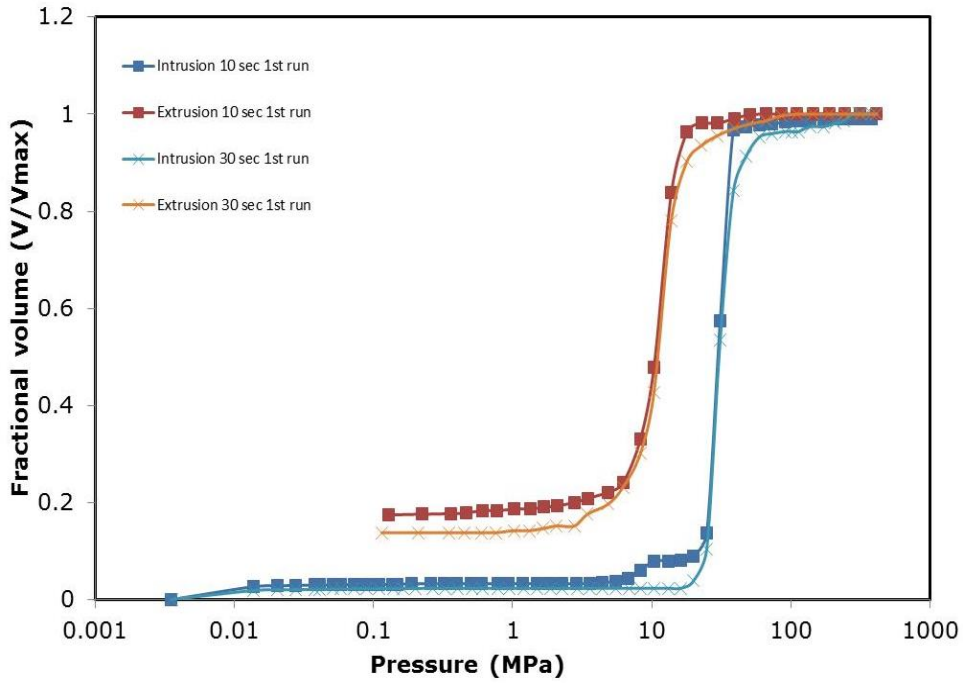

(b)

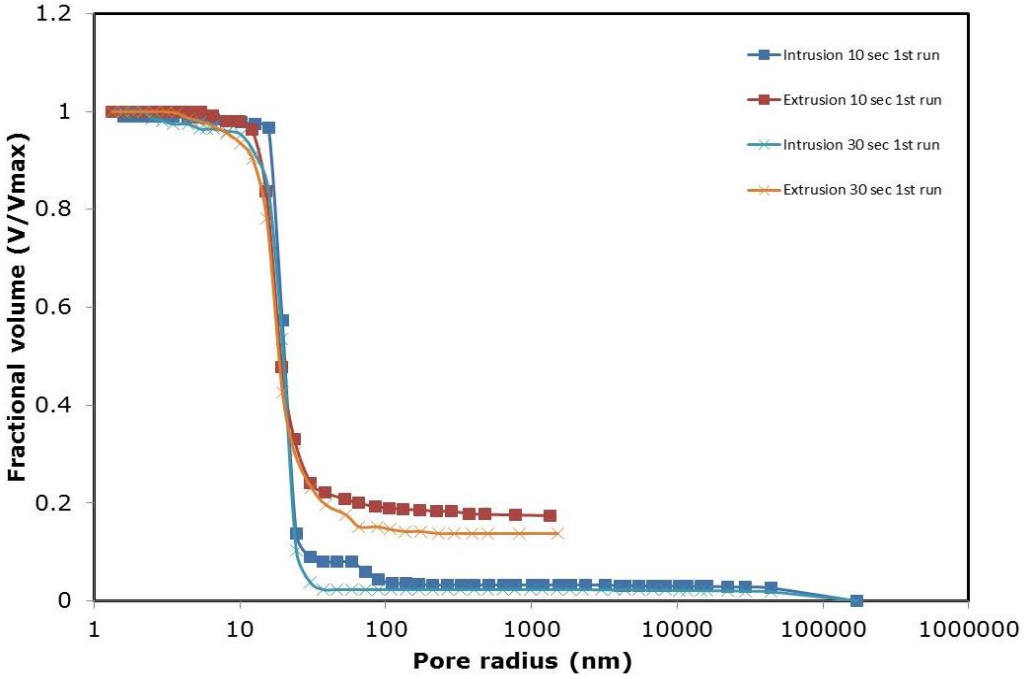

Figure 4. 3: (a) Raw mercury intrusion and extrusion data for S980G (S2) samples at different equilibration times of 10s (■) and 30s (x). (b) Mercury intrusion/extrusion curves S2 sample analysed using Kloubek correlations. The lines shown are to guide the eye.

(a)

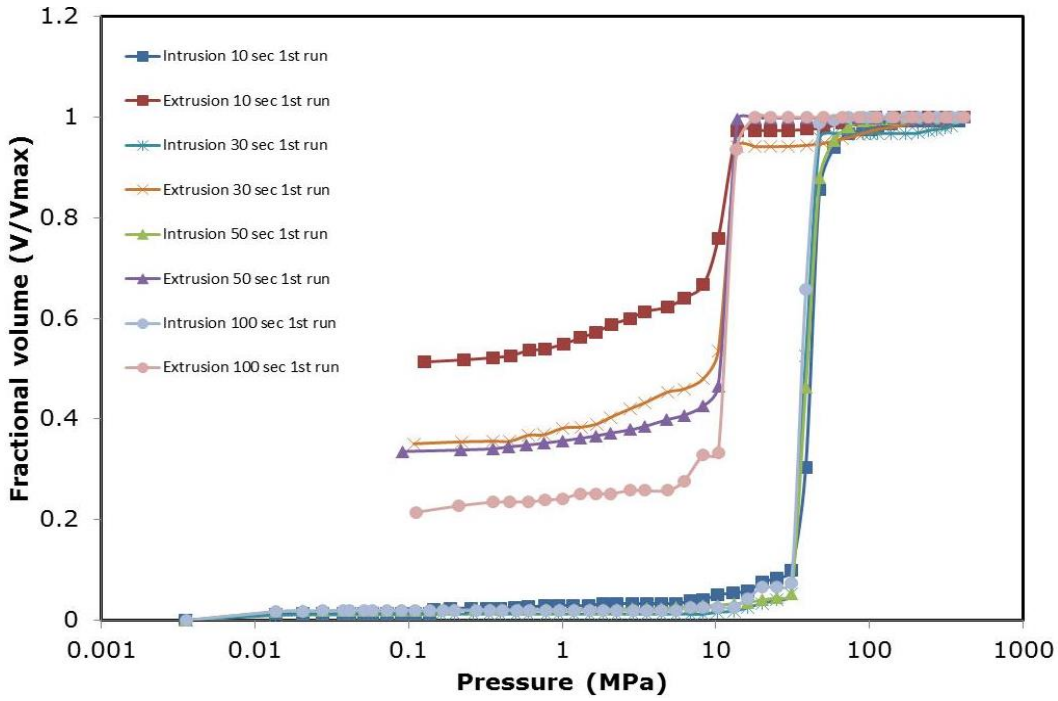

(b)

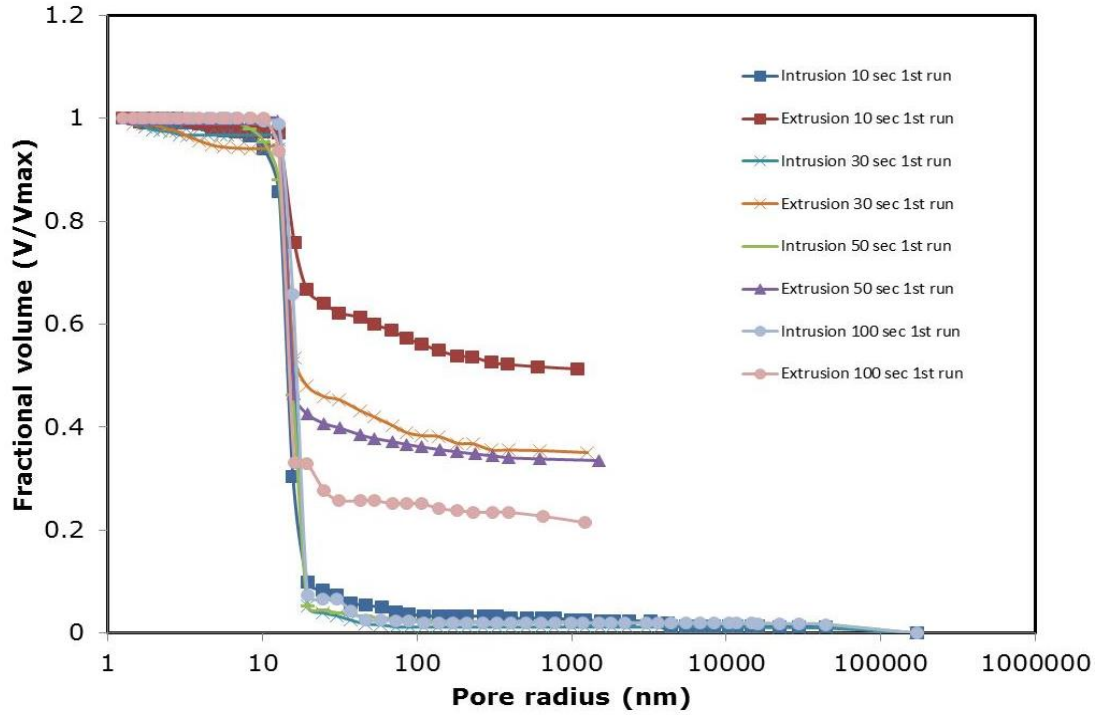

Figure 4. 4: (a) Raw mercury intrusion and extrusion data for C30 (G2) samples at different equilibration times of 10s (■), 30s (x), 50s (▲), and 100 s (●) (b) Mercury intrusion/extrusion curves G2 sample analysed using Kloubek correlations. The lines shown are to guide the eye.

4.3.2. Alumina samples

Fig. 4.5(a) to Fig. 4.7(a) shows raw mercury porosimetry data for experiments consisting of intrusion and extrusion curves on three different alumina samples (S3, A1, and A2) listed in Table 4.3 to 4.5. It can be seen that on all the retraction curves on the alumina samples analysed using the Kloubek correlation (Eqn. 3.2) with alumina parameters, from Fig. 4.5(b) to Fig. 4.7(b) are superimposed over each other. In Fig. 4.7(a), for sample from batch A2, it can be seen that the significant initial rises in the mercury intrusion curve occurring at low pressures can be said to be due to inter particle intrusion because of the relatively small particle sizes of the sample. Also, from the alumina samples, it can be seen that the shape of the intrusion curve is independent of equilibration time, whereas the shape of the extrusion curves varies with equilibration time.

A comparison of Fig. 4.4(a) of G2 silica sample and Fig. 4.5(a) for the standard silica alumina sample, S3 shows the overall entrapment level are much smaller for the standard silica alumina at ~22%, than for the G2 silica sample at ~50% using 10s equilibration time. This can be due to different pore connectivity and accessibility in the silica and alumina material samples.

(a)

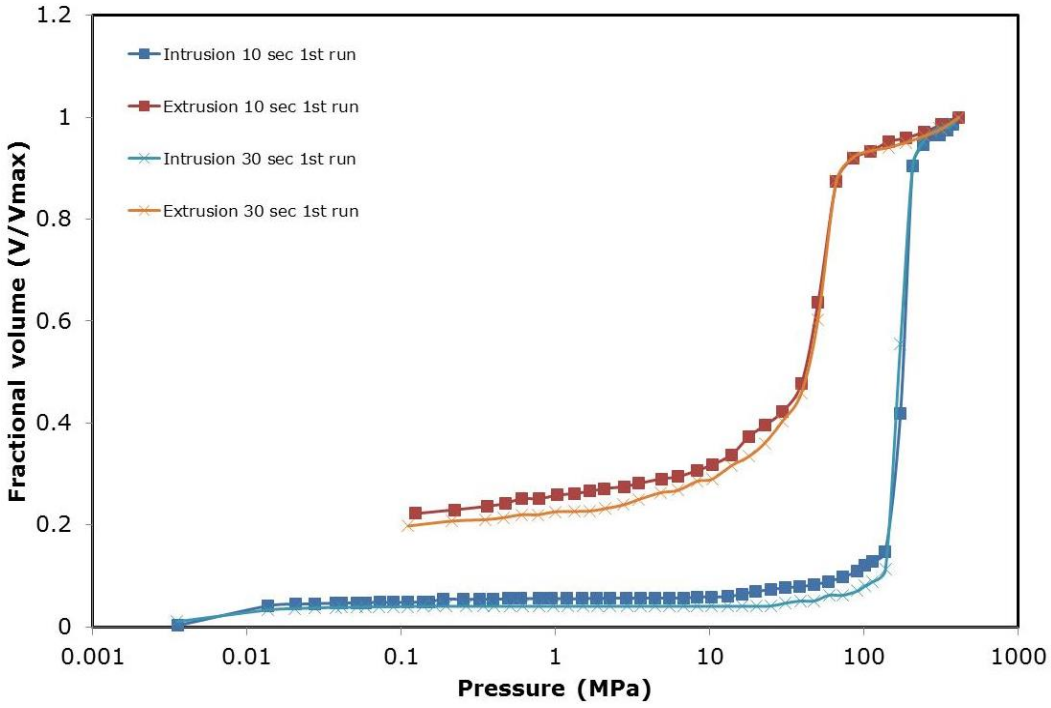

(b)

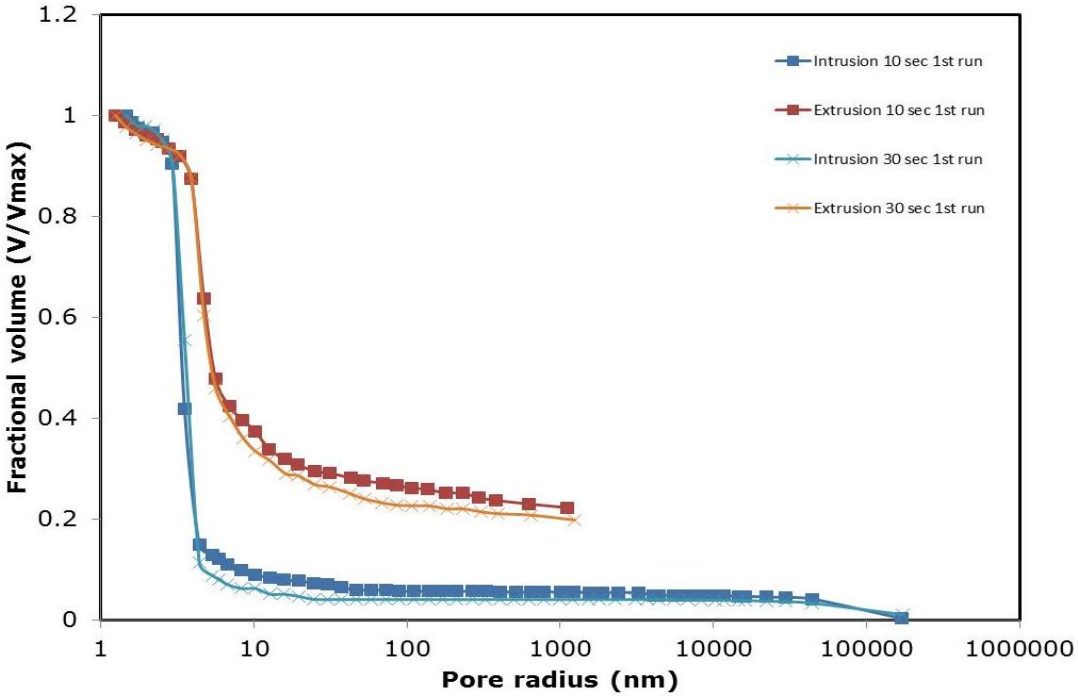

Figure 4. 5: Raw mercury intrusion and extrusion data for standard silica alumina (S3) samples at different equilibration times of 10s (■) and 30s (x). (b) Mercury intrusion/extrusion curves S3 sample analysed using Kloubek correlations. The lines shown are to guide the eye.

(a)

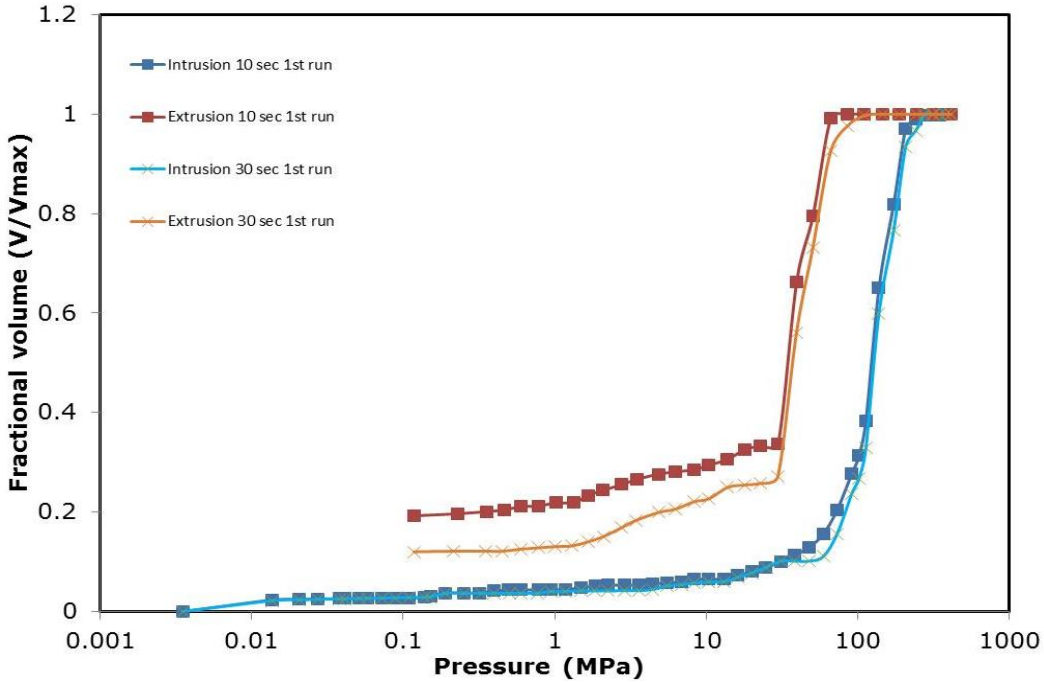

(b)

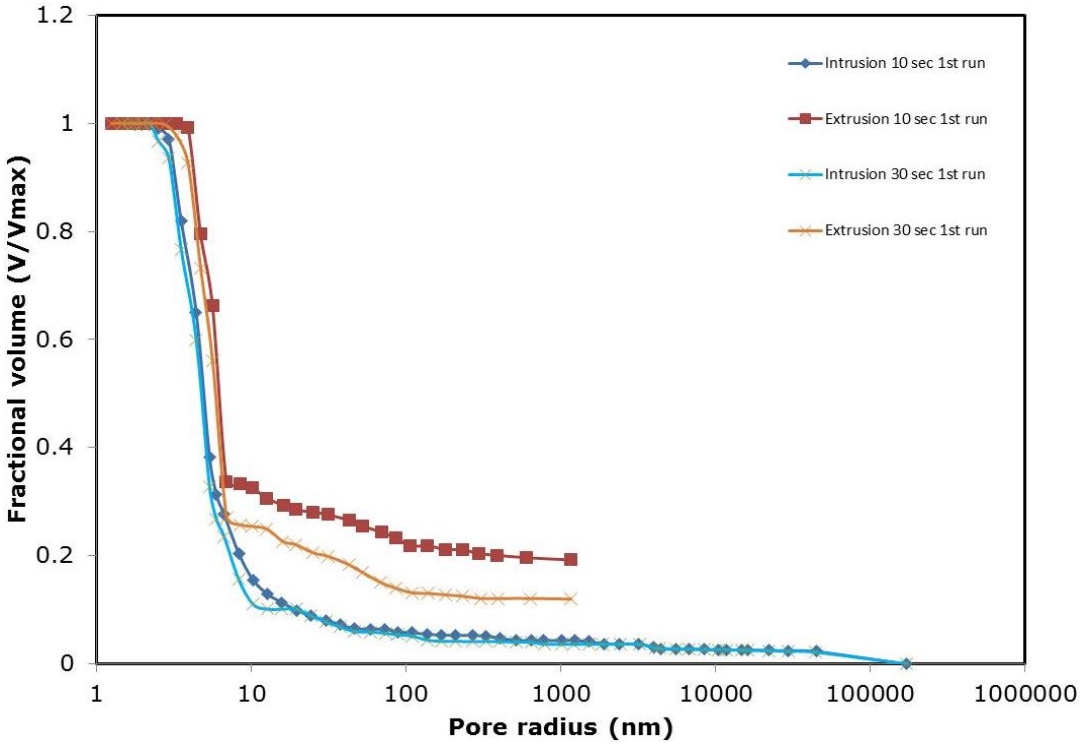

Figure 4. 6: Raw mercury intrusion and extrusion data for Al-3992E (A1) samples at different equilibration times of 10s (■) and 30s (x). (b) Mercury intrusion/extrusion curves A1 sample analysed using Kloubek correlations. The lines shown are to guide the eye.

(a)

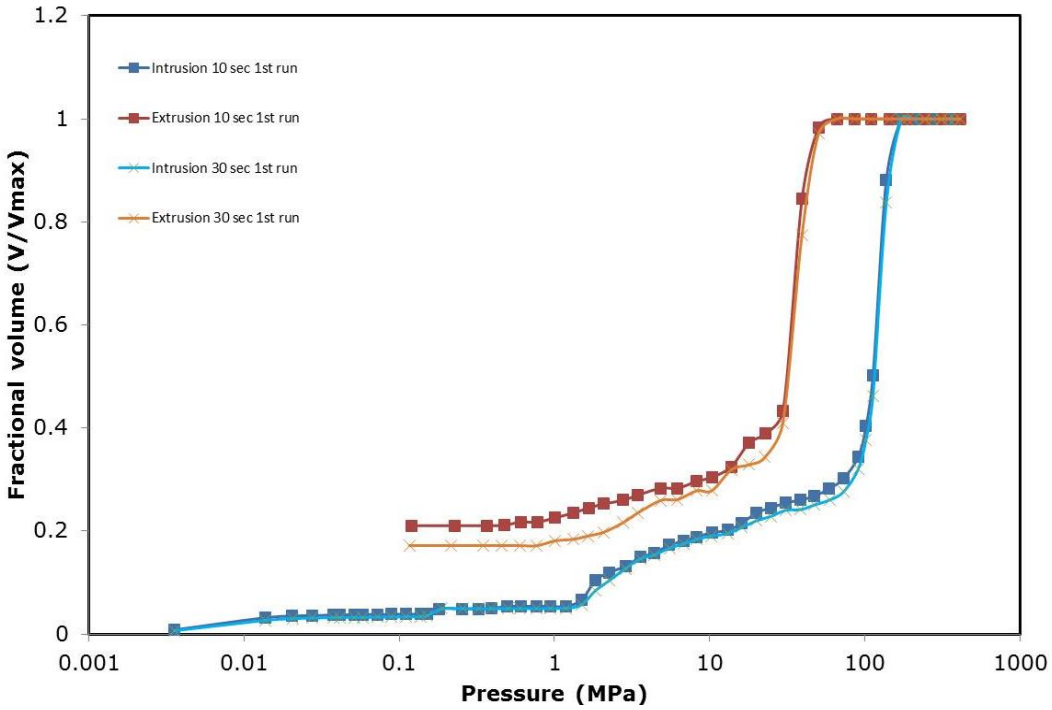

(b)

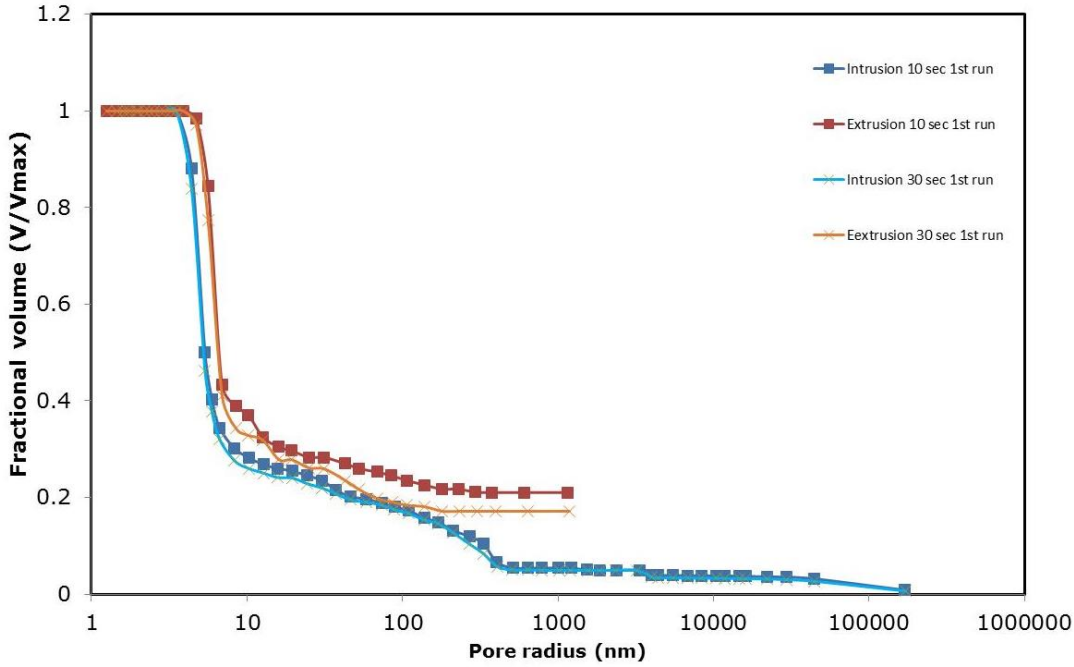

Figure 4. 7: Raw mercury intrusion and extrusion data for Al-3984T (A2) samples at different equilibration times of 10s (■) and 30s (x). (b) Mercury intrusion/extrusion curves A2 sample analysed using Kloubek correlations. The lines shown are to guide the eye.

(a)

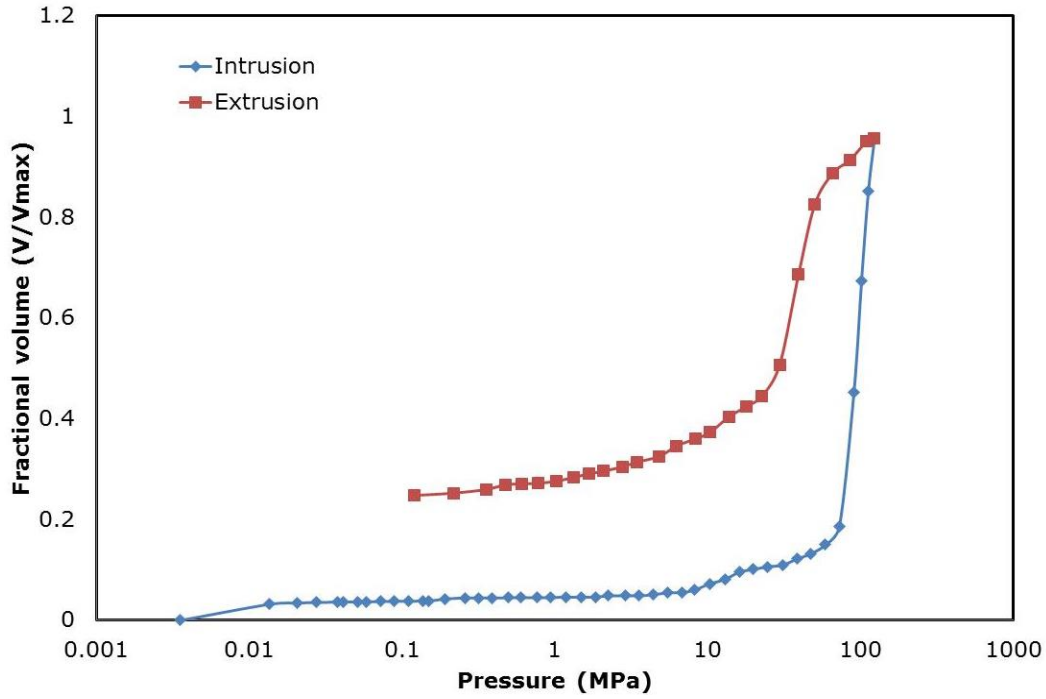

(b)

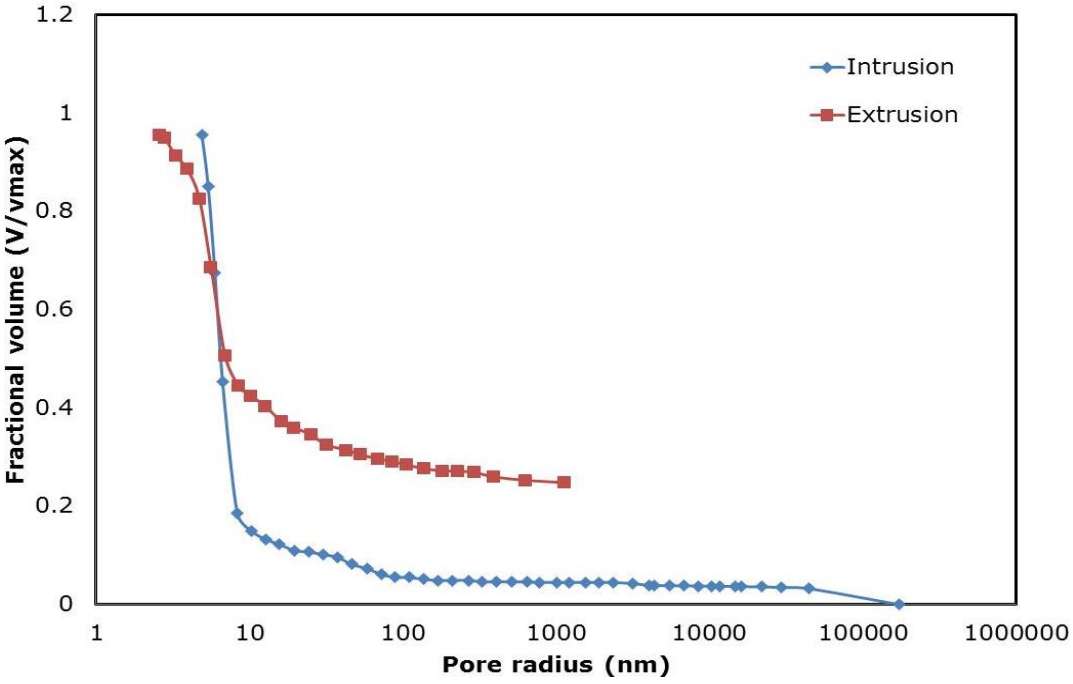

Figure 4. 8: (a) Mercury intrusion/extrusion scanning curve for S1 sample with intrusion pressure of 124 MPa. (b) Mercury intrusion/extrusion scanning curve for (S1) sample analysed using the Kloubek correlation

(a)

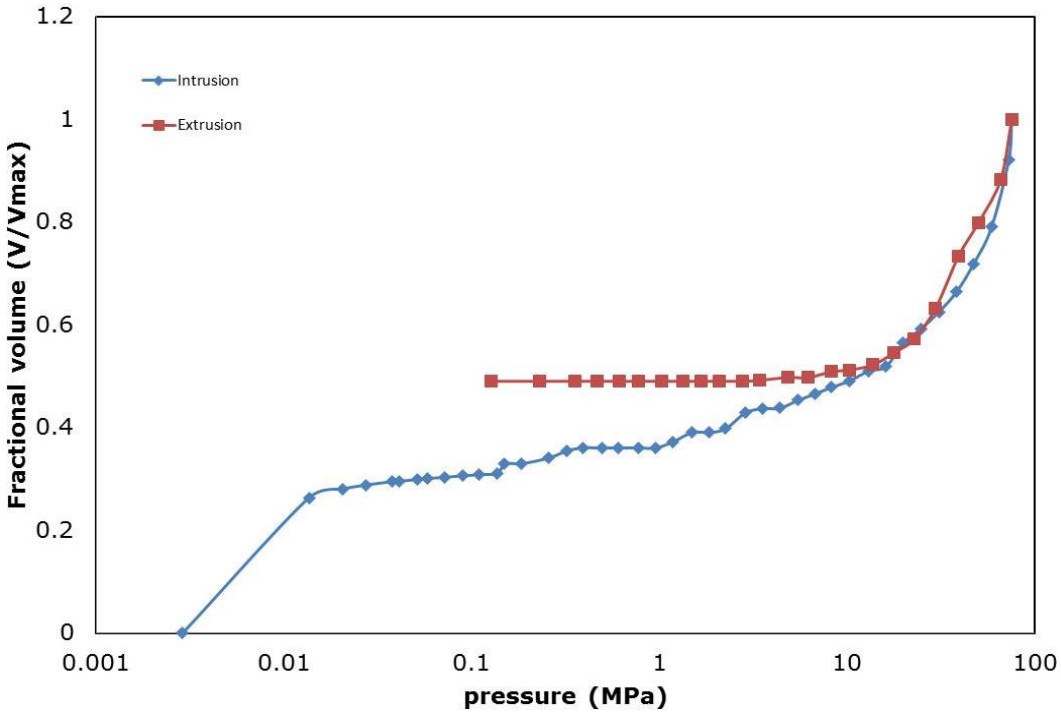

(b)

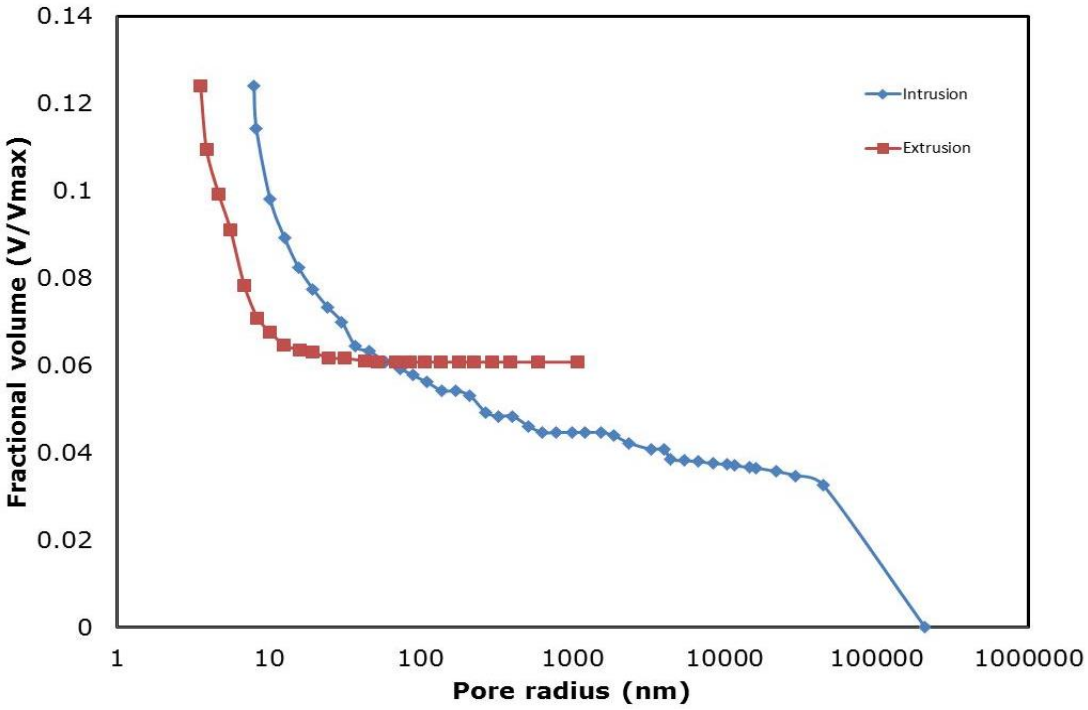

Figure 4. 9: Mercury intrusion/extrusion scanning curve for S1 sample with intrusion pressure of76 MPa. (b) Mercury intrusion/extrusion scanning curve for (S1) sample analysed using the Kloubek correlation

Table 4. 1: Average mercury porosimetry results for S980A (S1) data at different equilibration times

Equilibration time (s)	Ultimate intrusion volume (mL/g)	Average pore diameter (nm)	Entrapment (%)	Surface area (m^2/g)
10	0.74±0.15	11.97±0.69	16.63±0.72	241.91±3.30
30	0.88±0.19	12.27±0.65	15.40±0.76	297.84±2.50

Table 4. 2: Average mercury porosimetry results for S980G (S2) data at different equilibration times

Equilibration time (s)	Ultimate intrusion volume (mL/g)	Average pore diameter (nm)	Entrapment (%)	Surface area (m^2/g)
10	0.97±0.25	39.45±0.59	21.98±2.70	93.01±0.46
30	0.97±0.22	37.05±0.96	14.27±0.83	126.33±1.48

Table 4. 3: Average mercury porosimetry results for silica alumina (S3) data at different equilibration times

Equilibration time (s)	Ultimate intrusion volume (mL/g)	Average pore diameter (nm)	Entrapment (%)	Surface area (m^2/g)
10	0.65±0.04	6.75±0.27	22.22±0.53	386.21±2.23
30	0.60±0.07	7.05±0.27	19.32±0.72	350.49±2.15

Table 4. 4: Average mercury porosimetry results for Al-3992E (A1) data at different equilibration times

Equilibration time (s)	Ultimate intrusion volume (mL/g)	Average pore diameter (nm)	Entrapment (%)	Surface area (m^2/g)
10	0.72±0.09	8.55±0.70	18.97±0.63	314.0±4.4
30	0.72±0.15	8.50±0.38	15.53±2.23	304.38±1.99

Table 4. 5: Average mercury porosimetry results for Al-3984T (A2) data at different equilibration times

Equilibration time (s)	Ultimate intrusion volume (mL/g)	Average pore diameter (nm)	Entrapment (%)	Surface area (m^2/g)
10	0.62±0.16	8.90±0.38	15.90±1.36	167.95±2.32
30	0.55±0.13	9.15±0.27	12.20±1.63	158.79±1.93

Table 4. 6: Average mercury porosimetry results for C10 (G1) data at different equilibration times

Equilibration time (s)	Ultimate intrusion volume (mL/g)	Average pore diameter (nm)	Entrapment (%)	Surface area (m^2/g)
10	1.23±0.18	7.75±0.27	14.77±0.75	540.50±3.01
30	1.13±0.04	7.85±0.27	12.29±0.45	553.24±2.57

Table 4. 7: Average mercury porosimetry results for C30 (G2) data at different equilibration times

Equilibration time (s)	Ultimate intrusion volume (mL/g)	Average pore diameter (nm)	Entrapment (%)	Surface area (m^2/g)
10	1.17±0.29	28.7±0.53	50.12±1.32	190.78±1.72
30	0.86±0.07	30.35±0.70	38.55±2.20	135.06±3.08
50	1.03±0.06	29.85±0.70	34.65±1.25	151.08±1.97
100	0.97±0.27	32.07±1.25	27.16±2.53	131.37±3.86

Table 4. 8: Mercury entrapment comparison for all samples at 10 and 30 sec equilibration times

Sample	Entrapment (%)	
	Equilibration time (10 sec)	**Equilibration time (30 sec)**
S980A	16.63±0.72	15.40±0.76
S980G	21.98±2.70	14.27±0.83
Silica alumina	22.22±0.53	19.32±0.72
Al-3992E	18.97±0.63	15.53±2.23
Al-3984T	15.90±1.36	12.20±1.63
C10	14.77±0.75	12.29±0.45
C30	**50.12±1.32**	**38.55±2.20**

4.3.3. X-ray tomography following mercury porosimetry

Results of x-ray CT are presented in this section following mercury porosimetry experiment. A total of 1008 CT slices were obtained for each of the sample and they were used to render a representative of 3D volume of the G2 sample. Fig. 4.10 (a,b,c) shows a few typical slices of the 200 projected images of mercury content of Individual pellets of G2 Silica samples containing entrapped mercury following mercury porosimetry experiment, where the mercury pressure was increased up to a pressure of 414 MPa and then back to ambient. The shadow images were picked at different locations near the centre of the sample. The equilibration times used were 30 and 100s. The samples were then imaged following removal of samples from the mercury porosimetry within a few hours of mercury porosimetry experiment. In the images, the black regions correspond to the entrapped mercury; this is due to the high electron density of mercury, whereas the grey regions correspond to the silica matrix. With most pellets from the G2 silica sample exhibiting a heterogeneous distribution of mercury as found in previous studies (Rigby et al., 2006), the G2 pellets, shown in Fig. 4.10 (a, b, c) reveals an egg shell of mercury surrounding the central region of the pellet. The shell of mercury surrounding the central region may be due to mercury moving outwards from the centre of the pellet, which is then trapped by snap-off, as several images from different pellets and places are identical, or due to the manufacturing process of sample.

Fig. 4.12 shows a blob of mercury on the surface of the sample, which has been imaged following mercury porosimetry experiment. Fig. 4.13 (a,b) show sets of two-dimensional reconstructed X-ray tomography slice images of a

silica sample containing high level of entrapped mercury which were run with either 30 sec or 100 sec equilibration time. It can be seen that in Fig. 4.13 (a) for 30 sec equilibration time, the entrapped mercury is centred at the middle of the pellet, which produces a mushroom like shape. There are also clearly visible regions containing little or no entrapped mercury. Fig. 4.13 (b) is also a 2D reconstructed x-ray tomography of a pellet following porosimetry experiment at 100 sec equilibration. It can be seen that the entrapped mercury is visible towards the edge of the pellet. This can also be due to the mercury moving outwards from the centre of the pellet as more time was given for the mercury to extrude from the pellet during mercury porosimetry experiment.

Radial mercury density profiles results for each of the G2 sample material studied for 1003 slices are presented in Fig. 4.14 (a,b) and were analysed in steps as follows. Firstly, all the images are read into a 3-d matrix that is constructed prior to storage of all the images. Since we know the size of the individual images and the number of images we can know the size of the overall 3-d matrix. Secondly, the centre of the matrix (centroid pixel) is selected, and then the distance from all the individual pixels to the centroid pixel is calculated to give a second matrix, which is a distance matrix based on the centroid pixel as the centre. And thirdly, the second matrix was binned in terms of a specified bin size, e.g. sqrt (1+1+1) so we can count how many pixels fall into each into each bin or shell. Fourthly, the value of pixels that fall into each bin (calculated from the third step from the original matrix) were summed. Finally, from the third and fourth steps we can obtain the azimuthally averaged intensity value.

However, considering non-spherical samples, the calculated radial averaged values based on the above algorithm will be less than the actual ones when the position is out of the sphere with the maximum radius fitting into the sample. However, the algorithm can be modified to cure this. For example, all the indices of the voxels that is within the pre-established matrix but outside the sample can be reset to a special value. Through this, these voxels do not contribute the corresponding values calculated for the distance matrix in the second step and bin values in the third step, respectively. Therefore, the part outside the sphere with the maximum radius fitting into the sample will be correctly averaged rather than under-calculated with zero-concentration contribution from the voxels outside of the sample.

(a)

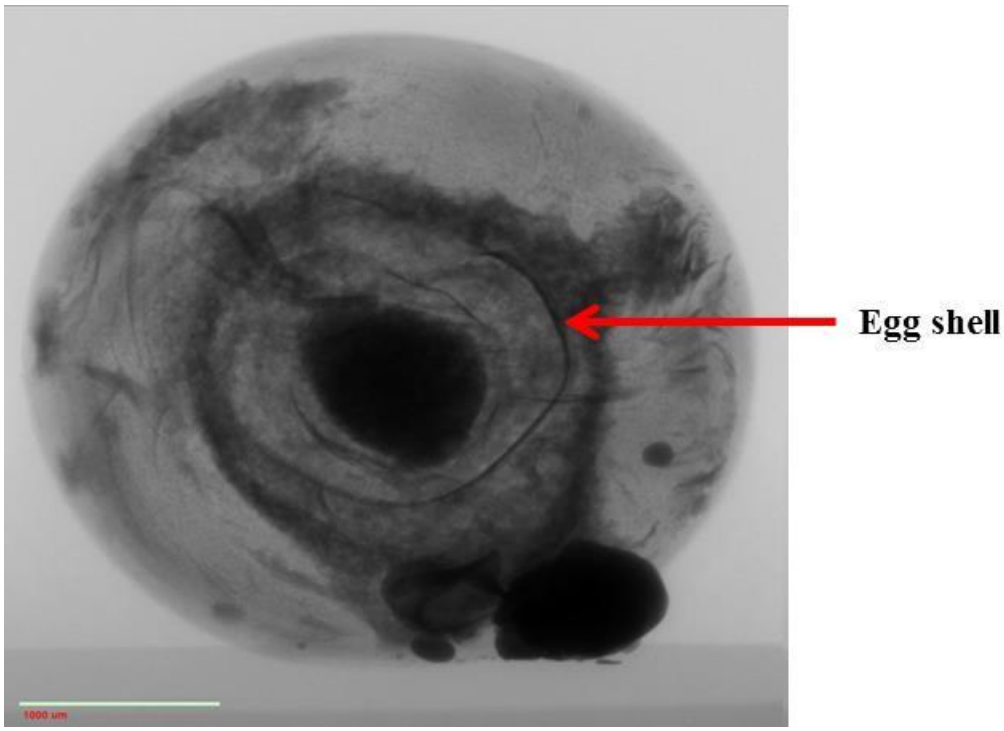

(b)

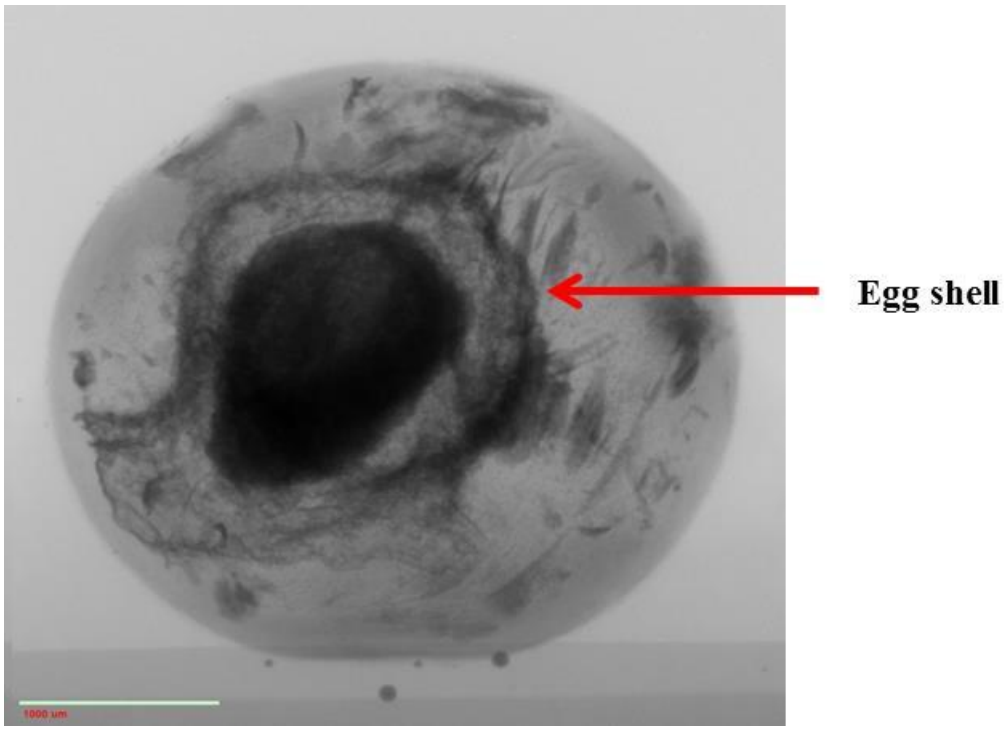

(c)

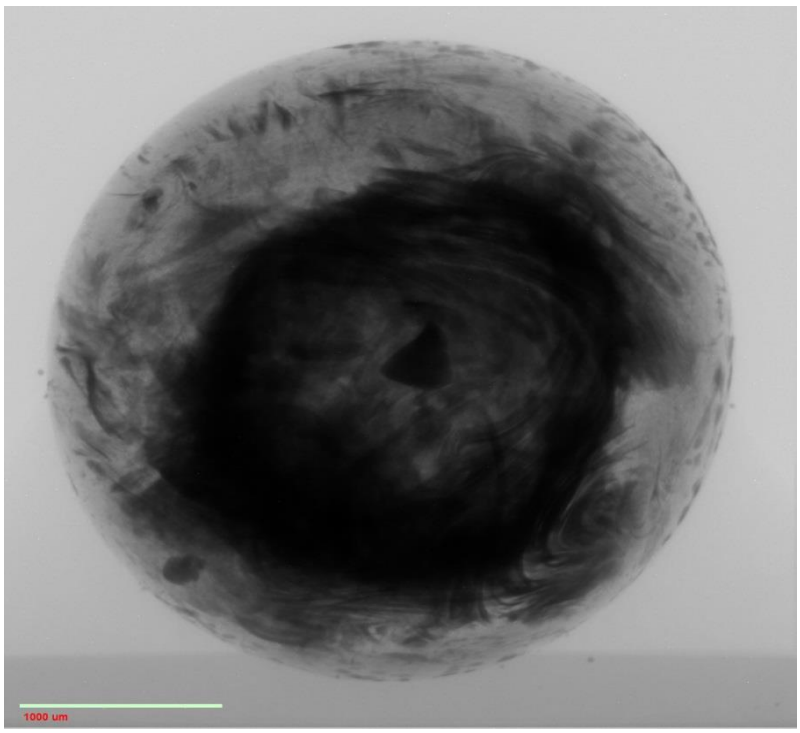

Figure 4. 10: 2D projection of X-ray CT images from equator region of pellet G2, following porosimetry. The equilibration time used was 30 sec.

(a)

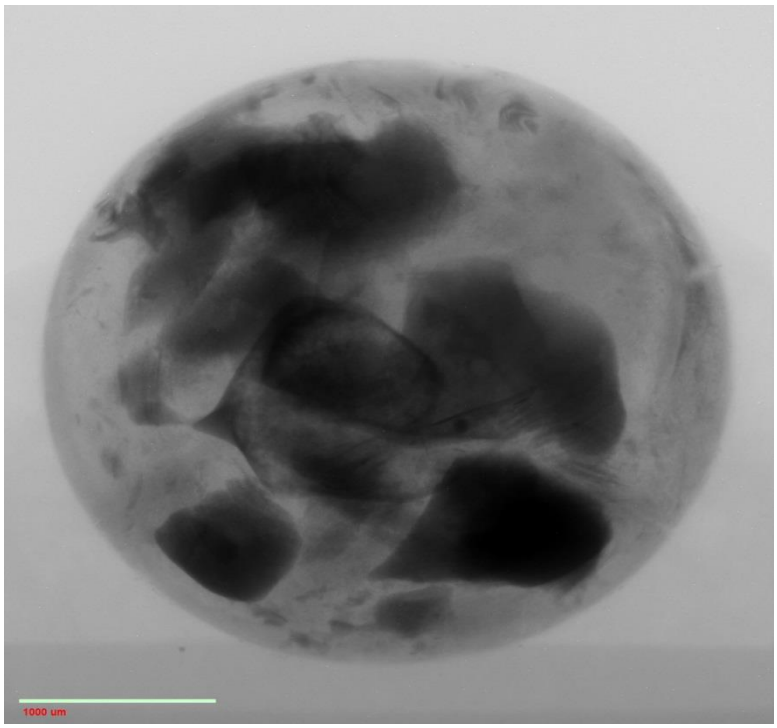

(b)

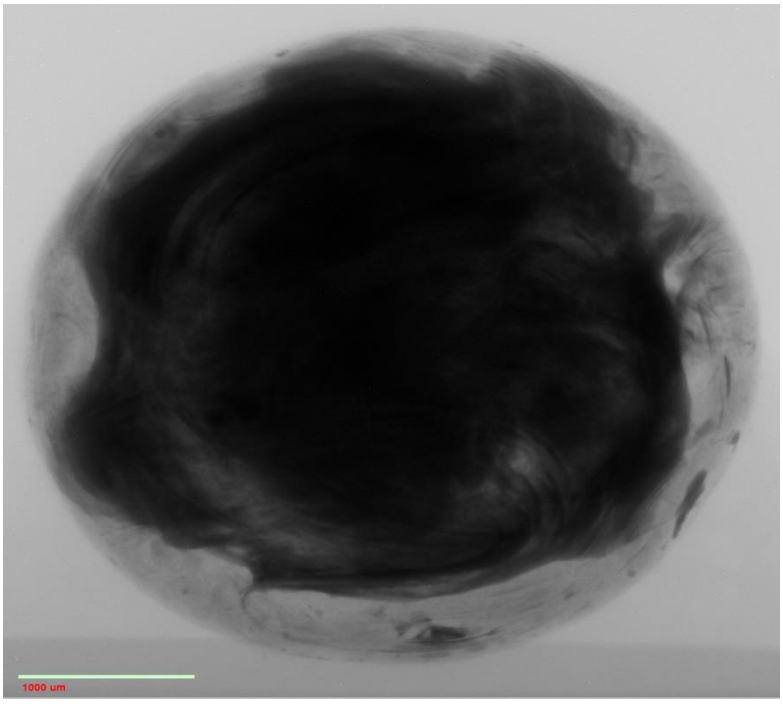

(c)

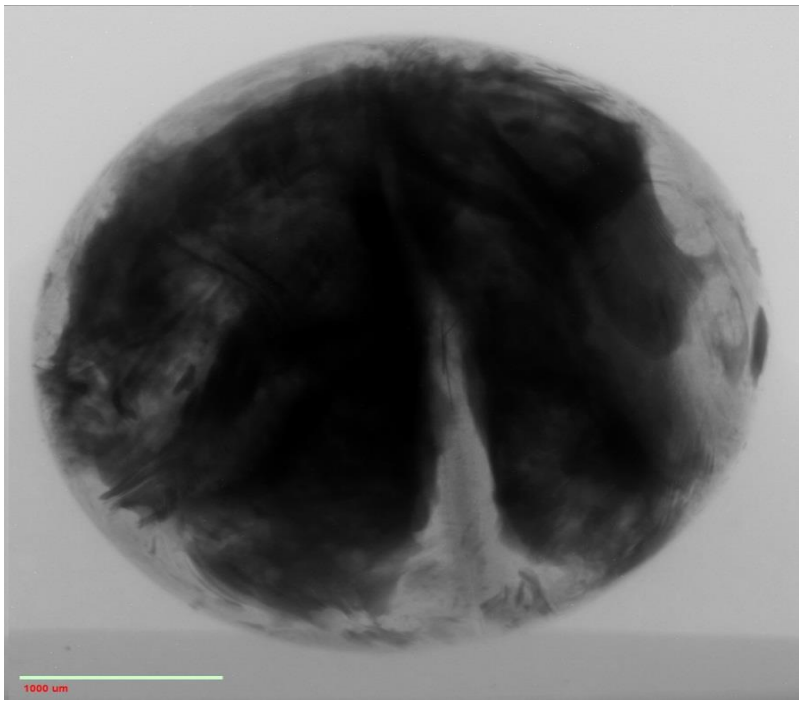

Figure 4. 11: 2D projection of X-ray CT image from equator region of pellet G2, following porosimetry. The equilibration time used was 100 sec

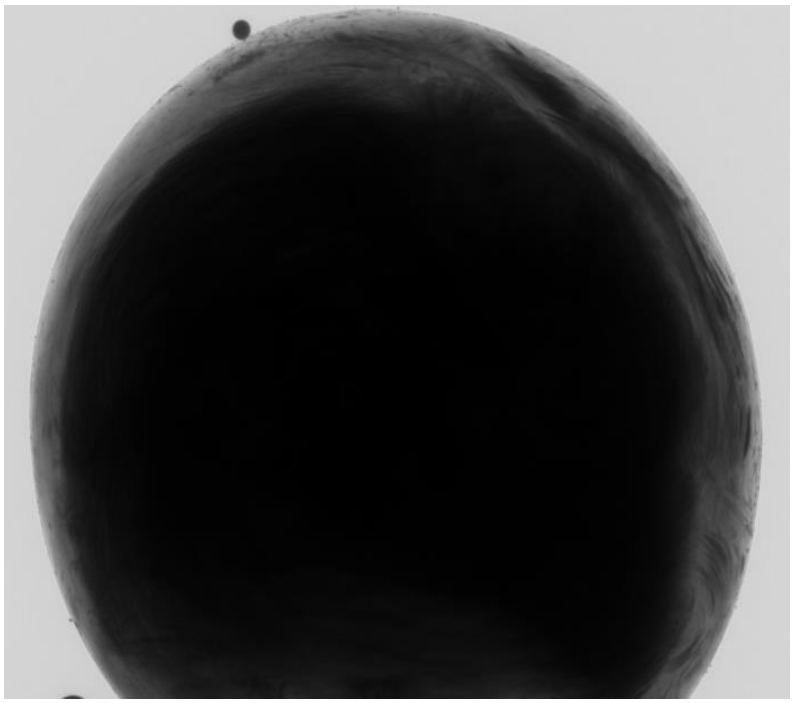

Figure 4. 12: Mercury ganglia seen on the surface of the C30 (G1) silica sample.

(a)

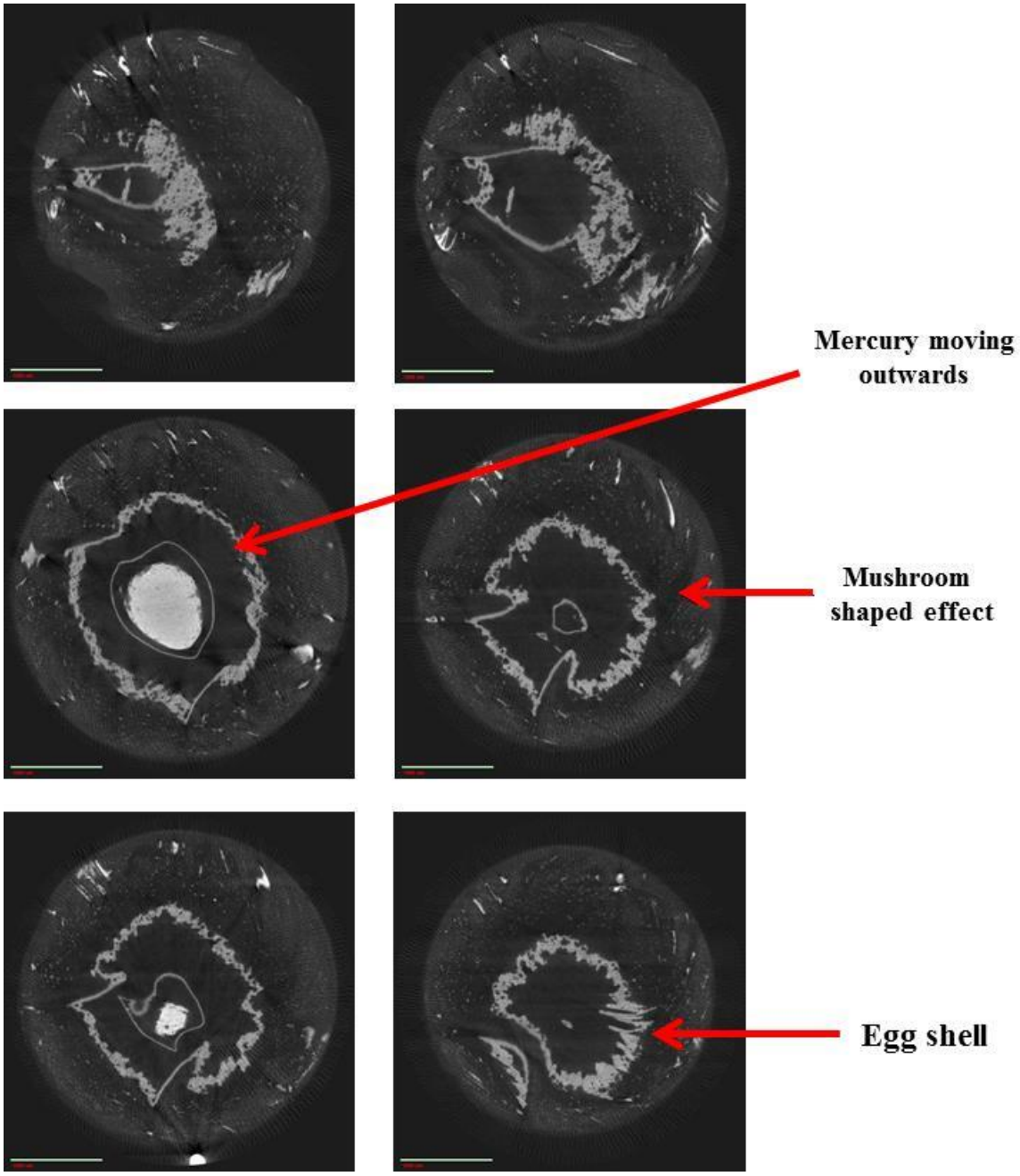

(b)

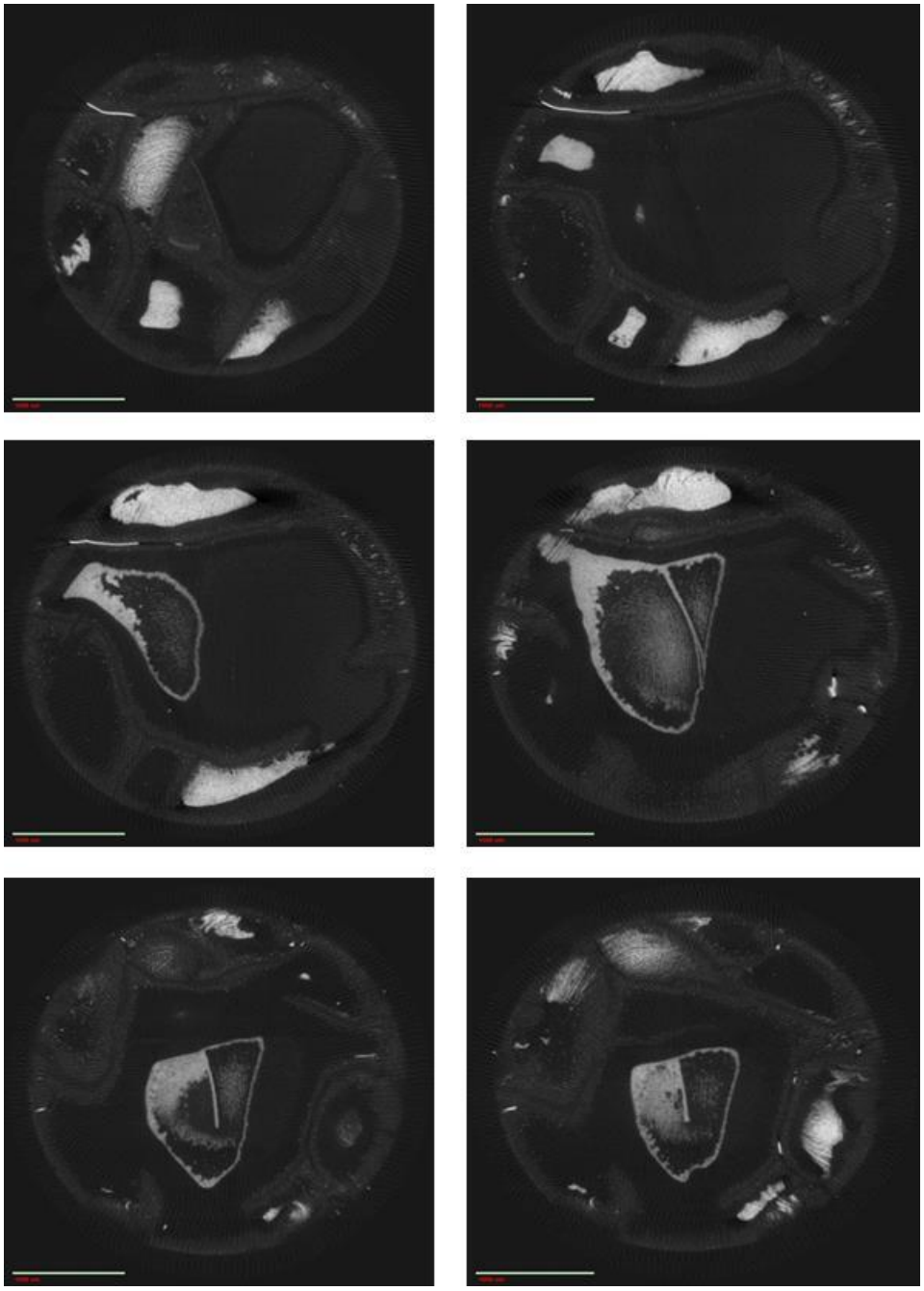

Figure 4. 13: Series of selected 2D reconstructed image different slices from equatorial region of a pellet G2 at equilibration time of (a) 30 sec and (b) 100 sec from mercury porosimetry experiment.

Fig. 4.14 shows the measurements of the average intensity profile for G2 samples studied at 30 and 100 sec equilibration from mercury porosimetry. The image distribution of each sample from the same batch of G2 is shown in Fig. 4.14 for comparison. Fig. 4.14(a) shows the average intensity profiles for the three samples calculated which were run under for 30 sec equilibration time from mercury porosimetry experiment, it can be seen that there is a steep decline as you move outward from the centre of pellet. However the intensity for the 100 sec equilibration time from mercury porosimetry, it can be seen that the intensity stays relatively high and flat and are summarized in Table 4.8. Also, the distance from ~450 to 800 shown in Fig. 4.14(a) which forms a flat plateau is the silica matrix where there is relatively no mercury distribution within the pores of the sample as indicated by the dash line.

(a)

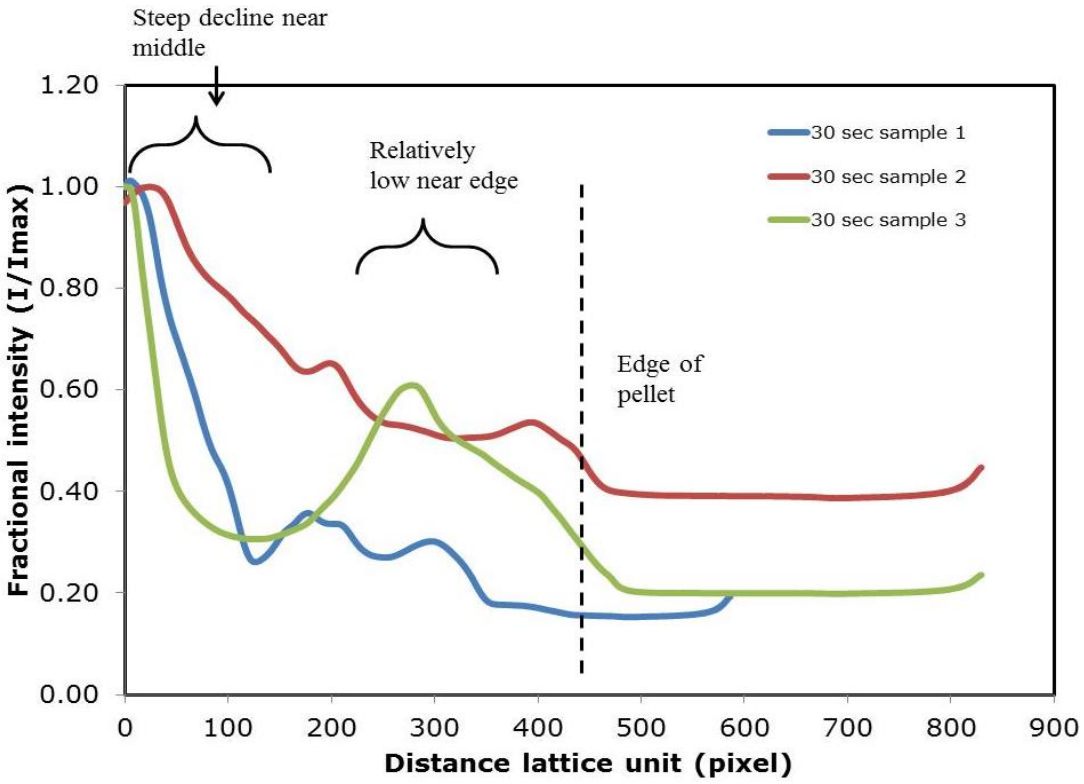

(b)

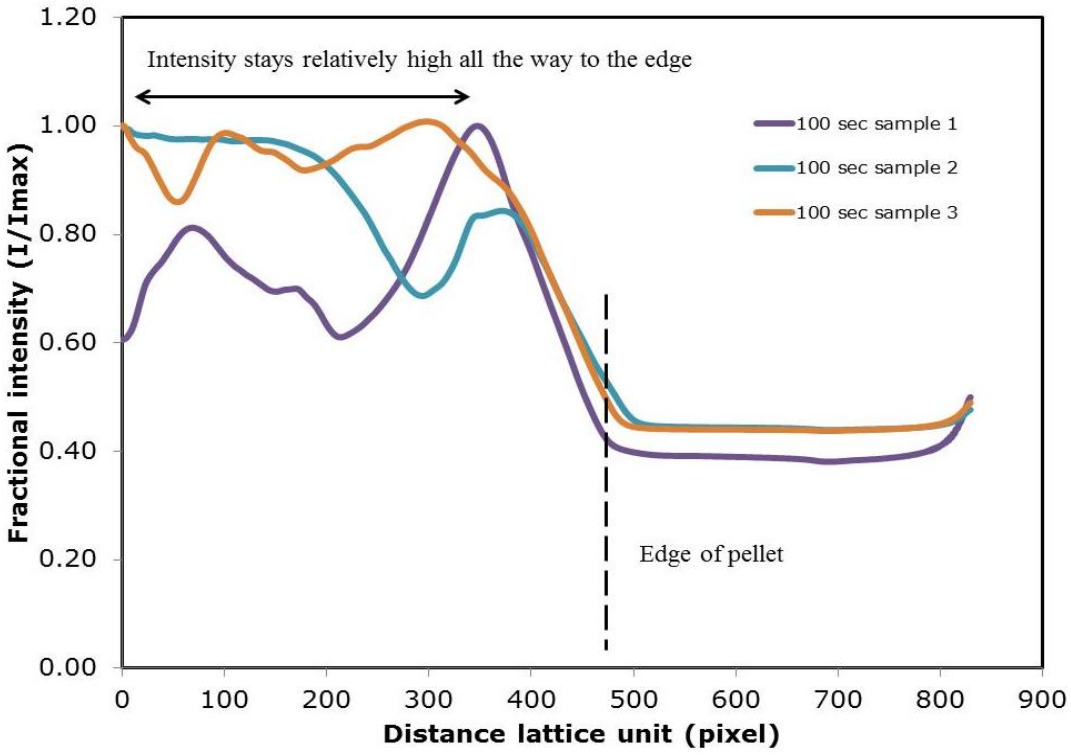

Figure 4. 14: 3D radial average intensity profile for G2 at equilibration time 30 sec (a) and 100 sec (b) from mercury porosimetry. (Courtesy of chunyu Jin from the university of Nottingham)

Table 4. 9: Average intensities for different sections of the radial mercury concentration profile for images from batch G2 of pellets filled with mercury following mercury porosimetry with different equilibration times.

Equilibration time	30 sec		100 sec	
Distance range	**0-100**	**200-300**	**0-100**	**200-300**
Sample 1	0.720	0.290	0.740	0.868
Sample 2	0.863	0.516	0.868	0.773
Sample 3	0.460	0.465	0.940	0.912

4.4. Discussion

The experimental results shown above have revealed a very important insight into the intrusion/retraction processes and the final amount of entrapped mercury (Rigby et al., 2003b; Androutsopoulos and Mann 1979) in different silica/alumina samples. Increasing pressure to intrude mercury into smaller pores may be able to cause structural damage, due to the fact that high pressure are required to force mercury into this smaller pores as explained in section 3.2 of the theory section. It was also reported (Julve et al., 2011) that, during the mercury intrusion experiment, the mercury completely wraps the particle, compresses (which reduces the size of the particle and increase their density) and then shrinks pores. However, from the experimental work done in this thesis, the results suggest that no structural deformation is occurring for all the samples studied. The samples were physically visualize to ensure that the high-pressure applied to the materials do not cause permanent structural damage. All samples retained their external structural stability except for G1 and S3. It is also clearly visible from the X-ray images of a particular sample of G2 studied following porosimetry in Fig 4.10 and Fig. 4.11 that no deformation of sample does occur after porosimetry experiment. It also agrees with previous (Rigby et al., 2004) work on light micrograph images of a typical silica sample following a full intrusion and retraction cycle. Their results have shown that the entrapped mercury is heterogeneously distributed in the pore structure and the spheres also maintain their overall structural integrity. It also agrees with the findings of the X-ray images studied using X-ray tomography technique which shows clearly how the mercury is distributed within the G2 silica sample as describe in section 3.2 of the theory section. This new work

contrasts with the work conducted by Androutsopoulos and Mann (1979), which have shown that in almost every case where a sample is broken to reveal the internal entrapped mercury distribution, the entrapped mercury is found to be homogeneously distributed.

The flat plateau at the highest possible pressure (~414 MPa) following mercury intrusion porosimetry, for samples of S1, S2, G2 A1, and A2 suggests all the pores are completely filled with mercury as earlier mentioned in section 4.4.1. A major difference between these samples and the G1 sample is their respective knee shapes during the extrusion at the maximum pressure. Also sample G1 doesn't exhibit the flat plateau at the highest pressure filling, like the G2 sample, which ended in an extended flat plateau suggesting that all pores are completely filled with mercury and there were no free menisci. In contrast, the mercury intrusion curves for G1 sample ended before the curve flattens out to a plateau. This suggest that some pore space is probably left unfilled with mercury at the top of the G1 intrusion curve, thus leading to an underestimation as some pores containing mercury have free menisci at the junction with residual empty pores. The results of the mercury porosimetry experiments obtained for the G1 sample is similar to that observed in glass micromodels of similar geometry by Wardlaw and McKellar (1981).

Also, as shown above in the results section, hysteresis was observed between the intrusion and extrusion curves in all the samples studied. It is frequently suggested that hysteresis and difference in mercury contact angle between pore sizes, may arise due to surface contaminants or surface roughness at different length scales. Also explained in the theory section, the hysteresis observed between the intrusion and extrusion curves could be as a result of ink-bottle

pore, percolation connectivity, pore potential, or network effects. Kloubek (1981) suggests that contact angle hysteresis cannot be caused by any adsorption of contaminants from the atmosphere due to the fact that at low pressure, the hysteresis observed is greater than that obtained in the normal atmosphere. Also, thermal treatment of silica materials is known (Bilinski, 1998) to be a factor that can change the surface of the material because heat treatment changes the nature and distribution of hydroxyl group. However the nature of the intrusion and extrusion curves allowed the use of Rigby and Edler equation (Eq. 3.2) to remove contact angle hysteresis. This helps to understand the special point of interest where the extrusion curve deviates from the intrusion curve. The deviation between the intrusion and extrusion curves observed at larger mesopore sizes, are attributed to mercury entrapment

The removal of contact angle and structural hysteresis from the experimental results for some samples using Eq. 3.2, have been previously observed (Rigby and Edler, 2002; Rigby et al., 2003a). Rigby *et al*. (2002) have shown that by using the Kloubek correlations (Eq. 3.2), for a fragmented sample of S1 with particle size 60-90 µm, the pore space no longer entrapped mercury following porosimetry experiment. Their findings suggest that the mercury entrapment within S1 is due to the macroscopic properties of the pellets and not by the presence of pore size effect. The entrapped mercury after porosimetry study may be able to migrate towards the surface and leave the material sample. However, previous work (Rigby et al., 2003b) have demonstrated that the entrapped mercury may be able to stay stationary over a long time after the experimental period. The level of mercury entrapment was found to be a function of pore connectivity and the width of pore size distribution.

Previous work (Rigby et al., 2008) found entrapment to be a strong function of equilibration time for G2 sample. They have shown that the volume of entrapped mercury decreases as the equilibration time is raised. The amount of mercury leaving the sample also follows similar pathways up to the highest equilibration time used. These pressures were of similar size and occurred when very similar total residual amounts of mercury were remaining within the sample, and therefore it might be expected that similar pathways remained to access the sample surface. In this work conducted, different samples have been studied to see if there is similar behaviour with the G2 sample. However, of the various samples studied, none of them seem to have any degree of effect of equilibration time as the G2 sample. Hence X-ray tomography technique was used to see the difference between the images of mercury in G2 depending on equilibration time.

X-ray tomography provides a non-destructive way to produce a 3D representation and analyse the structural characterisation of porous solids. A 2D reconstruction image shown in Fig. 4.13 can be useful in analysing the topological features of heterogeneous silica materials. Also, X-ray tomography provides a flexible way of selecting any section of the material studied and to analyse the pore structure. This makes it a unique method compared to mercury porosimetry technique. One of the main cause of mercury entrapment as mentioned in the literature is the throat-pore co-ordination. Also, previous studies have shown that lower pore co-ordination numbers results in greater pore shielding (Wardlaw and McKellar 1981). From the high level of mercury entrapment found, these suggest that the connectivity between macrospores in the pellets is low. In Fig. 4.13 (a), all the percolation routes are highlighted by

entrapped mercury that is clearly seen within the image resolution, suggesting a low number of pore connections on macroporous level. Another cause of mercury entrapment is the pore geometry. Mercury ganglia observed in the X-ray images can be due to higher pore-throat size ratios. Previous studies on glass micro-model and modelling (Ioannidis and Chatzis, 1993, Wardlaw and McKellar, 1981) have shown that the pressure decrease during retraction process causes the mercury threads to have saddle-shaped configurations as they become unstable. All the X-ray images studied have shown the presence of mercury in heterogeneous pores, which are distributed in wide pore size range. This is in good agreement with the work obtained in previous work (Rigby et al., 2006), which demonstrates the distribution of mercury in highly heterogeneous pore spaces. More recently (Rigby et al., 2011), similar results have also been found which shows a high degree of heterogeneity in the entrapment of mercury within alumina pore network. However, the results obtained from mercury porosimetry would not match exactly with the results from X-ray tomography. This is due to the fact that mercury porosimetry only measure pores that are accessible to the pressurized mercury whereas X-ray tomography measures both the isolated and connected pores contributing to the total pore volume.

4.5. Conclusion

A typical mercury porosimetry experiments, consisting of intrusion and extrusion curves have shown a flat plateau at the highest filling. This indicates that mercury has completely filled the pores and is awaiting pressure reduction for extrusion of the mercury to be attained. It has been shown that by using the suggested alternatives Eqn. 3.2 to the Washburn equation for the analysis of the raw mercury porosimetry data, the wide range of pore sizes corresponding to the mercury intrusion and extrusion curves completely overlay each other. Also, as observed, the deviations between the intrusion and extrusion curves for the silica gel pellets at larger pore sizes are attributed to mercury entrapment. It has also been shown that pore structural damage does not occur during mercury porosimetry experiments on a particular type of sol –gel silica sphere. Also, x-ray image of G2 silica sample have suggested that mercury entrapment occurs in heterogeneously distributed domains within the sample,

It is also concluded that, the hysteresis observed between the intrusion and extrusion curves is due to either of the following causes or a combination of all. The first which is the contact angle hysteresis (due to differences in advancing and receding contact angles), and ink-bottle hysteresis (due to mercury entrapment in ink bottle pores) and the last which is the percolation connectivity hysteresis (due to connection between the pores and ink bottle pores). It can be concluded that the pore networks derived from x-ray tomography data can provide a valuable representations of reservoir rocks for transport property modelling.

4.6. References

ANDROUTSOPOULOS, G. P. & MANN, R. 1979. Evaluation of mercury porosimeter experiments using a network pore structure model. *Chemical Engineering Science,* 34**,** 1203-1212.

BILIŃSKI, B. 1998. The Influence of Thermal Treatment of Silica Gel on Surface–Molecule Interactions: I. Finite Coverage Region. *Journal of Colloid and Interface Science,* 201**,** 180-185.

GIESCHE, H. 2006. Mercury Porosimetry: A General (Practical) Overview. *Particle & Particle Systems Characterization,* 23**,** 9-19.

IOANNIDIS, M. A. & CHATZIS, I. 1993. A Mixed-Percolation Model of Capillary Hysteresis and Entrapment in Mercury Porosimetry. *Journal of Colloid and Interface Science,* 161**,** 278-291.

JULVE, D., RAMOS, J., PÉREZ, J. & MENÉNDEZ, M. 2011. Analysis of mercury porosimetry curves of precipitated silica, as an example of compressible porous solids. *Journal of Non-Crystalline Solids,* 357**,** 1319-1327.

RIGBY, S., FLETCHER, R. & RILEY, S. 2004. Characterisation of porous solids using integrated nitrogen sorption and mercury porosimetry. *Chemical Engineering Science,* 59**,** 41-51.

RIGBY, S. P. 2002. New methodologies in mercury porosimetry. *In:* F. RODRIGUEZ-REINOSO, B. M. J. R. & UNGER, K. (eds.) *Studies in Surface Science and Catalysis.* Elsevier.

RIGBY, S. P., BARWICK, D., FLETCHER, R. S. & RILEY, S. N. 2003a. Interpreting mercury porosimetry data for catalyst supports using semi-empirical alternatives to the Washburn equation. *Applied Catalysis A: General,* 238**,** 303-318.

RIGBY, S. P., CHIGADA, P. I., EVBUOMVAN, I. O., CHUDEK, J. A., MIRI, T., WOOD, J. & BAKALIS, S. 2008. Experimental and modelling studies of the kinetics of mercury retraction from highly confined geometries during porosimetry in the transport and the quasi-equilibrium regimes. *Chemical Engineering Science,* 63**,** 5771-5788.

RIGBY, S. P., CHIGADA, P. I., WANG, J., WILKINSON, S. K., BATEMAN, H., AL-DURI, B., WOOD, J., BAKALIS, S. & MIRI, T. 2011. Improving the interpretation of mercury porosimetry data using computerised X-ray tomography and mean-field DFT. *Chemical Engineering Science,* 66**,** 2328-2339.

RIGBY, S. P. & EDLER, K. J. 2002. The Influence of Mercury Contact Angle, Surface Tension, and Retraction Mechanism on the Interpretation of Mercury Porosimetry Data. *Journal of Colloid and Interface Science,* 250**,** 175-190.

RIGBY, S. P., FLETCHER, R. S. & RILEY, S. N. 2003b. Determination of the cause of mercury entrapment during porosimetry experiments on sol–gel silica catalyst supports. *Applied Catalysis A: General,* 247**,** 27-39.

RIGBY, S. P., WATT-SMITH, M. J., CHIGADA, P., CHUDEK, J. A., FLETCHER, R. S., WOOD, J., BAKALIS, S. & MIRI, T. 2006. Studies of the entrapment of non-wetting fluid within nanoporous media using a synergistic combination of MRI and micro-computed X-ray tomography. *Chemical Engineering Science,* 61**,** 7579-7592.

WARDLAW, N. C. & MCKELLAR, M. 1981. Mercury porosimetry and the interpretation of pore geometry in sedimentary rocks and artificial models. *Powder Technology,* 29**,** 127-143.

Chapter 5: Using Thermoporosimetry to Improve Accuracy of Pore-size Distributions for Disordered Solids

5.1. Introduction

This chapter will discuss the use of the Thermoporosimetry characterization technique, which can be implemented using the Differential Scanning Calorimetry (DSC) method. The DSC technique was used to determine the pore size distributions from the melting and freezing point depression of a fluid, in this case water and mercury, when confined within a porous material. Thermoporosimetry technique was used to determine the pore size from porosimetry and whether melting occurs by hemispherical or cylindrical shaped menisci by combining both the thermoporosimetry experiment with a mercury porosimetry experiment, which is termed the 'mercury thermoporosimetry' experiment.

Thermoporosimetry method has several advantages compared to conventional characterisation methods, such as mercury porosimetry. There are no extraordinary preparation steps and specialised instrument required, it also has the ability to study wet samples. The mercury porosimetry technique has already been carried out in chapter 4 of this thesis. The thermoporosimetry work in this thesis was first used to study and to understand the phase behaviour of water in the confined pores of silica materials when they are fully saturated with water and also to see the effects of different melting and freezing ramp rates on silica materials.

5.2. Sample preparation and experimental considerations

Case I: Mesoporous silica gels samples (S1, G1, and G2) shown in Table 5.1 were obtained from Grace/Fuji and the CPG from Sigma-Aldrich. The samples were prepared in different ways; first the pellets were exposed to the atmosphere to adsorb water vapour. The pellets tend to crack as soon as they are immersed into water before exposing them. This might be due to calcinations at high temperature which de-hydoxylates the surface and change the internal pore space in two ways. First, by breaking the pores of closed pores if present, and secondly by breaking particles along larger pores that result in decrease of the relative volume of larger pores. The pellets are then immersed in deionised water obtained from in-house distilled source for approximately 2 hours to get them fully saturated and to remove air trapped in the pores. The probe liquid (water) used has a melting point temperature of 273.15 K, enthalpy of fusion 334 J/g, and liquid density of 1.00 g/cm^3 at 273 K (Perry et al., 1999).

Case II: This is the mercury thermoporosimetry experiment. The experiment protocol is shown in Fig. 5.1. Three different samples were used in this study, namely: S1, S2 and G2. All the samples were prepared using the same experimental procedures. Firstly, the sample was dried under vacuum at 150 $^{\circ}$C in order drive out any moisture content within the samples, as they are prone to adsorb water. This is necessary in order to carry out mercury porosimetry experiment. The sample preparation has been discussed already in section 4.2.1. The sample from mercury porosimetry experiment was allowed to reach ambient temperature before performing thermoporosimetry analysis.

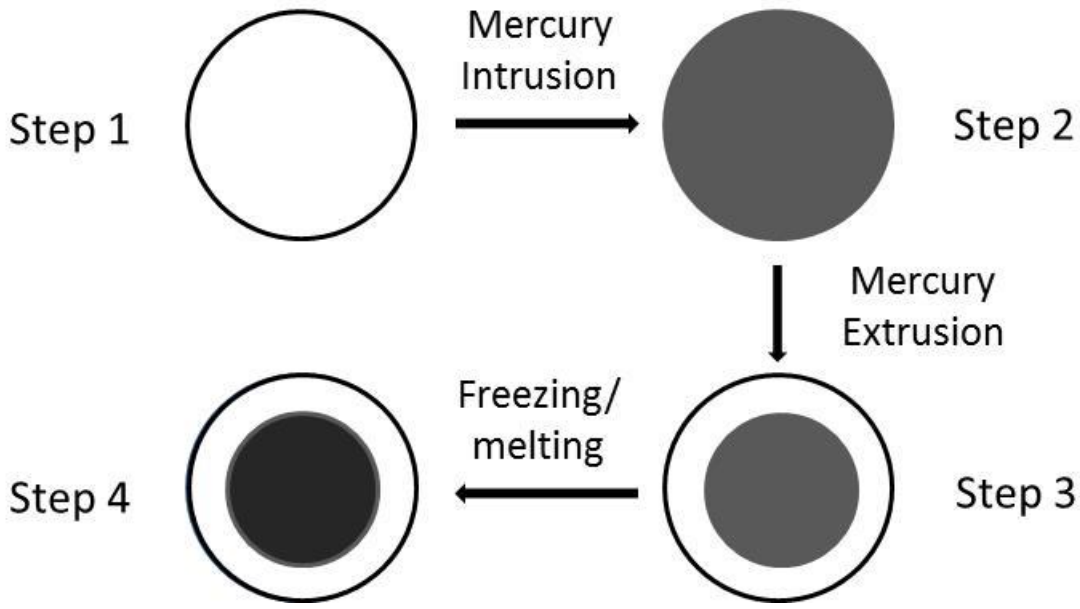

Figure 5. 1: Schematic representation of the mercury thermoporosimetry experiment. The grey is the entrapped mercury and the white is the silica matrix.

Fig. 5.1 shows a schematic representation of the procedures used in the mercury thermoporosimetry experiment. A clean sample was dried in an oven for 15 hours before the mercury porosimetry experiment (step 1). A mercury porosimetry experiment was performed on a clean sample by applying pressure to intrude mercury into the sample (step 2). The intruded pressure is then lowered which extruded mercury from the sample leaving some to become entrapped (step 3). And finally the mercury thermoporosimetry experiment is conducted on the entrapped mercury sample by freezing both the sample pellet and entrapped mercury (step 4). A temperature range of -85 $^{\circ}$C to -37 $^{\circ}$C for the melting process and a ramp rate of 0.1 $^{\circ}$C/min were used for this set of experiment.

5.3. Sample analysis

Thermoporosimetry experiments were carried out using a TA Instruments DSC with model number Q10 V9. The machine is equipped with cooling apparatus and with a data processing system that passes cool nitrogen gas over the sample to freeze the probe fluid. The temperature stability was ±0.01 K, while the accuracy was ±0.1 K, according to the product specifications. The equipment was used to measure the melting and freezing curves of the fluid in the silica gels in order to determine the pore size distribution. The sample S1, containing pore water (~18 mg), was loaded into the DSC machine at ~25 °C and the temperature was lowered to -33°C, and kept at this temperature for 10 minutes to provide temperature homogeneity. After the samples were allowed to come to a thermal equilibrium, the cooling curves were measured over the temperature range from -10 °C to -1.5 °C. The DSC measurements for all samples S1, G1, G2, and CPG were all carried out at a low scanning rate, 0.1 °C/min, to avoid thermal and time delays in the DSC curve.

A single pellet imbibed with water was placed in an aluminium pan and crimped with a pan lid. This was done to avoid evaporation during the course of the experiment. The total mass for each sample pellet used is shown in Table 5.1. A repeated experiment was carried out to check that water didn't evaporate, and. also, check that the expansion and contraction of water during DSC experiment did not cause fractures of the pore.

In case II, the sample containing mercury which had previously been heated to -38 °C, were frozen in the DSC cell to the required temperature of -85 °C and kept at this temperature for 10 minutes to provide temperature homogeneity.

After the samples were allowed to come to a thermal equilibrium, the melting curves were measured over the temperature range from -50 °C to -38 °C. The DSC measurements were carried out at low scanning rate of 0.1 ºC/min to avoid thermal and time delays in the DSC curve.

5.4. Results

5.4.1. Study of the behaviour of water in silica samples

The DSC solidification thermograms recorded for three different silica samples of S1, G1, and G2 saturated with water are shown in Fig. 5.2, Fig. 5.3 and Fig. 5.4 respectively. All samples were conducted twice by freezing and melting the probe liquid to check the repeatability. Melting and freezing curves for S1, G1 and G2 samples were all achieved through melting or freezing of the pore fluid, and then cooling or warming the system. In Fig. 5.2 for S1, the thermogram obtained shows the amount of heat being released and used by the system respectively. It shows the melting process from -10 ºC to -1.5 ºC. As the temperature is increased, the ice starts to melt at ~-8 °C and peaks at approximately ~-4 °C. This process requires energy and is termed as endothermic process. The flat plateau region between -2.3 °C to -1.5 °C is when all the intra-particle water within the sample is molten but remains with an outer frozen layer of ice. The process is reversed to freeze the intra-particle water which releases energy and peaks at ~ -7.3 °C. This process of releasing energy is called exothermic process.

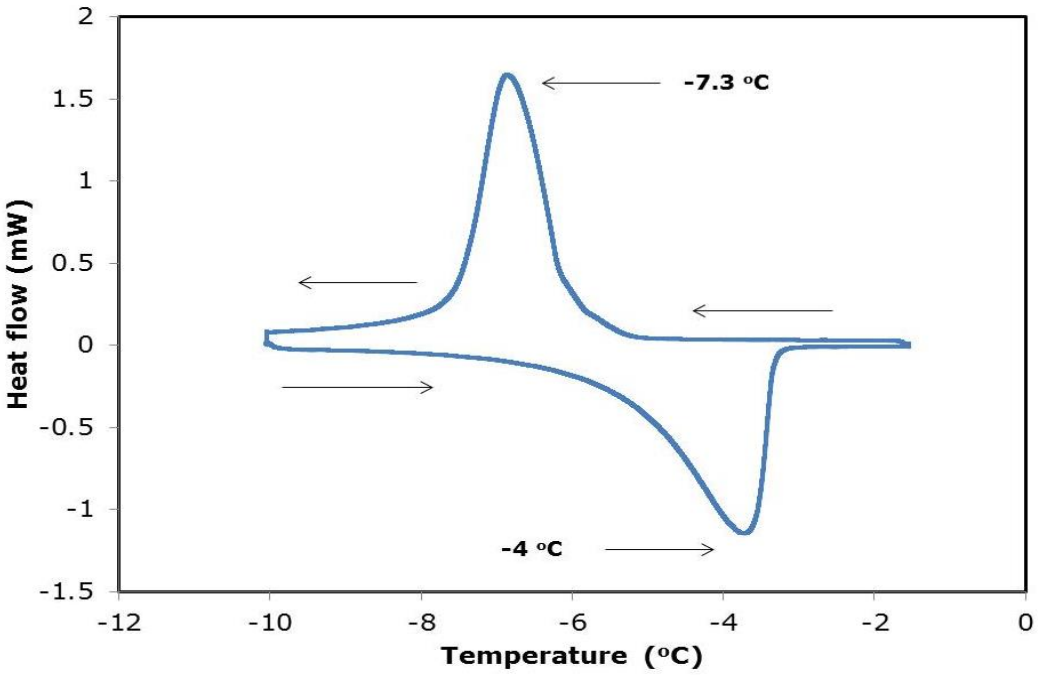

Figure 5. 2: Thermal transitions for a fully saturated S1 pellet as measured by DSC in melting and freezing

The same process was repeated for different samples of G1 and G2. Fig. 5.3 shows the thermogram for G1 sample. In this particular sample, the ice starts to melt at ~-10 °C and peaks at ~5.2 °C. The freezing process peaks at approximately ~9.5 °C. The sample is frozen again to -13 °C and peaks at ~ 9.2 °C. It is evident from Fig. 5.2, Fig. 5.3 and Fig. 5.4 that the exotherm and endotherms overlay, which suggests that the same amount of energy is being released and used by the system, respectively, for each freezing and melting cycle. This suggests that no water has evaporated during the experimental time scale.

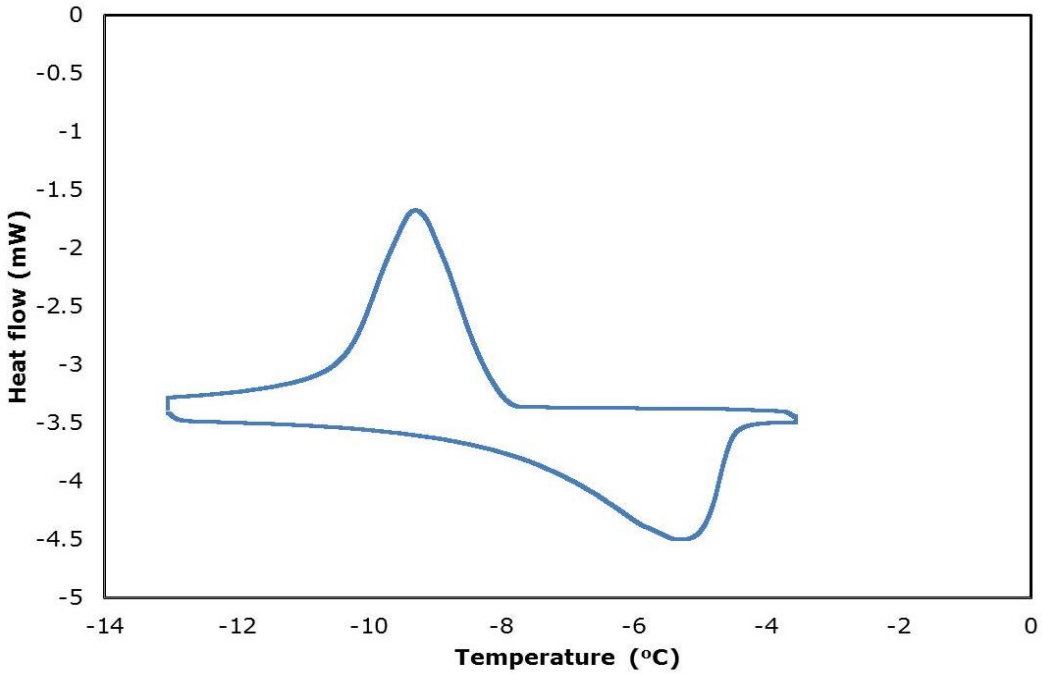

Figure 5. 3: Thermal transitions for a fully saturated G1 pellet as measured by DSC in melting and freezing

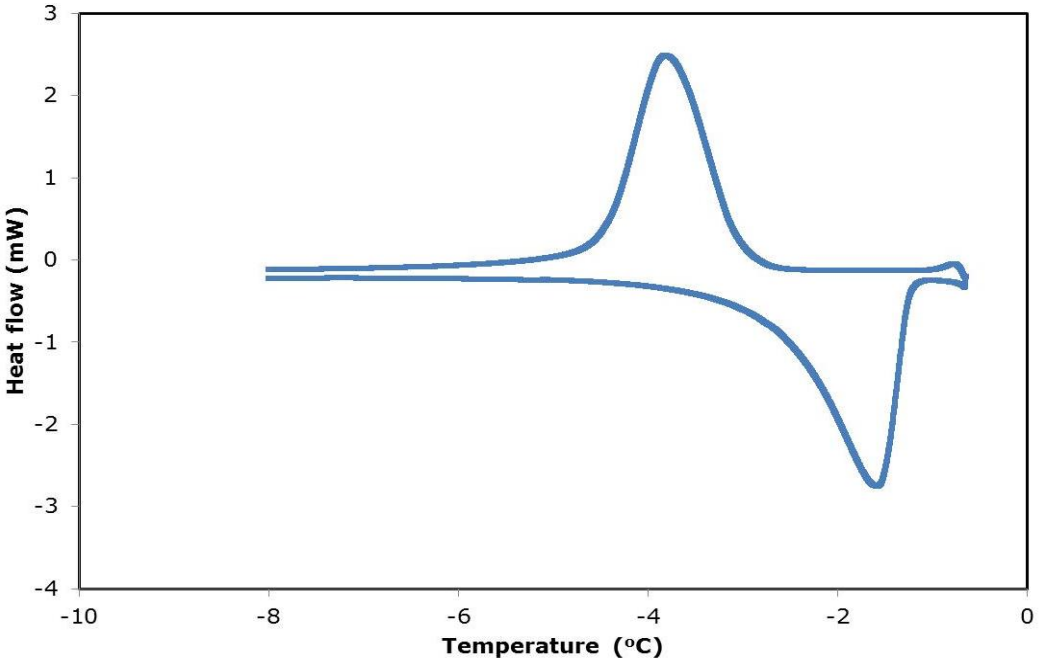

Figure 5. 4: Thermal transitions for a fully saturated G2 pellet as measured by DSC in melting and freezing

Fig. 5.5 shows an experiment conducted on S1 sample, to see the effect of different heating and cooling ramp rates which froze and melted the intra-particle water using different ramp rates that ranges from 0.2 to 1.4 $^{\circ}C\ min^{-1}$. It is seen in Fig. 5.5 that the heating rate does not affect the start of the melting and heating processes. From the melting and freezing curves, it can be seen that more heat is being released or consumed, by the system at higher ramp rates as is evident from the exotherms, and endotherms, shown respectively in Fig. 5.5. It is also evident from the melting process that as the ramp rate is increased, the exotherms were progressively shifted to lower temperatures. The peak temperature ranges for the endotherms becomes broader and shifts to higher temperatures with increasing melting ramp rate. Also, noted is the continuous increase in peak maximum temperature as the melting rate increases. Fig. 5.6 shows the pore size distributions calculated using Eqs. (3.8, 3.9 and 3.12) derived by Iza *et al*. (2000) for thermoporosimetry data. The mercury porosimetry pore size distribution was calculated using the Washburn Eq. 3.1. Table 5.1 shows the sample investigated in this chapter with different probe fluid. Although Gibbs-Thompson equation assumes that the enthalpy of melting of water is constant, the melting enthalpy calculated is the enthalpy of melting for the samples experimented. If the sample has a higher voidage fraction it will have a higher enthalpy of melting, which represents the amount of fluid present in the sample. The overall enthalpy of melting observed depends on the water content of the sample, which depends on the porosity of the pellet.

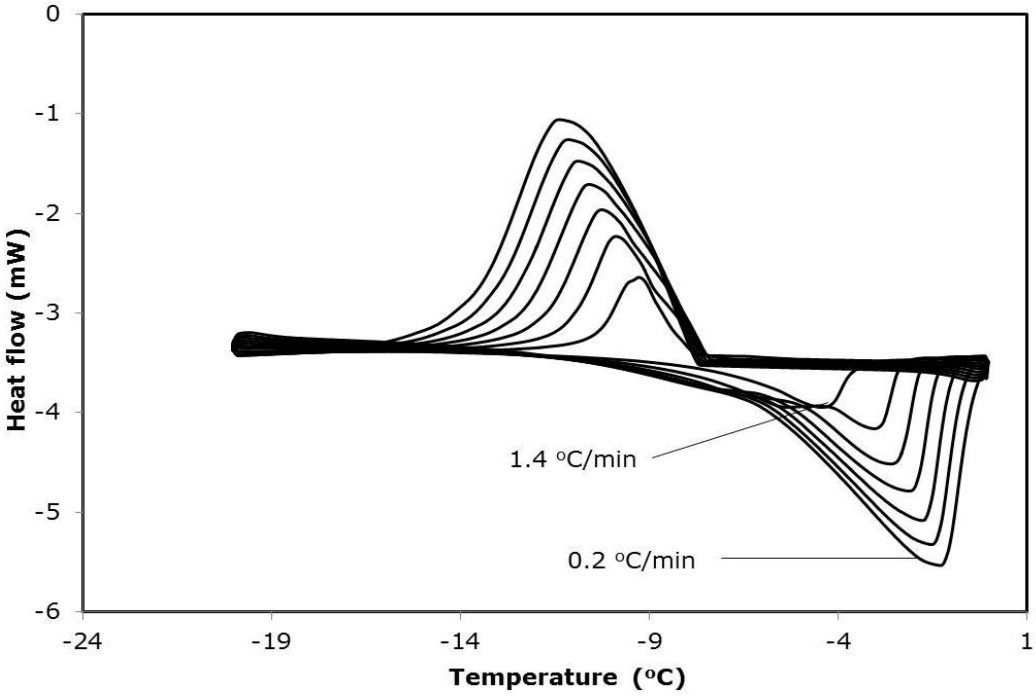

Figure 5. 5: DSC curves at various melting and heating curves for distilled water in S1 sample at ramp rates of 0.2-1.4 ^{0}C/min.

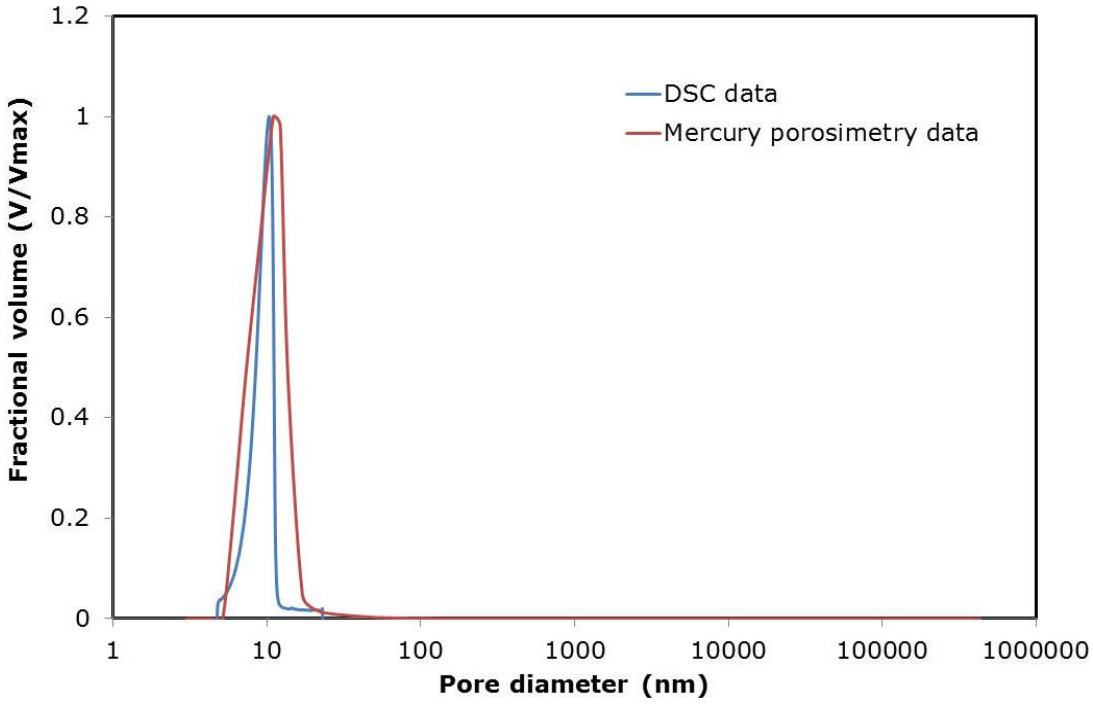

Figure 5. 6: Typical Pore size distributions from DSC experiment (blue) and mercury porosimetry experiment (red) for S1 silica pellet.

Table 5. 1: Material sample results studied using thermoporosimetry

Sample	Probe fluid	Mass of sample (mg)	Enthalpy of melting (J/g)	Onset melting temperature (^{o}C)	Peak melting temperature (^{o}C)
S980A	Water	17.5	49.12	-5.34	-3.82
C10	Water	20	67.32	7.78	-5.2
C30	Water	20	14.89	2.87	-1.5
CPG	Mercury	94.5	0.57	41.15	-38.8

5.4.2. Mercury thermoporometry studies

5.4.2.1. CPG1 samples

The pores of CPG were observed using FL-30 FEG-ESEM microscope under 15kV. All samples were coated with a thin gold layer using polaron SC7640 sputter coater. Fig. 5.7 reveals the morphologies and structure of controlled pore glass (CPG 2400) at different resolution of 500 and 200 nm using scanning electron microscopy. It is evident from the micrographs that the CPG materials possess spherical pores. The mean pore diameters can be determined by image analysis of digital SEM micrograph, using image pro plus image analysis software. For each material, nine micrographs were taken with different magnifications from different regions of three sections were used.

(a)

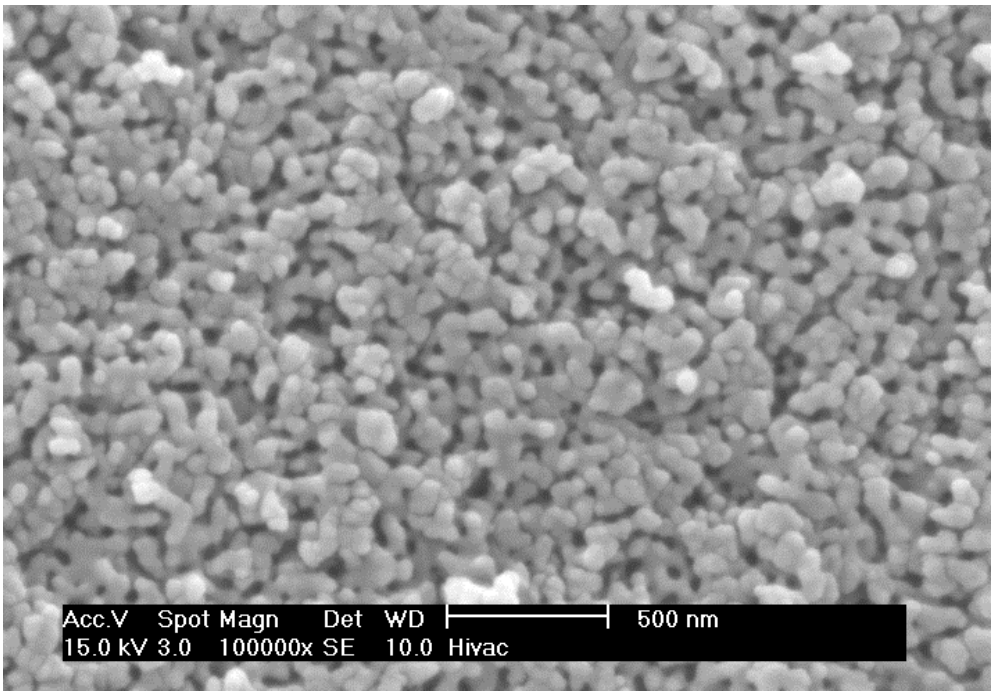

(b)

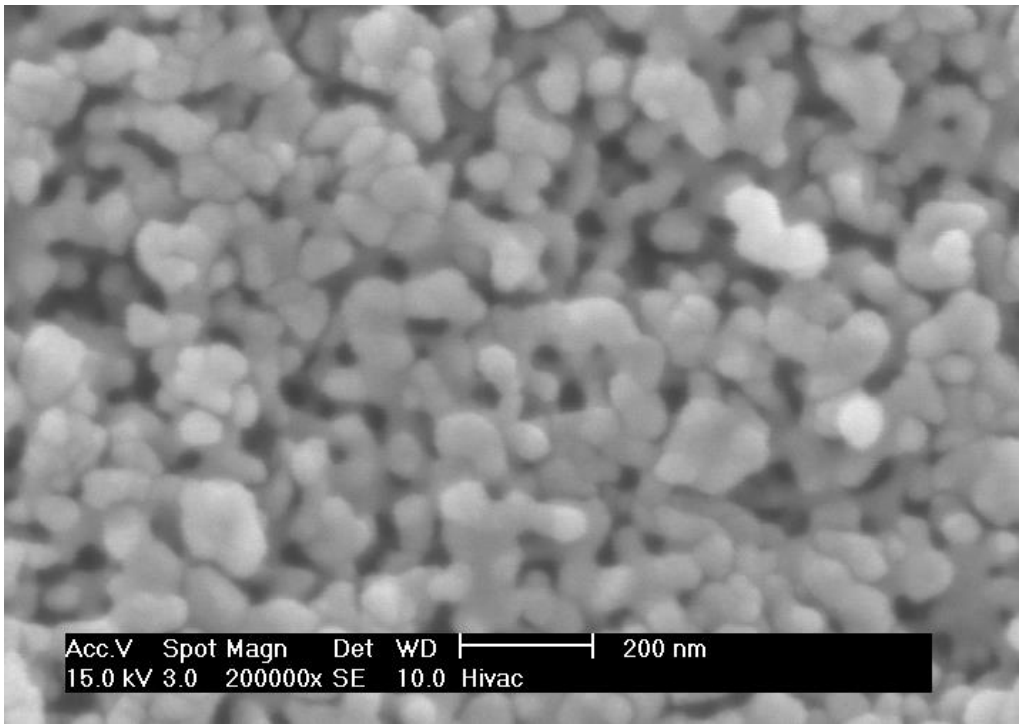

Figure 5. 7: Scanning electron microscopy photographs of nominal CPG 2400 at 500 (a) and 200 nm (b) field of view.

Figure 5.8 shows the mercury intrusion and extrusion curve data for experiments with ultimate pressures of 414 MPa and 48.2 MPa, and equilibration time of 10 s, for samples of CPG1. The equilibration time did not affect the shape of the curves in the range studied. It can be seen that intrusion up to 414 MPa leads to complete pore-filling, since the top of the intrusion curve exhibits a horizontal plateau at high pressure, and the retraction curve retains a similar flat plateau all of the way down to the pressure when the main extrusion step begins. In contrast, the intrusion curve for the experiment up to only 48.2 MPa is a scanning curve, since it stops while the curve is still ascending, and some retraction starts immediately on reversing the direction of the change in pressure. The width of the hysteresis between intrusion and extrusion is narrower for the scanning curve than for the boundary curve. Also, from Fig. 5.8, the very steep mercury intrusion and extrusion experiment from porosimetry curve is consistent with the very narrow pore size distribution. The step up increase and the step decrease is very sharp which is consistent with the narrow pore size distribution as observed in the electron micrograph images.

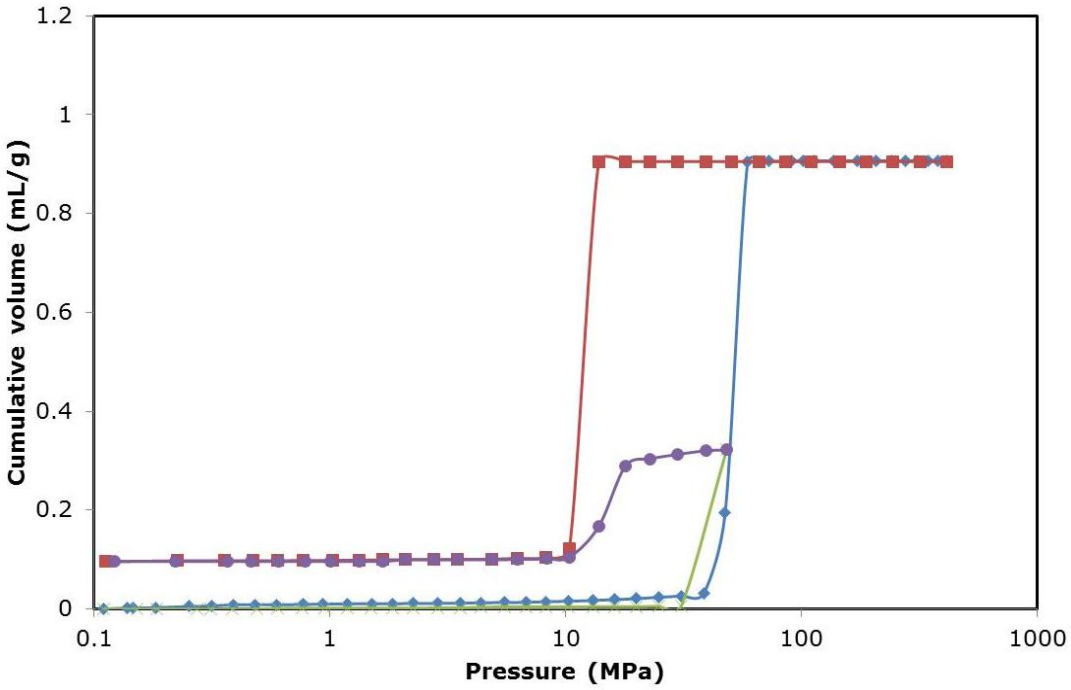

Figure 5. 8: Mercury intrusion and extrusion curves for porosimetry experiments on samples of CPG1 with ultimate pressures of 414 MPa (♦ intrusion, ■ extrusion) and 48.2 MPa (x intrusion, ● extrusion). The lines shown are to guide the eye.

(a)

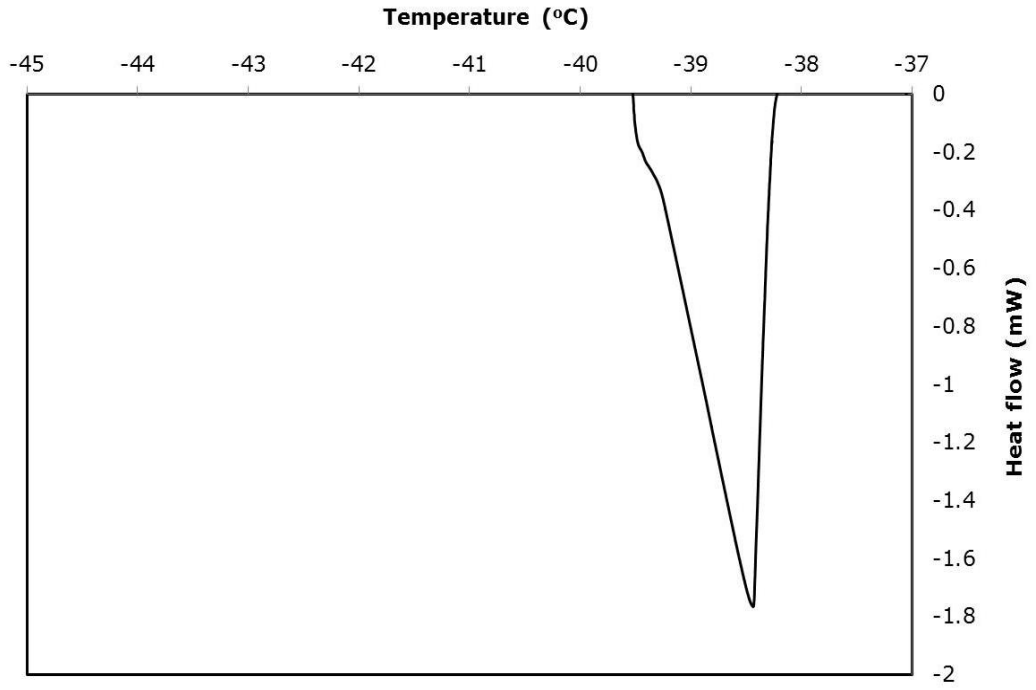

(b)

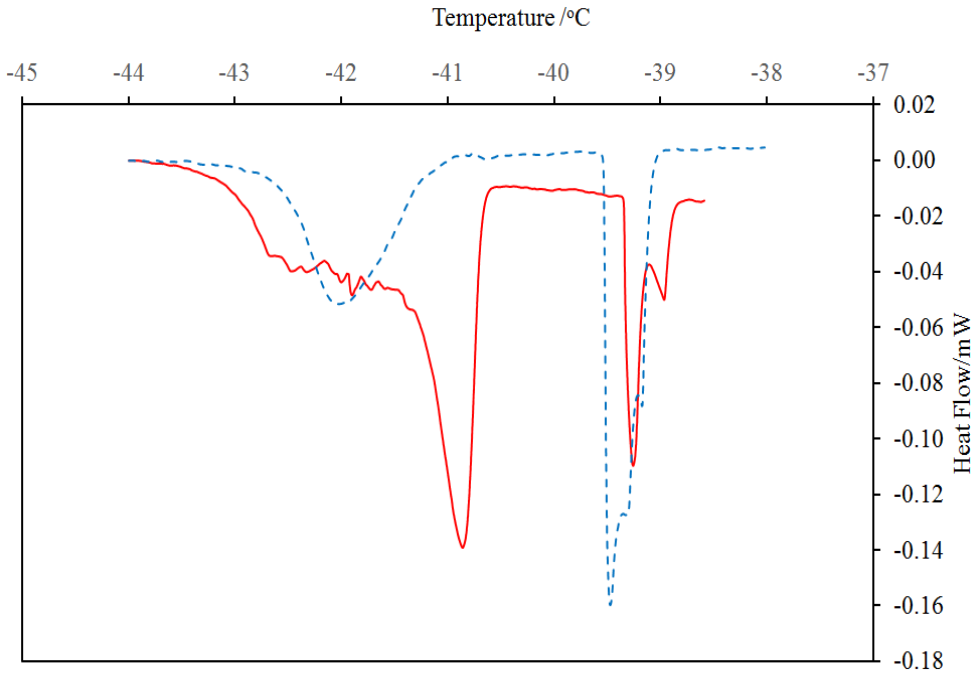

Figure 5. 9: DSC melting curves for (a) macroscopic droplet of bulk mercury, and (b) entrapped mercury following porosimetry experiments on samples of CPG1 with ultimate pressures of 414 MPa (solid line) and 48.2 MPa (dashed line).

Figure 5.9 (a) shows a DSC melting curve for macroscopic blob of bulk mercury. It shows a relatively sharp peak around the known bulk melting temperature for mercury of -38.8 °C. Figure 5.9 (b) shows DSC melting curve for the entrapped mercury left after the porosimetry experiment with ultimate intrusion pressure of 414 MPa. The data shows a sharp peak at the known bulk melting point of mercury (~ -39 °C), and a broader, asymmetric peak with a mode at -40.9 °C and a slight tail to lower temperatures both attributed to mercury entrapped within the sample pores. It can thus be seen that the melting point depression of the pore fluid peak relative to the bulk liquid value is 1.9 °C. The atomic diameter of mercury is ~0.3 nm. If the non-freezing, *t*-layer, at the pore walls, is assumed to be 1 atomic diameter thick for mercury ganglia

(Borisov et al., 1998; Kumzerov et al., 1995), then the Gibbs-Thomson parameter from the CPG data is ~45 K nm (based on diameter). If the observed melting is occurring via a cylindrical sleeve meniscus, this implies the Gibbs-Thomson parameter would be 90 K nm for freezing/melting via a hemispherical meniscus. However, if the observed melting of mercury in the CPG is occurring via a hemispherical meniscus, this implies the Gibbs-Thomson parameter would be 22.5 K nm for melting via a cylindrical sleeve meniscus.

Fig. 5.9 (b) also compares the DSC melting curves for entrapped mercury left in a further sample of CPG1 following a mercury intrusion scanning curve up to 48.2 MPa. Both DSC data sets in Figure 4.9 show a bulk liquid peak at ~38.9 $^{\circ}$C. The presence of shoulders on the main bulk peak may reflect that mercury on the exterior surface of the sample can be confined to cracks and gaps of slightly different sizes/geometries, as well as larger blobs of mercury liquid more like bulk. The variation in the position of the main bulk melting peak suggests the DSC data has an error of ~0.1-0.2 $^{\circ}$C. However, it is noted that the mode of the melting peak assigned to the mercury entrapped in the sample following the porosimetry scanning curve occurs at a temperature of ~ -42.0 to -42.1 $^{\circ}$C, corresponding to a melting point depression of 3-3.1 $^{\circ}$C, which is significantly (i.e. greatly exceeds the experimental error) larger than for the sample following intrusion to 414 MPa. This peak for the scanning curve occurs over the same range of temperatures as the broad shoulder on the peak for the full intrusion experiment (up to 414 MPa).

5.4.2.2. CPG2 sample

Fig. 5.10 shows mercury intrusion and extrusion curve data for an experiment with ultimate pressure of 414 MPa, and equilibration time of 10 s, for sample of CPG2. It can be seen that intrusion up to 414 MPa leads to complete pore-filling. The intrusion curve exhibits a horizontal flat plateau at the highest pressure, and the retraction curve retains a similar flat plateau until the pressure where extrusion curve begins as seen similar to CPG1 in Fig. 5.8. The SEM images for the CPG2 samples are given in Appendix A1.

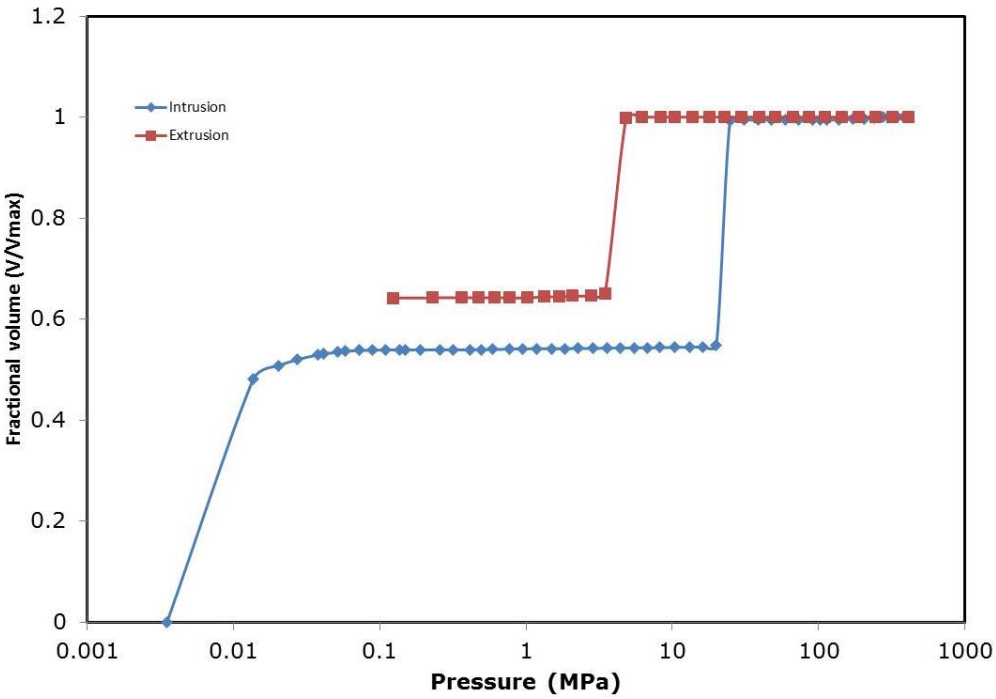

Figure 5. 10: **Mercury intrusion and extrusion curves for porosimetry experiments on samples of CPG2 with ultimate pressures of 414 MPa (♦ intrusion, ■ extrusion. The lines shown are to guide the eye.**

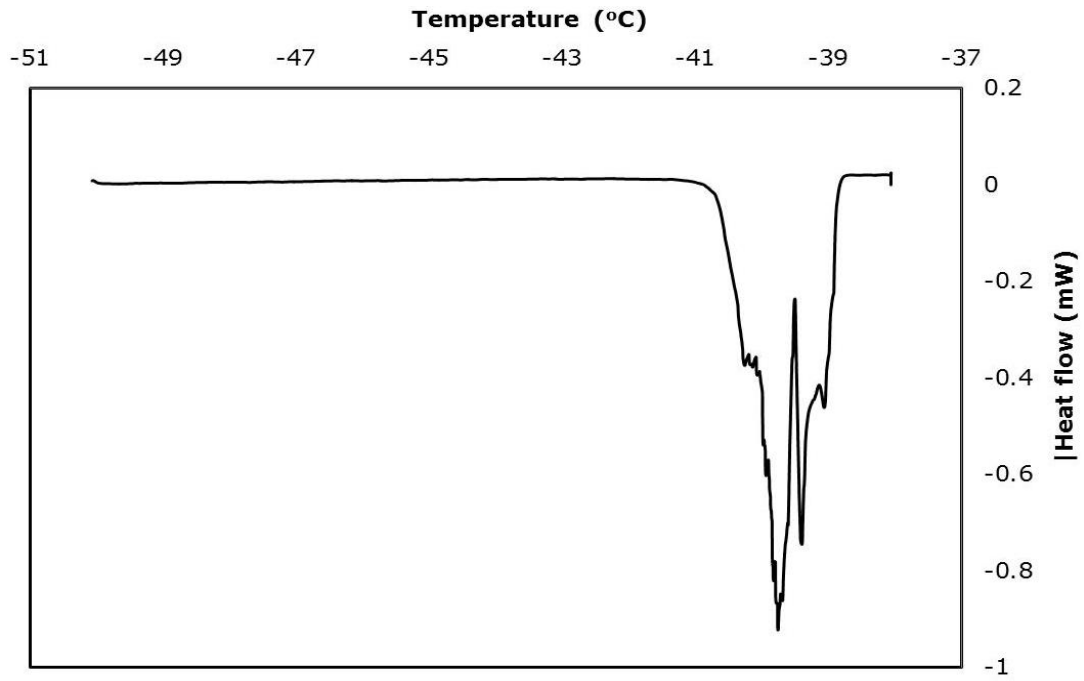

Figure 5. 11: **DSC melting curves for entrapped mercury following porosimetry experiments on samples of CPG2 with ultimate pressures of 414 MPa**

Fig. 5.11 shows the DSC melting curve for the entrapped mercury left after mercury porosimetry experiment with ultimate pressure of 414 MPa. The peak at (~-39 ^{o}C) is the bulk mercury as expected, and the large peak at ~39.4 $^{\circ}$C is probably mercury in gaps between the powder particles of the CPG2 sample. However, the peak from -39.6 to 40.2 is probably the entrapped mercury within the pores of CPG2. The melting point depression was ~0.9 K as would be expected for melting via cylindrical meniscus. The irregular pore shape of the peak for entrapped mercury could be due to more pore size variability or blobs of mercury being a bit smaller than the pore size.

5.4.2.3. S1-silica

Fig. 5.12 shows typical mercury intrusion and extrusion curves for a whole pellet sample of S1, and the mercury intrusion and extrusion curves for a fragmented sample of S1, all analysed using the Kloubek (Kloubek, 1981)

correlations. It is noted that the mercury extrusion curve obtained for the fragmented sample overlays the intrusion curve. Using linear interpolation between pore radius points where necessary, the data for the whole pellet and fragmented pellet sample was adjusted to have the same set pore radius points (Rigby et al., 2008). The incremental changes in mercury volume over each step in pore radius for the whole pellet extrusion curve were subtracted from those for the powder intrusion/extrusion curve to give the difference plot shown in Fig. 5.13. The peak in this plot corresponds to pore radii (via the Kloubek (Kloubek, 1981) correlation) where mercury is apparently getting entrapped. The peak has a baseline range in pore radius from ~5.5-9 nm, with the mode at 7.3 nm.

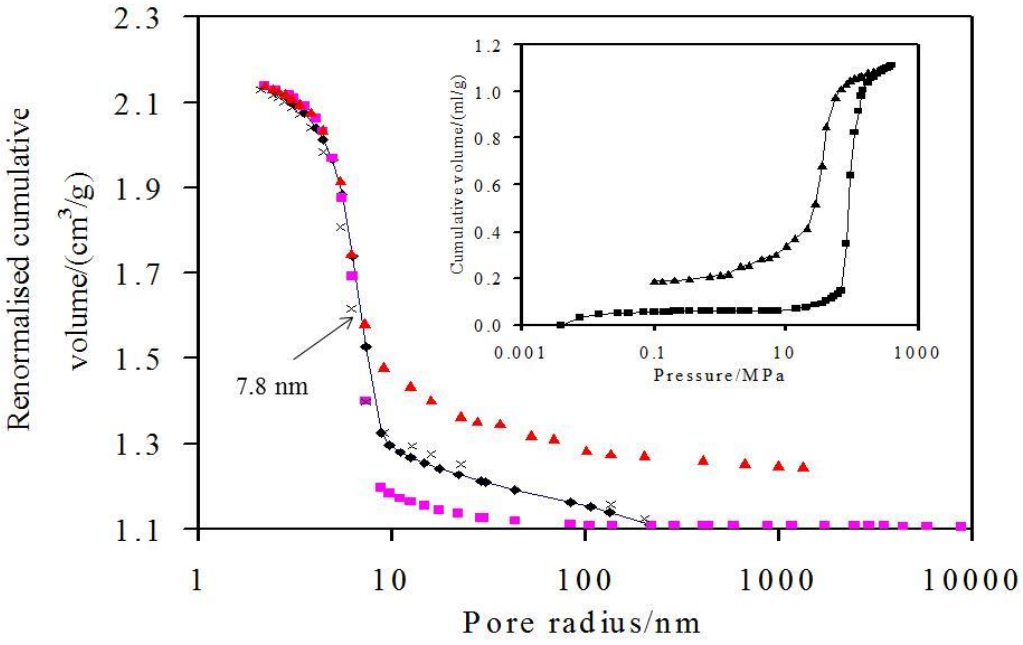

Figure 5. 12: **Mercury porosimetry data for whole (■ intrusion, ▲extrusion) and powdered (■♦ intrusion, ×▲ extrusion) samples from batch S1 analysed using semi-empirical alternatives to the Washburn equation (Rigby et al., 2002). The ultimate intrusion volume for the whole pellet sample has been renormalised to that for the powder sample to facilitate direct comparison of the intra-particle intrusion. The inset shows the raw data for the whole pellet sample (■ intrusion, ▲ extrusion) (Rigby et al., 2008)**

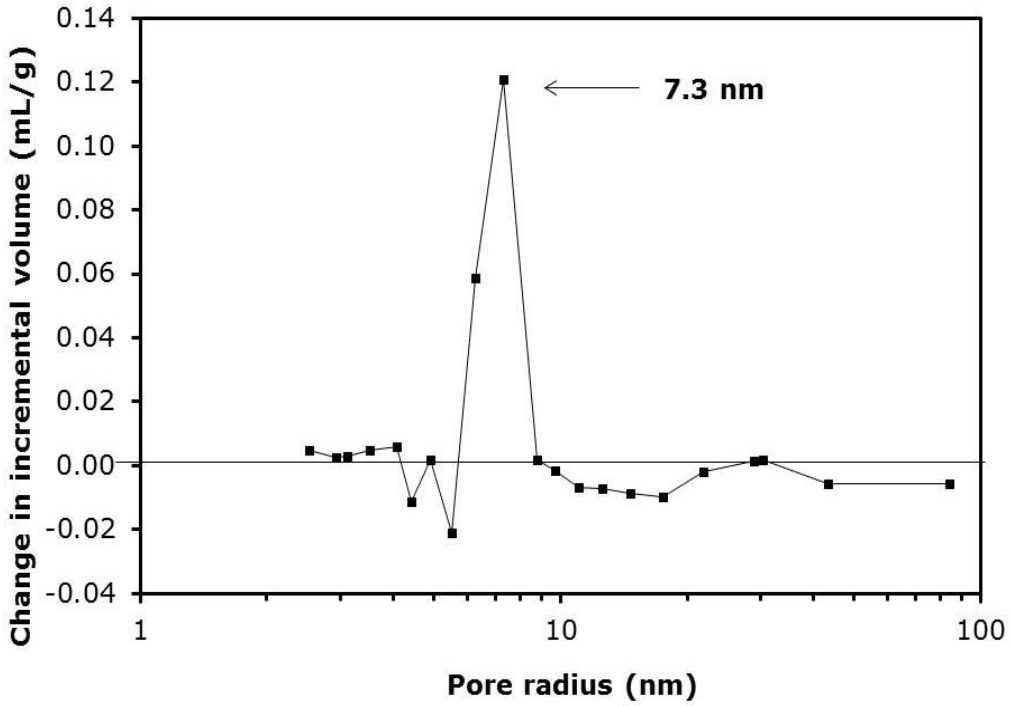

Figure 5. 13: Variation with pore radius of the difference in incremental volumes (using the same set of pore size bins) between the powder intrusion curve and whole pellet extrusion curve shown in Fig. 5.12 (Rigby et al., 2008)

It can be seen from Fig. 5.12 that, for the whole pellet sample, the mercury extrusion curve follows the mercury intrusion curves for the smallest pores up to a particular pore size, where, thereafter, the extrusion curve deviates from the intrusion curves. Hence, analysis of the mercury porosimetry data for S1 using Eq. 3.2 leads to an identification of a special point on the mercury intrusion curve where the extrusion curve deviates from the intrusion. At the point when the intrusion and extrusion curves diverge, this indicates that less mercury extrudes from the sample compared to the amount that was intruded. This means the pore size where the curves diverge is when mercury entrapment begins. In order to test the validity of the assumptions underlying the application of Eq. 3.2, a series of porosimetry scanning curves to different ultimate pressures were performed on samples from batch S1, and the level of mercury entrapment at the end of the scanning curves was determined.

(a)

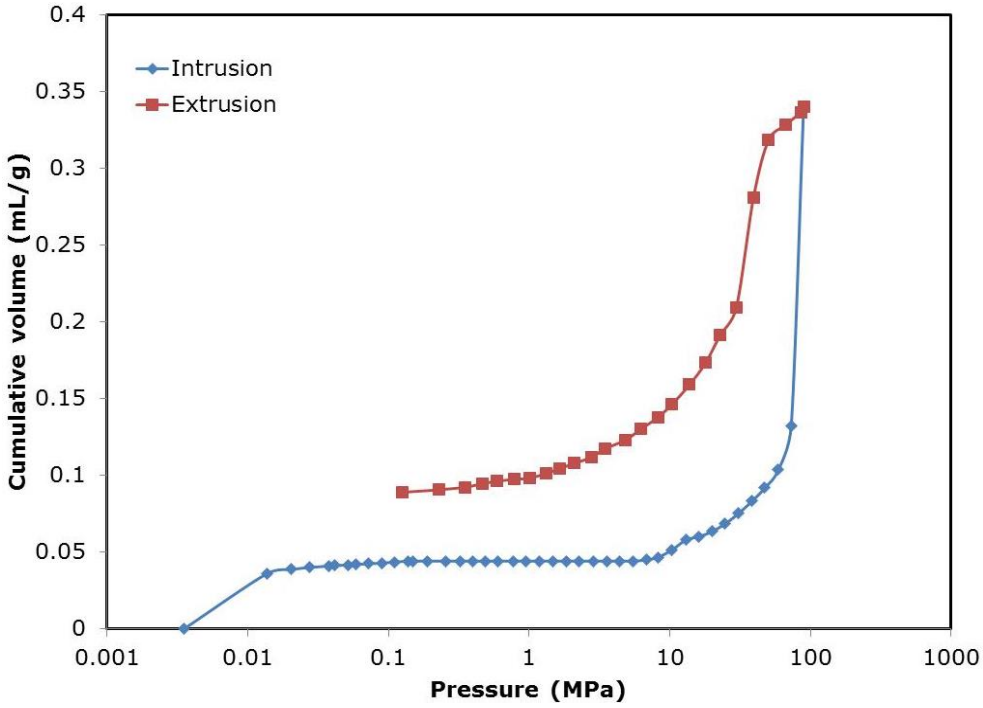
Intrusion
Extrusion
Cumulative volume (mL/g)
0.4
0.35
0.3
0.25
0.2
0.15
0.1
0.05
0
0.001
0.01
0.1
1
10
100
1000
Pressure (MPa)

(b)

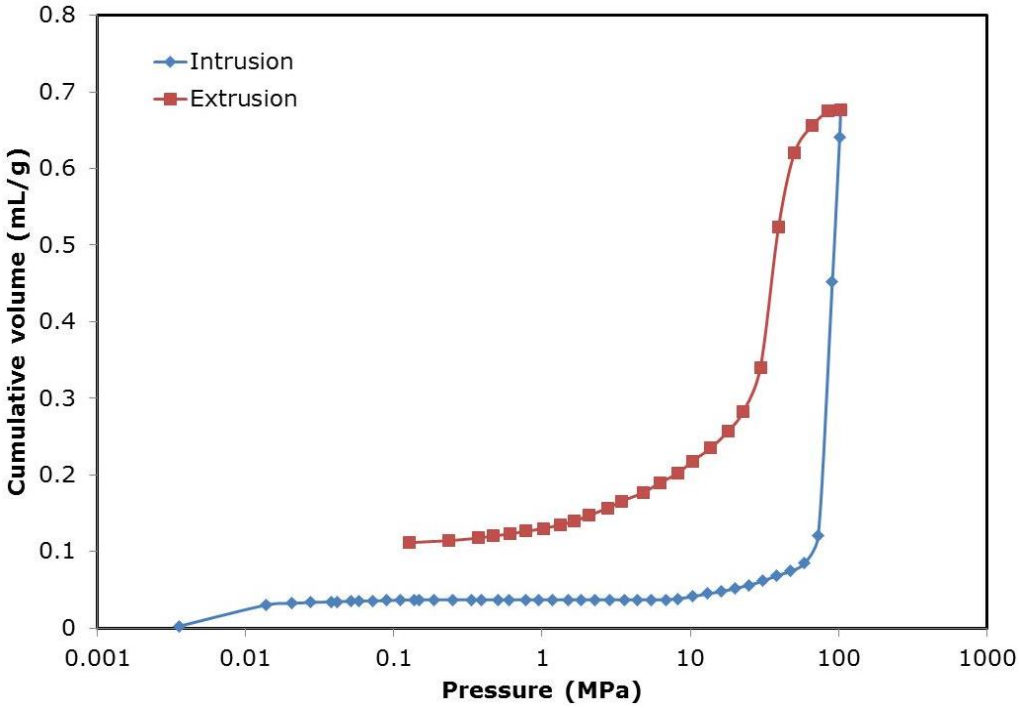
Intrusion
Extrusion
Cumulative volume (mL/g)
0.8
0.7
0.6
0.5
0.4
0.3
0.2
0.1
0
0.001
0.01
0.1
1
10
100
1000
Pressure (MPa)

(c)

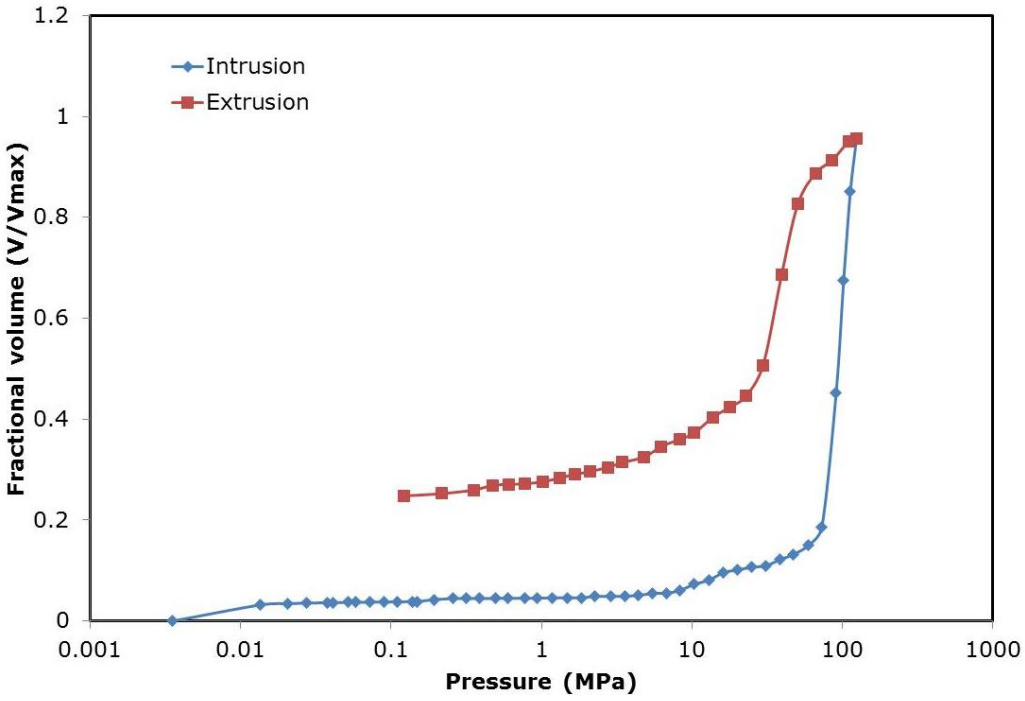

Figure 5. 14: Scanning curves at different pressures of (a) 89 MPa, (b) 103 MPa, (c) 124 MPa. The lines are to guide the eye.

Fig. 5.14 shows some examples of the scanning curves for S1 sample that were used to derive the variation in the amount of entrapped mercury at different pressures from where the mercury entrapment begins as shown in Fig. 5.12. The entrapment begins at a pore radius of ~7.8 nm, which corresponds to a pressure of 103 MPa. Separate 89 MPa and 124 MPa were conducted above and below the pressure where entrapment begins.

Fig. 5.15 shows a plot of the variation in the amount of mercury entrapment following a scanning curve against the pore radius (via the Kloubek correlation) corresponding to the ultimate pressure at the end of the scanning curve. Each data point shown is the mean of a minimum of three samples from the same batch. It can be seen that the entrapment arises predominantly over

the particular pore size range ~5-7.3 nm. This range also corresponds to the range covered by the bulk of the asymmetric peak in Fig. 5.13.

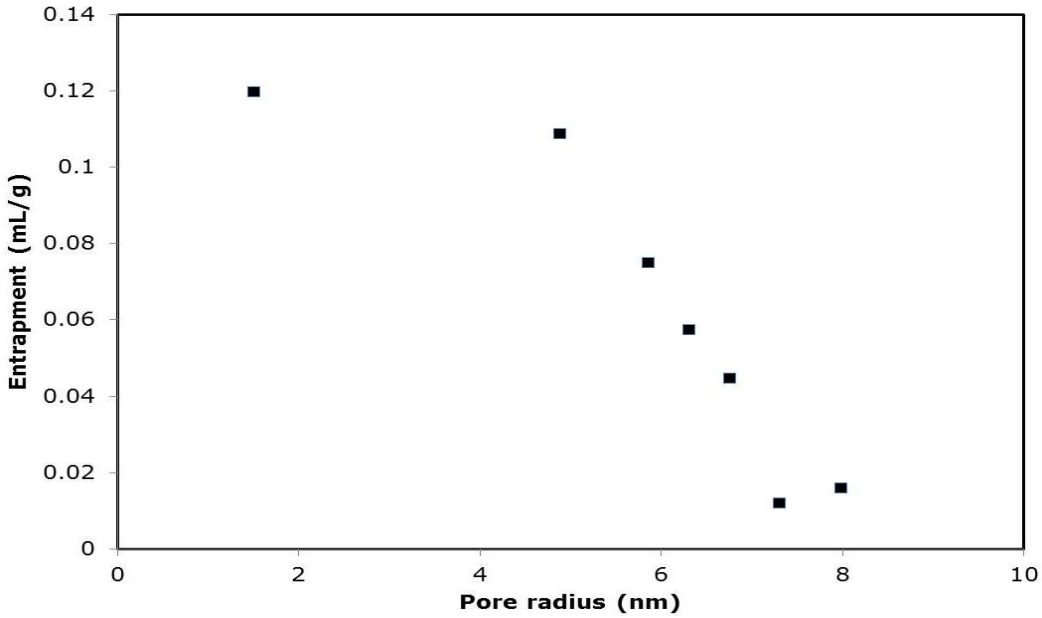

Figure 5. 15: A plot of the variation in the amount of mercury entrapment following a scanning curve against the pore radius via the Kloubek (1981) correlation corresponding to the ultimate pressure at the end of the scanning curve for samples taken from batch S1 (Fig. 5.13). Each data point is the sample mean result from at least three samples from batch S1.

Fig. 5.16 shows a typical example of a DSC melting curve for a sample of S1 following intrusion in mercury porosimetry up to 414 MPa. The batch sample mean value of the melting point depression for the peak in the melting curve for the entrapped mercury was 5.8±0.2 $^{\circ}$C. The sample mean value for the melting point depression of the tail of this peak was 8 $^{\circ}$C. The uncertainty in this value is estimated to be ±1 $^{\circ}$C. Using a Gibbs-Thomson parameter of 90 K nm, thereby assuming freezing/melting via a hemispherical meniscus, the pore radii corresponding to the modal peak, and low temperature tail tip, are 7.8±0.3 nm, and 6±1 nm, respectively.

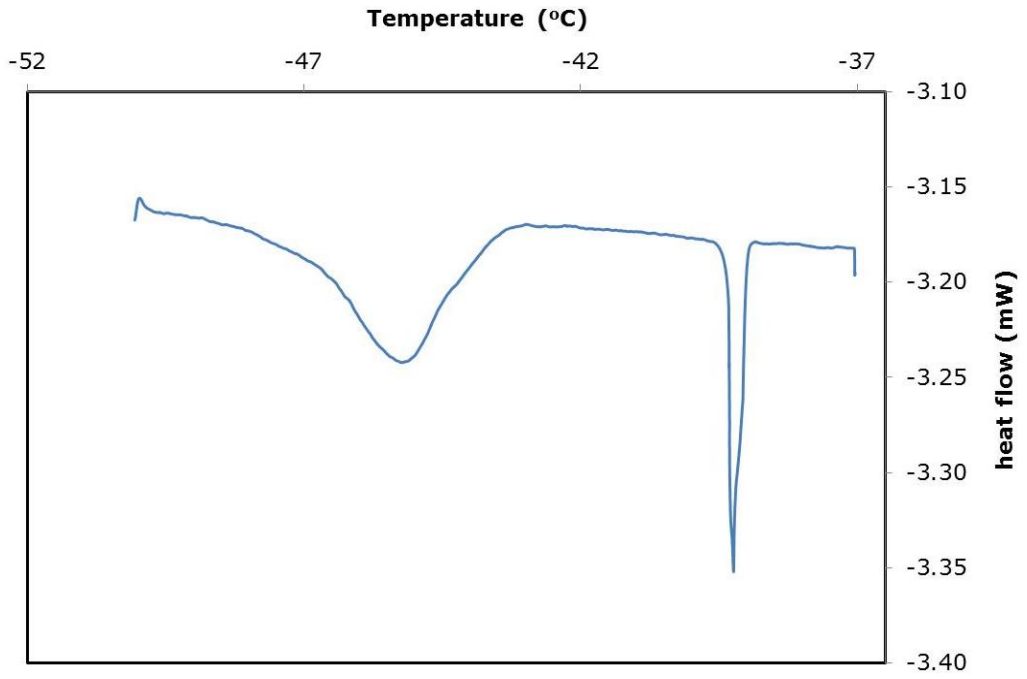

Figure 5. 16: **A typical example of a DSC melting curve for the mercury entrapped within a sample of S1 following intrusion in mercury porosimetry up to 414 MPa.**

5.4.2.4. G2 sol-gel silica

Fig. 5.17 shows the mercury porosimetry data for a typical sample from G2 analysed using equation 3.2 in chapter 3 of the methodology section and the parameters for silica given in chapter 3, Table 3.1. It can be seen that equation 3.2 brings the main retraction step into superposition on top of the main intrusion step. The point of deviation between the intrusion and extrusion curves, when entrapment starts, occurs in the pore radius range ~13-16 nm.

Fig. 5.18 shows a plot similar to Fig. 5.15 of the variation of the amount of mercury entrapment following scanning curve against the pore radius (via the Kloubek correlation) corresponding to the maximum pressure at the end of the scanning curve. It can be seen that entrapment arises over the particular pore size range ~ 8.5-14 nm.

Fig. 5.19 shows the DSC melting curve obtained for the mercury entrapped following the porosimetry experiment that gave rise to the results shown in Fig. 5.17. The data show a sharp peak from the melting of the bulk mercury droplet, added as a standard, at a temperature similar to that in Fig. 5.9 (a), and a broader peak at low temperature corresponding to the melting of the entrapped mercury within the pellets. From Fig. 5.19, it can be seen that the entrapped mercury peaks at a temperature ~-41.4 $^{\circ}$C. Using a Gibbs-Thomson parameter of 90 K nm, thereby assuming freezing/melting via a hemispherical meniscus, the pore radii corresponding to the temperature range of the low temperature tail tip was determined as around ~22.5 nm. This size range is close to that where entrapment begins in the porosimetry data analysed using Eq. 3.2. The wide distribution in the first peak in Fig. 5.19 have shown that the same difference in blob sizes (e.g. 1nm) is reflected in a bigger difference in melting point as absolute blob sizes decreases because melting point is inversely related to pore size.

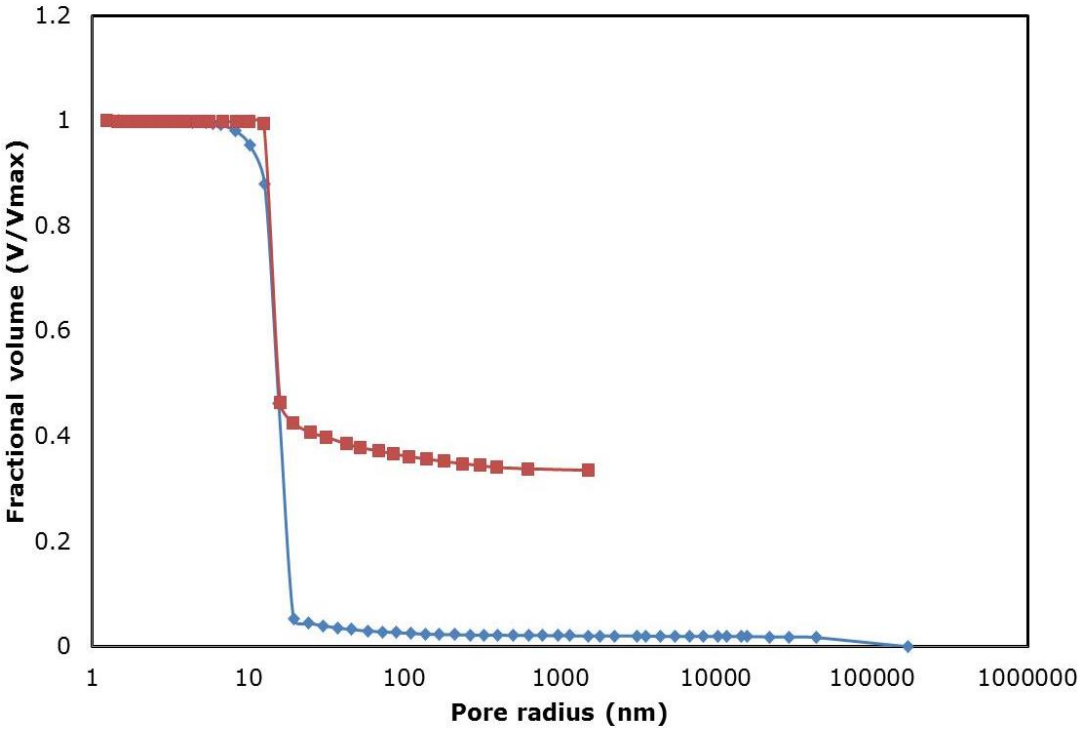

Figure 5. 17: **Mercury porosimetry intrusion (♦) and extrusion (■) data for a typical sample from G2 analysed using equation 1 and the parameters for silica with surface fractal dimension of 2.3 given in Table 3.2.**

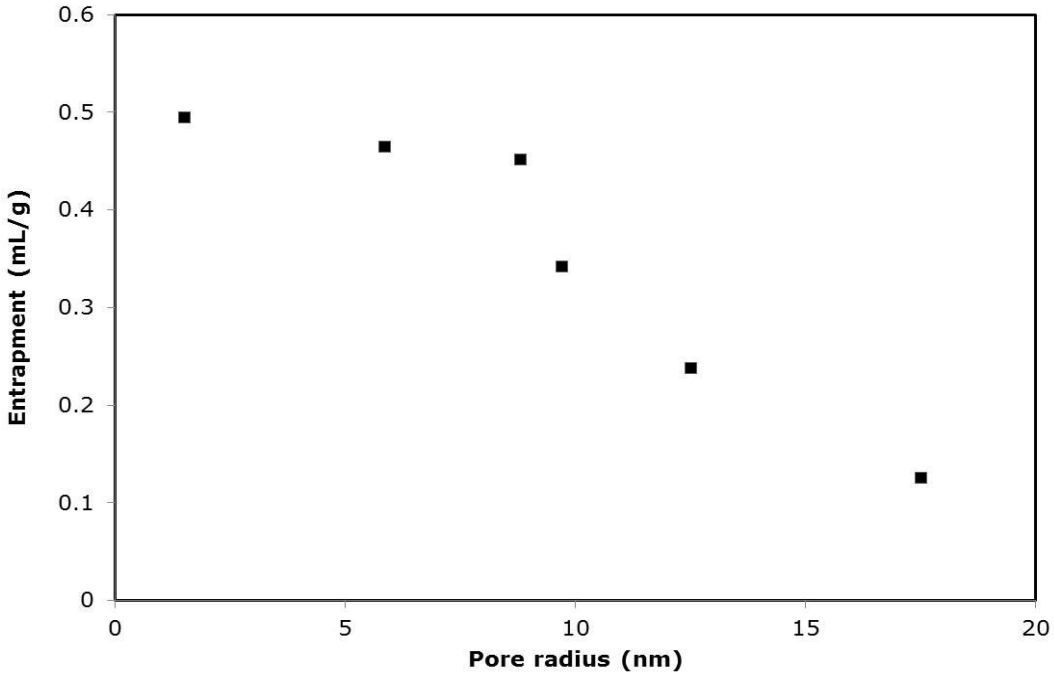

Figure 5. 18: A plot of the variation in the amount of mercury entrapment following a scanning curve against the pore radius via the Kloubek (1981) correlation corresponding to the ultimate pressure at the end of the scanning curve for samples taken from batch G2

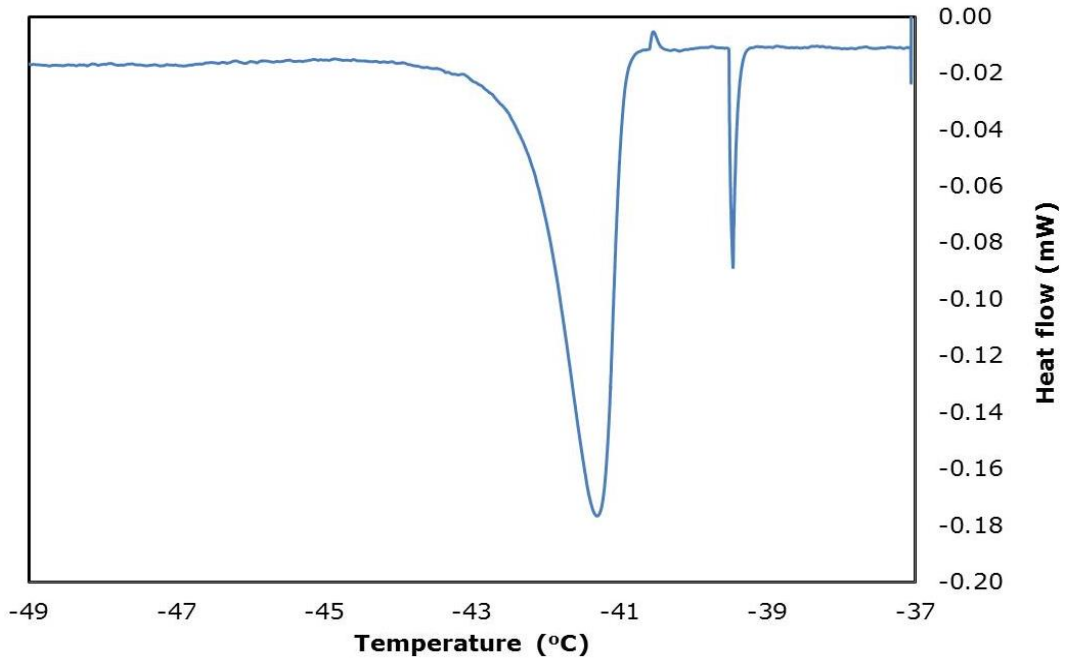

Figure 5. 19: **DSC melting curve obtained for the mercury entrapped following the porosimetry experiment on the sample from batch G2 that gave rise to the results shown in Fig. 5.17.**

5.4.2.5. S2 sol-gel silica

Fig. 5.20 shows mercury porosimetry data for an experiment on a sample from batch S2, with an ultimate intrusion pressure of 414 MPa, which has been analysed using a variant of the Kloubek correlations appropriate to a sample with different surface roughness to CPG1, S1 and G2 shown in Table 3.1. Previous SAXS studies (Rigby and Chigada, 2009) have shown that S2 has a different surface roughness to S1, G2 and the CPGs used to derive the original Kloubek (Kloubek, 1981) correlation. From Figure 5.20 it can be seen that the onset of mercury entrapment occurs over the range of pore sizes ~20.7-30 nm.

Fig. 5.21 shows the DSC data for a sample from batch S2 following mercury intrusion to 414 MPa. The melting of bulk mercury was observed at -39.2 °C, the modal peak in the melting curve for the mercury in the pores occurs at -

40.8 ˚C, and the low temperature tail of this peak starts at around -43.2 ˚C. The melting point depression of the peak in the melting curve for the entrapped mercury was ~1.6 ˚C. Using a Gibbs-Thomson parameter of 90 K nm (based on diameter), thereby, assuming freezing/melting via a hemispherical meniscus, the radius of the smallest pores containing entrapped mercury is 28.1 nm. This is similar to the value of pore size at the onset of mercury entrapment in the mercury porosimetry data.

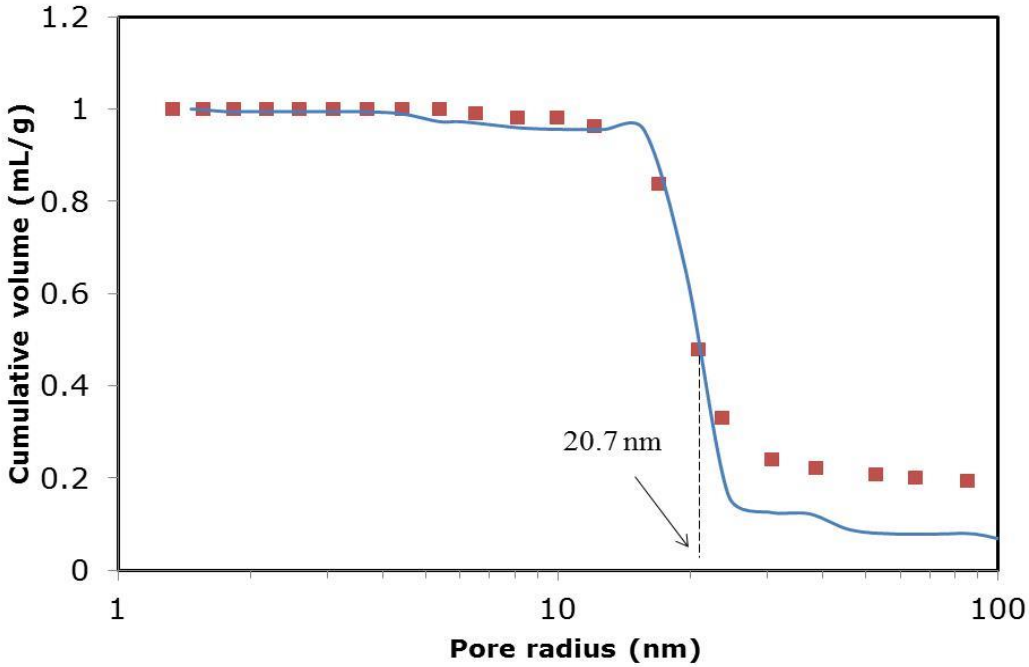

Figure 5. 20: **Mercury porosimetry intrusion (line) and extrusion (■) data from an experiment on a sample from batch S2 with ultimate intrusion pressure of 414 MPa, analysed using the variant of the Kloubek correlations appropriate to a sample with high surface fractal dimension.**

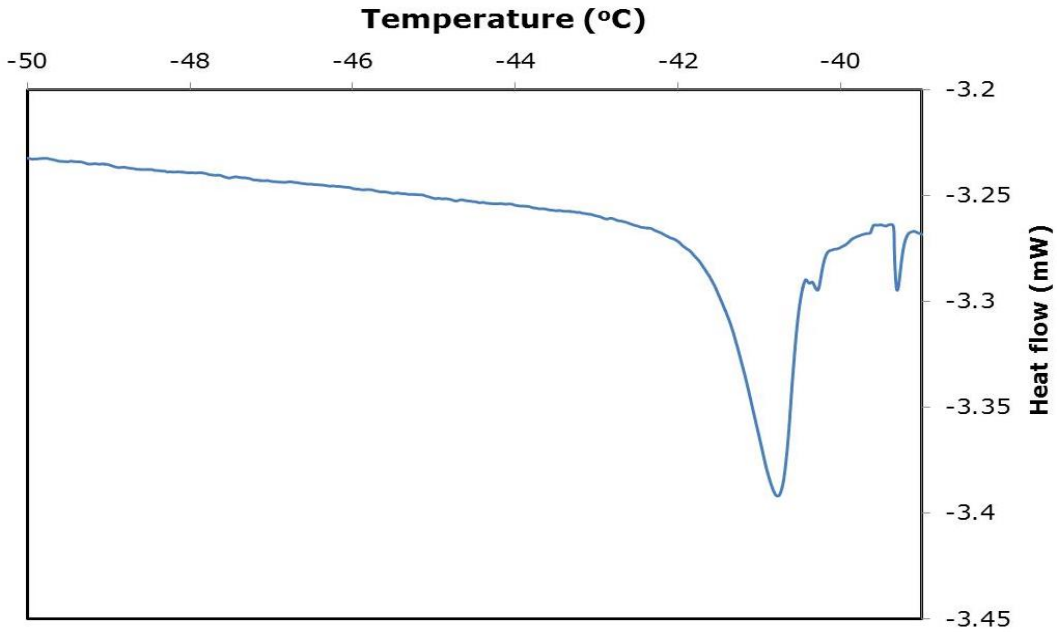

Figure 5. 21: **DSC melting curve data for the entrapped mercury in a sample from batch S2 following mercury intrusion to 414 MPa.**

5.4.2.6. G1 sol-gel silica

Fig. 5.22 shows a mercury porosimetry data for an experiment on a sample from batch G1, with an ultimate pressure of 414 MPa. The data has been analysed using the Kloubek correlation (Eq. 3.2). It can be seen that that the Kloubek correlation does brings the main retraction step into superimposition on top of the main intrusion step. The point of deviation between the intrusion and extrusion curves, when entrapment starts, occurs in the pore radius range ~3-4 nm. Fig. 5.23 shows a plot of the variation of the amount of mercury entrapment following scanning curve against the pore radius (via the Kloubek correlation) corresponding to the maximum pressure at the end of the scanning curve. It can be seen that entrapment arises over the particular pore size range ~ 3-4.5 nm. The DSC melting curve for the mercury entrapped following porosimetry experiment was attempted several times but the amount of entrapped mercury is too small to detect the mercury signal.

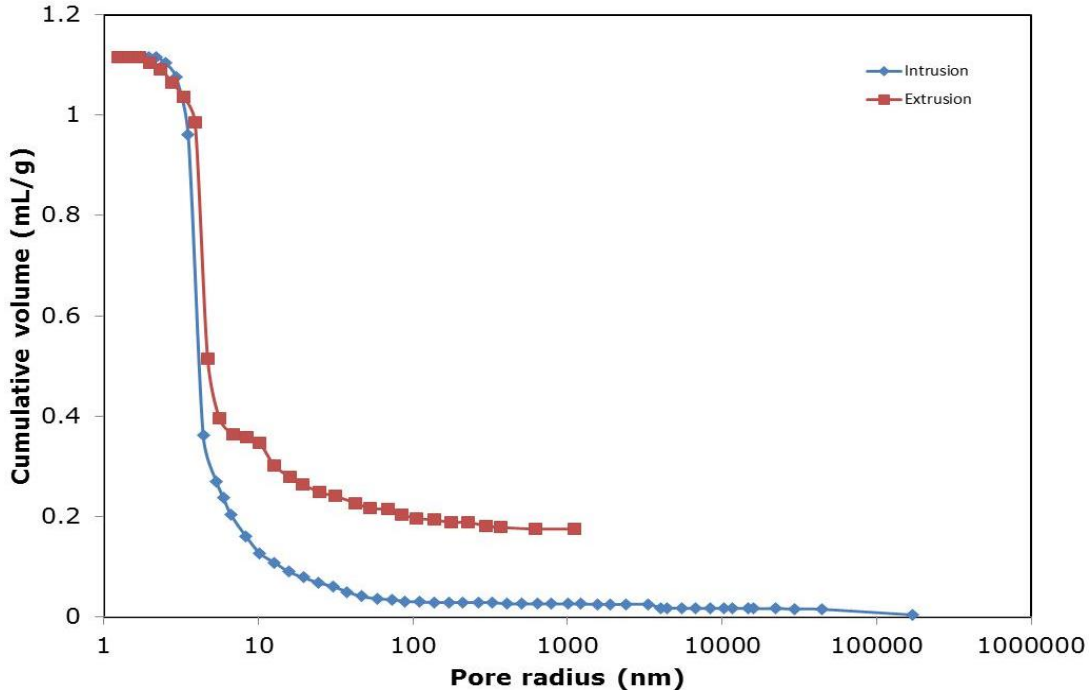

Figure 5. 22: Mercury porosimetry intrusion (♦) and extrusion (■) data for a typical sample from G1 with ultimate pressure of 414 MPa, analysed using equation 3.2

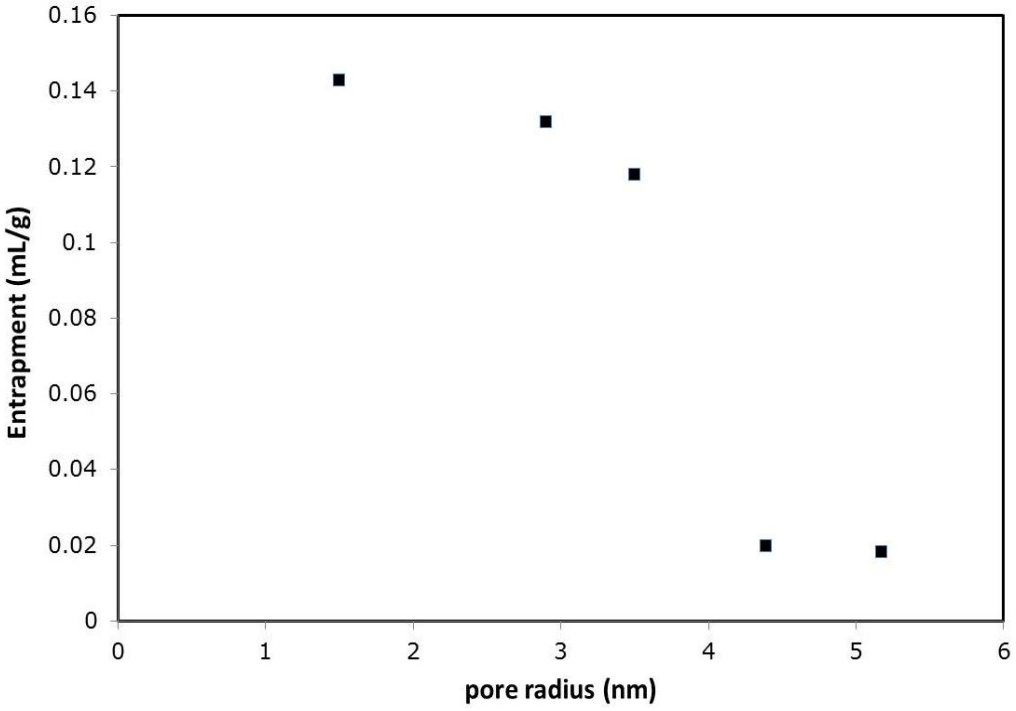

Figure 5. 23: A plot of the variation in the amount of mercury entrapment following a scanning curve against the pore radius via the Kloubek (1981) correlation corresponding to the ultimate pressure at the end of the scanning curve for samples taken from batch G1

Table 5. 2: The pore size at the onset of mercury entrapment obtained by analysing the mercury porosimetry data using Kloubek correlations, and the pore sizes corresponding to the onset point using Gibbs Thompson

Sample	Pore radius size where mercury entrapment starts (nm)	Calculated pore radius from Gibbs Thompson (nm)	
		Meniscus geometry	
		Cylindrical (45 K nm)	Hemispherical (90 K nm)
S1	5.3-8.3	3.9	**7.8**
S2	20.7- 30.6	14.1	**28.1**
G2	12.7-16.0	11.3	22.5

5.5. Discussion

Thermoporosimetry is a calorimetric method that determines pore sizes from melting or freezing point depression of liquid confined in a pore as earlier stated. To transform the DSC profile data into a size distribution, the temperature record is converted into an equivalent length scale (e.g. pore radius) and the heat flow output from the melting or solidification into a differential pore volume. The accuracy of pore size distribution and properties of mesoporous samples have been examined using CPG, S1, G1 and G2 materials. The pore size distributions of the three samples evaluated by thermoporosimetry using water as the probe fluid coincided well with the results of the mercury porosimetry method as expected. However, the mechanism of melting and solidification of the materials studied can be affected by a number of factors, which can dramatically change the structure and introduce large errors in the experimental results. A factor that can bring these changes is the compression effect. This effect can occur during the

sealing of the pan when the sample is placed in, which can slightly compress the sample and consequently change its structure. Previous researchers have shown that mesoporous materials are very sensitive to compression (Iza et al., 2000). However this effect was not recognised from all the samples studied in this thesis.

The flat plateau at the top of the high-pressure mercury intrusion of CPG1 suggests complete pore filling is achieved. Hence, it is likely that the mercury ganglia would have coalesced throughout the pore network, such that cylindrical-sleeve shaped menisci would have been formed between the mercury thread and the pore walls. In contrast, the immediate decreases in intruded volume on reversal of the direction of pressure change for the scanning curve experiment suggests that free mercury menisci existed at this point. Hence, it seems likely that these free menisci would have been similar to hemispherical in form, since experiments in cylindrical pore models bored through glass suggest intrusion-retraction is piston-like (Hitchcock et al., 2014). Therefore it seems likely that the high ultimate pressure intrusion would have created cylindrical sleeve menisci, and the scanning curve would have generated hemispherical menisci.

The lower melting temperature in the DSC data for the mercury entrapped following the scanning curve porosimetry experiment (up to an ultimate pressure of 48.2 MPa) on CPG1 is such that the melting point depression is about twice that of the modal melting peak for the mercury entrapped following the full intrusion experiment. Since the scanning curve is likely to give rise to more hemispherical menisci than the full intrusion it seems likely that the melting peak position for the scanning curve experiment corresponds

to that for a hemispherical meniscus, and the melting curve peak position for the full intrusion experiment corresponds to that for a cylindrical sleeve meniscus. Hence, overall, the CPG1 DSC data suggest that the Gibbs-Thomson parameter is ~45 K nm (for diameter) melting is occurring via a cylindrical sleeve meniscus, and 90 K nm for freezing/melting via a hemispherical meniscus.

It has been found that, once the appropriate values of the Gibbs-Thomson parameter have been determined for melting according to hemispherical and cylindrical-sleeve menisci in CPG1, those same values can be used to show that the sizes of the pores containing entrapped mercury, in three different sol-gel silicas, obtained using thermoporosimetry agrees well with the equivalent sizes determined from corresponding mercury porosimetry data and Eq. 3.2. Hence, these data suggest that thermoporosimetry can validate pore sizes obtained from mercury porosimetry and Eq. 3.2.

When the raw mercury porosimetry data is analysed using the Kloubek (Kloubek, 1981) correlations, and superposition of intrusion and retraction curves is obtained over part of the pore size range, it leads to the identification of a previously undistinguished point on the intrusion curve where deviation from the extrusion curve occurs. This point could be just an artefact of the analysis process but it leads to a prediction about which ultimate pressures of intrusion will lead to any entrapment, or the end of entrapment. This prediction has been tested using scanning curve experiments. It has been found that mercury entrapment in pellets from batch S1 happens for scanning curves with ultimate pressures around that of the point of deviation, and entrapment is virtually non-existent for scanning curve ultimate pressures corresponding to

pore sizes above the point of deviation for S1 where intrusion and extrusion curves overlap. Hence, the scanning curve experiments confirm that the point of deviation has physical significance, and is not just an artefact of the data analysis. Therefore, these data validate the use of Eq. 3.2 to analyse mercury porosimetry data.

5.6. Conclusions

The melting and freezing behaviour of pore in confined porous silica gel and silica glasses has been studied. It has been shown that mercury porosimetry scanning curves can be used to establish the correct correspondence between the appropriate Gibbs-Thomson parameter, and the nature of the meniscus geometry in melting, for thermoporosimetry measurements using entrapped mercury as the probe fluid. Mercury thermoporosimetry has been used to validate the pore sizes obtained from mercury porosimetry data using the Kloubek correlations.

Therefore, thermoporosimetry, using mercury entrapped following mercury porosimetry as the probe fluid, has been shown to provide independent validation of the pore structural information obtained from porosimetry. Hence, this new type of combined thermoporosimetry enables independent adjudication of the discrepancy between pore sizes derived from porosimetry and other techniques, such as gas sorption. Novel use of thermoporosimetry is thus proposed as a straightforward and essential supplement to porosimetry experiments to ensure greater accuracy of pore size distributions and improved structural characterisation.

5.7. Reference

BORISOV, B. F., CHARNAYA, E. V., PLOTNIKOV, P. G., HOFFMANN, W. D., MICHEL, D., KUMZEROV, Y. A., TIEN, C. & WUR, C. S. 1998. Solidification and melting of mercury in a porous glass as studied by NMR and acoustic techniques. *Physical Review B,* 58**,** 5329-5335.

HITCHCOCK, I., LUNEL, M., BAKALIS, S., FLETCHER, R. S., HOLT, E. M. & RIGBY, S. P. 2014. Improving sensitivity and accuracy of pore structural characterisation using scanning curves in integrated gas sorption and mercury porosimetry experiments. *Journal of Colloid and Interface Science,* 417**,** 88-99.

IZA, M., WOERLY, S., DANUMAH, C., KALIAGUINE, S. & BOUSMINA, M. 2000. Determination of pore size distribution for mesoporous materials and polymeric gels by means of DSC measurements: thermoporometry. *Polymer,* 41**,** 5885-5893.

KLOUBEK, J. 1981. Hysteresis in porosimetry. *Powder Technology,* 29**,** 63-73.

KUMZEROV, Y. A., NABEREZNOV, A. A., VAKHRUSHEV, S. B. & SAVENKO, B. N. 1995. Freezing and melting of mercury in porous glass. *Physical Review B,* 52**,** 4772-4774.

PERRY, R. H., GREEN, D. W. & MALONEY, J. O. 1999. *Perry's Chemical Engineers' Handbook,* McGraw-Hill.

RIGBY, S., CHIGADA, P., PERKINS, E., WATT-SMITH, M., LOWE, J. & EDLER, K. 2008. Fundamental studies of gas sorption within mesopores situated amidst an inter-connected, irregular network. *Adsorption,* 14**,** 289-307.

RIGBY, S. P. & CHIGADA, P. I. 2009. MF-DFT and Experimental Investigations of the Origins of Hysteresis in Mercury Porosimetry of Silica Materials. *Langmuir,* 26**,** 241-248.

RIGBY, S. P. & EDLER, K. J. 2002. The Influence of Mercury Contact Angle, Surface Tension, and Retraction Mechanism on the Interpretation of Mercury Porosimetry Data. *Journal of Colloid and Interface Science,* 250**,** 175-190.

Chapter 6: Porous Media Characterisation Using NMR

6.1. Introduction

Chapter 6 will introduce the reader to the characterisation methods using the nuclear magnetic resonance (NMR) technique. A Liquid-liquid exchange (LLE) process, within two different mesoporous sol gel silica spheres S1 and G2 (available commercially), has been investigated using NMR relaxometry in order to study the mechanism of the displacing hydrocarbon with water. Mercury ganglia sizes obtained in chapter 5, from mercury thermoporosimetry data will be compared with the ganglia sizes of cyclohexane obtained from the NMR relaxometry experiment. In addition, the effect of temperature on the saturation level and the diffusion properties of pentane in mesoporous (G1) sample were also investigated using the pulsed field gradient NMR. A description of the NMR method, parameters used in the experiment were all given earlier in section 3.5 of the thesis. Experimental results as well as the particular considerations used in performing each of the experiments are given below in this chapter of the report. The aim of the experiments has been given already in section 3.5.7.

6.2. Methodology and sample preparation

6.2.1. Partially saturated sample prepared by adsorption of cyclohexane (case I)

In this study, silica samples, S1, G1 and G2 were prepared by drying the pellets under vacuum at 150 $^{\circ}$C for 15 hours to drive off moisture and other adsorbed contaminant content from the sample leaving the morphology of the

sample unchanged. The sample was then allowed to reach room temperature. The experiment was done in a closed system in order to establish the equilibrium. The closed system containing two separate reservoirs, one for deionised water and the other for cyclohexane (adsorbate) as illustrated in Fig. 6.1. The pellets of G2 (adsorbent) at time t=0, were suspended with the aid of gauze above separate reservoirs as shown in Figure 6.1. The setup was then sealed using para-film to avoid any invasion of extraneous fluid into the container. The set up was then clamped down and immersed in an oil bath maintained at 25 $^{\circ}$C. The pellets were first suspended above cyclohexane alone for 72hrs to allow full saturation. This process of filling was based on the action of capillary forces, in surface tension, which pulled cyclohexane into the pores. A separate reservoir containing water (250ml) was then introduced into the container to start the displacement process. Prior to the NMR experiments, the sample was transferred from the container to a 5mm NMR tube. The NMR tube contained cyclohexane at the bottom of the tube and the pellets were supported with the aid of glass rod to avoid direct contact with the sample. Water wet tissue was also used at the top of the NMR tube as shown in Fig. 6.1. This is to ensure that the sample experienced the same atmosphere as in the original container.

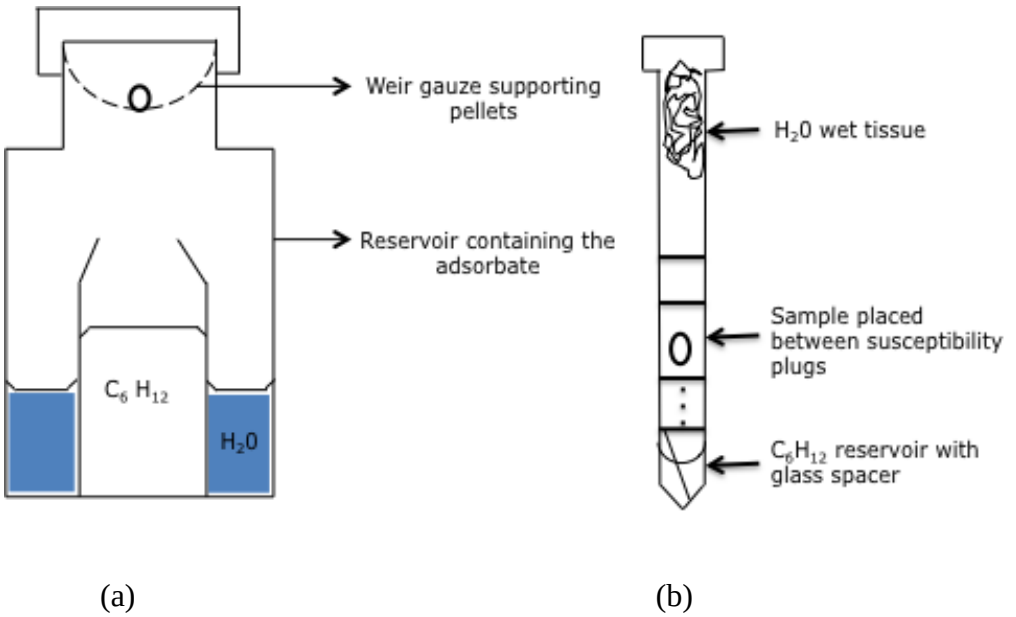

(a) (b)

Figure 6. 1: (a) Schematic representations of the closed adsorption system of C_6H_{12}, H_2O and sample. (b) 5cm NMR tube with silica beads and wet tissue

6.2.2. Transverse relaxation T2, experiments

Two different commercially available sol-gel silica spheres S1 and G2 were used for the spontaneous cyclohexane expulsion experiment. The samples were placed in an oil bath at 25 $^{\circ}$C. To start the experiment, a water reservoir was added to sample container. During the spontaneous water imbibition, the beads were taken out of the oil bath at different selected times and placed in an NMR tube, which is then placed again in the NMR spectrometer to measure T_2 relaxation times. The length of time for each imbibition was 24 hours for G2 sample. Before each measurement, a wet tissue containing water was inserted at the top of the NMR tube, and a cyclohexane reservoir at the bottom to maintain saturated atmosphere in both the fluids. As expulsion proceeded, T_2 relaxation times were measured at different water saturations, using the NMR CPMG sequence. All relaxation time measurements were conducted with at least 16 scans.

The Carr-Purcell-Meiboom-Gill (CPMG) sequence was used to generate the magnetisation decay and measure the transverse relaxation time (T_2), as earlier mentioned in section 3.5.3. This sequence eliminates dephasing effects, which are produced by local variations in the magnetic field and therefore measures the true T_2 of the sample. Hence, the signal decay is due to interactions with neighbouring spins and surfaces. The CPMG echo train comprises of a 90° pulse, which is then followed by a train of 180° pulses (see Fig 3.19). The CMPG sequence takes only a few seconds, which makes it practical to run. The experimental sequence for the LLE experiments is summarised in Fig 6.3.

6.2.3. Fully saturated sample prepared by immersion into a 5ml pentane reservoir (case II)

In this study, the molecular diffusion of n-pentane within pellets in a closed sample tube has been measured. A dried sample, pellets of G1 from the oven were allowed to cool down before they were transferred into a container containing liquid pentane at 25 $^{\circ}$C. This is done in order to get them fully saturated. After 25-30 minutes, the pentane soaked pellets were then put into an NMR tube with the aid of tweezers. A small piece of soaked tissue was inserted into the cap of the NMR tube and then the tube closed. The wet tissue in the cap was necessary in order to prevent unwanted evaporation during the course of the experiments. The sample tube was set up by introducing pentane into the NMR tube with a pipette to form a reservoir of ~1cm height. A doty susceptibility plug (~1 cm in height), with the aid of a small glass rod, was used to support the pellet above the pentane reservoir. Three fully saturated pellets from the vial were transferred into the NMR tube as illustrated in Fig. 6.2(a). This was done in order to ensure there is no contact between the

reservoir inside the tube and the saturated pellets. Fig. 6.2(b) shows G1 samples saturated fully with *n*-pentane and without the excess fluid at the bottom of the NMR tube. Each experiment was conducted at a series of one dimensional acquisition with the length of the applied field gradient, δ, the diffusion time, Δ, and the gyromagnetic ration, γ, generally maintained at constant values of 0.001s, 0.025s and 4.258 Hz/G.

6.2.4. Pulsed field gradient experiments

The sample under investigation is a sol-gel silica sphere denoted as G1. The sample has been prepared in two distinct different conditions. The first sample was fully saturated and prepared in an NMR tube with excess *n*-pentane reservoir at the bottom (Fig. 6.2 (a)). This is to ensure that the liquid under study should always completely fill the porous materials in the whole temperature range probed in the experiments by capillary condensed phase. The second sample was saturated with *n*-pentane without excess n-pentane at the bottom of the NMR tube (Fig.6.2 (b)). In this case, only at the lowest temperature, were the material samples completely filled with the probe fluid. The diffusion experiment was started at a vapour pressure close to the saturated vapour pressure of n-pentane at T=250 K. Signal attenuation was used in PFG NMR to measure the diffusion coefficient of *n*-pentane imbibed within the silica spheres at different temperatures, from 250 K to 315 K (just above the boiling point of n-pentane). All PFG experiments were first started at a temperature of 25 $^{\circ}$C and the acquisition parameters used are shown in Table 6.1. The diffusivities measured are the intra-particle diffusivities. The data obtained were analysed using TOPSPIN 3.1 software to determine the

variation in T_2 as the LLE continued and also the diffusivity of n-pentane at different temperatures.

(a)

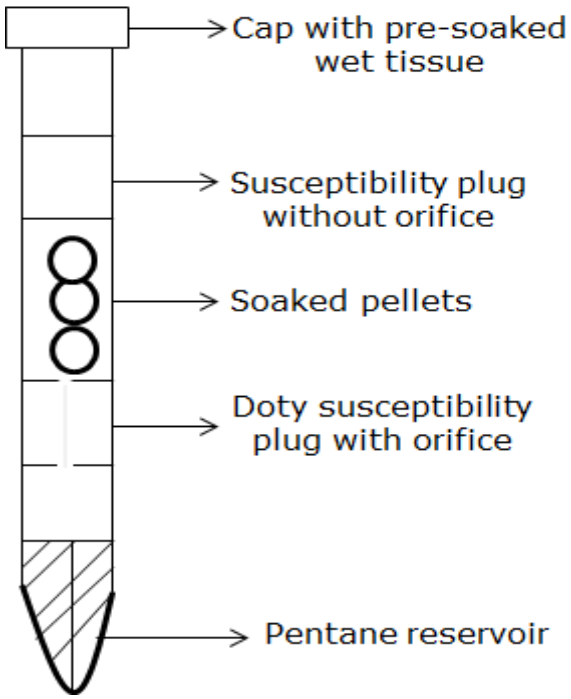

(b)

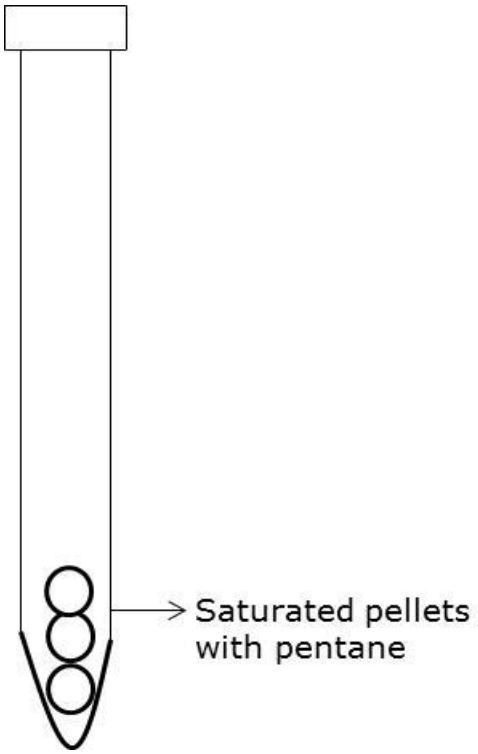

Figure 6. 2: Samples saturated with excess fluid at the bottom of A 5mm NMR tube with susceptibility plug (a), saturated sample without excess fluid (b).

6.3. Sample analysis and experimental consideration

All NMR relaxometry and diffusion experiments were performed using a Bruker Ultra-shield plus 400 NMR spectrometer, with a Bruker tuneable multinuclear BBO (broadband) probe, equipped with Z-gradient coils. The magnet had static field strength of 9.4 T, yielding a proton resonant frequency of 400.07 MHz for ^{1}H nuclei, and a computer controlled the data acquisition. Proton intensities were also obtained before and after each set of relaxation and diffusion experiments using a simple spin echo sequence. The operating temperature inside the NMR machine was maintained at 25 ± 0.5°C, similar to adsorption conditions for the relaxation experiments. This minimized the effect of evaporation during the course of the experiment. However, the temperature

was changed for the PFG experiments using pentane as the probe fluid. All experiments were conducted twice and similar sets of results were obtained. Thence only one set of results will be discussed here. The second set of results will be made available in Appendix C.

Table 6. 1: Experimental acquisition parameters used for NMR PFG experiments.

Parameters	Units	Acquisition
Gradient strength, g	G cm^{-1}	2.41 to 45.74
Diffusion time, Δ	s	0.025
Gyromagnetic ratio, γ	Hz/G	4.258
Length of applied field gradient, δ	s	0.001

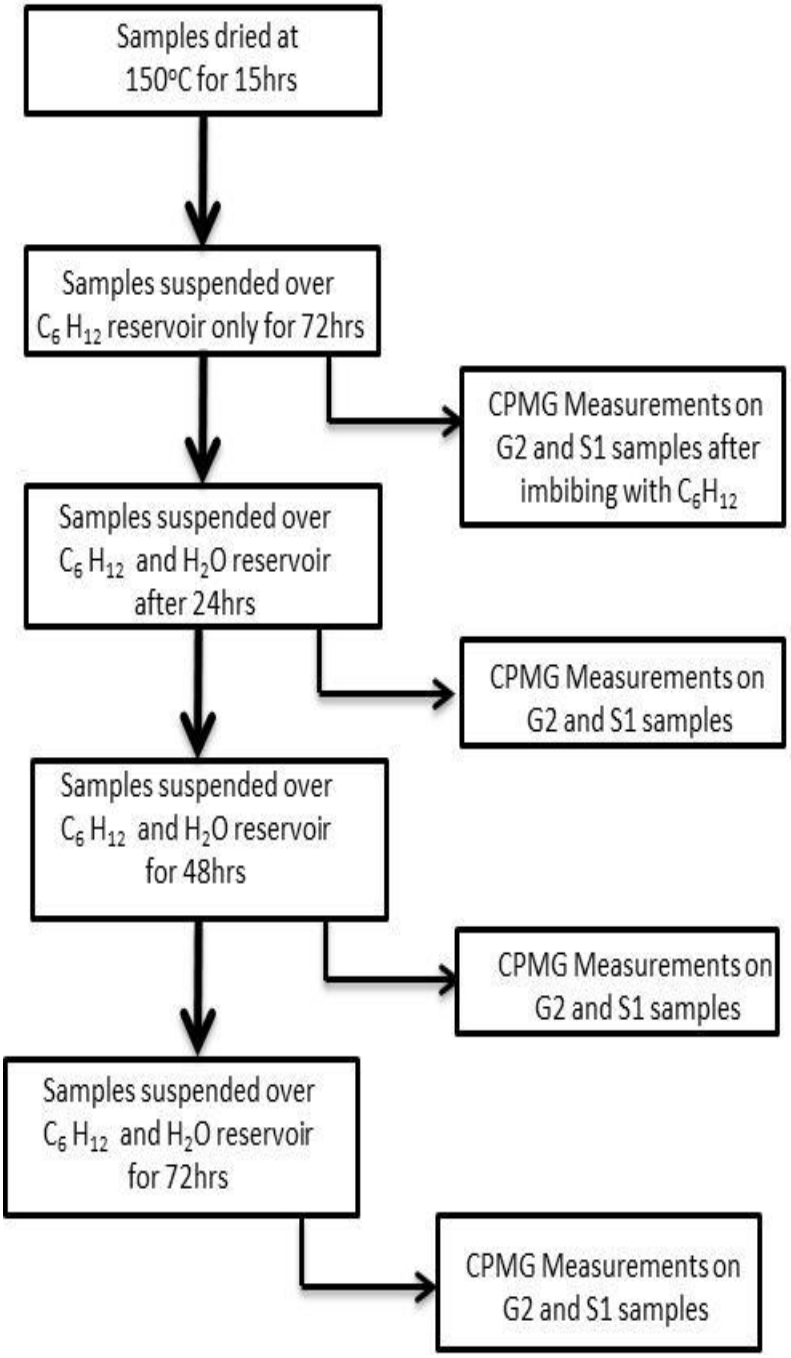

Figure 6. 3: Summary of the experimental sequence for G2 and S1 samples for LLE experiment.

6.4. Results

6.4.1. Relaxation experiment for G2 silica sample

Fig. 6.4 shows a typical set of results for the variation in signal intensity for water and cyclohexane, over time during the LLE experiment on a sol-gel silica sample, G2. It can be seen that at the start of the experiment, the sample was fully saturated with cyclohexane at t = 0, however as time passes the cyclohexane content drops drastically and then decreases gradually until it plateaus out. This indicates that water has displaced most of the cyclohexane content within the sample material by ~96 hrs. The cyclohexane content at this time after ~96hrs is 32%, this is similarly to the amount of mercury entrapped during mercury porosimetry experiment at 50s equilibration time. (See Fig. 6.6)

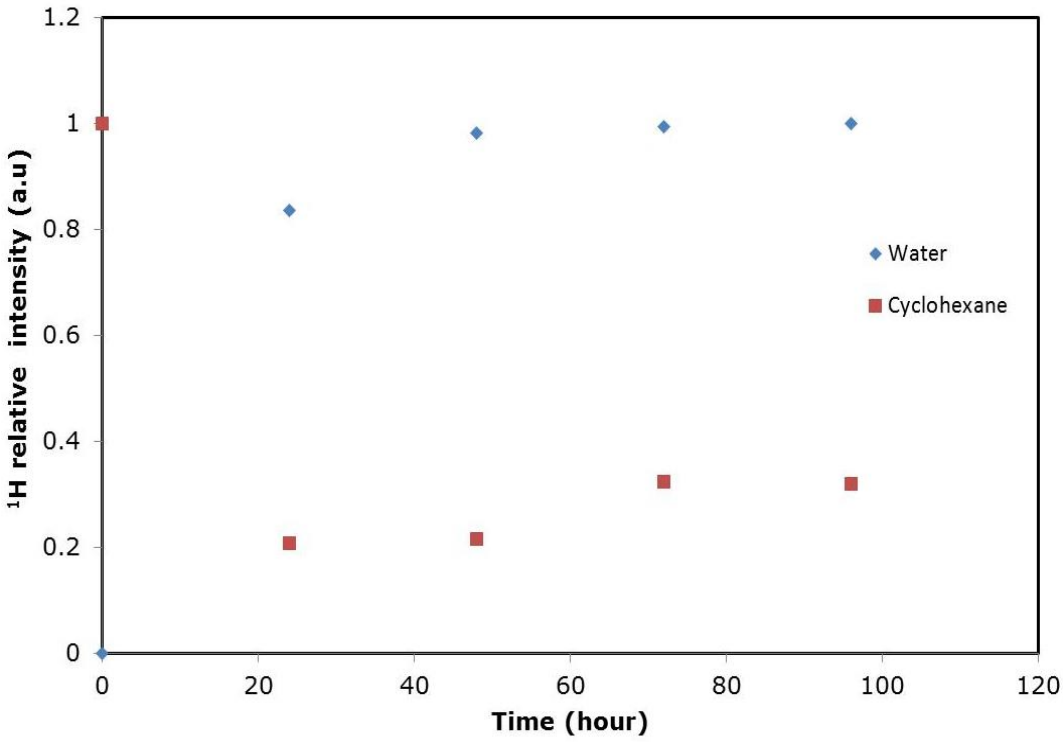

Figure 6. 4: Variation of fractional proton intensities for water and cyclohexane for G2 silica sample against experimental time.

It is independently known from mercury porosimetry and thermoporosimetry techniques that all pores in this material are ~30 nm in size. When fully filled with cyclohexane, the T_2 relaxation time would be characteristic of the pore size. And since the T_2 relaxation time is proportional to the pore size (Eq. 3.27), one can estimate the size of entrapped cyclohexane ganglia. It can be seen from Fig. 6.5 that entrapped cyclohexane phase has lesser relaxation times. This is likely to mean that the entrapped cyclohexane ganglia are likely to be surrounded by water that wets the silica surface. Also, Fig. 6.5 shows the variation of average T_2 value for both water and cyclohexane during the same experiment. It can be seen that the T_2 for cyclohexane rapidly decreases up to ~24hrs and thereafter it remains constant up to ~96hrs. Whereas, the water T_2 increases up to ~72hrs and then stays constant until ~96hrs, during which the cyclohexane T_2 is approximately constant.

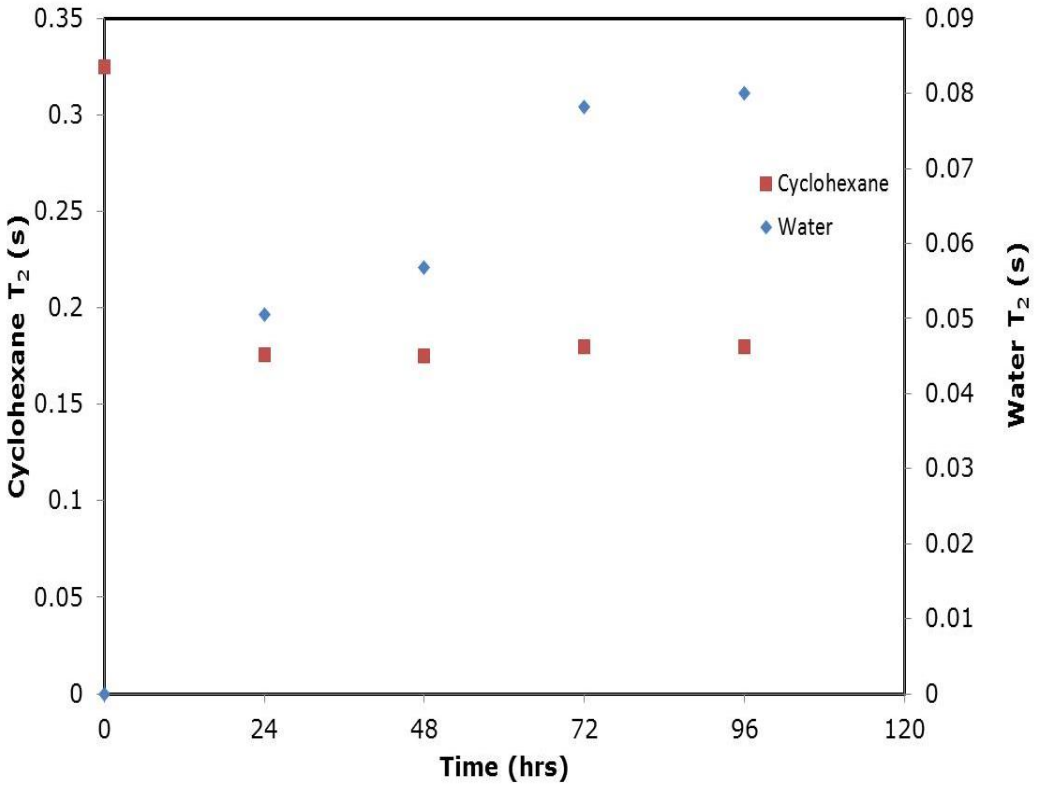

Figure 6. 5: Variation of average T_2 for cyclohexane and water with time during LLE experiment for G2 silica sample.

Fig. 6.6 shows a typical cumulative pore volume data for G2 silica sample obtained using mercury porosimetry with equilibration time of 50 seconds. This work has been reported earlier in chapter 4 of this thesis. It can be seen from the extrusion curve that the entrapment level of mercury is ~34%.

The diffusion log attenuation plot for cyclohexane phase was characterised by straight line as shown in Fig. 6.7. Slope of straight-line fits yield a diffusion coefficient. The straight line indicates a single diffusional component present.

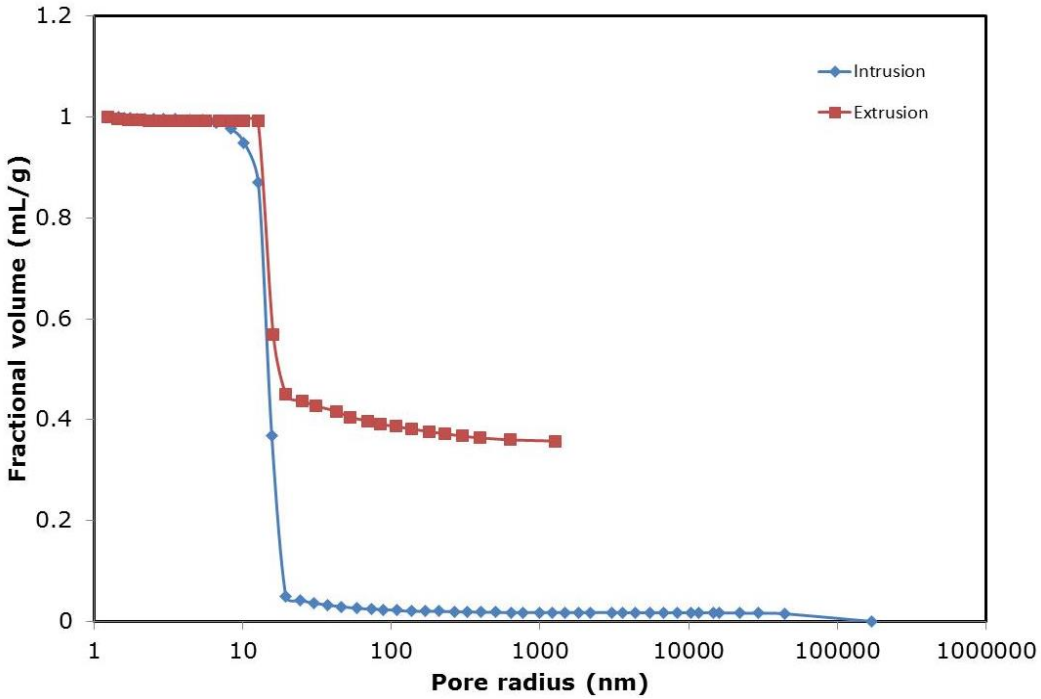

Figure 6. 6: Mercury porosimetry data analysed using kloubek correlations for G2 sample at 50s equilibration time.

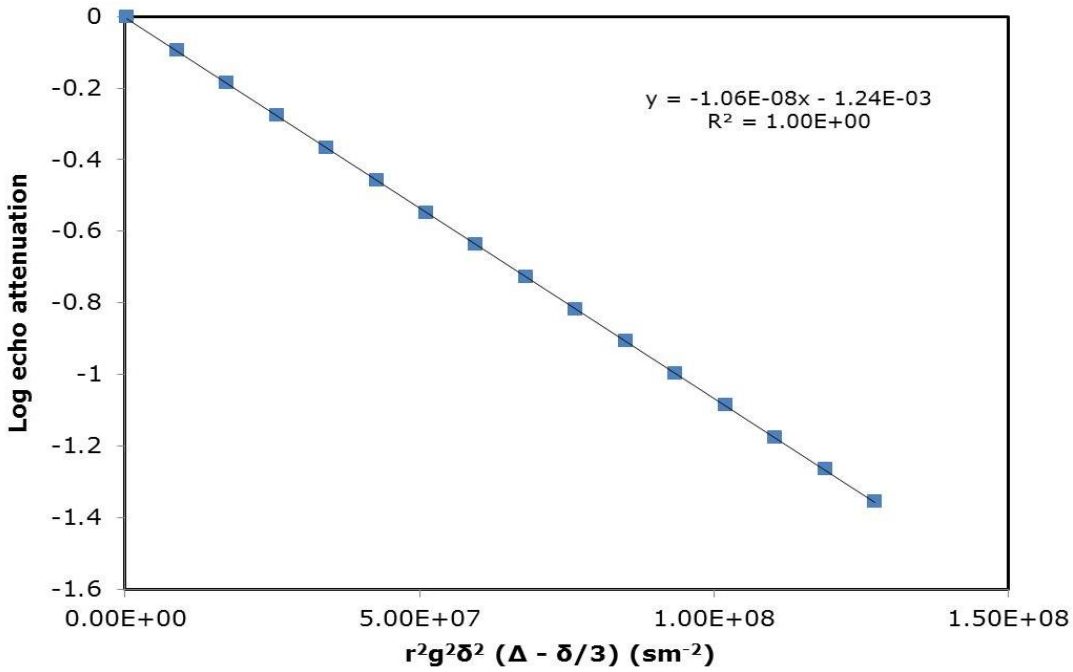

Figure 6. 7: NMR diffusion data for cyclohexane in material G2 at 298 K

Table 6. 2: Parameters used for NMR CPMG pulse sequence

Frequency/ MHz	400
Number of scans	16
P90 (**µs**)	15
P180 (**µs**)	25

6.4.2. Relaxation experiment for S1 silica sample

Fig. 6.8 shows the variation of the ^{1}H NMR signal intensity for water and cyclohexane in a LLE experiment conducted for a different silica sample, with pore size of ~12 nm, denoted as S1. Fig. 6.8 shows the S1 sample is completely filled with cyclohexane at t = 0 h and filling happens very quickly due to the high vapour pressure of cyclohexane relative to water. However, after the sample has been exposed to water, the signal intensity value of cyclohexane initially drops drastically and there after decreases gradually, which signifies that cyclohexane is slowly displaced by water over a period of time. Although, there is reason to believe the slow trend in cyclohexane content, which occurs between 30 to 80 mins, which is indicted by the dash line before a sharp decrease up to 400 mins, the deviation in the shape is larger than the error in the individual point, therefore more data set will be needed to clarify the trend on this particular S1 sample. The cyclohexane content at t=380 min is 18%.

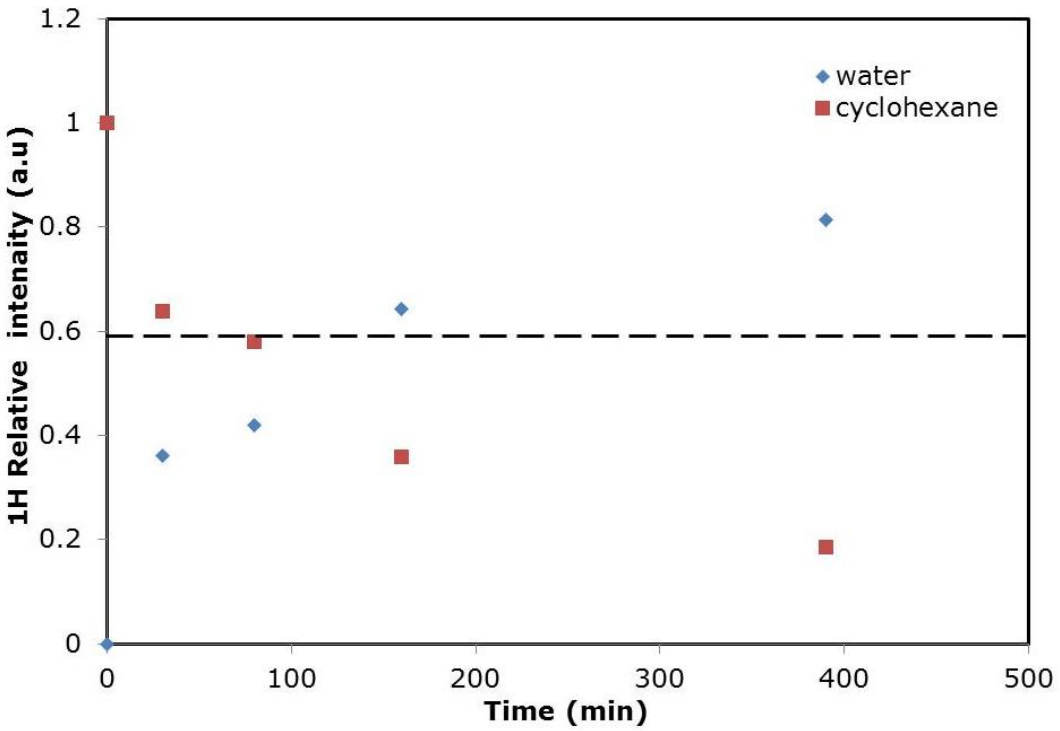

Figure 6. 8: Variation of fractional proton intensities for water and cyclohexane for S1 silica sample against experimental time. The dashed line indicates the position of a temporary plateau in the signal decay for cyclohexane

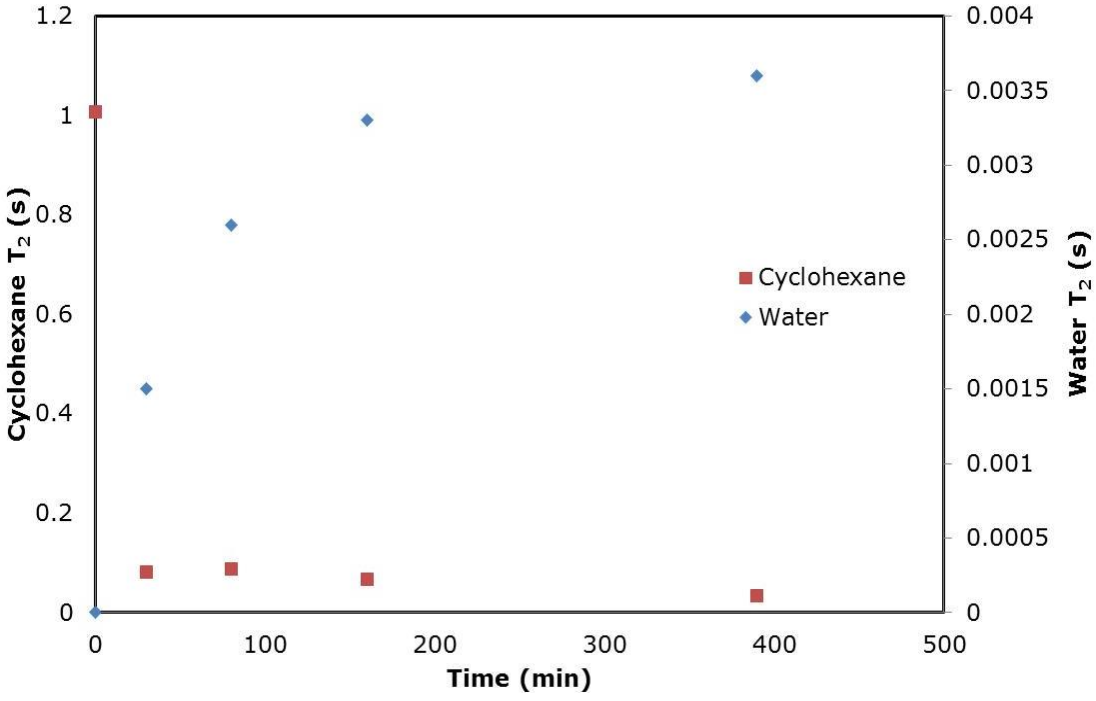

Figure 6. 9: The variation of average T_2 for cyclohexane and water with time during LLE experiment for S1 silica sample.

Fig. 6.9 shows the variation of T_2, for the two liquids (cyclohexane and water) in sample S1, with time during the same experiment as the data in Fig 6.8. It can be seen that the T_2 of cyclohexane drops very rapidly in the course of a few minutes in this particular sample. It can also be seen that the water T_2 continued to rise until 380 minutes while the cyclohexane T_2 remained almost unchanged. The distinct T_2 values for cyclohexane and water content can be seen in Fig. 6.9 showing the changes in distribution of cyclohexane and water over time during the progressive imbibition of water into S1 sample. It can be seen from Fig. 6.9, the cyclohexane initial value decreases up till the highest water saturation time.

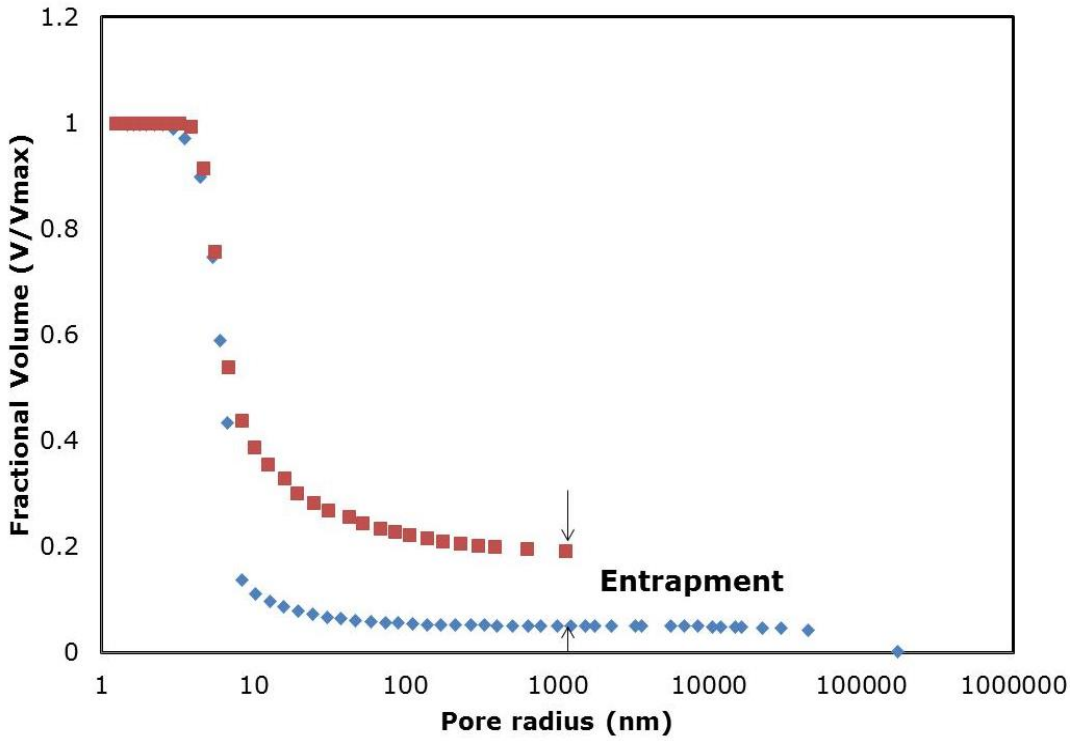

Figure 6. 10: Mercury porosimetry data for whole pellet of S1 sample.

Fig. 6.10 shows mercury porosimetry data for sample of S1 conducted at 10s equilibration time. The cyclohexane content at 380 min is ~17%, this corresponds closely to the amount of mercury entrapment for the mercury porosimetry experiment, conducted at 10s equilibration time which was found to be ~15%. The data for this particular experiment has already been discussed in section 4.4.

6.4.3. Comparison of ganglia sizes of cyclohexane with mercury porosimetry

The total entrapment of hydrocarbons has been investigated (Appel et al., 1998), however the work in this section has been focused on entrapment of different liquids using Hg/DSC and CPMG NMR techniques. The calculations for this section are shown in Appendix A1. The BET surface area for samples S1 and G2 were found to be 217±5 and 102±9 respectively (Rigby and Edler, 2002). Since the T_2 relaxation time depends on surface to volume ratio size as stated in Eq. 3.27, one can estimate the size of residual cyclohexane. The ganglia sizes of cyclohexane from the LLE exchange experiment have been determined to compare with the ganglia sizes of mercury after intrusion and retraction into samples of S1 and G1. The ganglia sizes for the entrapped fluid for the S1 sample seen in Table 6.3 are in reasonably good agreement for the two techniques investigated. The ganglia sizes for the Hg/DSC shown in Table 6.3 have been calculated already in chapter 5. However, for the G2 sample, the ganglia sizes for the mercury porosimetry are much larger than the ganglia sizes of hydrocarbon in the CPMG NMR technique.

Table 6. 3: Ganglia sizes of mercury and cyclohexane from two different sol-gel silica spheres.

Material	Mercury ganglia sizes from Hg/DSC (nm)	C_6H_{12} ganglia sizes from CPMG NMR (nm)
S1	7.80	7.47
G2	22.5	11.75

6.4.4. Diffusion of pentane on G1 silica sample

In this study, the phase behaviour and diffusion in mesoporous sol-gel silica sample, G1 has been studied using the PFG NMR. This set of experiments was conducted twice to check the reproducibility of the results. The complete results of these fits, and the data obtained can be found in Appendix A4. It can be seen from Table 6.4, that a simple linear behaviour ($R \geq 0.999$) was attained in all the data sets for diffusion experiments for both with, and without, excess fluid.

Table 6. 4: Coefficients of determination for the log attenuation plots of the same sample in case II for one component fit.

Temperature (K)	Coefficient of determination, R^2	
	Number of scans = 16	Number of scans = 16
	With excess liquid	Without excess liquid
250	0.9997	1.000
257	0.9998	1.000
265	0.9998	1.000
273	0.9998	1.000
280	0.9997	1.000

288	0.9997	1.000
293	1.000	1.000
298	0.9996	1.000
303	0.9998	0.9999
309	1.0000	0.9998
311	0.9999	0.9996
313	0.9999	0.9992
315	0.9997	0.9986

Fig. 6.11 shows the PFG NMR log attenuation plots for the samples measured with excess liquid and without excess liquid at different temperatures. The plots are linear and the diffusion coefficients of pentane in the G1 sample were determined from the slope of the plots using echo intensity Eq. 3.30. The corresponding root mean square displacement of pentane molecules in the G1 sample observed at the lowest temperature of 250K was 17 μm. Whilst the root mean square displacement for pentane molecules at 315K was 28 μm. These values were calculated using the Einstein equation, Eq. 3.34. The mean square displacement calculated over the observation time at the lowest temperature of the experiment is much larger than the pore diameter (8 nm), thus the diffusing molecules move through many different pores during the time of the experiment. This experiment was conducted twice to check the repeatability of the experiment.

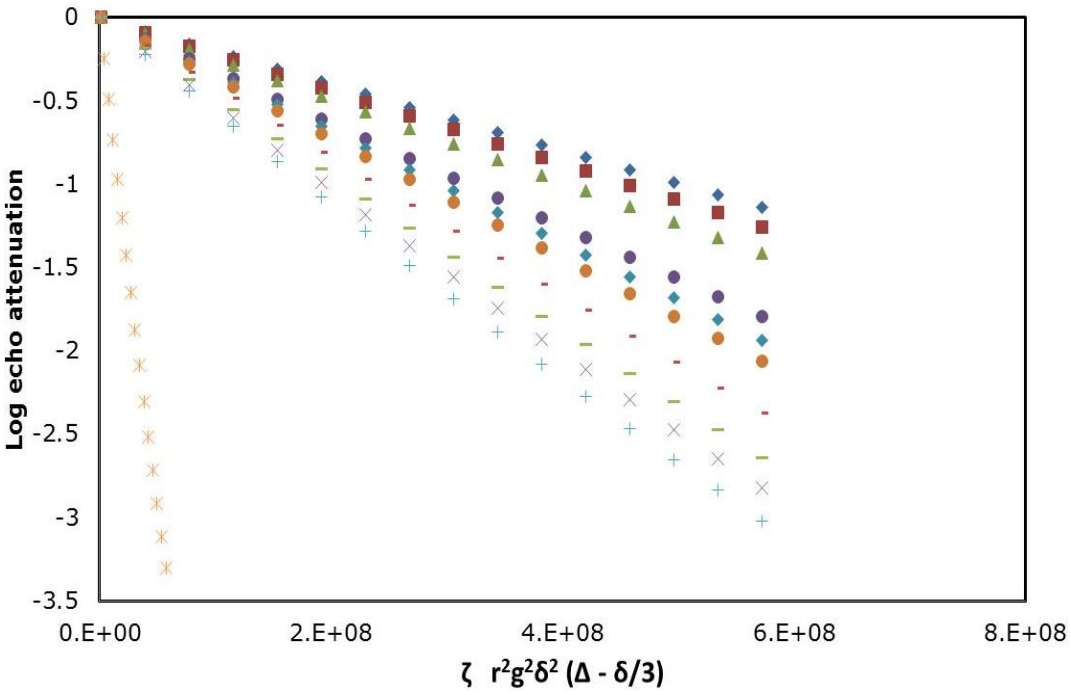

Figure 6. 11: PFG NMR spin-echo attenuation plot for samples of G1 without excess pentane performed at different temperatures from 250 K (filled squares) to T=315 K (crosses)

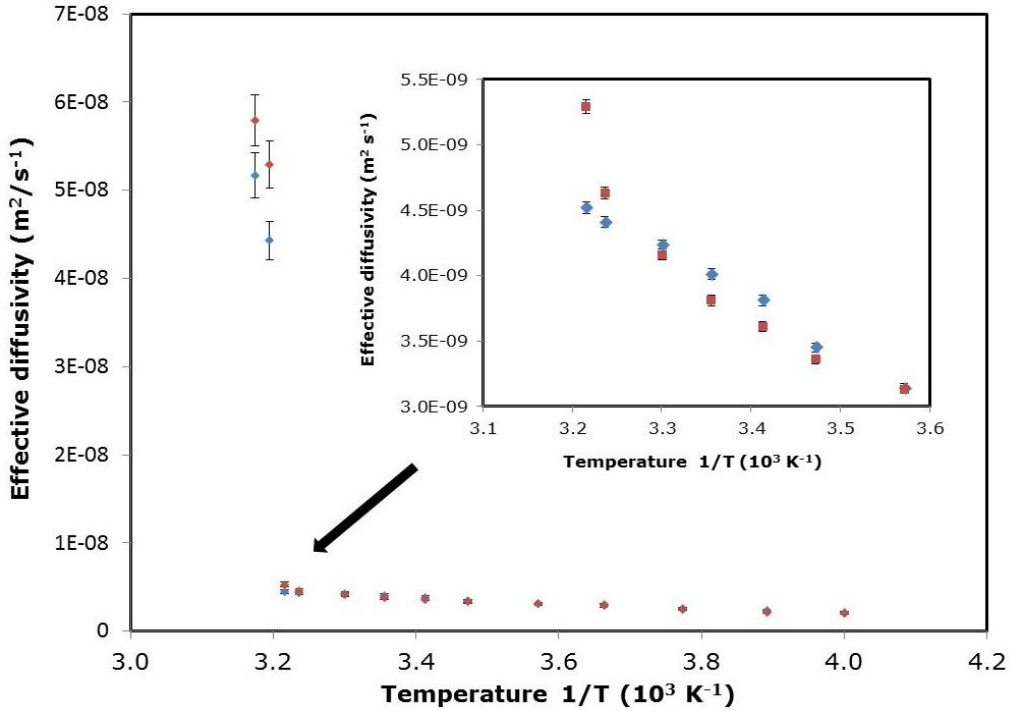

Figure 6. 12: Effective intra-pore diffusivities for n-pentane obtained from diffusion spin echo attenuation in Fig. 6.10 for the sample with (blue diamonds) and without (red squares) excess pentane as a function of inverse temperature. The inset shows the notable point of the two set of experiments.

The diffusivities of *n*-pentane have been measured directly by means of the PFG NMR technique in the temperature range of 250-315 K. Fig. 6.12 shows the diffusivities values of *n*-pentane within the pore system of G1 sample as a function of temperature obtained for both with and without excess fluid. It is noted that the measured diffusivities for both samples increased as the temperature increased. It can also be seen that for low temperatures there is good agreement between the two sets of results for with and without excess pentane liquid. However, starting from about 303 K, the effective intra-porous diffusivities in the sample with no excess fluid deviate to higher values; this is attributed to the appearance of void space within the pore system with increasing temperature due to evaporation of condensate. The sample G1 contained a large amount of liquid in excess up to 311K. However, the sharp jump in the diffusivities at the highest temperature of 313 and 315 K considered in this study is due to large-scale evaporation of condensed liquid and large contributions from gas phase diffusion. Thus, the diffusivity of these two temperatures measured is near that of the vapour phase of the liquid at that particular given temperature.

6.5. Discussion

The T_2 relaxation experiment has been used to probe the exchange behaviour of cyclohexane with water using CPMG experiments. The displacement of cyclohexane by water within set pores is due to the higher vapour pressure of cyclohexane. Also, as water has hydroxyl groups and thus a high surface affinity, it wets the surface of silica materials better than cyclohexane. The water imbibition results obtained for S1 and G2 samples, from the relaxation experiments, are similar to that observed by Gopinathan et al., (2010) for

different silica samples. The relaxometry data suggest that, for both samples S1 and G2, as cyclohexane is displaced by water from particular set of pores, the T_2 value for cyclohexane decreases, while that of water increases. It has been noted that it takes longer times for water to displace cyclohexane from the pores in G2 samples relative to S1 samples. This might be due to reach smaller pores located deeper within the sample that is further away from the outside where the water penetration is initiated. Thus, suggesting that the accessibility of the sample is likely to be very poor for the G2 sample. This is in line with the findings from other studies (Wardlaw and McKellar, 1981) of liquid entrapment that the connectivity and accessibility of a material is very important. It was also noted from the S1 sample, the displacement of cyclohexane by water happens very rapidly with shorter T_2 values for the entrapped hydrocarbon, suggesting that cyclohexane is being displaced from larger pores within the sample. Also, it is likely to mean that the entrapped cyclohexane ganglia are surrounded by water that wets the silica surface. The pellet spin-spin relaxation times calculated for S1, and G2 samples are compared with the mercury porosimetry data obtained in chapter 5 for the entrapment of non-wetting fluid. It shows that the entrapment values for the LLE experiment for both samples correspond to that of the mercury porosimetry. Thus, suggesting the importance of using LLE technique to determine the entrapment of a less hazardous probe fluid than mercury that is used in mercury porosimetry technique. The use CMPG NMR to determine the entrapment of fluid in porous materials agreed with the work of Appel et al., (1998). These researchers found that the bound volume index values

determined from CPMG NMR and mercury porosimetry techniques are in good agreement.

On the other hand, the study of diffusion of liquid (n-pentane) within a pore system of mesoporous materials over wide range of temperatures, including those of boiling point using Pulsed Field Gradient NMR, has shown to be a successful technique for the determination of diffusion of liquids probe molecules imbibed within mesoporous G1 sample. The diffusivities obtained for the two samples with and without excess fluid starts to deviate at a temperature of 300 K in this sample, an amount of guest molecules ensures complete pore filling only at the lowest temperature. However, with increase in temperature, there is a competing process between either maintaining the liquid phase in the mesopores contiguous or maintaining the vapour pressure in the gas phase surrounding the porous particles as saturated. Saturation was found to be relatively small at lower temperatures, up to about 300 K, this is attributed to be due to evaporation of liquid from the pores. Also, at temperatures above 300 K, and with decrease in relative pressure, cavitation might occur in larger pores of the mesoporous material. Thus the deviation in sample without excess fluid begins from the impact of fast molecular diffusion in such cavitated regions of the porous materials. Therefore, molecular transport is considered to follow Knudsen diffusion. Furthermore, the increase in the diffusivity value measured at the maximum temperature of 315 K is attributed to the evaporation of pentane molecules within the pore system. Thus, suggesting that the diffusivity measured at the highest temperature is that of the gaseous phase, which are controlled by collisions with the gas-liquid interface and by intermolecular collisions. The results obtained here are similar

to the findings from other studies (Dvoyashkin et al., 2005) on the effects of temperature on the diffusion of fluids in mesopores.

6.6. Conclusion

The use CPMG NMR in LLE experiments has shown that we can predict the amount of fluid trapped during the course of the experiment, just as it was observed in mercury porosimetry experiments. Also, the comparison of the size of the ganglia for cyclohexane and mercury is a stiffer test of the idea mercury porosimetry can predict behaviour of hydrocarbons. Also, a deeper understanding of the phase behaviour may lead to promising options in the use of mesoporous materials in a diverse range of applications. The PFG NMR technique have shown to allow the direct observation of the various mechanisms contributing to overall mass transfer in porous media and the quantification of the relevant parameters, including diffusivities of the molecules confined to mesoporous materials in different sample regions.

6.7. References

APPEL, M., STALLMACH, F. & THOMANN, H. 1998. Irreducible fluid saturation determined by pulsed field gradient NMR. *Journal of Petroleum Science and Engineering,* 19**,** 45-54.

DVOYASHKIN, M., VALIULLIN, R. & KÄRGER, J. 2007. Temperature effects on phase equilibrium and diffusion in mesopores. *Physical Review E,* 75**,** 041202.

GOPINATHAN, N., GREAVES, M., LOWE, J. P., WOOD, J. & RIGBY, S. P. 2012. Determination of the location of coke in catalysts by a novel NMR-based, liquid-porosimetry approach. *Journal of Colloid and Interface Science,* 381**,** 164-170.

KIMMICH, R., STAPF, S., MAKLAKOV, A. I., SKIRDA, V. D. & KHOZINA, E. V. 1996. Self-diffusion in fluids in porous glass: Confinement by pores and liquid adsorption layers. *Magnetic Resonance Imaging,* 14**,** 793-797.

RIGBY, S. P. & EDLER, K. J. 2002. The Influence of Mercury Contact Angle, Surface Tension, and Retraction Mechanism on the Interpretation of Mercury Porosimetry Data. *Journal of Colloid and Interface Science,* 250**,** 175-190.

VALIULLIN, R., KORTUNOV, P., KÄRGER, J. & TIMOSHENKO, V. 2005. Concentration-dependent self-diffusion of adsorbates in mesoporous materials. *Magnetic Resonance Imaging,* 23**,** 209-214.

WARDLAW, N. C. & MCKELLAR, M. 1981. Mercury porosimetry and the interpretation of pore geometry in sedimentary rocks and artificial models. *Powder Technology,* 29**,** 127-143.

Chapter 7: Conclusions and Future Work

The work carried out in this thesis has shown the importance of using multiple techniques to characterise heterogeneous materials. Below, a summary of each chapter discussed in this thesis is summarized along with main findings of the work. Also, recommendations for the future work are also given in this chapter.

7.1. General conclusions

Chapter 4 presented the combined use of mercury porosimetry and x-ray tomography to determine the structural properties of mesoporous samples and also, the spatial distribution of mercury within mesoporous materials. It was found that the use of both techniques together has enabled a more detailed understanding of the pore structure. A consideration of the effect of experimental time scales in the silica and alumina samples studied has shown a significant effect of the equilibration time for sol-gel silica G2. Also, mercury entrapment was found for all the materials studied, irrespective of equilibration time used. Also, by combining mercury porosimetry and X-ray imaging of pellets after mercury porosimetry, it was shown that the spatial distribution of entrapped mercury is highly heterogeneous, suggesting that the materials are also macroscopically heterogeneous. The X-ray images have also shown that mercury entrapment occurs towards the centre of pellet, at low equilibration times. However, using a longer equilibration time of 100 sec, the images have shown that the distribution of residual mercury tends towards the surface of the silica materials.

Chapter 5 reported the use of a novel thermoporosimetry technique using mercury entrapped following mercury porosimetry as the probe fluid. This method has been shown to provide independent validation of pore structural information obtained from porosimetry. Hence, this new type of combined porosimetry and thermoporosimetry enables independent adjudication of the discrepancy between pore sizes derived from porosimetry and other techniques, such as gas sorption. It has been shown that mercury porosimetry in combination with thermoporosimetry method can be used to determine the pore sizes of mercury entrapped on different sol-gel silicas studied within this research and whether a set of pores melt by hemispherical or cylindrical shaped menisci. The method also validates the size of pores which entrapped mercury.

Chapter 6 described the use of LLE studied by CPMG NMR to further the characterization and understanding of entrapment of fluids, where water displaces cyclohexane within a set of interconnected pores. In this chapter, LLE was achieved by the co-adsorption of two liquids, namely cyclohexane and water. It has been shown that the extent and sites of entrapment of cyclohexane in sol-gel silica materials were found to be similar to that which occurs for mercury in mercury porosimetry. The T_2 relaxation time helped in understanding the displacement mechanism of cyclohexane by water and also the size of pores the entrapped liquid occupies. The signal intensity as a function of time was used to determine the amount of entrapped liquid that is left. Also, the use of PFG NMR to study the diffusion of *n*-pentane within the pore system of mesopore materials over wide range of temperatures has been studied. It has been found that the temperature dependence of the diffusivity

dramatically depends on the state of the fluid surrounding the mesoporous materials.

In general, it has been found that the traditional methods of pore characterisation have limitations and thus require further development. The research conducted by the author in this thesis makes valuable contribution to the field of pore characterisation and chemical industries, by predicting the transport phenomena in different range of silica and alumina samples with different geometries using different experimental techniques. This thesis has reported on variety of methods that can be explored in determining the entrapment of hydrocarbons. The entrapment of non-wetting fluid and hydrocarbons were investigated using mercury porosimetry at different experiment time scales and CPMG NMR. It was found that the entrapment of non-wetting fluid occurred at larger mesopore radii, and was present in all experimental time-scales of the materials investigated. The effect of experimental time scales in silica materials was significantly greater in G2 samples, and thus suggests that the retraction is a flow-rate controlled process. Also, the heterogeneous entrapped mercury distribution within the G2 sample was revealed by X-ray tomography studies of the samples following the porosimetry experiments. The ganglia sizes of non-wetting fluid were obtained with a novel mercury thermoporosimetry experiment using mercury entrapped following mercury porosimetry as the probe fluid. The novel technique also validates the sizes of pores, which entrapped mercury following mercury porosimetry experiment. However, the work completed for this thesis has also opened avenues that require further research aiding the development of the new characterisation techniques.

7.2. Future work

Based on findings of this study, it has been found that the characterization methods adopted should have some limitations and thus require further development. Proposed recommendations for the extension of the work contained in this thesis are summarized below:

- **Mercury/X-ray tomography studies on rocks**

The X-ray study of entrapped mercury on disordered materials has enabled a detailed understanding of the possibility of combining both techniques to see the spatial distribution of entrapped mercury. The combination of both techniques using reservoir rock has not been carried out. A preliminary mercury porosimetry study has already been carried out on reservoir sandstone with, 60% porosity and results are shown in Fig. 7.1. It is thus suggested that the combined mercury porosimetry and x-ray tomography techniques could be used to check, in more detail, the entrapment mechanism, as well as structural features of the sandstone material so as to compare with the studies done already on the entrapment of mercury on model disordered materials.

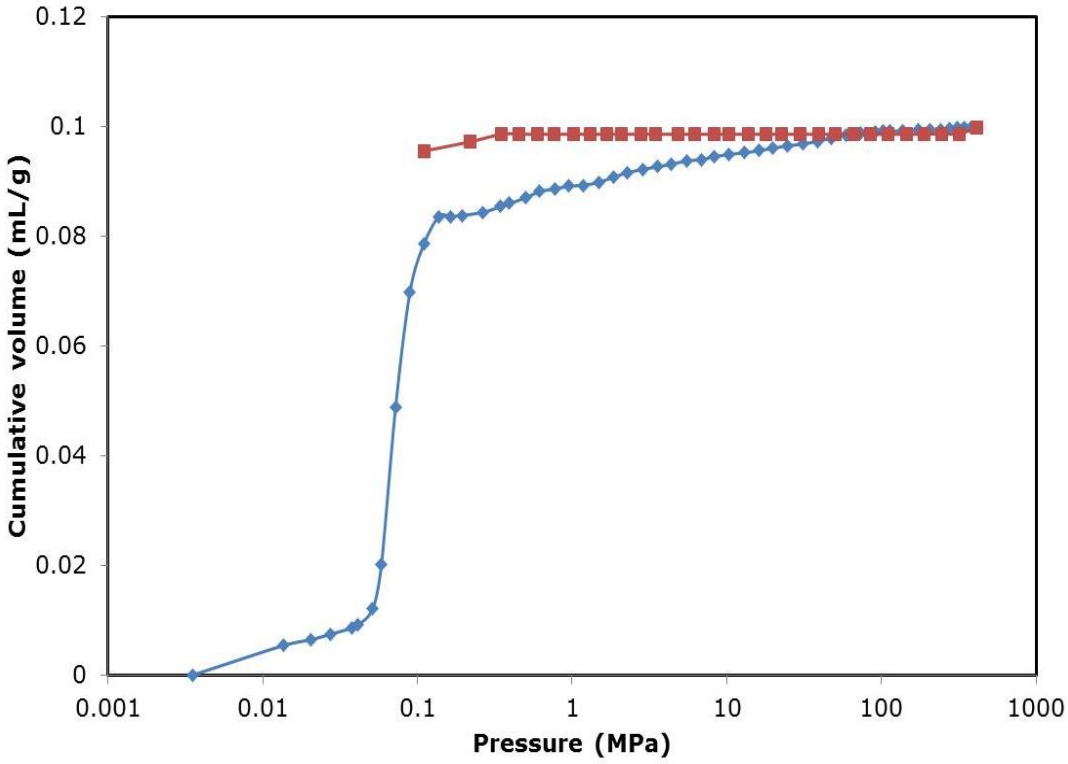

Figure 7. 1: Mercury intrusion/extrusion curves for a sandstone material conducted at 30 sec equilibration time. The lines shown are to guide the eye.

- **Prediction of permeability in porous rock**

The work carried out in chapter four did not study the permeability of non-wetting fluid in mesoporous materials. The estimations of rock permeabilities are necessary in the oil and gas industries. The pore size distribution of a rock is an important characteristic that controls permeability. This parameter can be estimated experimentally from mercury porosimetry data using the using the Katz-Thompson equation (Katz and Thompson, 1986). The permeability could be compared with experimental measurements.

- **Simulation studies of mercury entrapment**

The hysteresis and entrapment of mercury within the pore space of mesoporous materials was observed at larger mesopore sizes. Also, the level of mercury entrapment is determined by the nature of macroscopic structure of

the porous medium and not the pore scale properties, as assumed by many researchers (Gopinathan et al., 2012; Dvoyashkin et al., 2007). Recently, Rigby *et al.* (2011), simulated mercury intrusion and extrusion curves using mean-field density-functional (MF-DFT) theory using disordered porous materials. Their findings suggest that materials analysed using Eq. 3.2 where a complete superposition of raw intrusion and extrusion curves at smaller pore sizes consist of pore systems with relatively low connectivity between the smallest pores and the larger pores. Thus MF-DFT could be used to further the interpretation of experimental mercury porosimetry data on chemically heterogeneous materials in terms of pore sizes that entrapped mercury.

- **Mercury thermoporosimetry**

The differential scanning calorimetry have shown to permit the validation of assumptions used by both mercury porosimetry and thermoporosimetry techniques using controlled pore glass as a model material to determine the appropriate Gibbs-Thompson parameter, and the nature of meniscus geometry in melting, for thermoporosimetry measurements on entrapped mercury. Based on these findings, it is suggested that we could use further tests on different catalysts containing metals and also use scanning curves in mercury thermoporosimetry. Mercury porosimetry works on the basis that it is a non-wetting fluid. The presence of heavy metals on the catalyst surface may change the wetting properties. Thence, interpretation of mercury porosimetry using standard approaches may be flawed for such catalysts. Mercury thermoporosimetry could be used to check pore size values obtained from porosimetry. Changes to the mercury wetting are likely to lead to oversize

pores from porosimetry. This may aid further in understanding regions within the catalyst that give rise to mercury entrapment.

- **Nuclear magnetic resonance**

The use of CPMG NMR has allowed the determination of entrapment of liquid in mesopore samples that was used to compare with entrapment of mercury using mercury porosimetry experiments. This technique could further be used to further the understanding of entrapment in a liquid-liquid exchange experiment using different liquids with more chemically heterogeneous samples.

7.3. References

DVOYASHKIN, M., VALIULLIN, R. & KÄRGER, J. 2007. Temperature effects on phase equilibrium and diffusion in mesopores. *Physical Review E,* 75**,** 041202.

FUSI, N. & MARTINEZ-MARTINEZ, J. 2013. Mercury porosimetry as a tool for improving quality of micro-CT images in low porosity carbonate rocks. *Engineering Geology,* 166**,** 272-282.

GOPINATHAN, N., GREAVES, M., LOWE, J. P., WOOD, J. & RIGBY, S. P. 2012. Determination of the location of coke in catalysts by a novel NMR-based, liquid-porosimetry approach. *Journal of Colloid and Interface Science,* 381**,** 164-170.

KATZ, A. J. & THOMPSON, A. H. 1986. Quantitative prediction of permeability in porous rock. *Physical Review B,* 34**,** 8179-8181.

Appendix A: Supporting information for DSC Thermoporometry technique

A1- A thermogram and Pore size distribution of different silica samples used during the course of the experiment

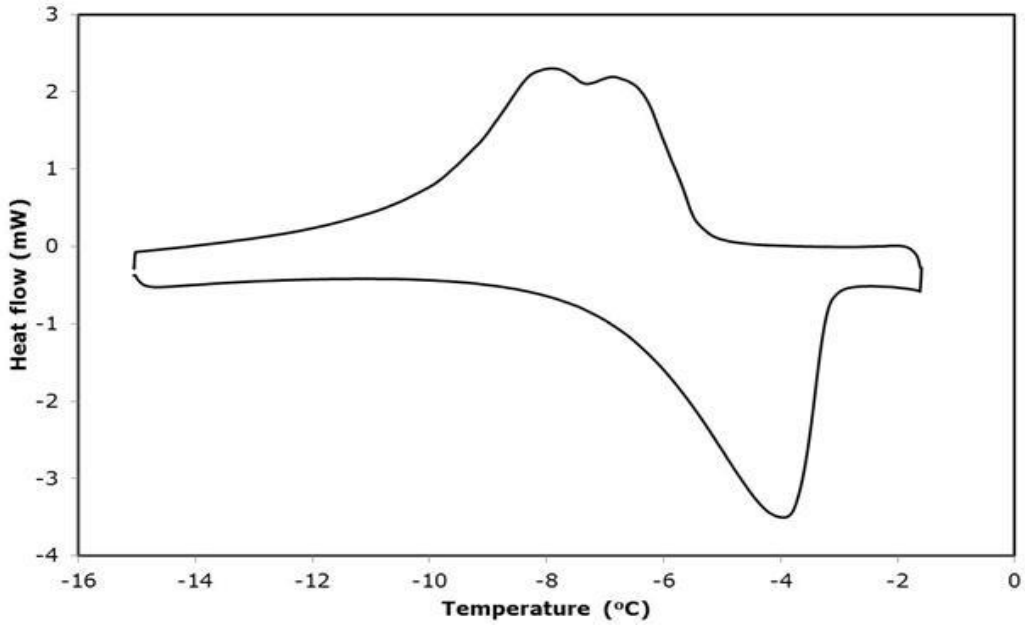

Figure A1. 1: Thermogram for a powdered S980A silica sample run at 0.1°C/min

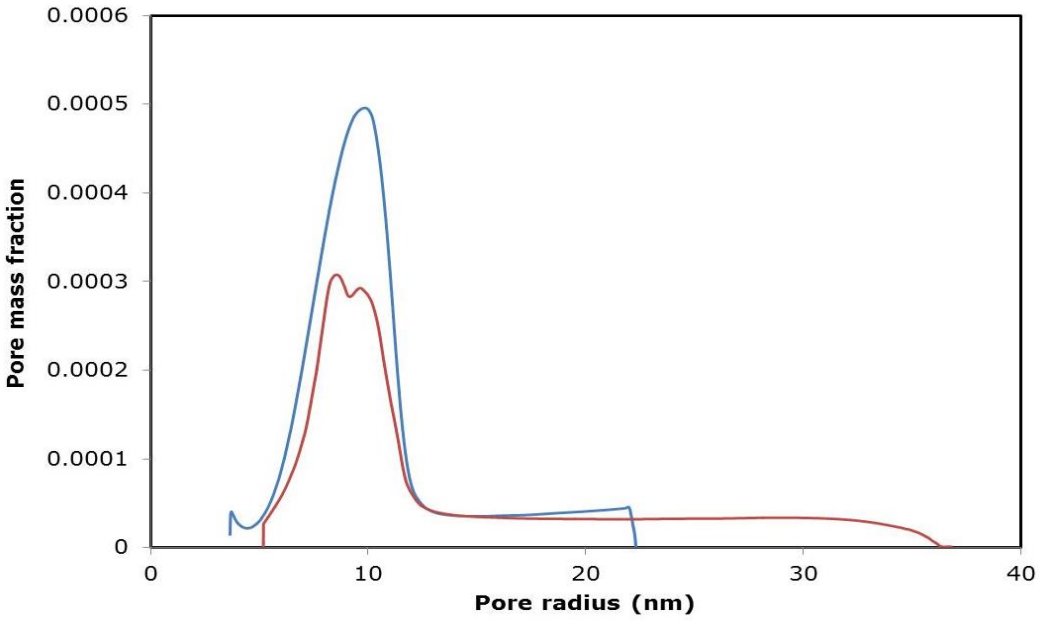

Figure A1. 2: Pore size distribution of S980A powdered sample determined from DSC experiment.

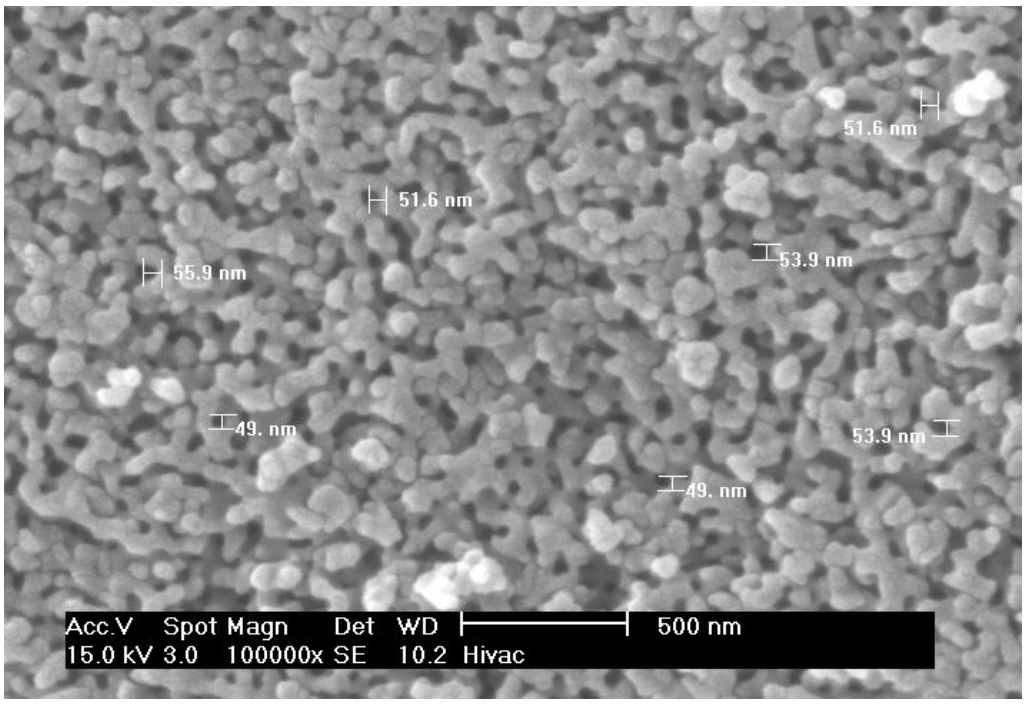

Figure A1. 3: Scanning electron microscopy image for a controlled pore glass at 500 nm spatial resolution.

Appendix B: Supporting information for mercury porosimetry experiments

This appendix contains extra supporting information on how structural properties of the materials studied were calculated.

B.1 surface area calculation using the Rootare and Prenzlow equation.

$$A = \frac{1}{\gamma_{Hg} cos\theta} \int_0^v P \, dV \qquad \text{(B1.1)}$$

Substituting the surface tension of Hg which was assumed as 0.485 Nm^{-1}, and the contact angle, $\theta = 130^o$ and the product of $P.dV$ which is calculated in the table below, yields the surface area.

$$A = -\frac{1}{0.485 cos 130}(71.913)$$

A = 230.67 m^2/g.

Table B1-1. Raw pressure and mercury volume date for a whole sample from batch S1. The last column is the product of pressure and incremental volume.

Pressure	Intrusion	Incremental volume	P.dV
MPa	mL/g		
0.002894	0.001		
0.013583	0.037823297	0.036823	0.000500167
0.02047	0.040057112	0.002234	4.57258E-05
0.027375	0.041251075	0.001194	3.26846E-05
0.037695	0.042252608	0.001002	3.77524E-05
0.041174	0.042445045	0.000192	7.92335E-06
0.051488	0.042868692	0.000424	2.18129E-05
0.058384	0.043099761	0.000231	1.34908E-05
0.072127	0.043446422	0.000347	2.50034E-05
0.089338	0.04375454	0.000308	2.75268E-05
0.110234	0.044062827	0.000308	3.39835E-05
0.1377	0.044447832	0.000385	5.30152E-05
0.149595	0.045205995	0.000758	0.000113417
0.184845	0.045335926	0.00013	2.40171E-05
0.264474	0.046199463	0.000864	0.000228383
0.323895	0.047135886	0.000936	0.000303302

0.391011	0.047698282	0.000562	0.000219903
0.502696	0.048249487	0.000551	0.000277089
0.601818	0.048423015	0.000174	0.000104432
0.780444	0.048633568	0.000211	0.000164325
0.947536	0.049161818	0.000528	0.000500536
1.177693	0.049363431	0.000202	0.000237438
1.496764	0.049823429	0.00046	0.00068851
1.838054	0.050029181	0.000206	0.000378182
2.257669	0.050029181	0	0
2.88348	0.051034093	0.001005	0.002897644
3.571577	0.051421288	0.000387	0.001382899
4.406321	0.052138571	0.000717	0.003160576
5.497153	0.052687477	0.000549	0.003017424
6.810584	0.053392325	0.000705	0.004800421
8.261613	0.053637203	0.000245	0.002023089
10.32524	0.054932028	0.001295	0.013369378
13.09245	0.056146417	0.001214	0.015899319
16.17775	0.057988681	0.001842	0.02980368
19.96583	0.06090546	0.002917	0.058235914
24.78825	0.063437447	0.002532	0.062763524
30.93932	0.066838861	0.003401	0.105237409
38.49537	0.071798332	0.004959	0.190916695
47.46449	0.077595234	0.005797	0.27514699
59.16608	0.08618404	0.008589	0.508165935
72.95539	0.110585622	0.024402	1.780226964
90.86225	0.283094466	0.172509	15.67454154
101.8791	0.444879919	0.161785	16.48255846
112.9047	0.570256174	0.125376	14.15556532
137.6982	0.698499918	0.128244	17.65893622
172.3072	0.726821423	0.028322	4.879998243
206.7799	0.726821423	0	0
241.2629	0.726821423	0	0
275.7167	0.726821423	0	0
310.1896	0.726821423	0	0
344.69	0.726821423	0	0
379.0772	0.726821423	0	0
413.4772	0.726821423	0	0
		$\sum P_i V_i$	**71.91268626**

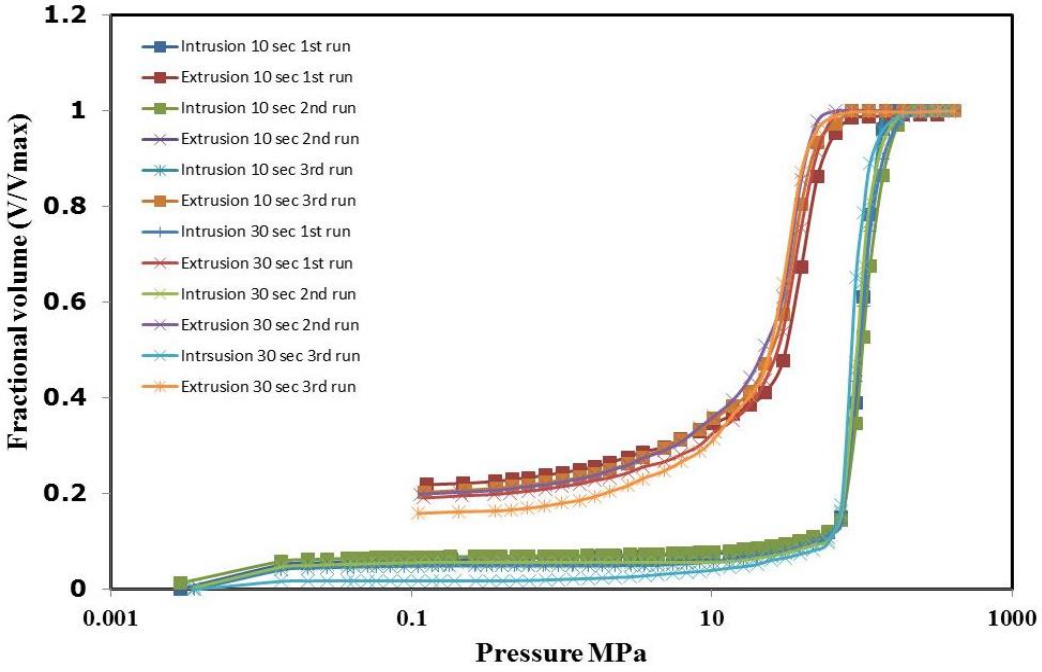

Figure B1. 1: mercury intrusion/extrusion data for S980A sample at different equilibration time.

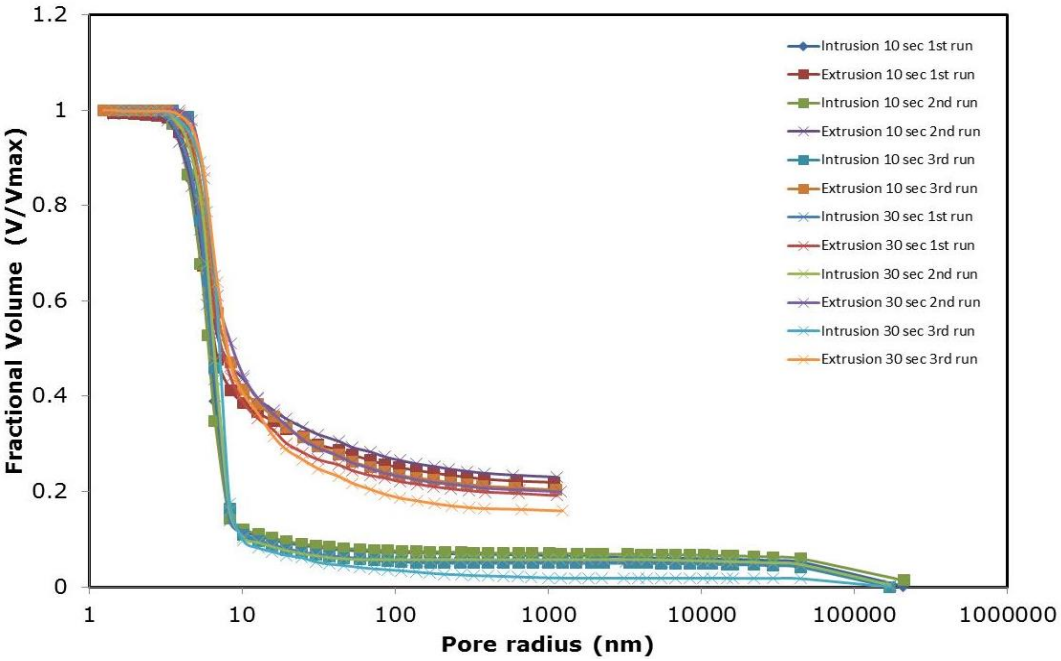

Figure B1. 2: mercury intrusion/extrusion data for S980A sample at different equilibration time analysed using the Kloubek correlations.

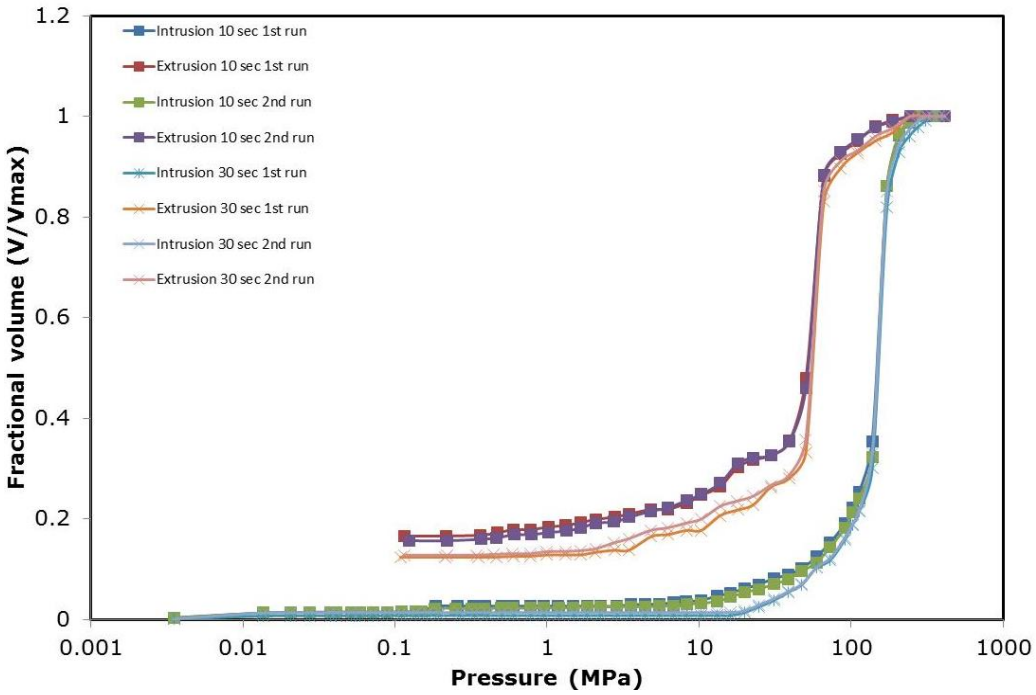

Figure B1. 3: mercury intrusion/extrusion data for C10 sample at different equilibration time.

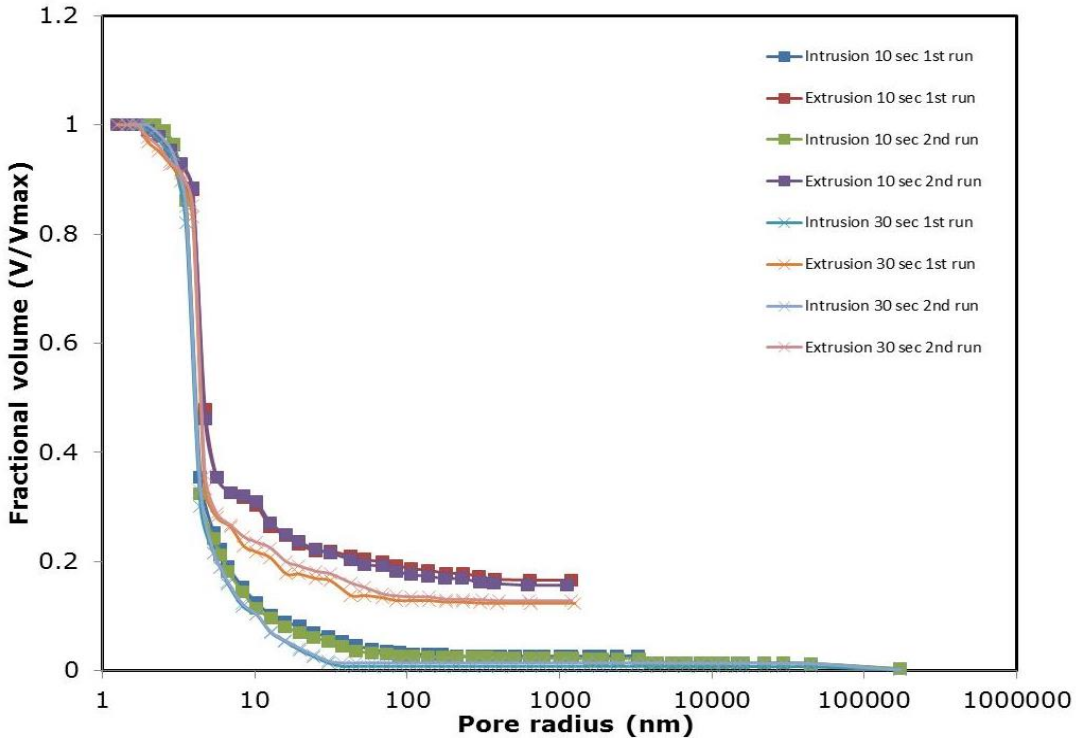

Figure B1. 4: mercury intrusion/extrusion data for C10 sample at different equilibration time analysed using the Kloubek correlations.

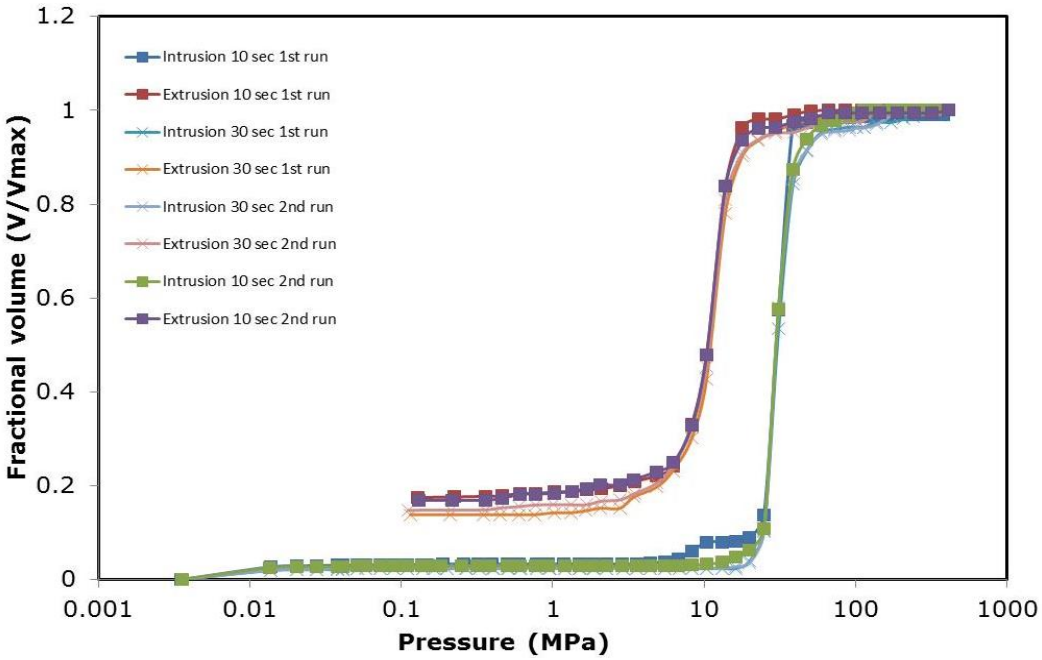

Figure B1. 5: mercury intrusion/extrusion data for S980G sample at different equilibration time.

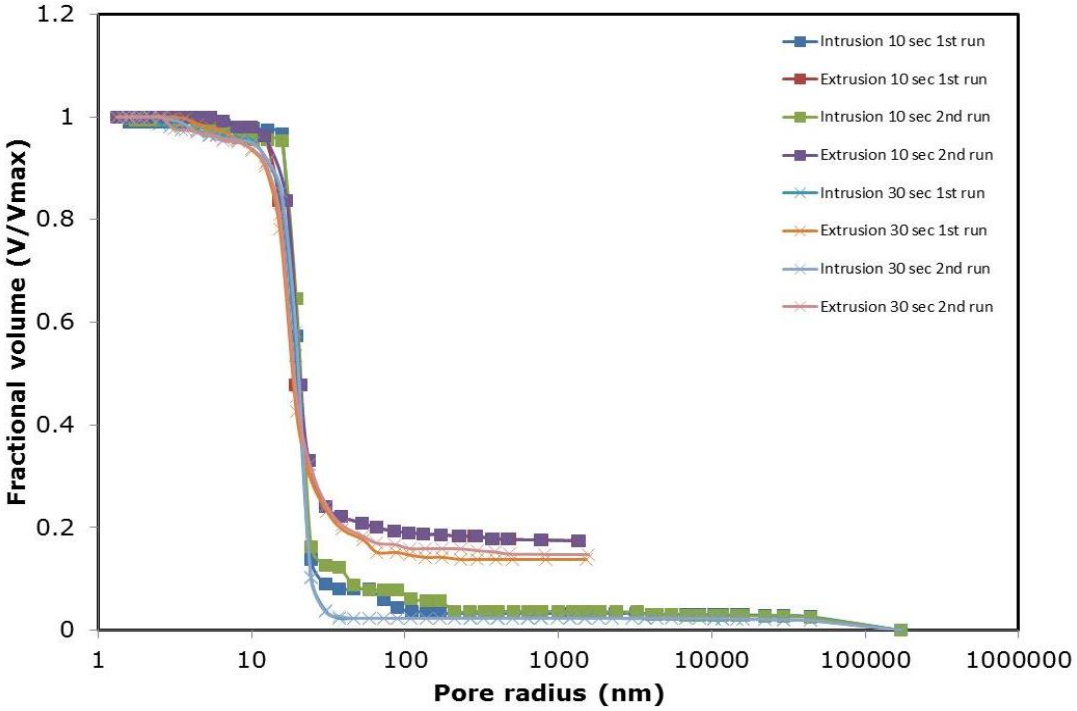

Figure B1. 6: mercury intrusion/extrusion data for S980G sample at different equilibration time analysed using the Kloubek correlations.

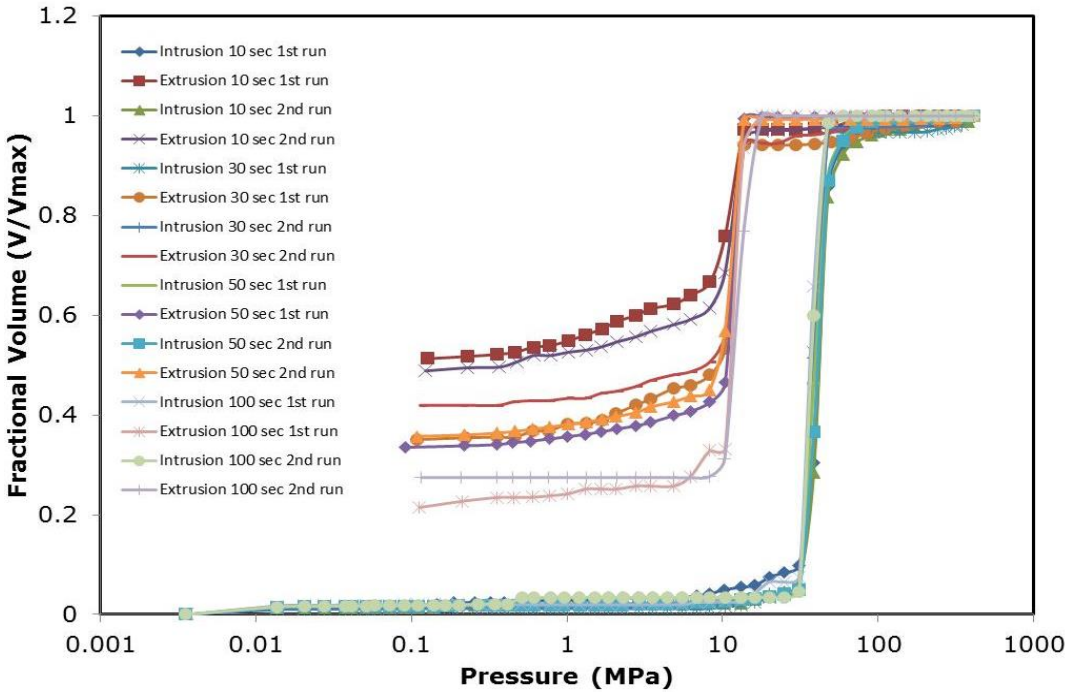

Figure B1. 7: mercury intrusion/extrusion data for C30 sample at different equilibration time.

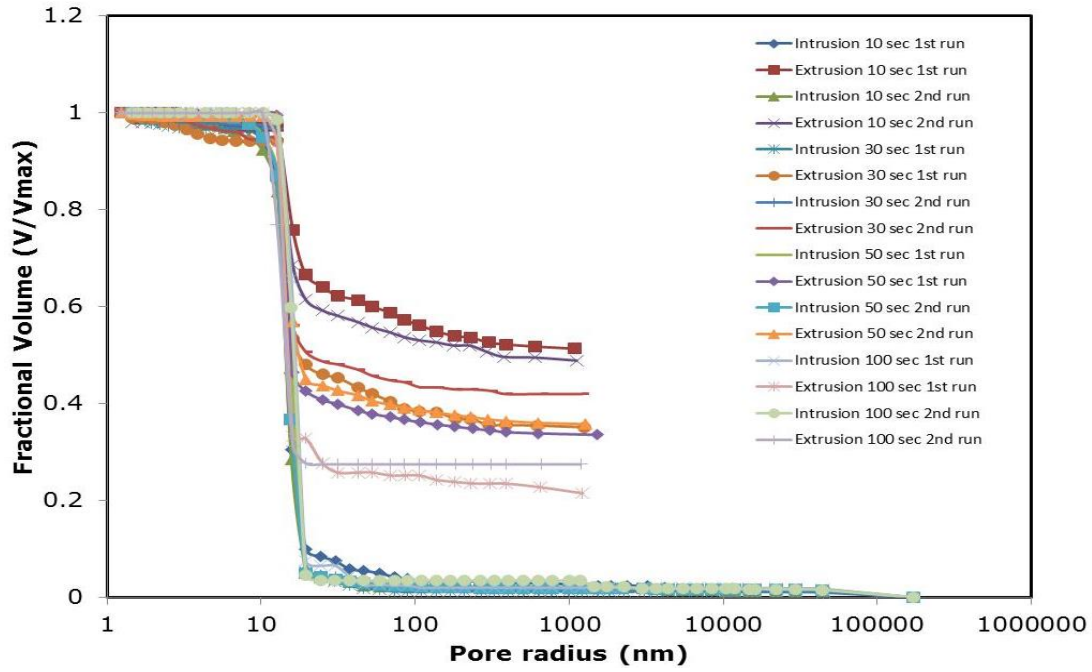

Figure B1. 8: mercury intrusion/extrusion data for C30 sample at different equilibration time analysed using the Kloubek correlations.

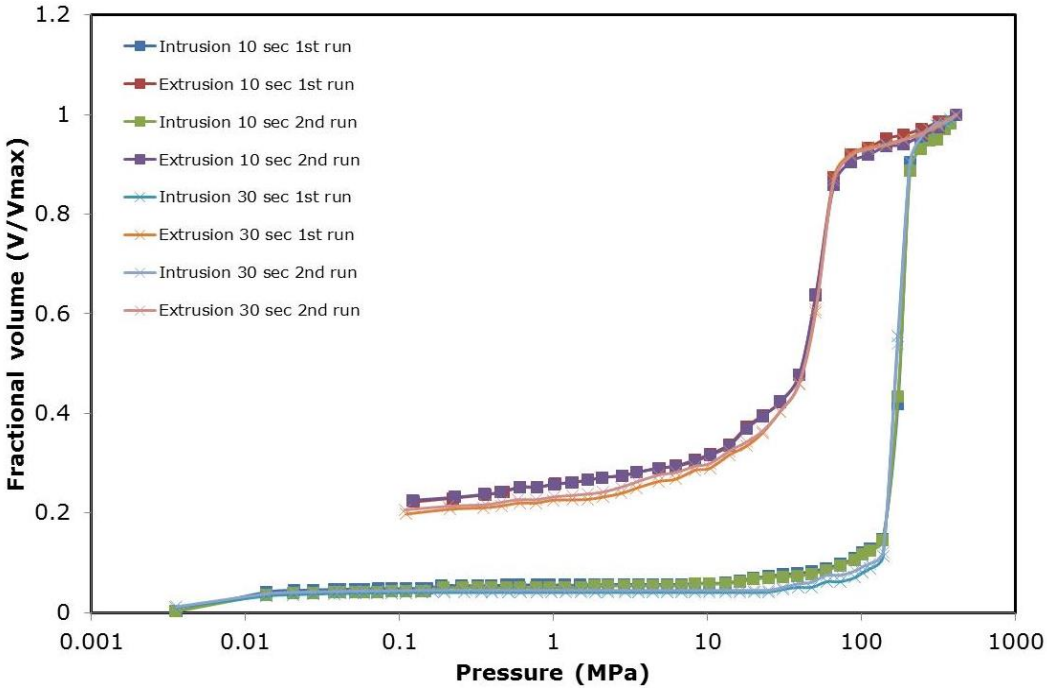

Figure B1. 9: mercury intrusion/extrusion data for standard silica alumina sample at different equilibration time.

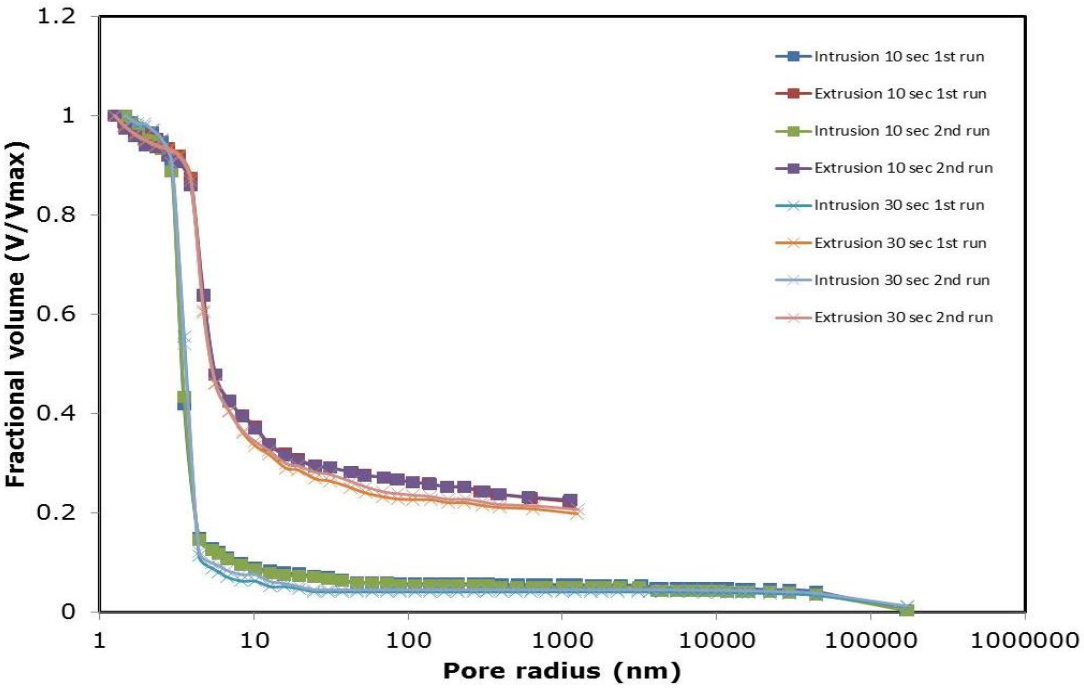

Figure B1. 10: mercury intrusion/extrusion data for standard silica alumina sample at different equilibration time analysed using the Kloubek correlations.

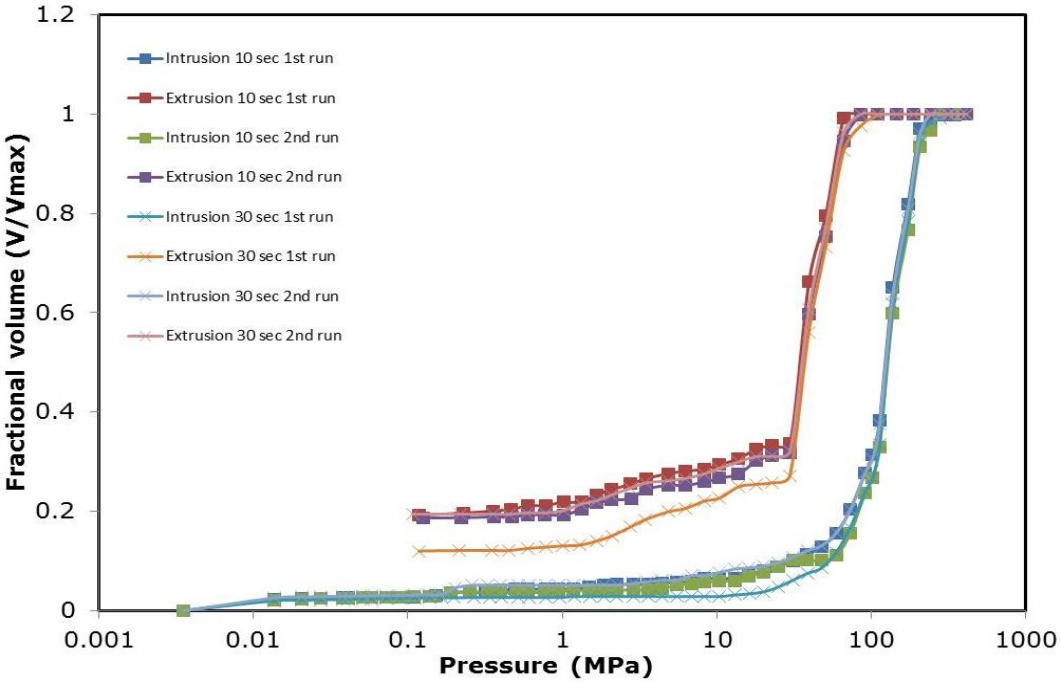

Figure B1. 11: mercury intrusion/extrusion data for Al-3992E sample at different equilibration time.

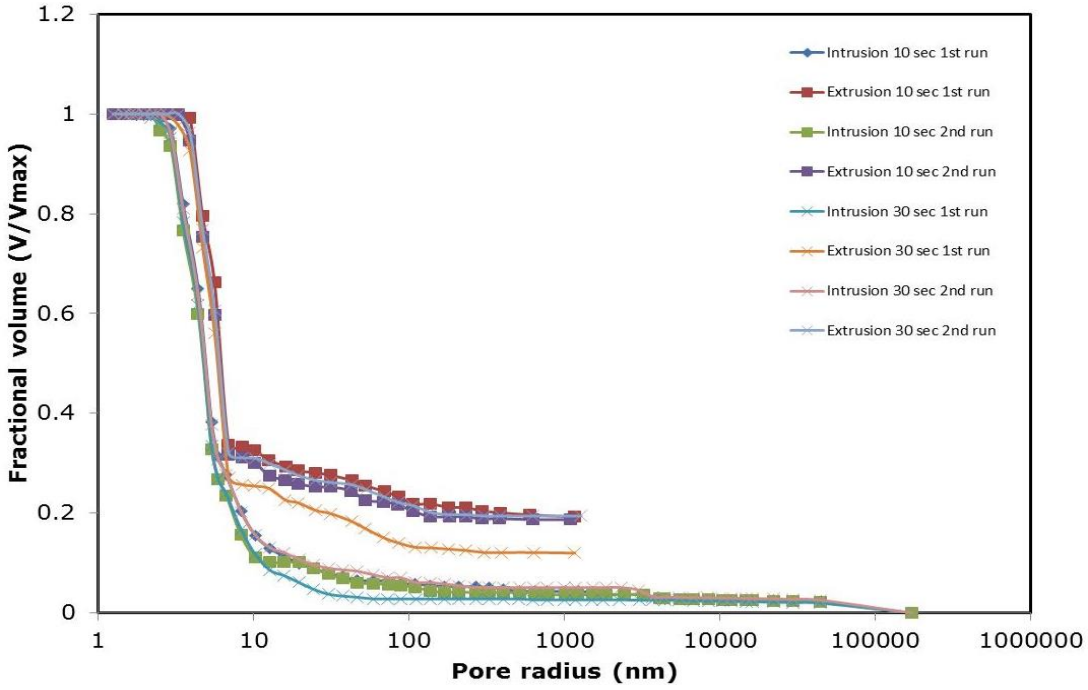

Figure B1. 12: mercury intrusion/extrusion data for Al-3992E sample at different equilibration time analysed using the Kloubek correlations.

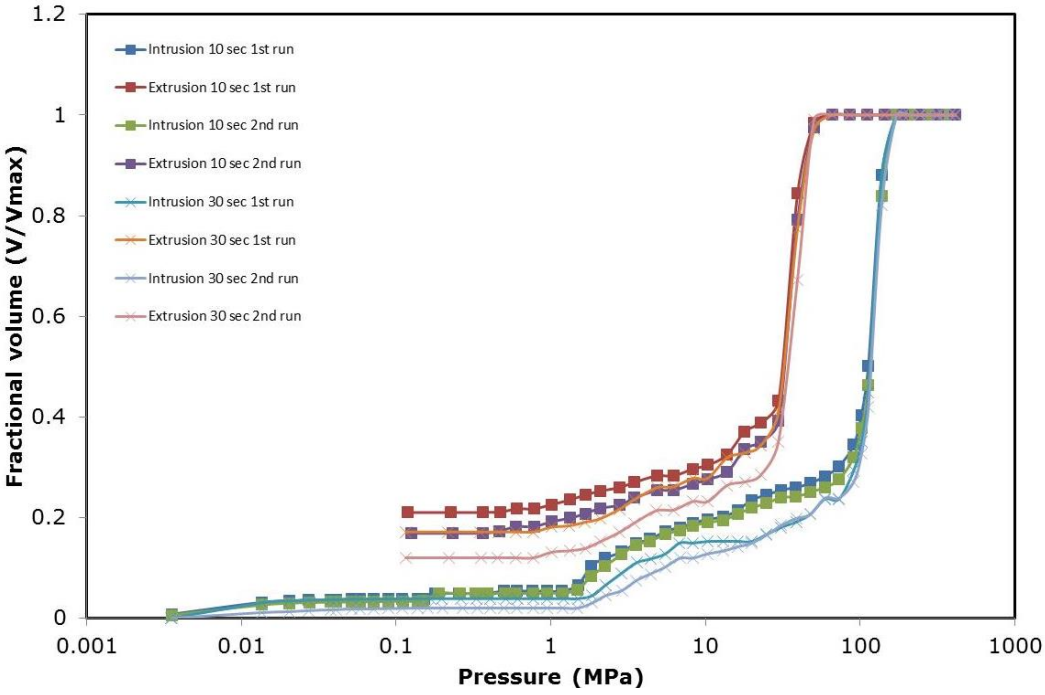

Figure B1. 13: mercury intrusion/extrusion data for Al-3984T sample at different equilibration time.

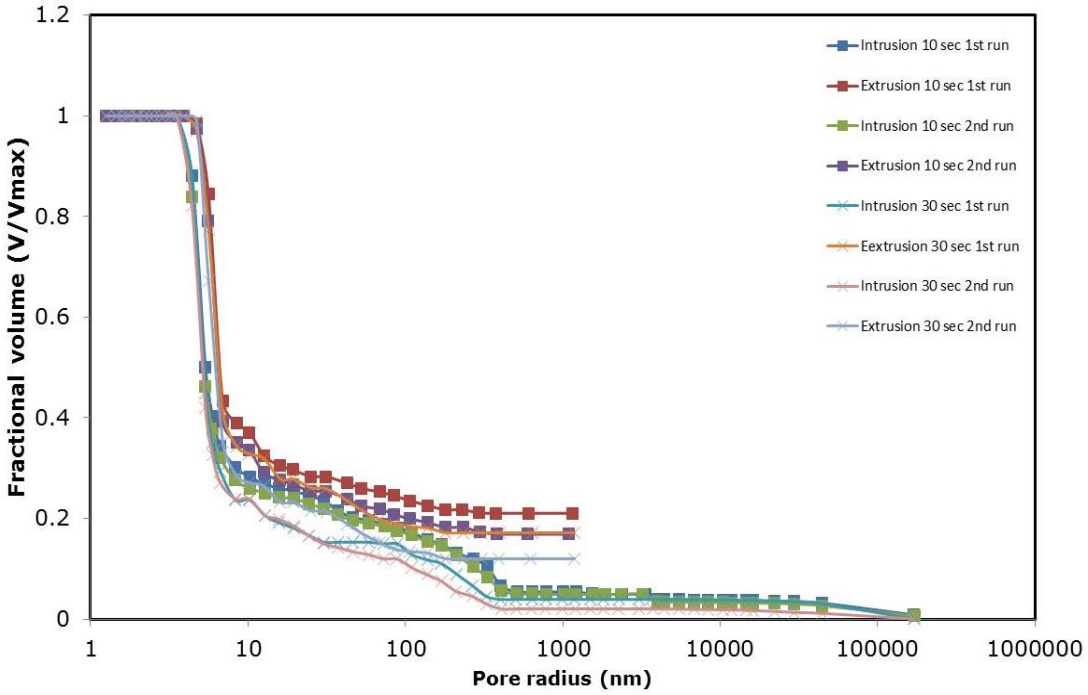

Figure B1. 14: mercury intrusion/extrusion data for Al-3984T sample at different equilibration time analysed using the Kloubek correlations.

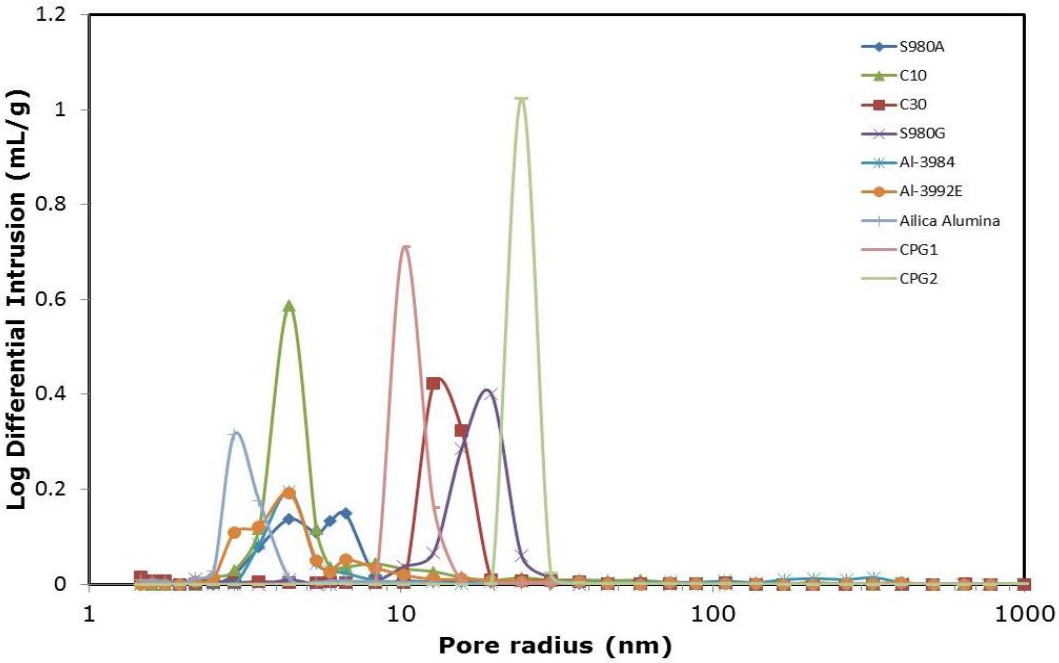

Figure B1. 15: Pore size distribution determined by mercury intrusion porosimetry for the samples used in this thesis.

B.2. Mercury entrapment calculation

The entrapment of mercury is defined as the percentage ratio of the extruded volume of mercury at the minimum pressure to the total amount of mercury intruded into the sample. Considering Fig, 4.1 for S1 sample with equilibration time of 10s. The maximum intrusion volume is 0.727 mL/g and the minimum intrusion volume is 0.0451 mL/g.

$$E_m = \left(\frac{0.1594-0.0451}{0.727}\right) \text{ x } 100$$

Mercury entrapment = 15.72%

Appendix C: Supporting information for CPMG NMR Technique

This appendix contains extra supporting information that the reader may find beneficial on how the ganglia sizes of mercury from mercury porosimetry and differential scanning calorimetric technique were calculated. It also shows how the ganglia sizes for cyclohexane were calculated from the CPMG NMR technique.

C1. Calculation for the ganglia sizes from Hg/DSC experiment for G2 sample.

Time (hour)	Relaxation time T_2 (s)
0	0.32495
24	0.17544
48	0.17482
72	0.17986
96	0.17996

Average T_2 values for G2 sample 0.1775±0.002

Melting point of mercury -39.4 ºC

Entrapped mercury peak -41.4 ºC

$\Delta T = -2$

$d_{DSC} = 90/2 = 45$ nm

$r_{dsc} = 22.5$

C2. Calculations for the cyclohexane ganglia sizes from CPMG experiment for G2 sample.

Volume = 1.1 ± 0.1 cc/g

BET surface area = 102±9

From Eq. 3.28, $\frac{S}{V} = \frac{2}{r}$ for cylindrical pore

Rearranging the equation, r = $\frac{2}{(S/V)}$

r = $\frac{2}{(\frac{102}{1.1\ x\ 10^{-6}})}$ = 21.5686

(0.177/0.325)*21.5686 =11.75 nm

C3. Calculation for the ganglia sizes from Hg/DSC experiment for s1 sample.

Time (min)	Relaxation time T_2 (s)
0	100
30	81.8
80	87

Average of T2 values for the plateau region 81.8+87 = 84.4

$\frac{84.4}{100} x\ 6 =$ 5.064 nm

Calculated value from mercury/DSC experiment = 7.8 ± 0.3

C4. Calculations for the cyclohexane ganglia sizes from CPMG experiment for S1 sample.

Volume = 0.9 ± 0.03 cc/g

BET surface area = 217±5

r = $\frac{2}{(\frac{217}{0.9\ x\ 10^{-6}})}$ = 8.8479 nm

$\frac{84.4}{100} x$ 8.8479 = **7.4676** nm

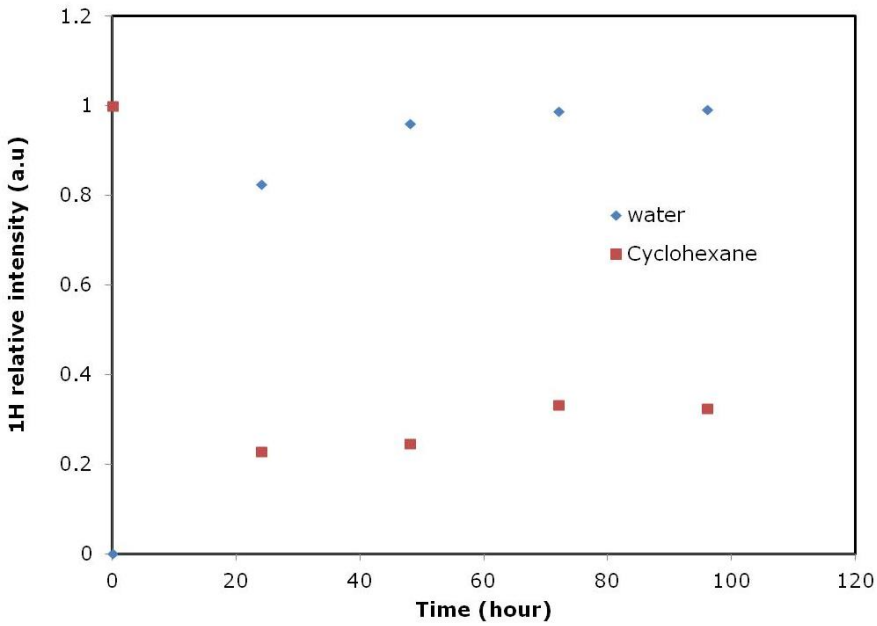

Figure C1.1: A repeat of the variation of fractional proton intensities for water and cyclohexane for G2 silica sample against experimental time.

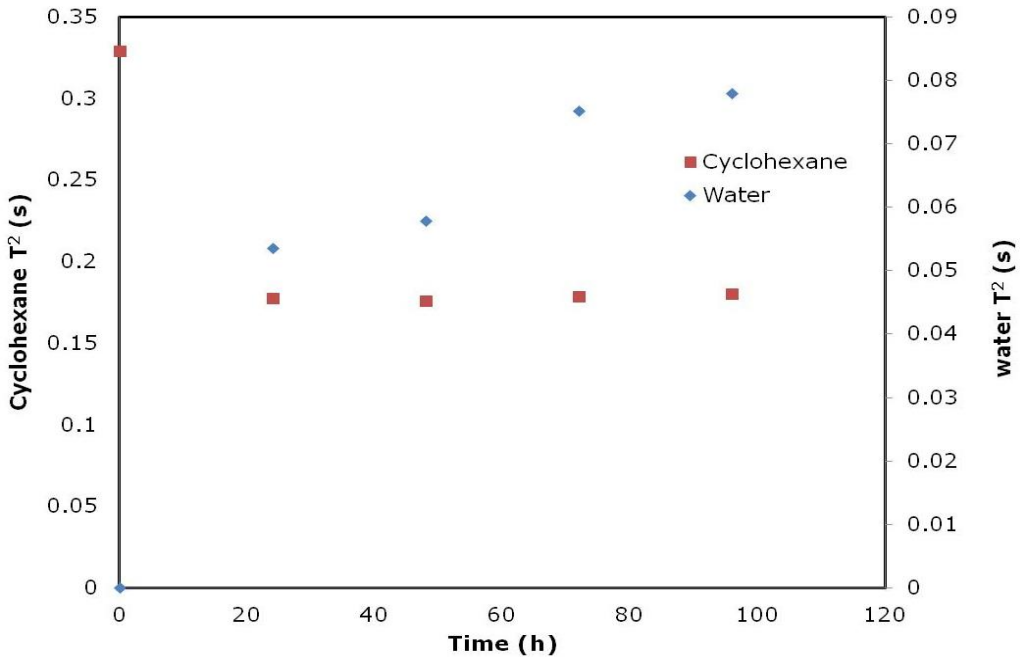

Figure C1.2: A repeat of the variation of average T_2 for cyclohexane and water with time during LLE experiment for G2 silica sample.

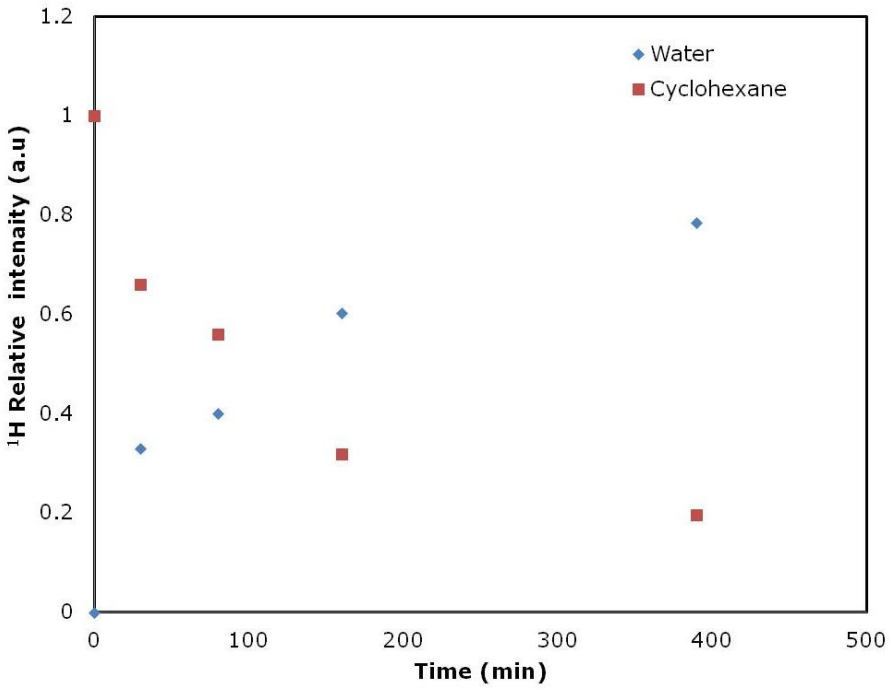

Figure C1.3: A repeat of the variation of fractional proton intensities for water and cyclohexane for S1 silica sample against experimental time.

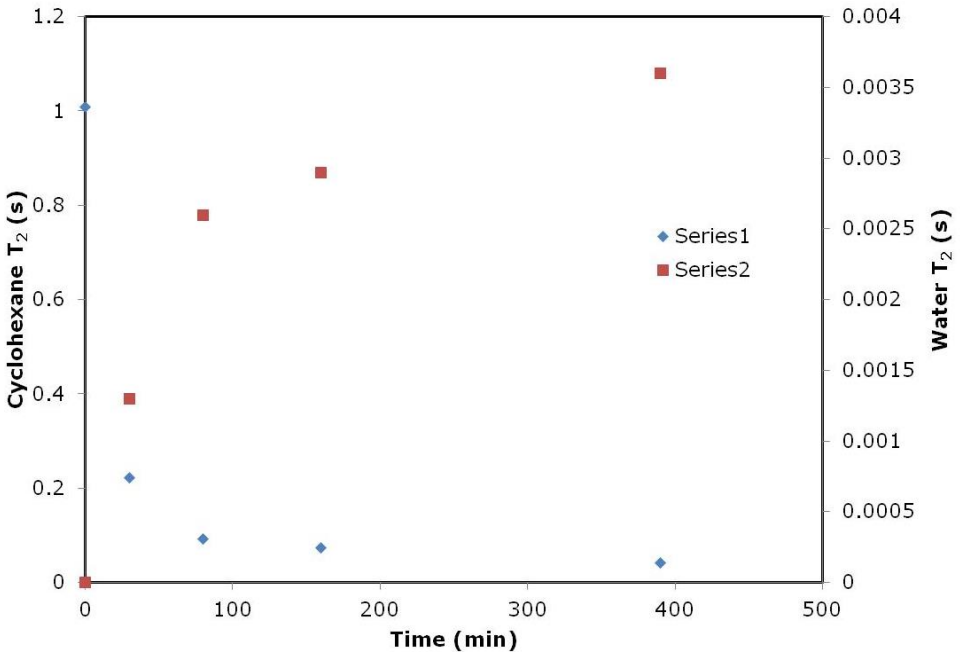

Figure C1.4: A repeat of the variation of average T_2 for cyclohexane and water with time during LLE experiment for S1 silica sample.

Appendix D: Supporting information for NMR PFG technique

This appendix contains extra supporting information on how the diffusivity and rms values were calculated.

The diffusivity values were measured using the change in echo intensity *R* for PFG experiments, which is given by:

$$R = \frac{I}{I_o} = exp\left[D\gamma^2 g^2 \delta^2 \left(\Delta - {}^{\delta}/_{3}\right)\right]$$

Gamma, γ = 4.26E3

Gradient from table D1

Applied field gradient, δ = 1.25E-3

Diffusion time, Δ = 2.49E-2

A plot of ln (I/I_o) versus $\gamma^2 g^2 \delta^2 \left(\Delta - \frac{\delta}{3}\right)$ from table D1 yields the diffusion coefficient from the slope of the straight line obtained.

And the root mean square displacement was calculated using the Einstein equation

$\langle r^2\ (t)\rangle = 6D_{PFG}t$

rms = (6*1.99E-9*2.49E-2)^0.5 = 1.73E-5

Table D1- Parameters used in calculating diffusion coefficient

Gradient	Experiment	Calculated	Difference	$r^2g^2\delta^2$ (Δ - δ/3)	ln(I)
2.41E+00	1.00E+00	9.95E-01	-4.90E-03	1.59E+06	0.00E+00
1.20E+01	9.21E-01	9.22E-01	1.46E-03	3.97E+07	-8.24E-02
1.69E+01	8.53E-01	8.55E-01	1.67E-03	7.77E+07	-1.59E-01
2.06E+01	7.91E-01	7.92E-01	1.25E-03	1.16E+08	-2.34E-01

2.37E+01	7.33E-01	7.35E-01	1.09E-03	1.54E+08	-3.10E-01
2.65E+01	6.80E-01	6.81E-01	1.12E-03	1.92E+08	-3.86E-01
2.90E+01	6.30E-01	6.31E-01	1.11E-03	2.30E+08	-4.62E-01
3.13E+01	5.84E-01	5.85E-01	8.21E-04	2.68E+08	-5.38E-01
3.35E+01	5.42E-01	5.42E-01	3.20E-04	3.06E+08	-6.13E-01
3.55E+01	5.03E-01	5.03E-01	-7.66E-05	3.44E+08	-6.88E-01
3.74E+01	4.66E-01	4.66E-01	-4.35E-04	3.82E+08	-7.63E-01
3.92E+01	4.32E-01	4.32E-01	-5.41E-04	4.20E+08	-8.39E-01
4.09E+01	4.01E-01	4.00E-01	-6.22E-04	4.58E+08	-9.15E-01
4.26E+01	3.72E-01	3.71E-01	-8.94E-04	4.96E+08	-9.89E-01
4.42E+01	3.45E-01	3.44E-01	-1.09E-03	5.34E+08	-1.06E+00
4.57E+01	3.20E-01	3.19E-01	-1.20E-03	5.72E+08	-1.14E+00

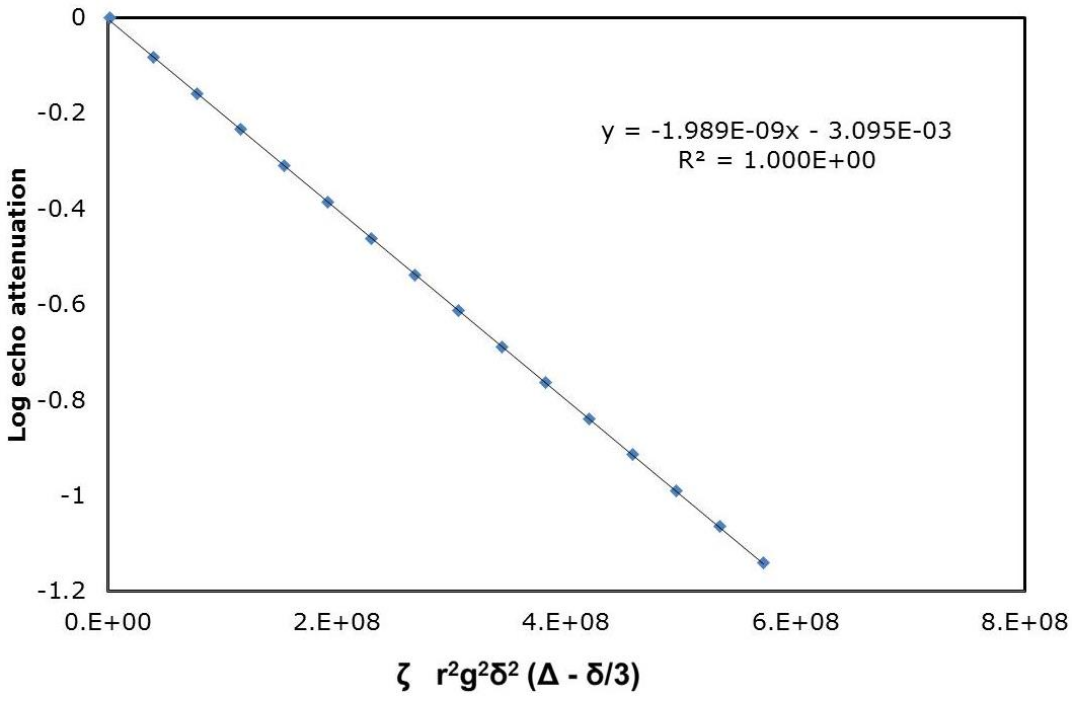

Figure D1. 1: NMR diffusion data for *n*-pentane at 250 K without excess fluid showing single component fit.

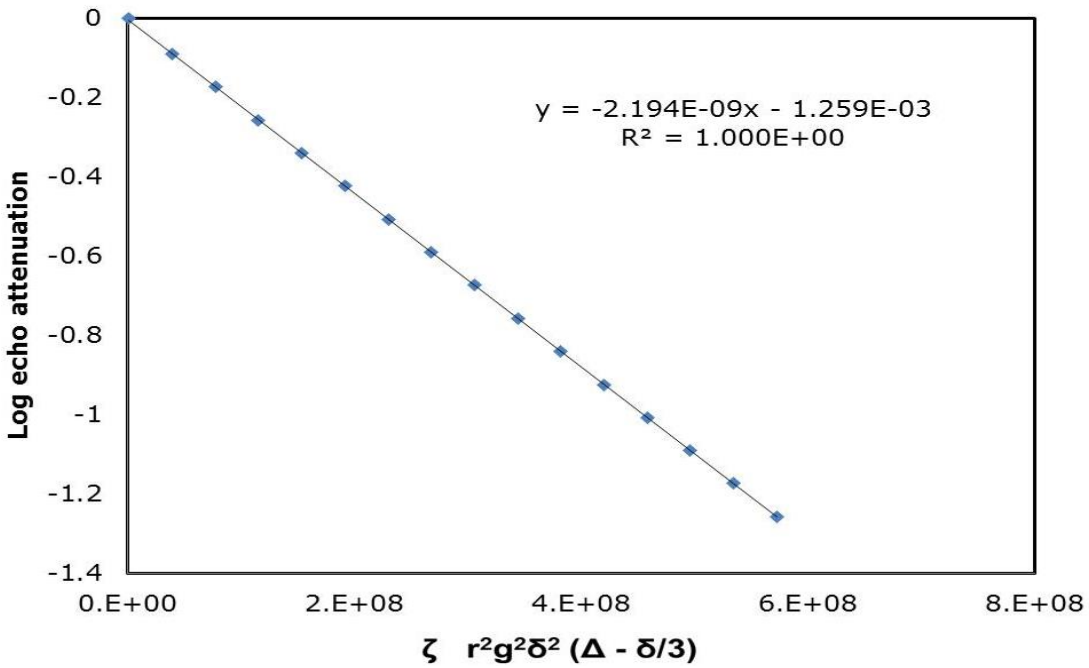

Figure D1. 2: NMR diffusion data for *n*-pentane at 257 K without excess fluid showing single component fit.

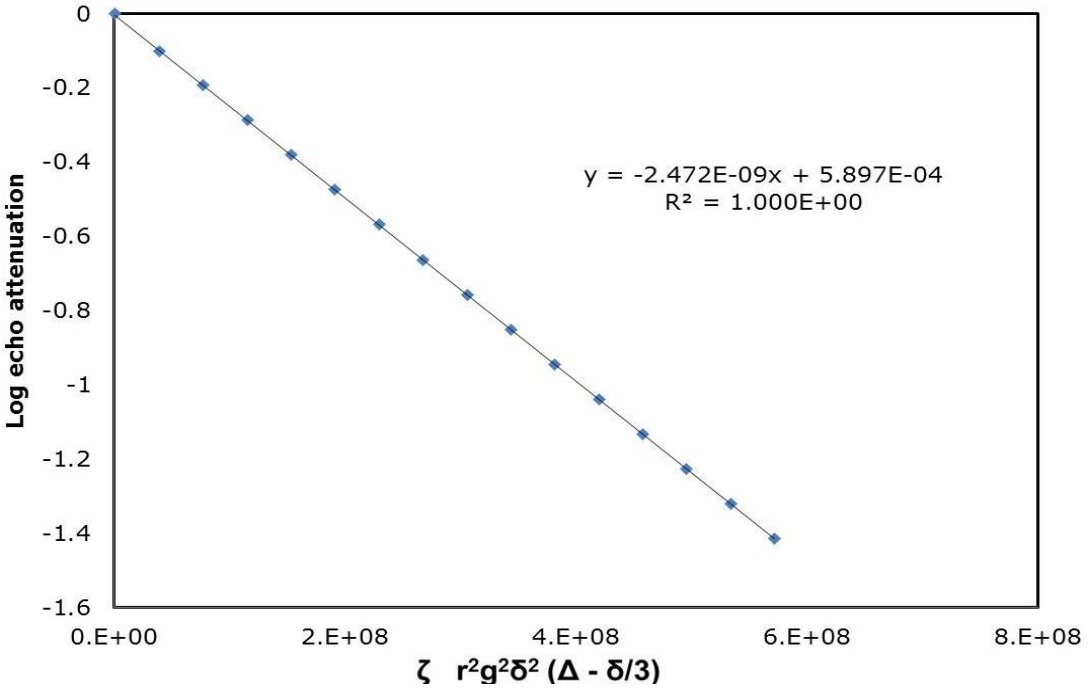

Figure D1. 3: NMR diffusion data for *n*-pentane at 265 K without excess fluid showing single component fit.

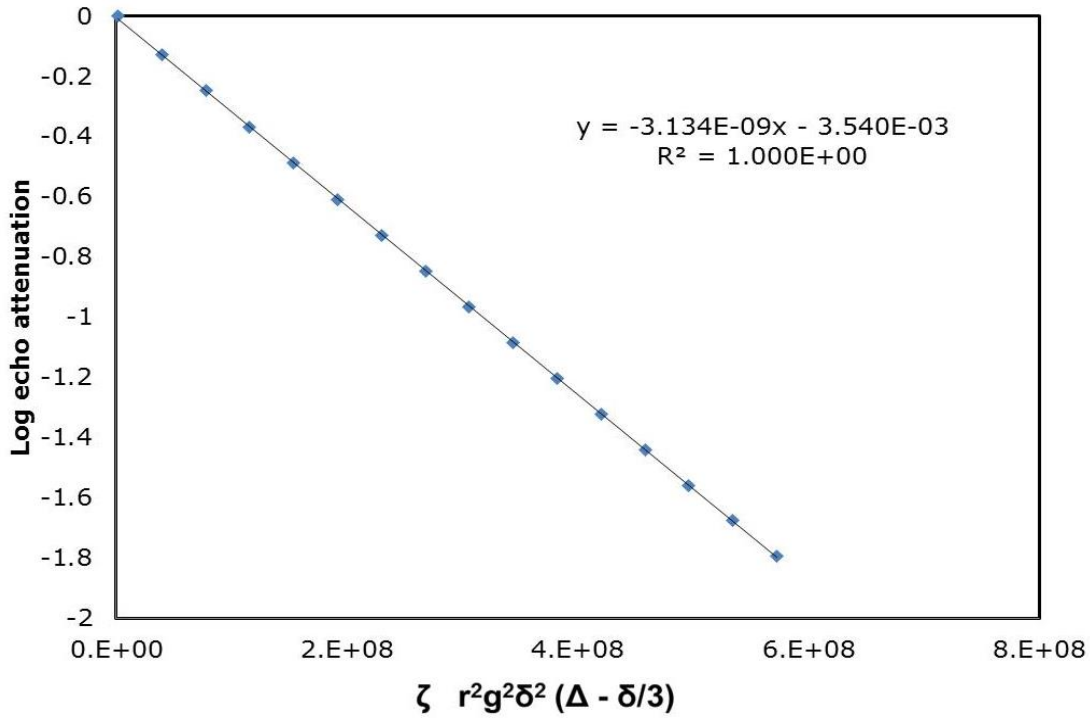

Figure D1. 4: NMR diffusion data for *n*-pentane at 280 K without excess fluid showing single component fit.

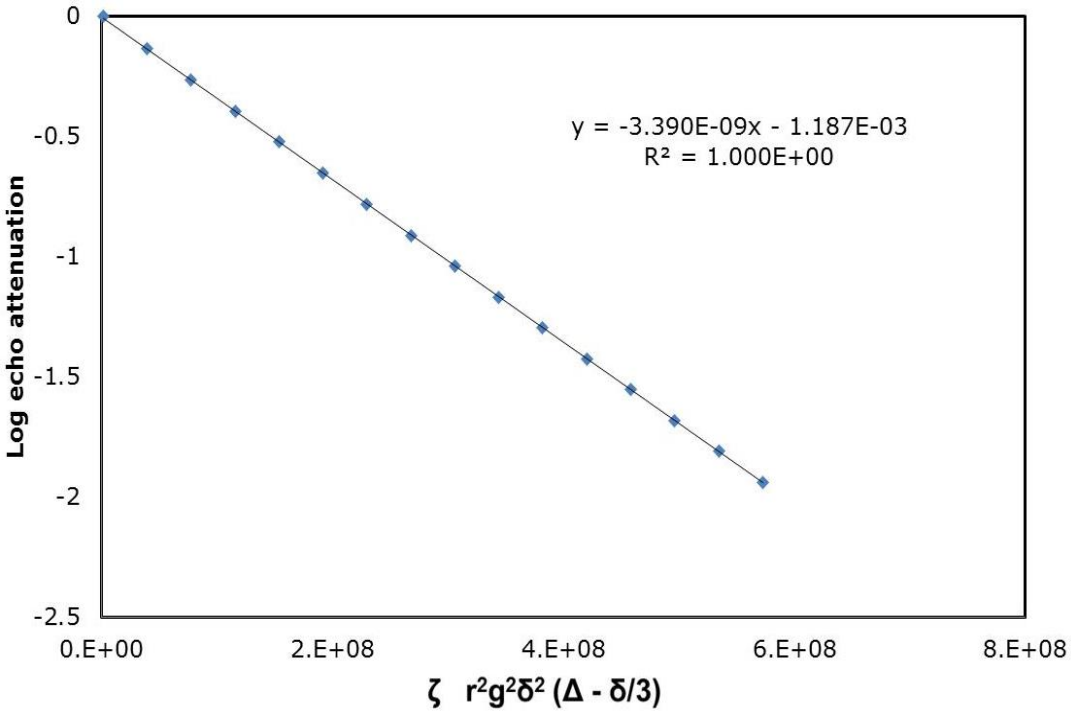

Figure D1. 5: NMR diffusion data for *n*-pentane at 288 K without excess fluid showing single component fit.

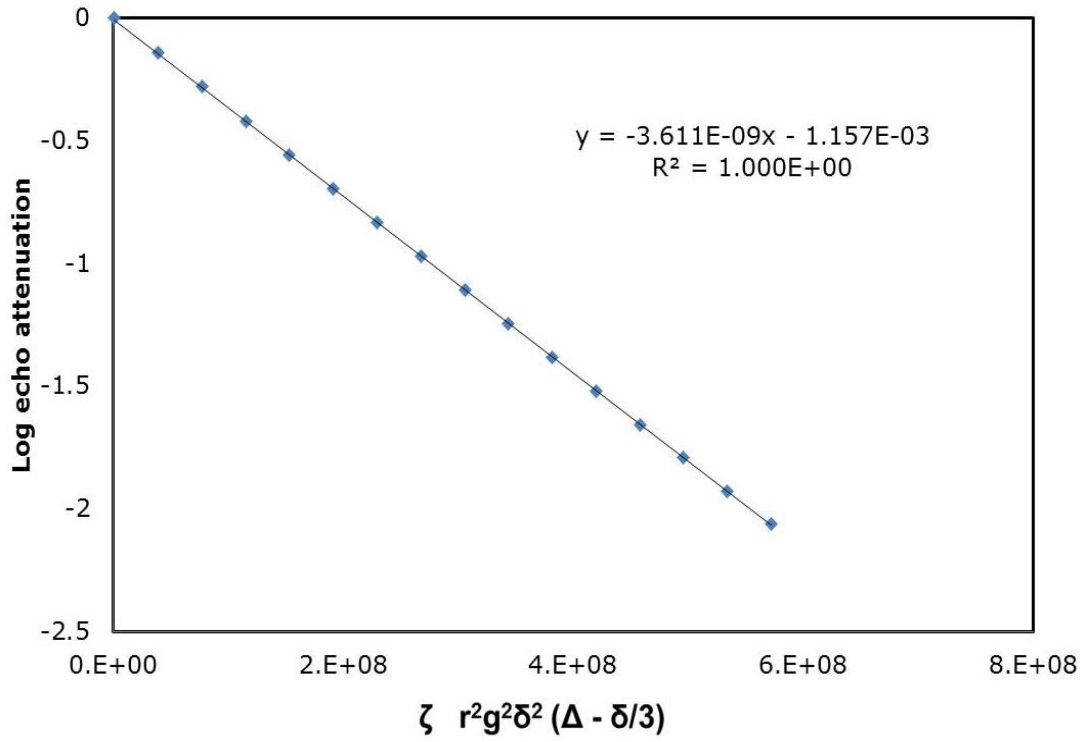

Figure D1. 6: NMR diffusion data for *n*-pentane at 293 K without excess fluid showing single component fit.

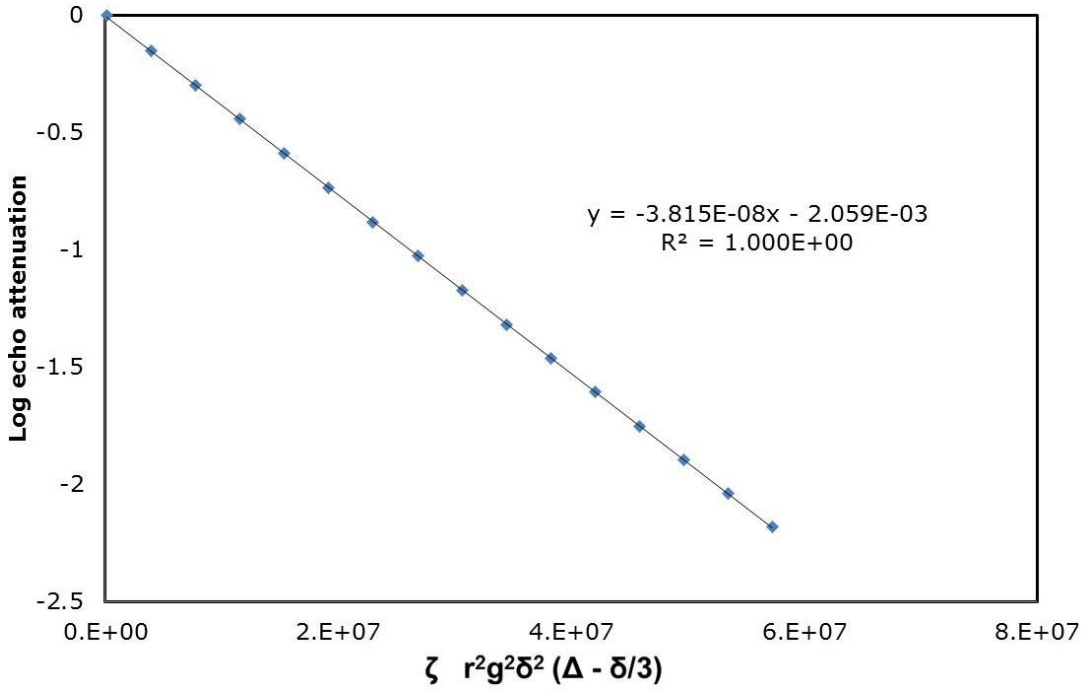

Figure D1. 7: NMR diffusion data for *n*-pentane at 298K without excess fluid showing single component fit.

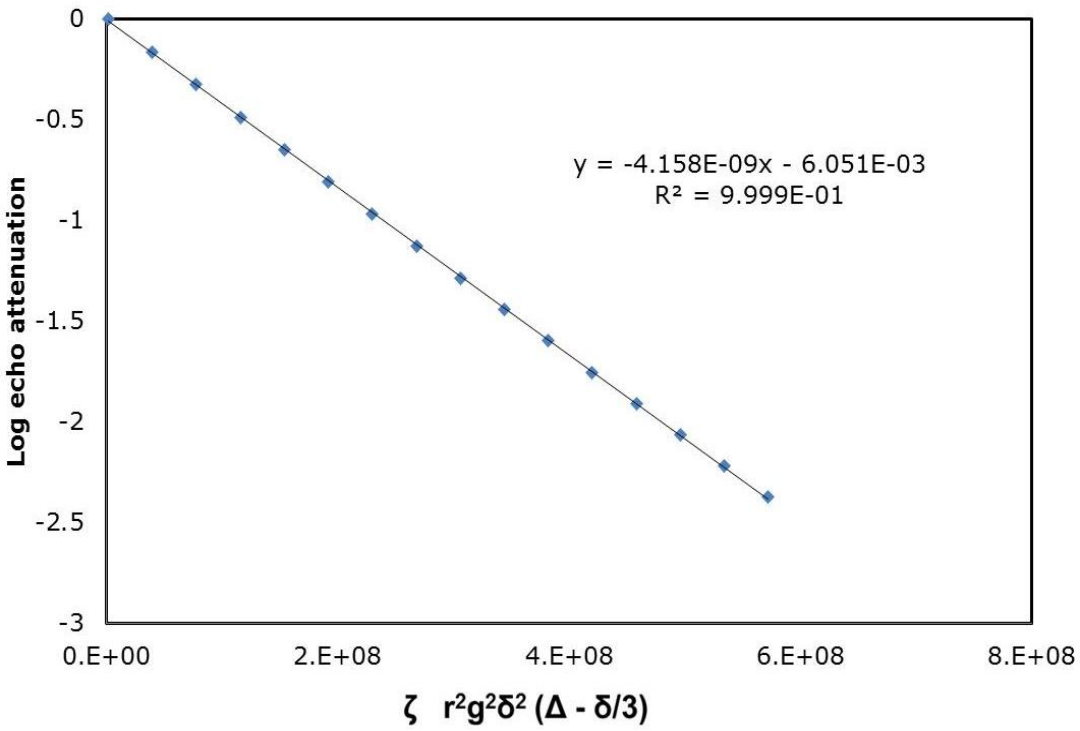

Figure D1. 8: NMR diffusion data for *n*-pentane at 303 K without excess fluid showing single component fit.

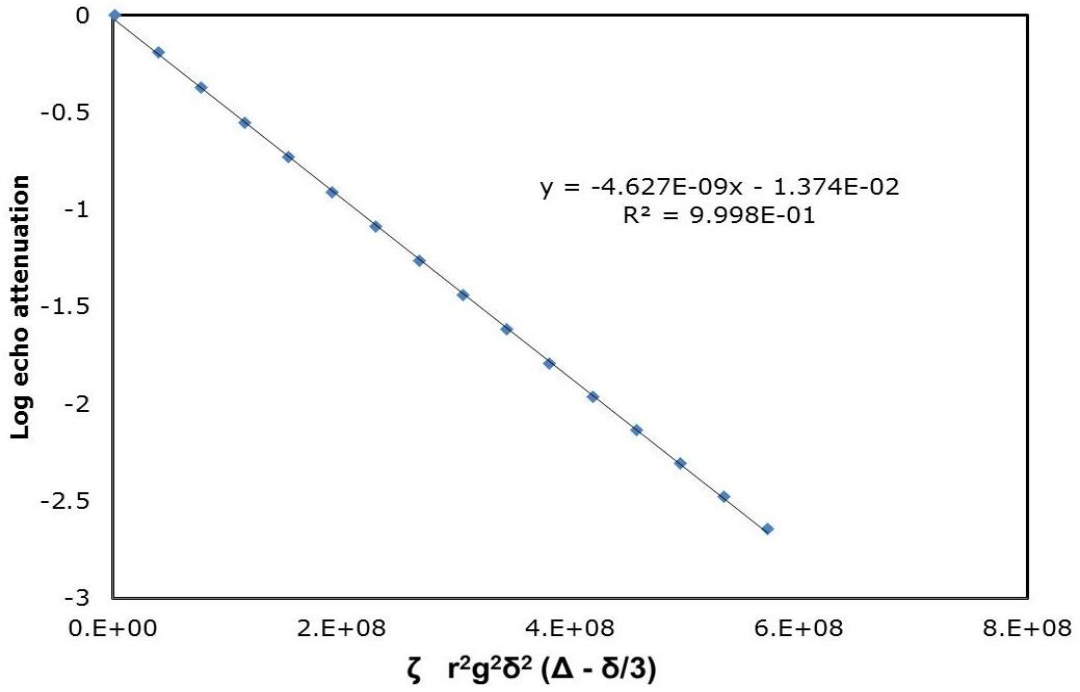

Figure D1. 9: NMR diffusion data for *n*-pentane at 309 K without excess fluid showing single component fit.

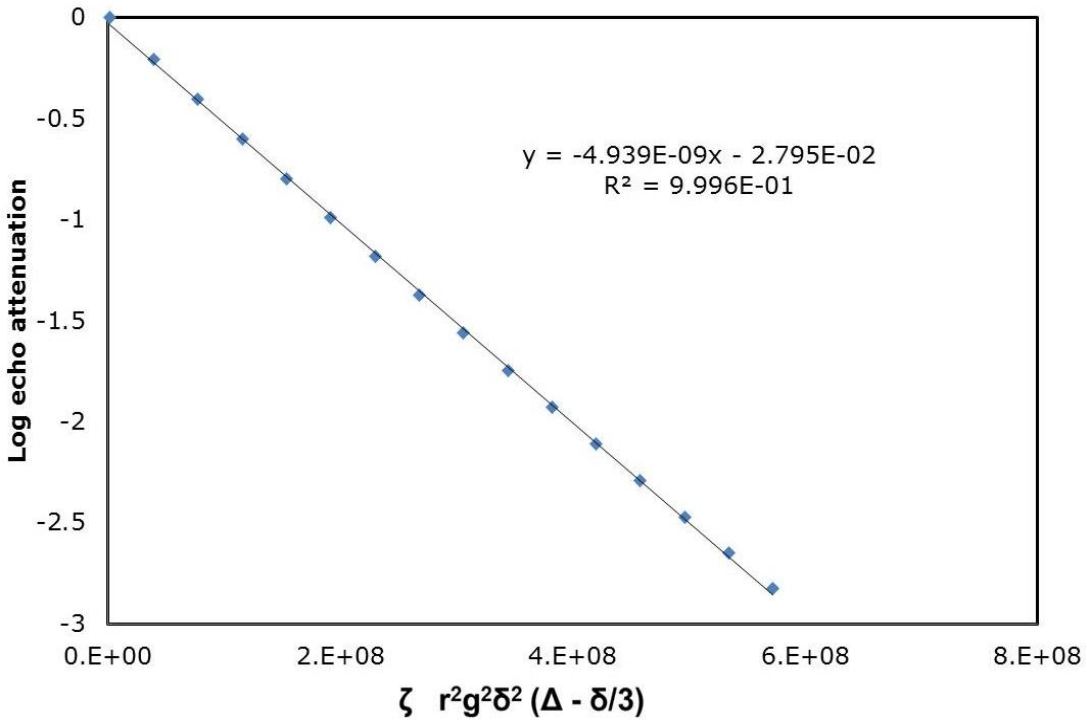

Figure D1. 10: NMR diffusion data for *n*-pentane at 311 K without excess fluid showing single component fit.

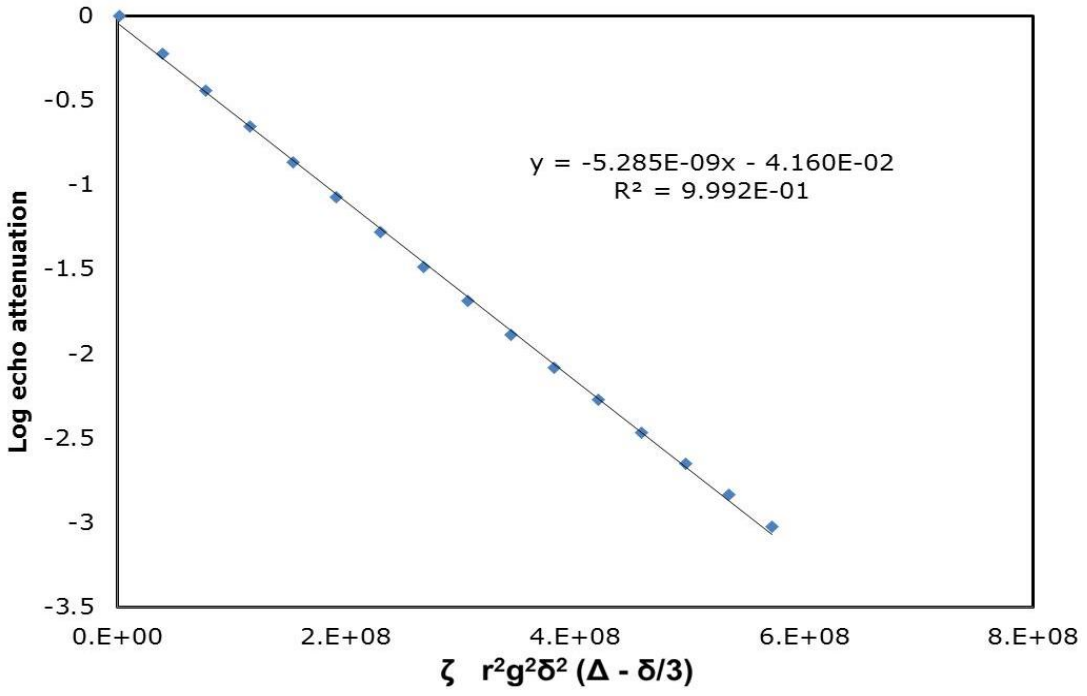

Figure D1. 11: NMR diffusion data for *n*-pentane at 313 K without excess fluid showing single component fit.

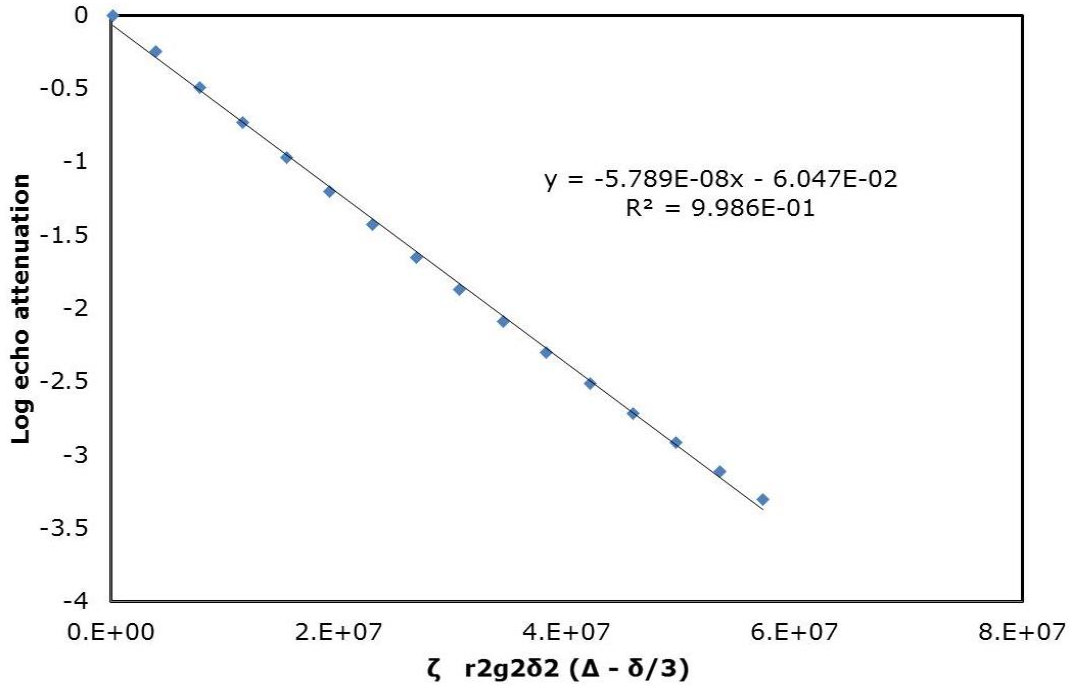

Figure D1. 12: NMR diffusion data for *n*-pentane at 315 K without excess fluid showing single component fit.

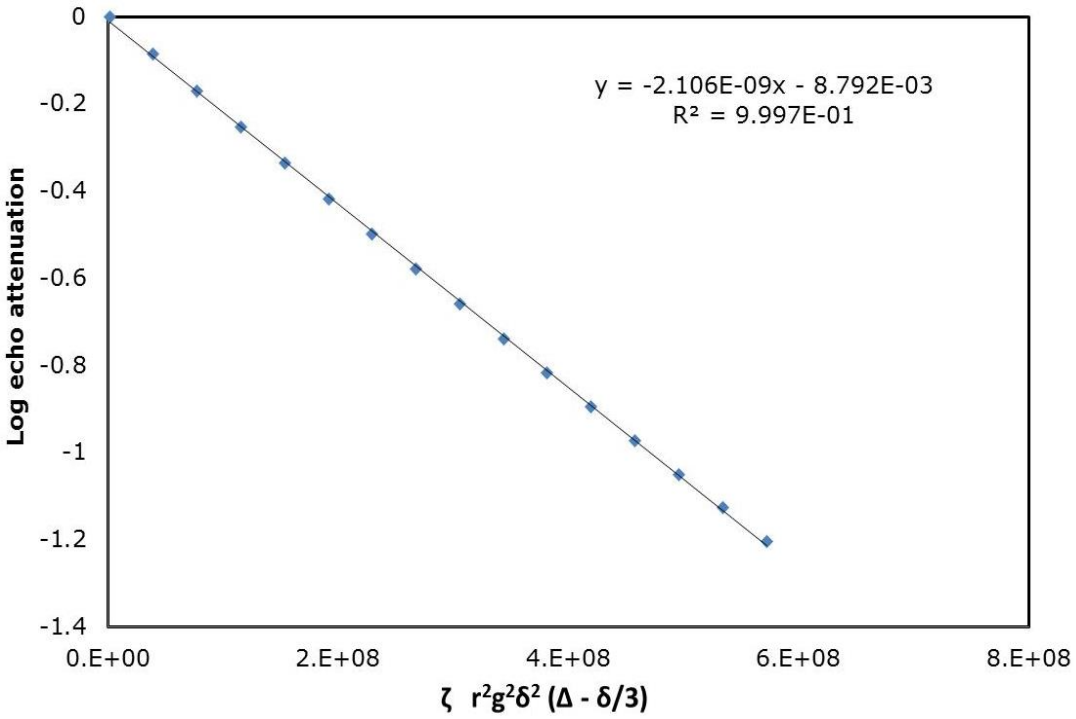

Figure D1. 13: NMR diffusion data for *n*-pentane at 250 K with excess fluid showing single component fit.

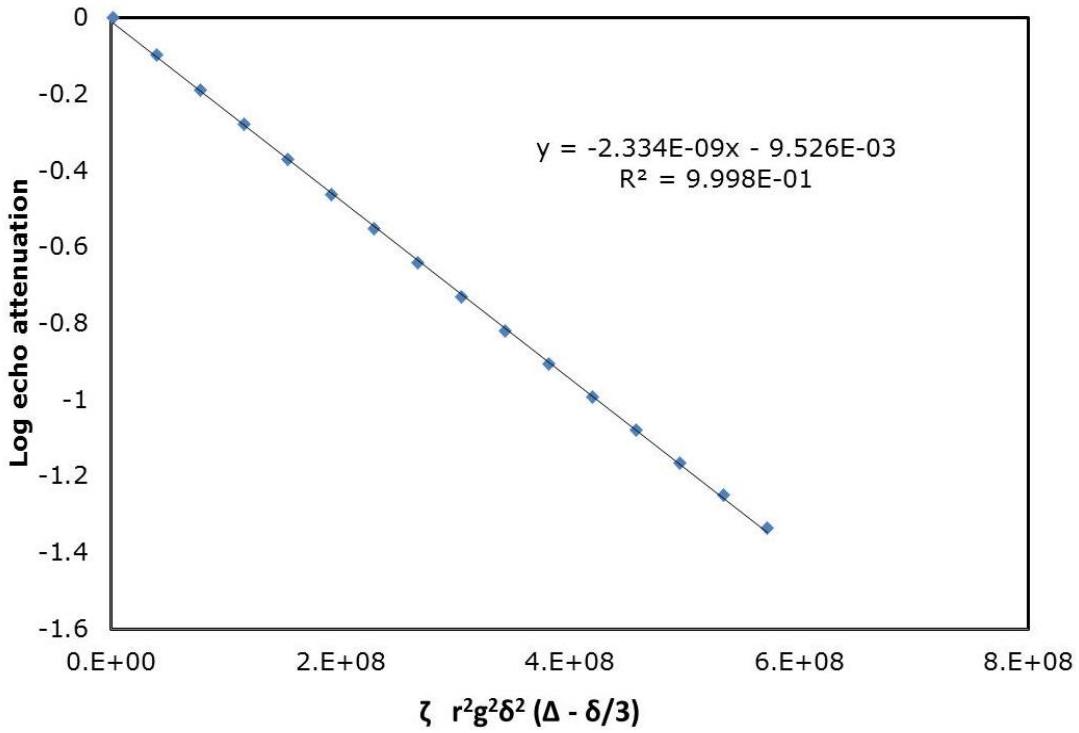

Figure D1. 14: NMR diffusion data for *n*-pentane at 257 K with excess fluid showing single component fit.

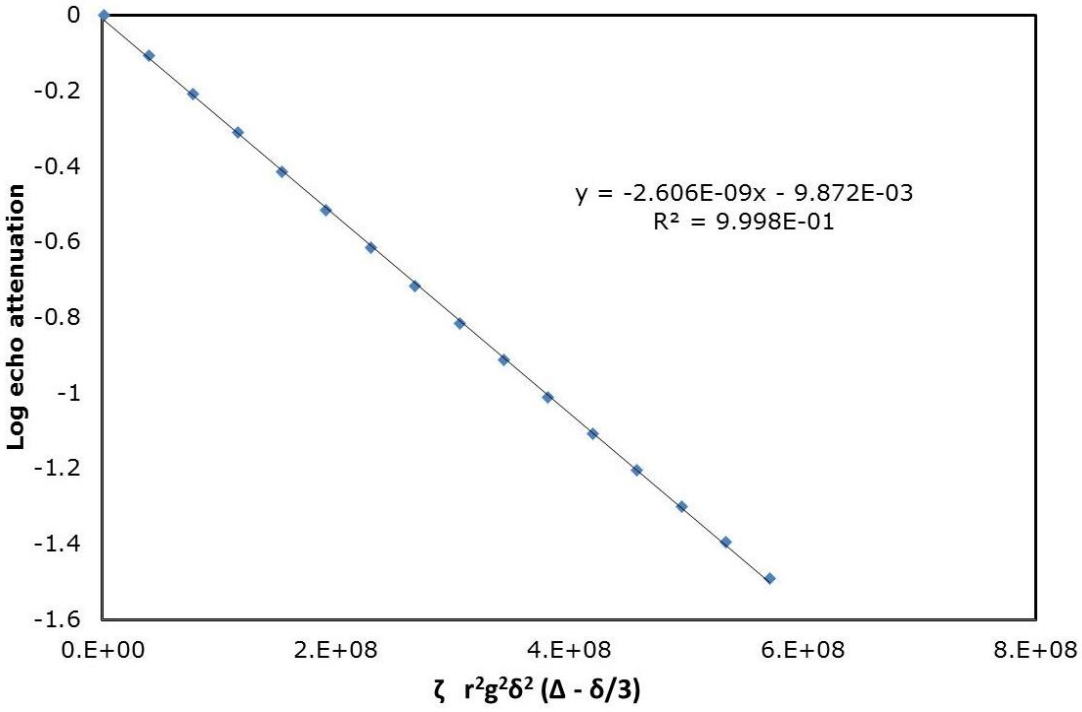

Figure D1. 15: NMR diffusion data for *n*-pentane at 265 K with excess fluid showing single component fit.

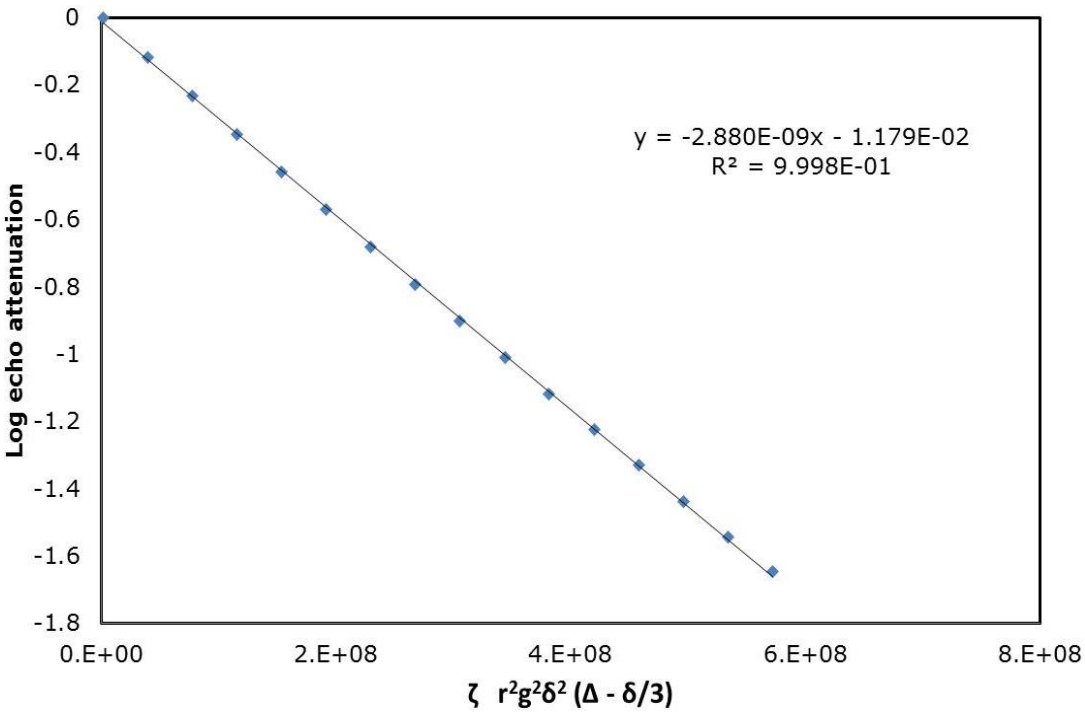

Figure D1. 16: NMR diffusion data for *n*-pentane at 273 K with excess fluid showing single component fit.

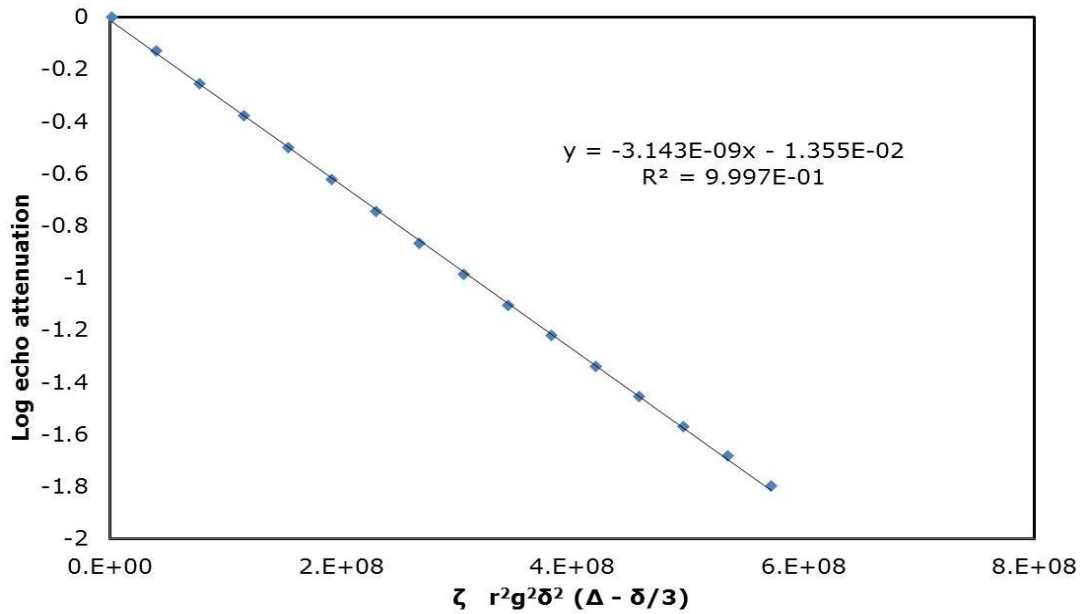

Figure D1. 17: NMR diffusion data for *n*-pentane at 280 K with excess fluid showing single component fit.

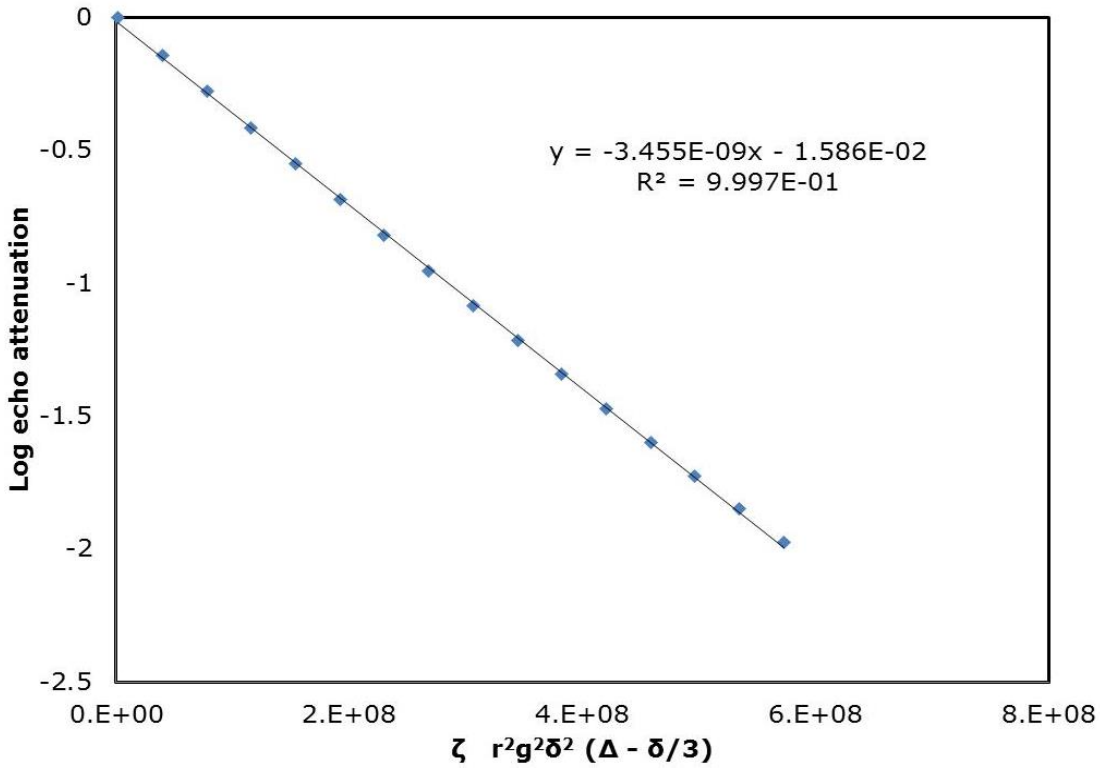

Figure D1. 18: NMR diffusion data for *n*-pentane at 288 K with excess fluid showing single component fit.

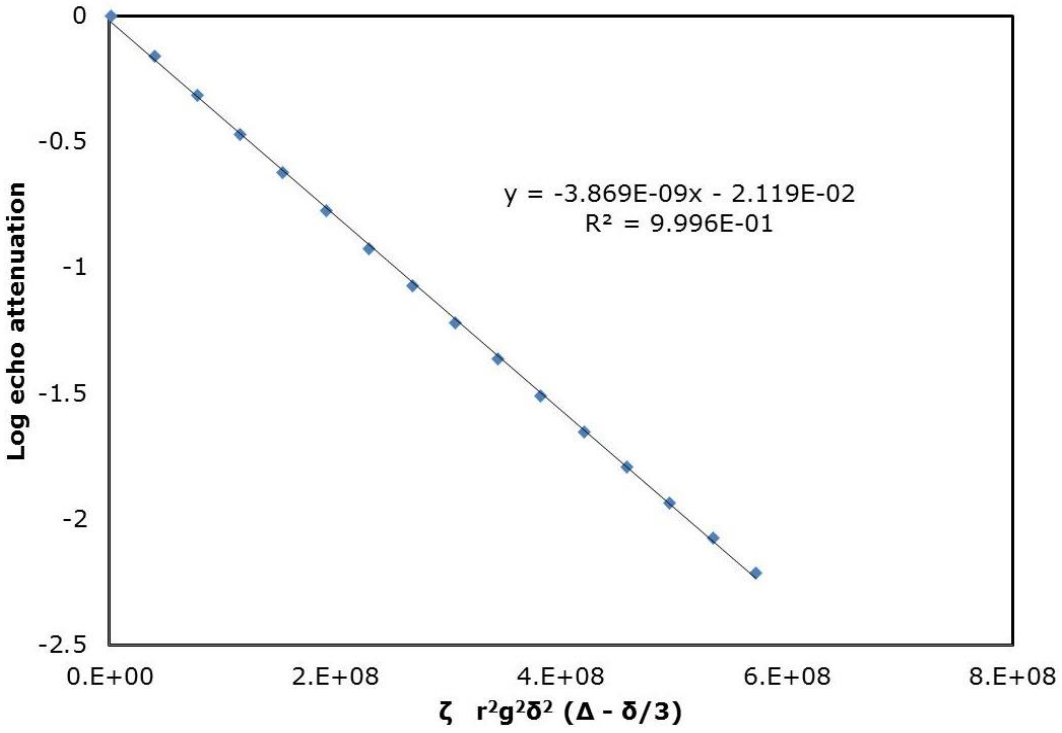

Figure D1. 19: NMR diffusion data for *n*-pentane at 298 K with excess fluid showing single component fit.

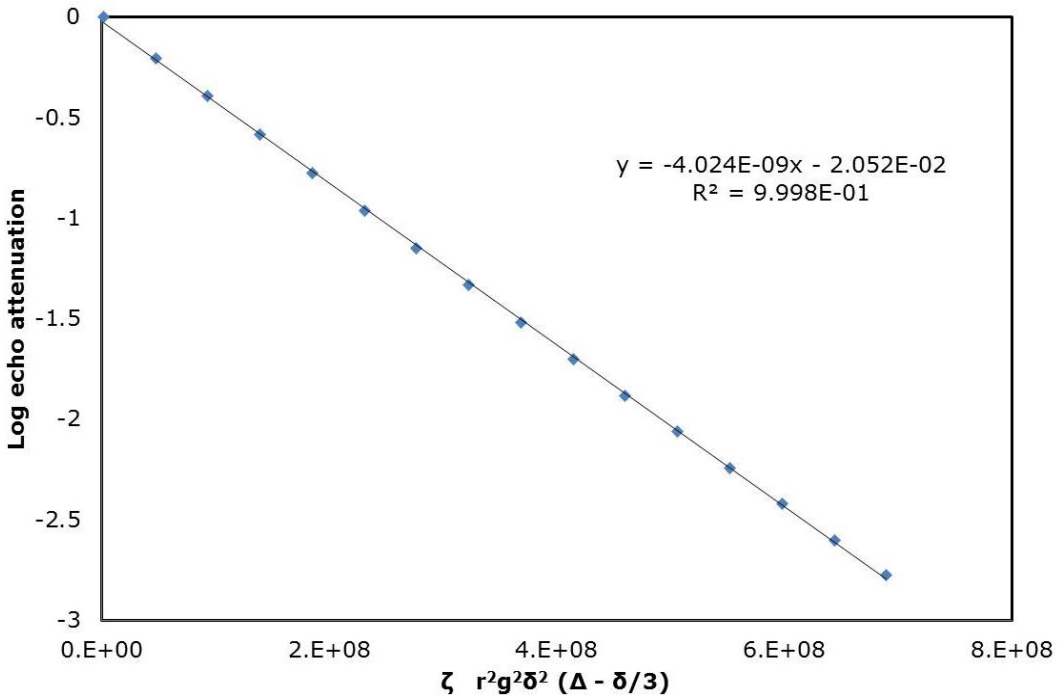

Figure D1. 20: NMR diffusion data for *n*-pentane at 303 K with excess fluid showing single component fit.

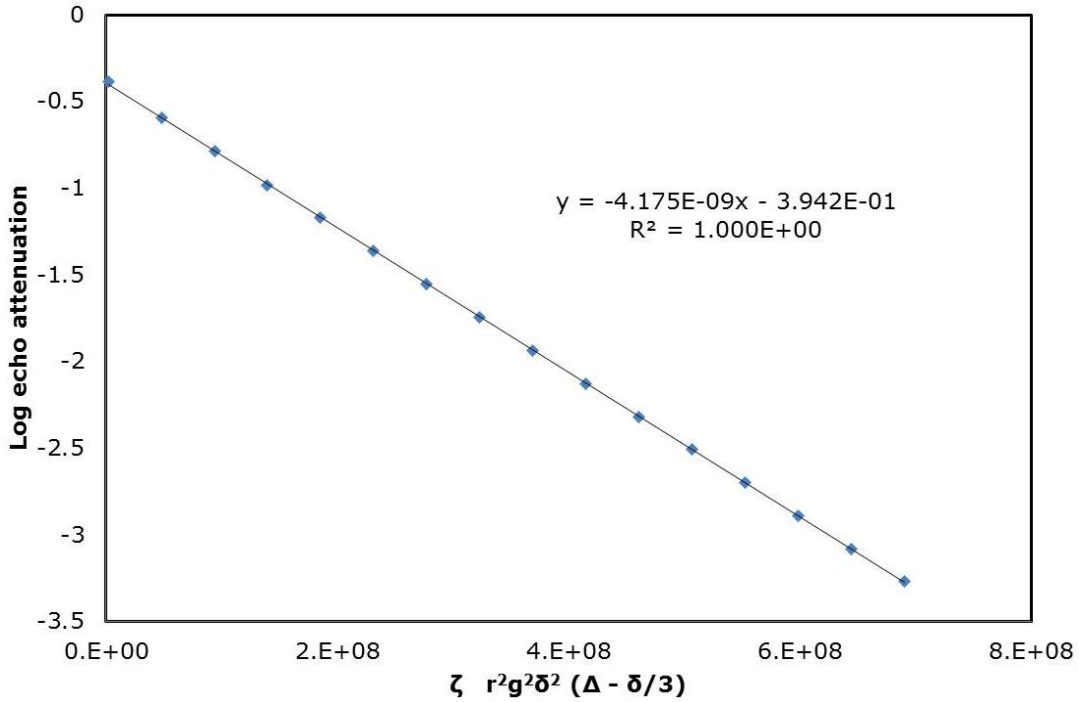

Figure D1. 21: NMR diffusion data for *n*-pentane at 309 K with excess fluid showing single component fit.

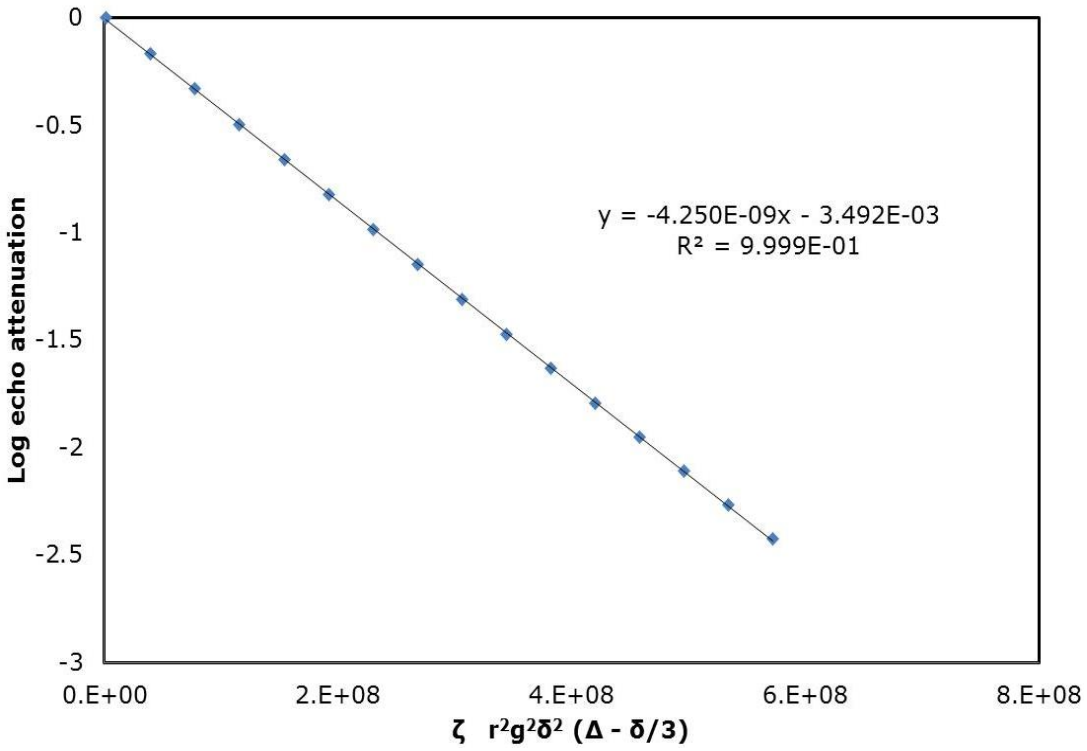

Figure D1. 22: NMR diffusion data for *n*-pentane at 311 K with excess fluid showing single component fit.

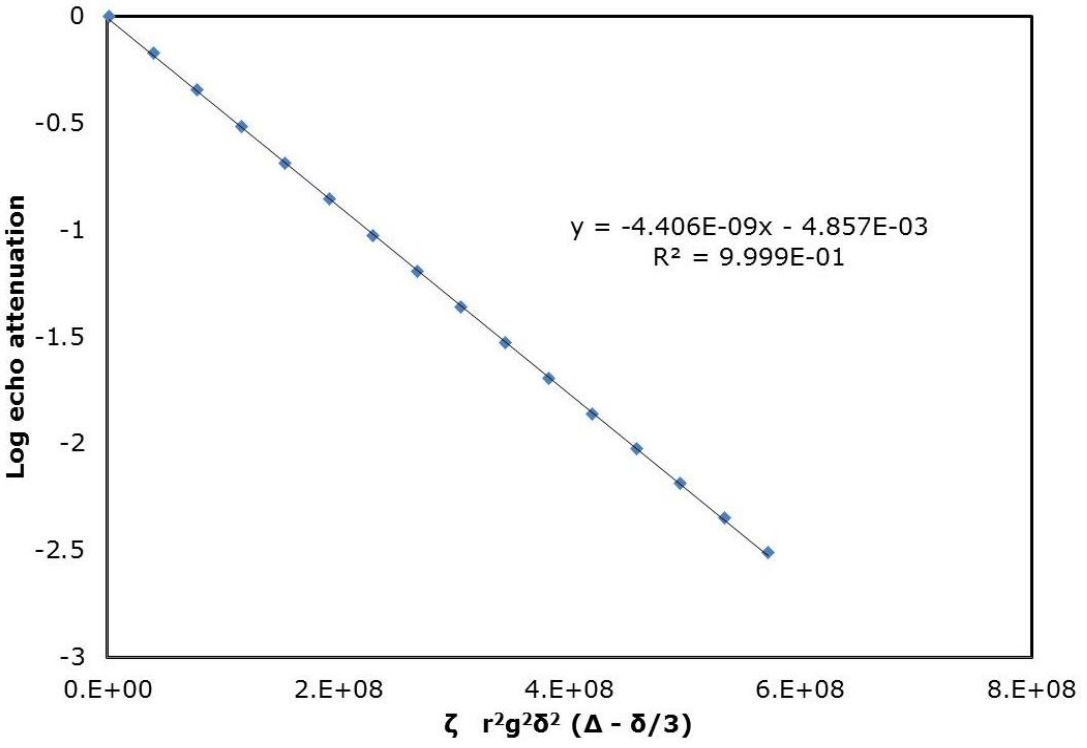

Figure D1. 23: NMR diffusion data for *n*-pentane at 313 K with excess fluid showing single component fit.

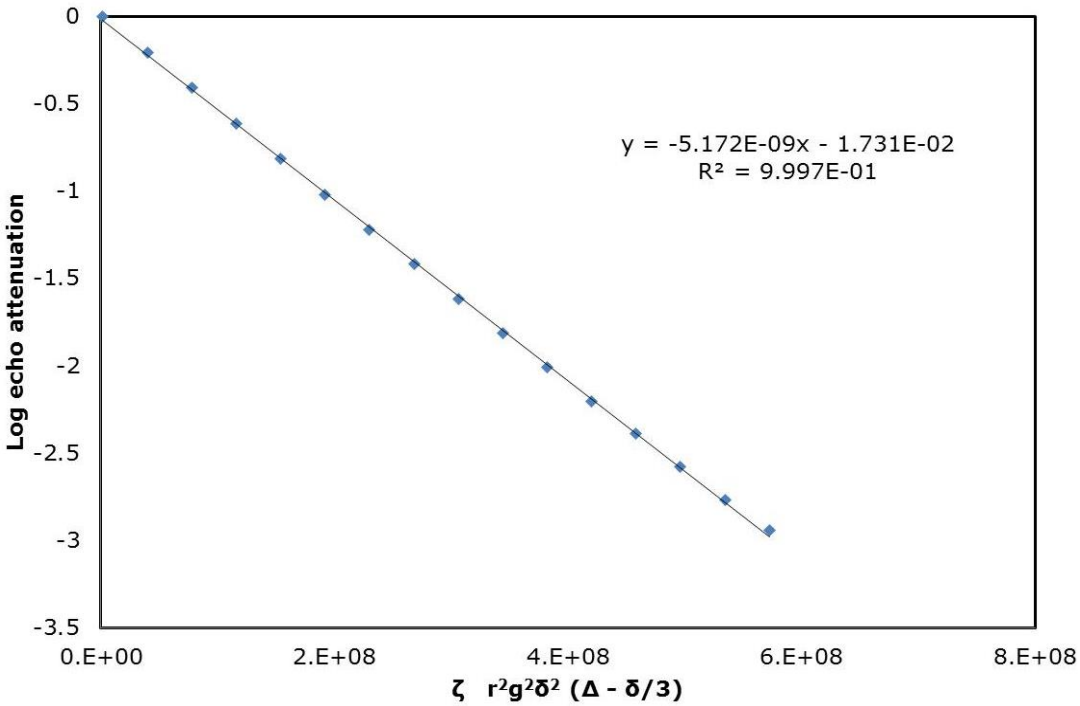

Figure D1. 24: NMR diffusion data for *n*-pentane at 315 K with excess fluid showing single component fit.